Laminar Analogues of Atmospheric Vortices

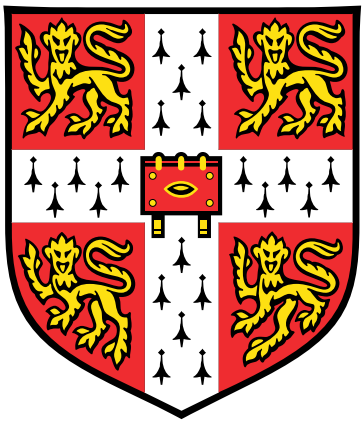

Jack W Atkinson

Supervisor: Prof. P.A. Davidson

Department of Engineering
University of Cambridge

This dissertation is submitted for the degree of
Doctor of Philosophy

Peterhouse September 2019

Declaration

I hereby declare that except where specific reference is made to the work of others, the contents of this dissertation are original and have not been submitted in whole or in part for consideration for any other degree or qualification in this, or any other university. This dissertation is my own work and contains nothing which is the outcome of work done in collaboration with others, except as specified in the text and Acknowledgements. This dissertation contains fewer than 65,000 words including appendices, bibliography, footnotes, tables and equations and has fewer than 150 figures.

Unless otherwise specified the images in this work are my own. Where possible all external images are licenced under Creative Commons and credit to the original owner is given. When this was not possible permission was sought from the owners of images for their reproduction in this thesis and credit is given. The only exception to this is for figures that have been reproduced from scientific publications.

Jack W Atkinson
September 2019

Abstract

Laminar Analogues of Atmospheric Vortices

This thesis comprises a series of investigations into isolated vortices that exist within the atmosphere. It consists of numerical and experimental investigations backed up by mathematical analysis. The main thrust of the work is in using laminar analogues of complex phenomena to aid the understanding of the key physical processes involved.

The first portion of the research concerns the dynamics of eyes (regions of reversed flow) at the centres of vortices. We expand upon previous work investigating the process of eye formation in shallow rotating convection. Through a series of numerical simulations we observe that, as thermal forcing is increased, the system undergoes a Hopf bifurcation from a steady state to one in which the eye oscillates. Examining the nature of the oscillations we propose that this behaviour results from a trapped inertial wave, providing a range of evidence to support this theory.

Following on from this we present a series of laboratory investigations designed to replicate our numerical studies. In addition to examining large scale circulations we also include some observations of rotating cellular convection. Though unsuccessful in generating a steady eye, our discussions of experiment design and implementation provide a number of insights, and we hope that future experimental work will build upon this preliminary study.

The latter portion of the thesis is given over to the study of thermals. We consider the life cycle of an axisymmetric laminar thermal as it transitions through a number of distinct stages undergoing several morphological changes. A significant achievement of the study is to establish a mathematical framework that can be used throughout the life cycle, allowing us to shed light on the transitions between stages and address some previously unresolved questions. Our numerical results show the early stages of development to be key in determining the final properties of the buoyant vortex ring that is produced, with thermals displaying an independence above a critical Reynolds number. Another notable observation is that the wake left behind by the first vortex ring can itself roll up to form a second ring that follows after the first. It is hoped that this framework and our observations of laminar thermals might perhaps be useful in providing new approaches for studying atmospheric convection.

Acknowledgements

A PhD is a long-term project and can often feel like a way of life. There are a number of people who have contributed either directly or indirectly to my work and life over the course of the last four years. Some were here at the beginning but not the end, others I have got to know over the course of my studies, and a few have been here throughout. I would like to take this opportunity to acknowledge a number of individuals and organisations who have made the following work possible.

Firstly I have to thank my supervisor Peter Davidson for both the assistance and freedom he has offered me, and for his advice in not only scientific, but also professional and personal matters. Perhaps the most valuable lesson I have learnt from him is how to write; not only to inform, but to also entertain. A quote by another Scotsman that sums up well what I have learnt, and I hope he will appreciate, reads as follows *"The difficulty of literature is not to write, but to write what you mean; not to affect your reader, but to affect him precisely as you wish."* – Robert Louis Stevenson, Truth of Intercourse.

My next thanks must go to my friends and colleagues of the geophysical fluids group – Oliver Bardsley, Avishek Ranjan, and Ben McDermott. It has been a pleasure to share so many discussions over the past few years, fluids related or otherwise, and their input to my work has been greatly appreciated. Similar thanks must also go to our neighbours and cake and coffee companions in the acoustics group.

Research involves collaboration, and there are a number of other academics that I wish to thank here. Firstly Peter Read from Oxford University for allowing me to visit his laboratory in the summer of 2018. His not only making facilities available, but welcoming me into his group and providing input into my work was

greatly appreciated. Closer to home I would like to acknowledge the many useful discussions I have had with Gary Hunt. My work, in particular the sixth chapter of this thesis, is significantly improved as a result of his helpful comments. Finally to James Perry for his assistance in developing my code as part of his masters project.

Nothing in life is free and, as such, there are a number of organisations to acknowledge for their financial contributions to this research. First and foremost the Department of Engineering and the Engineering and Physical Sciences Research Council for providing me with the Doctoral Training Award through which the majority of my research has been funded. Another body that deserves credit is the UK Fluids Network headed by Nick Daish. It was with his support that I applied for a short research visit grant to perform experiments in Oxford. Linked to this I would also like to thank my college Peterhouse for providing funding for these experiments through the Max Perutz Award. Finally I wish to credit the Cambridge Philosophical Society for providing me with a research studentship at the end of my studies. This allowed me to finish my writing and successfully publish two research articles.

When seeking respite from my work I have often found solace on the archery range with Cambridge University Bowmen. Shooting has provided me with much needed down-time and an alternative focus when needing to switch off. It has been pleasing to finish my university archery career on a high this summer and my experiences in the club have been, at times, just as valuable as those in the department. There are too many to name here, but some of my longest and closest friends can be found behind a bow and I am sure they know who they are. I am also incredibly grateful for the community of Peterhouse which has been my home for the past eight years. Throughout this formative time the college has provided a wealth of opportunities and has always been incredibly supportive. My college family, especially those I have lived with, has been extremely important to me on a day-to-day basis. Again, there are many individuals, each of whom I am sure knows how much their friendship means.

The final and most substantial thanks must go to my family to whom I will always owe a great debt of gratitude. Especially to my parents who have supported and encouraged me throughout my entire academic career from an early age. Without them none of this would have been possible.

Table of contents

List of figures

List of tables

Nomenclature

Roman Symbols

$\mathbf{c}_g$	group velocity
$\mathbf{c}_p$	phase velocity
c_p	specific heat capacity
Ek	Ekman number
$\mathbf{F}$	generic body force
$\mathbf{g}$	gravity vector
H	height
h	specific enthalpy
i	$\sqrt{-1}$
$\mathbf{k}$	wave vector
$\mathbf{L}$	impulse
l	characteristic length
p	pressure
Pr	Prandtl number
$\mathbf{q}$	heat flux

R	radius
Ra	Rayleigh number
Re	Reynolds number
Ro	Rossby number
t	time
$\mathbf{u}$	velocity vector
U	characteristic velocity
V	volume
$\mathbf{x}$	position vector

Greek Symbols

α	thermal diffusivity
β	coefficient of thermal expansion
Γ	angular momentum
γ	ratio of moments of vorticity
ϵ	strain rate
θ	temperature perturbation
κ	thermal conductivity
Λ	Aspect ratio
ν	kinematic viscosity
ρ	density
Φ	vorticity flux
Ψ	Stokes stream function

$\mathbf{\Omega}$ rotation vector

Ω rotation rate

$\boldsymbol{\omega}$ vorticity vector

ϖ frequency

Subscripts

0 background or bulk value

l local value

ϕ azimuthal component

r radial component

z axial component

Other Symbols

$\hat{\mathbf{e}}$ unit vector

$\hat{\mathbf{n}}$ unit vector normal to boundary

$\otimes$ tensor product

∇^2_* Stokes Operator

Acronyms / Abbreviations

CFL Courant–Friedrichs–Lewy

CIV correlation imaging velocimetry

GFD geophysical fluid dynamics

MAC marker and cell

NASA The National Aeronautics and Space Administration

NOAA The National Oceanic and Atmospheric Administration

PIV particle imaging velocimetry

Chapter 1

Introduction

The planet earth is a complex system. To understand it better we might break it down into a series of 'spheres'; the atmosphere, hydrosphere, cryosphere, lithosphere, magnetosphere, and biosphere. Several of these are visible in NASA's 'blue marble' photograph of the Earth in figure 1.1. The aurora australis shines above the icy plains of Antarctica, with the continental landmass of Australia visible in the top left across the cloud covered Antarctic ocean.

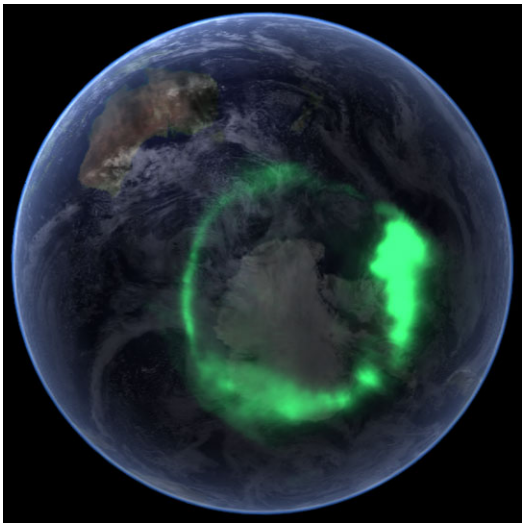

Fig. 1.1 A Blue Marble image of the Earth showing the aurora australis from the IMAGE satellite. NASA.

The future of the planet, and of those that inhabit it, is greatly dependant on how these systems interact with one another. This is the main thrust of the Gaia hypothesis developed by Lovelock & Margulis (1974). It proposes that organisms are engaged in a symbiotic relationship with the planet that helps maintain and advance life. The unprecedented increase in global temperatures over the course of the last century (Munroe, 2016) might lead some to question this notion however. Lovelock takes a rather bleak outlook on global warming predicting that global temperatures will continue to rise and that the latter part of the century will see a cull of up to 90% of the human population (Vince, 2009).

Anthropogenic climate change might be viewed as an antithesis of the Great Oxygenation Event of around 2,400 million years ago. This was a dramatic change in the composition of the atmosphere that triggered the 'snowball Earth' or Huronian glaciation period. Following the IPCC 'business-as-usual' scenario the outlook does not end well for our species; life may continue, but not as we know it.

The bulk of the scientific community, however, seek to prevent excessive global temperature rise. To achieve this requires an understanding of the climate and the Earth system. By studying the atmosphere, hydrosphere, cryosphere, and the way in which they interact it is hoped that we might gain insight into how to preserve them and repair damage. An example of this is the global initiative since 1989 to phase out ozone depleting chemicals following the discovery of the Antarctic ozone hole by the British Antarctic Survey in 1985 (Farman *et al.*, 1985). Nearly 30 years later NASA has finally been able to provide the first confirmation that the ozone layer is beginning to recover (Strahan & Douglass, 2018).

In this thesis we hope to explore some atmospheric phenomena and improve our physical understanding of them through the use of simple models.

1.1 Geophysical fluid dynamics

A number of the spheres in the Earth system are comprised of fluids. This is where the role of the geophysical fluid dynamiscist comes in. The field of geophysical fluid dynamics, GFD for short, is the branch of fluid dynamics concerned with any geophysical phenomena. These might range from the large scale circulations of atmospheres and oceans to volcanic plumes and avalanches. From explaining

Saturn's hexagonal polar vortex to the sustainment of the geodynamo. A number of these phenomena are illustrated in figure 1.2. The general paradigm of GFD is to take a seemingly complex problem and make as many simplifications as possible to expose the core principles and underlying mechanisms. By stripping away inessential details one can come to a fundamental understanding of why, rather than simply observing what. This covers one of the main drivers of GFD research - understanding as an end in itself. Understanding a phenomenon provides an appreciation of its beauty and often only furthers our sense of wonderment. All geophysical fluid dynamiscists are inspired in their work by at least one captivating phenomenon.

The other reason for GFD research is to benefit society. This often ties it closely to another field of research, that of modelling. As computational facilities have increased over the course of the last century there has been an exponential rise in the use and complexity of numerical models in all areas of science. Weather forecasting has come a long way since the first computation performed by the scientist Lewis Fry Richardson (1922) for the Western Front. These days forecasting models can be run faster than real time, solving the primitive equations for ever more complex scenarios with improving accuracy. Their ability to take an initial condition and then solve into the future does not mean that the field of GFD is redundant, however. As phenomena emerge from computational models any meaningful interpretation of the results requires an understanding of the basic principles. When something unexpected occurs it is down to the scientist to interpret the results. Doing this requires a firm grasp of the key concepts, an understanding of the field, and the ability to apply these skills to provide physical insight.

It must also be remembered that no computational model is ever perfectly correct. What happens when things go wrong, and how to fix or improve them requires an understanding of GFD. If a model does not replicate some physical behaviour we must ask why, and what might be missing. Despite the advances in computational capabilities, there is still a limit in the abilities of all numerical models. These usually manifest as restrictions in the resolution due to the quantities of data required or the time taken to perform calculations. In an effort to sidestep these restrictions, many models make use of parametrisations in order to represent processes that occur at scales finer than the resolution of a model. Examples of

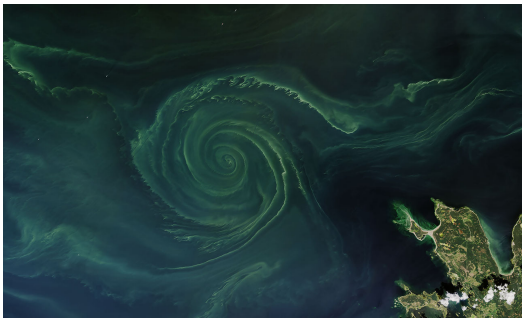

(a) July 2018 phytoplankton bloom in the Gulf of Finland. Landsat 8, NASA.

(b) Plume from the eruption of Mount Redoubt. USGS.

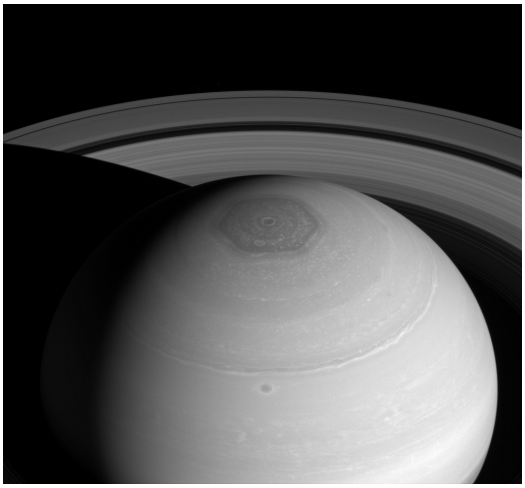

(c) Saturn's hexagonal polar vortex. Cassini, NASA.

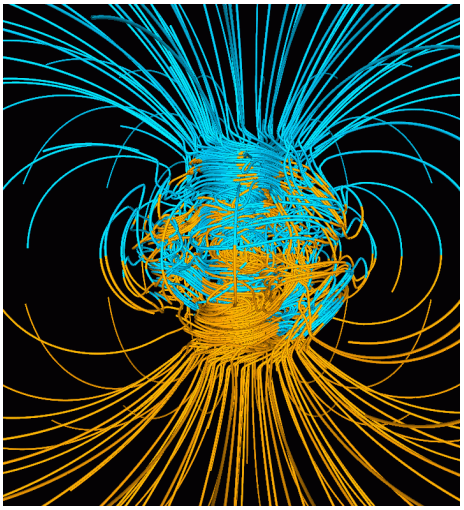

(d) An image from the famous Glatzmaier-Roberts geodynamo simulation. NASA.

(e) Avalanche in Zinal, Switzerland. Zacharie Grossen.

Fig. 1.2 Examples of geophysical fluid dynamics phenomena.

this might be cloud microphysics in an atmospheric model, or pollutant dispersion from ground sources. These parametrisations are often developed from simple models and physical laws, requiring an in depth understanding in order to perform correctly as part of a larger simulation.

The field of GFD will forever be intertwined with the numerical modelling, and there are still plenty of challenges. An excellent overview of the field that influenced and expands upon the ideas set out here is given by Vallis (2016).

1.2 The menagerie of atmospheric vortices

Before discussing atmospheric vortices, let us first consider what is meant by the word vortex. In the context of fluid dynamics a vortex is a flow that rotates about some axis. Flows that satisfy this statement exist in a variety of settings and exhibit a wide range of behaviours, a few examples are illustrated in figure 1.3. *Vortex Flow in Nature and Technology* by Lugt (1983) provides a wonderful description of how widespread and influential vortex phenomena are and makes for excellent bedtime reading. These swirling flows have awed and fascinated mankind throughout history up to the present day, whether it be Odysseus facing the whirlpool Charybdis in Homer's Odyssey, or God speaking out of whirlwinds in the Bible. It is broadly accepted nowadays that vortices are not manifestations of supernatural beings, nor do they hide any deep symbolism, yet still they maintain an air of wonder and mystery. The scientific study of vortices has existed for a long time and has attracted the attention of a number of great scientists and thinkers including Aristotle, da Vinci, and Kelvin, yet there is still much to be understood.

The atmosphere is rich in vortices across a wide range of scales, from the Hadley cells that span the troposphere (Vallis, 2017) down to turbulent dissipation at the Kolmogorov scale (Davidson, 2013). In contrast to daily, annual, and longer global circulations, there are many aperiodic phenomena that occur on the synoptic, meso- and microscales as a result of instabilities. These isolated vortices are particularly fascinating and we now provide a review of some of the common types.

(a) Corryvreckan Maelstrom off the coast of Scotland.
Walter Baxter

(b) Wingtip vortices behind an aircraft.
NASA

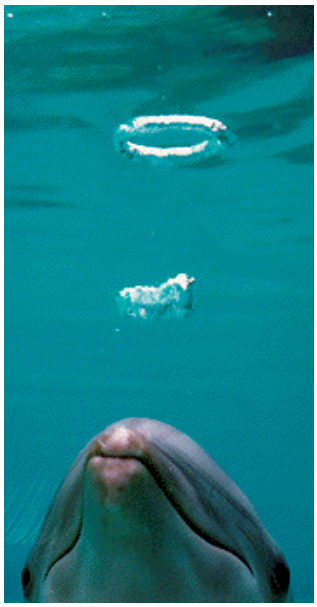

(c) A dolphin blowing an underwater vortex ring.
Dr. Ken Marten

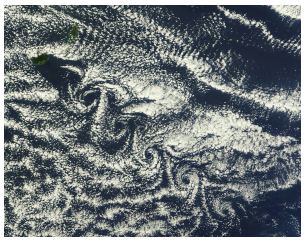

(d) Kármán vortex street behind Yakushima.
NASA

(e) Volcanic ring above Mount Etna.
Angelo Salemi

Fig. 1.3 Examples of the wide range of vortex flows

1.2.1 Tropical cyclones

Also known as typhoons or hurricanes, these are perhaps the largest isolated atmospheric vortex. They have a vast diameter of the order of 1000 km, covering a large region, and extend up to the height of the tropopause. This puts them firmly into the category of disklike vortices. One of their most striking features is the cloud free eye that often forms at the centre, as seen in figure 1.4. Although a number of explanations have been put forward for how and why eyes form, it remains a strongly debated topic.

Fig. 1.4 Hurricane Isabel from the International Space Station 2003 NASA

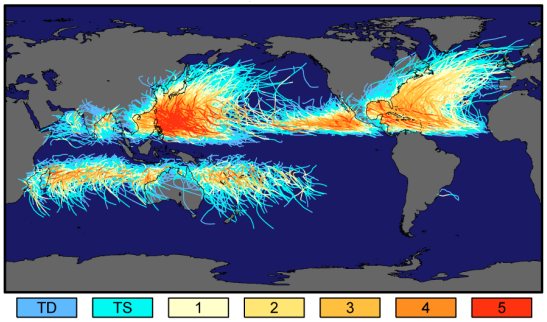

Fig. 1.5 Tropical cyclone tracks and intensity over the last 150 years Robert A. Rohde, NASA

Cyclogenesis, the conditions for and process of cyclone formation, is a large field of research important to meteorologists and forecasters (Gray, 1967). Although our research is not concerned with the formation process it is useful to have a general understanding. There is a vast body of literature on tropical cyclones, but a good review of the formation and mature structure can be found in Wang (2012). Tropical cyclones typically form over warm oceans in the tropics. It is from these warm waters that they obtain their energy through heat transfer. A low pressure disturbance (depression) in the atmosphere draws in surrounding air. As it converges, this air acquires a cyclonic component of rotation through the action of the Coriolis force. Tropical cyclones are generally only observed to form within ±5-15° of the equator where the conditions of both warm ocean waters and a sufficiently strong Coriolis force can be met.

The air spiralling inwards along the ocean surface increases in speed. When the maximum substained windspeed is above 33 m s^{-1} the storm is regarded as a

category 1 cyclone on the Saffir-Simpson scale. This ranges up to category 5 for storms with windspeeds in excess of $70\,\mathrm{m\,s^{-1}}$. As the air converges towards the low pressure centre an updraft forms. Latent heat is released by the moist air as it ascends, increasing its buoyancy and driving it further upwards as more air is drawn in from below. Eventually the air reaches the tropopause where a sharp change in temperature gradient prevents it from ascending further. It then moves radially outwards, acquiring anticyclonic spin before descending back to the ocean surface.

Once a tropical cyclone has formed, it moves predominantly with the environmental flow (the trade winds) from east to west. Storms are sufficiently large that the Coriolis force has a secondary effect, however, steering them polewards. Eventually the storms move over cooler waters or land and their energy source is removed causing them to decay in strength, although often not before they cause catastrophic damage. This is clearly illustrated in figure 1.5 which shows storm tracks coloured by intensity according to the Saffir-Simpson scale ranging from tropical depression up to a category 5 storm.

There is a wealth of observational data from tropical cyclones, much of it from NASA and NOAA, with the majority of studies conducted by meteorologists focussing on the overall structure, cyclogenesis, and motion. Much of this work involves complex models, often numerical, with many different parameters in order to emulate real world behaviour.

In Chapter 4 we shall present a simplified model of a tropical cyclone and provide an explanation for recently observed oscillations in the eye.

1.2.2 Tornadoes

Much smaller than tropical cyclones, tornadoes display a columnar structure consisting of a rapidly rotating pillar of air that reaches from the ground up to the cloud base. Though they can take on a range of sizes and strengths, they are typically $50 - 100\,\mathrm{m}$ in radius and $2\,\mathrm{km}$ in height, with windspeeds up to $180\,\mathrm{km\,h^{-1}}$ (Rotunno, 2013; Wurman *et al.*, 1996). The flow is, to a leading order, in a cyclostrophic balance between pressure and inertia, and is often made visible by the condensation funnel that forms at the low pressure centre.

Fig. 1.6 Tornado in Manitoba
Justin Hobson

Fig. 1.7 Supercell on the Great Plains
Topazwoolenwick

Rossby numbers are large for tornadoes so it is perhaps surprising that only around 1% are anticyclonic. The reason for this is that the majority (around 80% (Markowski & Richardson, 2009)) form beneath large thunderstorms known as a supercells (figure 1.7). These are rotating storm systems characterised by the presence of a mesocyclone resulting from a combination of wind shear and convective updrafts (Holton & Hakim, 2012). The wind shear comes from large scale circulations in the atmosphere, thereby indirectly providing the cyclonic preference. The precise formation mechanisms of tornadoes are complex and there is still much to be understood (Markowski & Richardson, 2009).

The intense winds and surrounding storm make it difficult to observe the internal structure and dynamics of tornadoes in detail, although progress has been made using techniques such as Doppler radar. These observations suggest that tornadoes possess a calm central core with slight downflow (Wurman *et al.*, 1996), although results are available for only a limited number of cases and are of relatively low resolution. An important factor that remains largely unknown is the detail of the flow at the top of a tornado. This presents a significant challenge when it comes to defining boundary conditions. Despite this, the study of tornadoes appeals to a wide range of communities and there is a large source of literature covering theoretical models and both numerical and laboratory experiments.

1.2.3 Devils

The broad class of vortices known as devils are all essentially the same flow, each with a different method of visualisation. The most well known of these is the dust devil, illustrated in figure 1.8, that forms in desert regions. There also exist snow devils, steam devils, coal devils, and ash devils. The following discussion will focus on the dust devil, though similar theory applies to all of these. An interesting derivative is the fire devil of figure 1.9. The processes that form a normal devil are highly accentuated by the heat release from combustion of material that is swept up into the vortex giving rise to a thin violent structure.

These columnar vortices form on hot days under clear skies as a result of convection and light winds. Solar heating of flat ground in turn heats the air above causing it to rise. The rising air stretches boundary layer vorticity into the vertical direction, eventually leading to the formation of a vortex (Rafkin *et al.*, 2016). Devils typically display a more parallel columnar shape than tornadoes with little broadening with height. They take on a range of sizes and strengths from 0.5 m wide and 10 m tall up to tens of m across and heights of a km or more. Windspeeds can range from $15 - 30\,\mathrm{m\,s^{-1}}$. Lifetimes are typically seconds to minutes, though larger devils have been observed to last for tens of minutes before dissipating.

A large number of observations and theoretical ideas about dust devils come from the work of Sinclair (1966). Of particular note is the discovery of weak downflow in the core, particularly at low levels, which was later backed up by observations made in California by Ryan & Carroll (1970). This structure is shown in figures 1.10 and 1.11. It is interesting how this core downflow bears a resemblance to the flow in the eye of the tropical cyclone, despite their differences in shape and size. We shall return to this point in Chapter 4.

1.2.4 Waterspouts

Another columnar vortex that forms over the oceans and other bodies of water, waterspouts are usually separated into two classes; tornadic and fair weather. Tornadic waterspouts are simply tornadoes that form over water, identical to those described above. Fair weather waterspouts (figure 1.12) are a very different phenomenon, however, more closely related to the dust devil.

Fig. 1.8 Dust Devil in Arizona
NASA

Fig. 1.9 Fire Devil in Missouri
Janae Copelin

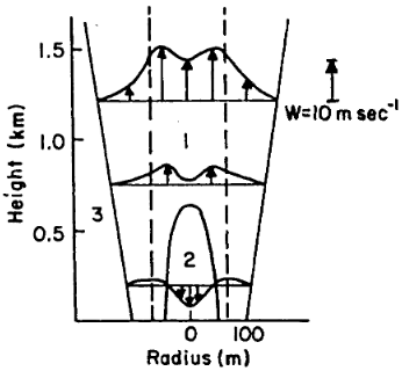

Fig. 1.10 Vertical velocities in the dust devil taken from Sinclair (1966)

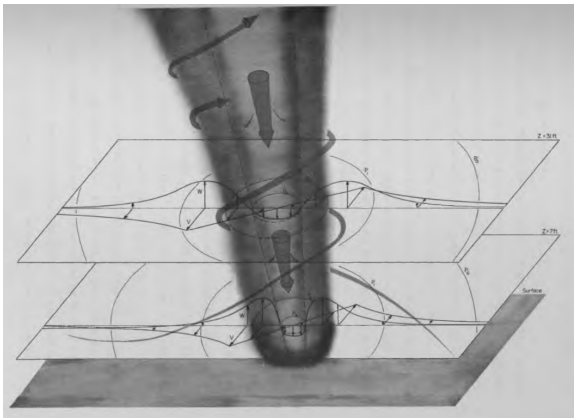

Fig. 1.11 Lower structure of a dust devil taken from Sinclair (1966)

Fig. 1.12 Waterspout in the Florida Keys
NOAA

Studies of waterspouts are limited, consisting almost entirely of observational data. The most notable studies were performed by the meteorologist Golden (1968, 1971, 1974), since which they have received little attention. Golden collected a large amount of data to build a detailed description of the structure of the mature waterspout and its life cycle. These are presented in his papers alongside excellent photographic images.

Focussing on the structure of the mature waterspout, Golden describes it as a rapidly rotating column of air approximately in cyclostrophic balance, typically displaying a 'stretched hourglass shape'. The upper region is often visible by a condensation funnel that forms at the low pressure centre. Above the sea surface there is a 'spray vortex', out of which rises the 'spray sheath' - an intense rising annulus, the vertical extent of which depends on spray size and vortex intensity.

Golden describes the spray sheath as having a 'central calm eye', surrounded by sharp gradients in tangential windspeed. Maximum tangential winds occur just outside of this 'eye' and particle tracking of the spray vortex suggests a Rankine vortex profile. The hollow core of the waterspout is observed to contain slowly subsiding air, although no reason for this is given.

The waterspout often reaches the cloud base where it becomes hard to observe flow structure, as was the case for tornadoes, and the details of the flow are unclear.

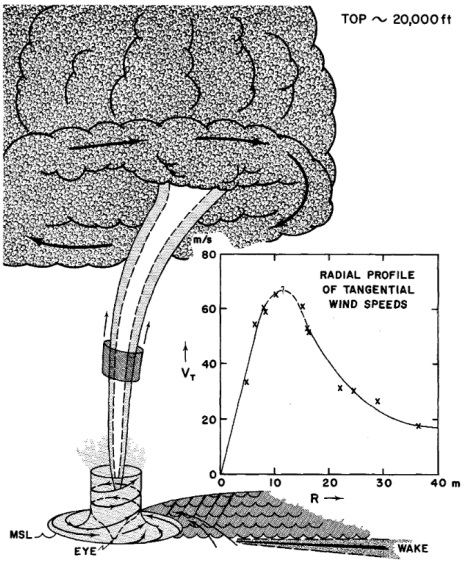

Fig. 1.13 Waterspout Structure taken from Golden (1971)

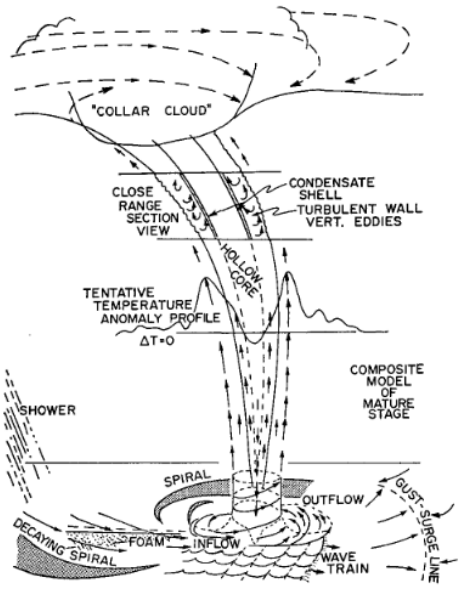

Fig. 1.14 Waterspout Structure taken from Golden (1974)

Two of Golden's diagrams of waterspout structure are shown in figures 1.13 and 1.14.

Golden's research follows the development of a waterspout from a weak vortex, visible from dark spots on the water surface, through the intensification process as it becomes wider in diameter with stronger windspeeds and a condensation funnel appears higher up. As it reaches maturity, the condensation funnel becomes visible over almost the entire length of the vortex, and the high velocities whip up the surface of the water giving rise to the spray vortex and sheath. Waterspouts generally exist in maturity for around 2-17 minutes before becoming greatly contorted, weakening, and disappearing. How the vortex forms prior to its first appearance as a dark spot is unclear, although the fact that spots appear together has led to the suggestion that the vorticity source may be a vertical vortex sheet produced by wind shear. Others propose the source is convective stretching of boundary layer vorticity in a manner similar to the dust devil.

Finally, it is worth noting that waterspouts, like dust devils, do not remain stationary, but are observed to propagate along the water surface with velocities of

up to $15\,\mathrm{m\,s^{-1}}$. The base often moves faster than the top leading to vertical tilting and can cause the vortex to become highly contorted.

1.2.5 Differences and similarities

All of these vortices have a broadly similar flow structure, with a swirling inflow at the base that turns upward near the centre and rises before diverging at the top. The cores of these vortices are often weaker than the surrounding flow, with downflow observed along the axis. The main difference between them appears to be the fact that they fall into one of two classes, columnar or disklike. Is there a structural reason that aspect ratios of around 1 are not observed? The formation mechanisms for each of these vortices are all very different, with buoyancy and thermodynamics being important in a number of cases. One might seek to quantify the similarities between the vortices, and ask whether there could be a general theory to explain certain features. One might also ask how similar the downflows at the cores of the vortices are; the tropical cyclone appears to have downflow starting from the highest levels, whilst Sinclair's observations of the dust devil suggest that the downflow has a broader region of upflow above it. Are these differences due to separate mechanisms, or can same theory be applied in different settings?

Table 1.1 contains a comparison of key numerical values taken from literature for a number of the vortices discussed above. For phenomena that occur across a range of scales this is best done using non-dimensional parameters. The aspect ratio, Λ, provides a clear indication of which vortices are disklike (< 1) and which are columnar (> 1). Consideration of the Reynolds numbers suggests that these are all turbulent flows, as one might expect. More interesting is the variation in Rossby number. We see that Ro is typically small for disklike vortices, and large for the smaller columnar vortices. However, although small and hence significant to the overall structure of the tropical cyclone we note that in the core, where velocities are large, the Rossby number rises above one meaning background rotation is relatively insignificant here.

Table 1.1 A comparison of properties for different atmospheric vortices
Data from a number of sources: Holton & Hakim (2012); Lugt (1983); Knaff *et al.* (2014); Emanuel (2000); Neumann (1993); McDonald & Mehta (2009); Rotunno (2013); Wurman *et al.* (1996); Brooks (2004); Sinclair (1966); Golden (1968, 1971, 1974); Rasmussen *et al.* (2004)

Property	Tropical Cyclone	Tropical Cyclone Core	Tornado	Dust Devil	Waterspout	Polar Low
Lifetime	days	days	min	sec-min	min	hrs
Height / m	15×10^3	15×10^3	2×10^3	100	1×10^3	15×10^3
Radius / m	500×10^3	50×10^3	100	10	10	150×10^3
$\mathbf{u}_{\theta,\,\max}$ / m s^{-1}	45	45	50	15	30	15
Aspect Ratio Λ	0.03	0.3	20	10	100	0.1
Ro	0.1	10	10^3	10^4	10^3	0.8
Re	5×10^{12}	1.5×10^{11}	1.0×10^8	1.0×10^7	1.0×10^8	2.0×10^{11}
Axial downflow / m s^{-1}	15	15	2	0.1	0.3	-

1.2.6 Thermals and rings

Before concluding our introduction to atmospheric vortices we discuss a different type of vortex to those that we have considered so far. Whilst all of the vortices discussed above have a linear axis of rotation, this does not have to be the case. As we saw in figure 1.3e, the axis of rotation can be curved, in some cases forming a closed ring. These types of structures are often associated with buoyant flow and known to fluid dynamicists as thermals. Thermals form from buoyant anomalies in a fluid and evolve under the action of the buoyancy force. As they move they twist and contort into different shapes, often ending up with a mushroom or ring-like structure.

Perhaps the most well-known example of a thermal is the mushroom cloud. These form after the rapid release of large amounts of energy, most commonly from explosions. The energy heats up its surroundings to form an isolated patch of buoyant fluid that begins to rise. As it does so, gradients in temperature generate vorticity causing the ball of heat to evolve into a distinctive mushroom shape. A cap forms at the top of the structure with a stem beneath, squeezed in by entrained fluid. An example of this can be seen in figure 1.15 which shows the development of a mushroom cloud following a nuclear explosion.

Although mushroom clouds are perhaps the most visually striking case of thermals, there are a number of other examples in the atmosphere. Perhaps the most common occurrence is atmospheric convection above a localised heat source. As the air above is warmed, it forms an isolated buoyant patch of fluid that begins to rise, developing a mushroom and then ring-like structure. As this air rises further these thermals may become visible as cumulus clouds. They are often used by birds and gliders as means to rise to greater heights to assist flight. Figure 1.16 shows this, with a cluster of paragliders riding a thermal. Note how they are grouped together inside an isolated patch of buoyant air.

Another interesting example of buoyant rings in the atmosphere are the smoke rings that have been observed at various volcanoes across the globe (Fuentes, 2014), an example of which was shown in figure 1.3e. They have been observed to persist as stable rings for relatively long periods of the order of several minutes up to an

Fig. 1.15 Mushroom cloud of the 'Greenhouse George' nuclear explosion
U.S. Federal Government

Fig. 1.16 A group of paragliders riding a thermal in WA, USA
Kozi radio

hour. Although there are many observations there is still no clear consensus as to how these buoyant rings form (Whitehouse, 2000).

As we shall see, both thermals and the axial vortices discussed above can be described by the same set of equations in which the evolution of azimuthal vorticity is key to their structure and development. This is highlighted further by the interesting analogy that exists between rotating and buoyant flows (Veronis, 1970). There is a mathematical equivalence between the equations for rotating flow and those for buoyant flow, as we shall soon see. As a result of this there are a number of phenomena that occur in one system that have a direct counterpart in the other, and it is sometimes useful to analyse the behaviour of one system in order to better understand the other. This is particularly useful in geophysical fluid dynamics where the effects of buoyancy and rotation are key. For example, the inertial waves present in rotating flows are a mathematical counterpart of the

internal gravity waves that occur in a stratified fluid. The parallels between different phenomena in each of these cases is explored in depth by Davidson (2013).

Returning to thermals, the evolution of a patch of heat into a mushroom, and then on into a ring is an interesting process. As we shall see, each of these stages have received attention in their own right by previous authors, but there is little discussion of the transitions between the stages. In addition to this, although the development of turbulent thermals has been studied (Scorer, 1957) there is very little discussion of their laminar counterpart. We shall discuss laminar thermals in Chapter 6.

1.3 Scientific models

Models, analogies, and cartoons hold an important role in scientific research and understanding. We have already discussed how one of the main objectives of GFD is to strip away inessential physics to leave a simple model that can replicate physical behaviour. This Occam's razor-like approach, describing complex phenomena with simple models can be found throughout the sciences however. To illustrate the ideas of using a simplified model to describe a complex system let us consider the eruptions of volcanoes.

When making meteorological predictions and evaluating health and flight risks due to volcanic ash it is useful to know the mass of volcanic material ejected into the atmosphere during a volcanic eruption. Although there exist many complex numerical models of volcanic eruptions, the inputs they require cannot be accurately gathered in real time. Instead meteorologists make use of more simple, local models to make predictions that can then be taken as inputs into a larger circulation model. Perhaps the most basic example is the well-known mathematical model for a buoyant plume by Morton *et al.* (1956). Using this model it is possible to accurately predict the mass flux of material from a volcano based upon how high the ash plume rises in a stratified atmosphere. This is an example of how a highly simplified model, limited to the necessary details, can be used to obtain important information.

All models have their limits however. For the buoyant plume model applied to volcanic eruptions one of these limitations is the assumption of a quiescent environment. This simplification was not appropriate in the case of the 2010

eruption of Eyjafjallajökull in Iceland, and led to incorrect predictions resulting in significant disruption to air travel over northern and western Europe. The inaccurate estimations of the model occurred as a result of a significant crosswind causing the plume to bend over and ash to be swept away instead of rising higher into the atmosphere. This behaviour can be seen in the photo of figure 1.17. Once this effect was retrospectively incorporated into the model it was found to make more accurate predictions of mass flux, as discussed by Woodhouse *et al.* (2013)

Fig. 1.17 The 2010 eruption of Eyjafjallajökull from Hella Boaworm

The statistician Box (1979) first coined the well known phrase 'all models are wrong, but some are useful.' This encapsulates the idea it is impossible to model every last detail of a physical system; there will always be some underlying assumptions or approximations. Provided these are well justified, however, a model can still shed light, provide understanding of a phenomenon, and replicate it with sufficient accuracy. It is always important to bear in mind why a model has been developed and what it is designed to do. Problems can arise when models are applied in inappropriate situations (as for Eyjafjallajökull above) or the results are assumed to be more realistic than the model was ever designed to be. Box suggests that the question that should be asked is 'Is the model illuminating and useful?'.

From the perspective of GFD a good model is one that can explain a complicated phenomenon by showing how it arises in a more simple system. By reducing a system down to a minimum number of variables and effects it becomes easier to inspect and isolate the causes for different behaviours. An approach that can be

often be useful in fluid dynamics is to construct a laminar model as an analogy to a more complicated system. In addition to reducing a problem down to a minimum number of variables and removing insignificant effects, this also removes turbulence making the system much easier to analyse. By understanding the behaviour of a laminar analogue we might then return to the complicated system and see where similar behaviours occur, and what the explanation for them in the analog is.

1.4 Scope and structure of thesis

The aim of this work is to develop models, or analogs, of fluid phenomena that might help explain and understand geophysical phenomena, in particular isolated vortex flows in the atmosphere. Many GFD phenomena occur as a result of two key effects; buoyancy and rotation. The work presented in this study is concerned with both of these. In the next chapter we shall review the relevant theory necessary to understand these effects and develop equations that will be used throughout the thesis. This is followed in Chapter 3 by a discussion of a numerical code that was developed in order to perform simulations of axisymmetric, buoyant, rotating flow.

This work was inspired by the atmospheric phenomenon of the tropical cyclone, as well as the other vortices discussed above. Although these storms are extensively studied due to the catastrophic damage they cause, there is still much that is not understood. The particular aspect that we choose to focus on is the eye that forms at the centre of the storm. Although several theories have been put forwards for how this occurs there is still no clear consensus or universally accepted theory. The ambition when starting this work was to extend the recent model proposed by Oruba *et al.* (2017) that is capable of displaying eyes. In addition to exploring its behaviour it was also hoped to examine if the mechanism by which eye formation occurs within this model could also be present in other atmospheric vortices. Chapter 4 contains a discussion of eye formation mechanisms and the results of numerical simulations. It is found that the model displays oscillations which we seek to provide an explanation for before tying the results and the model back to real storms.

In Chapter 5 a series of laboratory experiments are presented. These were performed with the intention of replicating the behaviour seen in the simulations

of Chapter 4. As laboratory experiments of this system have not been performed before we shall discuss the design of the experiment and how it differs from the simulations of chapter 4. Results for large vortices are presented alongside observations that were made of cellular convection on a smaller scale. The chapter finishes by reviewing the results of what can be taken as a preliminary study in this area that might serve to inform future experiments.

Finally in Chapter 6 we shall discuss the evolution of a laminar thermal. We present a unified mathematical framework by which the system can be analysed in order to make links between the different stages of development. By following the entire life cycle of a thermal using this framework it is possible to link the properties of the end state to the initial conditions, and come to a better understanding of how and why the different structures form and behave as they do.

The nature of research is that one never knows exactly what is going to happen. Indeed, this is its raison d'être. The discovery of oscillations that makes up much of the discussion of Chapter 4 was unexpected prior to beginning this work. Similarly the observations of cellular convection in Chapter 5 were made whilst exploring outside the main parameter space. The entirety of Chapter 6 began as a test case for our numerical code that displayed interesting behaviour and we decided was worthy of further exploration. The voyage comes to a conclusion in Chapter 7, where we summarise the work of this thesis, reviewing its contributions with an outlook to the future.

Chapter 2

Theoretical review

This chapter reviews the key mathematics and fluid dynamics that forms a basis for this thesis. We begin with the governing equations of fluid mechanics, extending them into a vortex dynamics approach. We discuss the merits of this paradigm and review some of the key aspects appropriate to this work, in particular the process of vortex stretching. Following this the effects of buoyancy and rotation are discussed. Both of these have a significant impact on fluid flow, sometimes in unexpected or counter-intuitive ways. Finally the equations for axisymmetric, swirling flow that form the basis for the analysis in future chapters are developed. Much of the material in this chapter can be found in the textbooks by Batchelor (1967), Acheson (1990), and Davidson (2013).

2.1 The equations of fluid mechanics

In what follows we consider the behaviour of an incompressible, viscous fluid. The motion of such a fluid is described by the well known incompressible Navier-Stokes equation,

$$\frac{\mathrm{D}\mathbf{u}}{\mathrm{D}t} = -\frac{1}{\rho}\nabla p + \nu\nabla^2\mathbf{u} + \frac{\mathbf{F}}{\rho}\,, \tag{2.1}$$

where $\mathbf{F}$ represents any body forces which may be acting on the fluid, and the continuity equation

$$\nabla \cdot \mathbf{u} = 0\,. \tag{2.2}$$

An insightful and oft-employed paradigm for analysing fluid flow is that of vortex dynamics (Saffman, 1992). Many flows can be more readily understood in terms of vorticity, mathematically given by the curl of the velocity field, than in terms of pressure and velocity. Physically the vorticity is a measure of the local rotation, or angular velocity of a fluid. The advantages of this approach can be seen by writing the governing equation in terms of vorticity. This is done by taking the curl of the Navier-Stokes equation (2.1):

$$\frac{\mathrm{D}\boldsymbol{\omega}}{\mathrm{D}t} = (\boldsymbol{\omega}\cdot\nabla)\,\mathbf{u} + \nu\nabla^2\boldsymbol{\omega} + \nabla\times\left(\frac{\mathbf{F}}{\rho}\right)\,. \tag{2.3}$$

The absence of the (non-local) pressure term avoids any misleading interpretations of cause and effect due to the coupled behaviour of pressure and velocity. Instead, all terms in the vorticity equation are local to the point under consideration. Vorticity can only be spread through advection or viscous diffusion. Both the pressure and velocity are easily recoverable, however, by inverting the vorticity relation, $\nabla\times\mathbf{u} = \boldsymbol{\omega}$.

In order to understand behaviour in terms of vorticity let us examine equation (2.3) in detail. On the left we see the familiar material derivative, whilst on the far right there is a viscous diffusion term. The first term on the left hand side represents the intensification of the vorticity field through the action of vortex stretching. To understand this process consider the vortex tube in figure 2.1. Assuming the vortex lines to be frozen into the fluid (as per Helmholtz's (1858) second theorem of vortex dynamics) the tube will be distorted through advection by the velocity

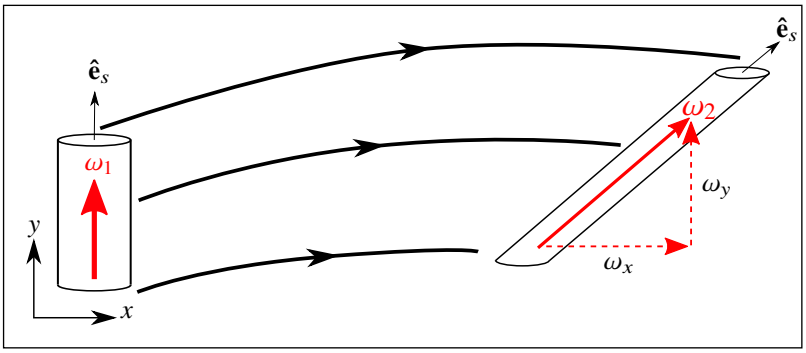

Fig. 2.1 Cartoon illustrating the process of vortex stretching

field. This takes it from its original position, with vorticity $\boldsymbol{\omega}_1$, to that at a later time with vorticity $\boldsymbol{\omega}_2$. Consider this behaviour in an intrinsic co-ordinate system aligned with the axis of the vortex tube, s. As the tube is distorted by the flow it lengthens along s. Continuity requires the cross-sectional area to decrease, thus reducing the moment of inertia along s. Since vorticity is a measure of the local spin, the vorticity of the material tube must increase in order to offset the decrease in moment of inertia and conserve angular momentum. The reverse is, of course, true should the tube have shrunk in length. This process is encapsulated in the third of Helmholtz's laws; the conservation of vorticity flux along a vortex tube.

Now consider the exact same process, but from the perspective of a Cartesian co-ordinate system (x, y), also illustrated in figure 2.1. We see that the distortion of the vortex tube by fluid motion leads to it having a component in both co-ordinate directions rather than just in y as it began. This process is sometimes described as 'vortex tilting', since vorticity has been transferred from the y to the x direction. However, as we can see, this is simply the result of vortex stretching being viewed in a fixed co-ordinate system. To avoid ambiguity we refer to any processes resulting from the $(\boldsymbol{\omega} \cdot \nabla)\,\mathbf{u}$ term as vortex stretching.

2.2 Buoyant flows

Many flows, especially those of a geophysical nature, involve thermodynamic processes. The effect of temperature variation on the density of a fluid can lead to

a variety of interesting behaviour. Some of these can be treated mathematically by an extension to the equations of motion as follows.

Consider a fluid in which the variations in density are small such that we can apply the commonly used Boussinesq approximation (Batchelor, 1967). This states that when density variations are small relative to the density of the fluid, the only effect they have is to contribute to the buoyancy body force. In this case density can be written as $\rho = \rho_0 + \rho'$, where ρ_0 is the background density distribution, and ρ' is a perturbation. The equation of motion (2.1) then becomes

$$\frac{\mathrm{D}\mathbf{u}}{\mathrm{D}t} = -\frac{1}{\rho_0}\nabla\widetilde{p} + \frac{\rho'}{\rho_0}\mathbf{g} + \nu\nabla^2\mathbf{u} \,, \tag{2.4}$$

where the hydrostatic pressure due to ρ_0 has been incorporated into the pressure term as $\widetilde{p} = p + p_0(z)$. Gravity is assumed to act in the negative z direction. The buoyancy term, $\mathbf{g}\,\rho'/\rho_0$, is then the (non-hydrostatic) gravitational force acting on the fluid. The corresponding vorticity equation is

$$\frac{\mathrm{D}\boldsymbol{\omega}}{\mathrm{D}t} = (\boldsymbol{\omega}\cdot\nabla)\,\mathbf{u} + \nabla\left(\frac{\rho'}{\rho_0}\right)\times\mathbf{g} + \nu\nabla^2\boldsymbol{\omega} \,, \tag{2.5}$$

where $\nabla(\rho'/\rho_0)\times\mathbf{g}$ is sometimes known as the Boussinesq baroclinic term. It encapsulates the processes of vorticity generation through misalignments between gravity and density gradients. We see that the component of vorticity aligned with $\mathbf{g}$ cannot be directly influenced by the buoyancy force.

Often density differences occur due to variations in temperature, especially in the atmosphere. In the same way as for density, it is often helpful to separate the temperature field into two parts; a background temperature T_0 and a perturbation θ such that $T = T_0 + \theta$. We can link density and temperature variations through a thermal expansion coefficient $\beta = \frac{1}{V}\left(\frac{\partial V}{\partial T}\right)\Big|_p$ as follows

$$\rho' = -\,\rho_0\,\beta\,\theta \,. \tag{2.6}$$

Doing this our equations of motion become, in terms of temperature,

$$\frac{\mathrm{D}\mathbf{u}}{\mathrm{D}t} = -\frac{1}{\rho_0}\nabla p - \beta\theta\mathbf{g} + \nu\nabla^2\mathbf{u} \,, \tag{2.7}$$

and

$$\frac{\mathrm{D}\boldsymbol{\omega}}{\mathrm{D}t} = (\boldsymbol{\omega}\cdot\nabla)\,\mathbf{u} - \beta\nabla\theta\times\mathbf{g} + \nu\nabla^2\boldsymbol{\omega}\ . \tag{2.8}$$

For an ideal gas it follows from the definition of β and the ideal gas laws that the thermal expansion coefficient is given by $\beta = 1/T_0$ (Batchelor, 1967).

Temperature is a scalar variable whose behaviour is coupled to that of the fluid. In addition to advection, heat may also be redistributed through thermal conduction. Both of these effects are combined in the following advection-diffusion equation for heat,

$$\frac{\mathrm{D}T}{\mathrm{D}t} = \alpha\nabla^2 T\ , \tag{2.9}$$

where α is the thermal diffusivity.

2.3 Rotating flows

Equally interesting and important to the following work is the behaviour of a rotating fluid. To analyse these flows we place ourselves in a frame of reference that rotates relative to the inertial frame at a constant rate $\boldsymbol{\Omega}$. With some manipulation equation (2.1) can be expressed in the rotating reference frame as

$$\frac{\mathrm{D}\mathbf{u}}{\mathrm{D}t} = -\frac{1}{\rho}\nabla\widetilde{p} + 2\mathbf{u}\times\boldsymbol{\Omega} + \nu\nabla^2\mathbf{u} + \frac{\mathbf{F}}{\rho}\ , \tag{2.10}$$

where all variables are now measured inside the rotating frame (Davidson, 2013). The resulting centrifugal term has been incorporated into the pressure as $\widetilde{p} = p - \frac{\rho}{2}(\boldsymbol{\Omega}\times\mathbf{x})^2$.

The remaining term, $2\mathbf{u}\times\boldsymbol{\Omega}$, is the Coriolis force; a fictitious body force that manifests as a result of moving in a non-inertial frame. We see that this force will always act in a direction perpendicular to motion in the rotating frame, deflecting fluid from its current path. This effect is illustrated in figure 2.2. Two characters are stood diametrically opposite one another on a rotating platform. One character throws a ball to the other. When viewed in the inertial reference frame $\mathbf{R}_i$ the ball travels in a straight line. It misses the receiving character who has, in the time it takes for the ball to cross the table, rotated away from his original position. Viewed in the rotating frame $\mathbf{R}_r$ the ball now appears to be deflected under the action of

an invisible force causing it to move in a curved path. This force is the Coriolis force. A key result is $\mathbf{u} \cdot (\mathbf{u} \times \mathbf{\Omega}) = 0$ indicating that the Coriolis force cannot do any work when acting upon a fluid, it may only change its direction; it is, after all, a fictitious force.

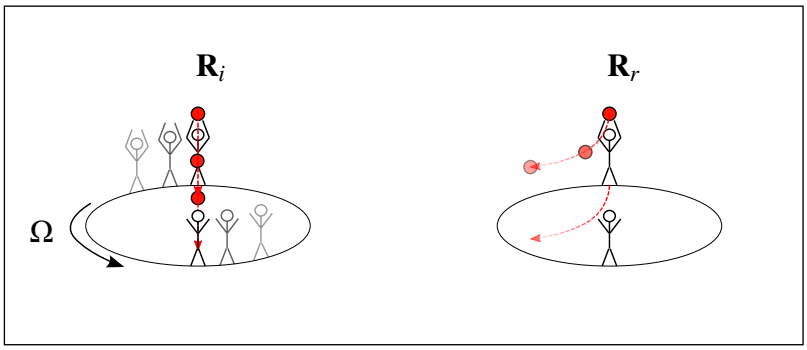

Fig. 2.2 Cartoon illustrating effect of the Coriolis force

The corresponding vorticity equation to (2.10) is

$$\frac{\mathrm{D}\boldsymbol{\omega}}{\mathrm{D}t} = (\boldsymbol{\omega}\cdot\nabla)\,\mathbf{u} + 2\,(\mathbf{\Omega}\cdot\nabla)\,\mathbf{u} + \nu\nabla^2\boldsymbol{\omega} + \nabla\times\left(\frac{\mathbf{F}}{\rho}\right) \,. \tag{2.11}$$

An interesting effect of the Coriolis force in a rotating system is its ability to act as a restoring force to perturbations, thereby making incompressible rotating fluids a wave bearing system. These waves are known as inertial waves, reflecting the fact that they are associated with rotational inertia. Taking the curl of the time derivative of equation (2.11) results in, after neglecting viscous terms and some manipulation,

$$\frac{\partial^2}{\partial t^2}\left(\nabla^2\mathbf{u}\right) + 4\,(\mathbf{\Omega}\cdot\nabla)^2\,\mathbf{u} = 0 \,, \tag{2.12}$$

which supports plane waves of the form $\mathbf{u} = \hat{\mathbf{u}}\,\exp\left[i\,(\mathbf{k}\cdot\mathbf{x} - \varpi t)\right]$. These waves have a dispersion relation of the form

$$\varpi = \pm\frac{2\,(\mathbf{k}\cdot\mathbf{\Omega})}{|\mathbf{k}|} \,, \tag{2.13}$$

which results in the following phase and group velocities

$$\mathbf{c}_p = \varpi \mathbf{k}/|\mathbf{k}^2| = \frac{2\,(\mathbf{k}\cdot\mathbf{\Omega})}{|\mathbf{k}|^3}\,\mathbf{k}\,, \tag{2.14}$$

and

$$\mathbf{c}_g = \nabla_k \varpi = \pm\frac{2\mathbf{k}\times(\mathbf{\Omega}\times\mathbf{k})}{|\mathbf{k}|^3}\,, \tag{2.15}$$

from which we see that there is a limit on the frequency of inertial waves of between 0 and $2\,\Omega$ (Davidson, 2013). Another key feature of inertial waves is that their phase velocity (direction of propogation of wave crests) is perpendicular to the group velocity (direction of energy propogation). This can lead to a variety of interesting and sometimes unexpected behaviours.

As for any closed wave bearing system, it is possible to form standing or stationary wave solutions. The most simple example of this for inertial waves is a cylindrical cavity of fluid rotating at rate Ω about the axis. For an axisymmetric cylinder of radius R and height H modal solutions can be formed consisting of a Bessel function variation in the radial direction and sinusoidal variation in the z direction. The Stokes stream function for a mode of the form $(r, z) = (m, n)$ can be written as

$$\Psi_{m,n} = A\,r\,J_1\left(\frac{\zeta_m}{R}r\right)\sin\left(\frac{n\pi}{H}z\right)e^{(i\varpi_{m,n}t)}\,, \tag{2.16}$$

where ζ_m is the mth zero of the bessel function J_1. These oscillations have a frequency of

$$\varpi_{m,n} = \frac{2\Omega}{\sqrt{1+\left(\frac{H\zeta_m}{n\pi R}\right)^2}}\,, \tag{2.17}$$

which we can see falls within the required range of 0 to $2\,\Omega$. Equation (2.16) can then be used to find expressions for ω_ϕ, Γ, and $\mathbf{u}$. A derivation of this solution is provided in appendix A.

2.4 Axisymmetric buoyant vortex flow

We now turn our attention to the analysis of buoyant vortex flow. Combining the previous results for both buoyant and rotating flows we obtain the overall governing

equations

$$\frac{\mathrm{D}\mathbf{u}}{\mathrm{D}t} = -\frac{1}{\rho_0}\nabla p + 2\mathbf{u}\times\boldsymbol{\Omega} - \beta\theta\mathbf{g} + \nu\nabla^2\mathbf{u}\ ,\ \nabla\cdot\mathbf{u} = 0\ . \tag{2.18}$$

with corresponding vorticity equation

$$\frac{\mathrm{D}\boldsymbol{\omega}}{\mathrm{D}t} = (\boldsymbol{\omega}\cdot\nabla)\,\mathbf{u} + 2\,(\boldsymbol{\Omega}\cdot\nabla)\,\mathbf{u} - \beta\nabla\theta\times\mathbf{g} + \nu\nabla^2\boldsymbol{\omega}\ . \tag{2.19}$$

One simplification we can make to aid the analysis of vortex flow is the assumption of axial symmetry. If we adopt a cylindrical polar co-ordinate system (r, ϕ, z) this states that there is no variation in properties with the azimuthal co-ordinate ϕ. It then becomes useful to separate the (r, z) and ϕ components of motion by performing the following poloidal-azimuthal decomposition,

$$\mathbf{u}_p = (u_r, 0, u_z) \qquad \mathbf{u}_\phi = \big(0, u_\phi, 0\big)\ .$$

Both the poloidal[1] and the azimuthal velocity fields are solenoidal for axisymmetric flows. Furthermore we note that the vorticity can be treated in a similar manner and that, under the assumption of axial symmetry,

$$\boldsymbol{\omega}_p = \nabla\times\mathbf{u}_\phi \qquad \boldsymbol{\omega}_\phi = \nabla\times\mathbf{u}_p\ .$$

Poloidal vorticity is associated with azimuthal motion and vice versa. We also introduce at this point the Stokes stream function Ψ, defined through the poloidal velocity and related to the azimuthal vorticity by

$$\mathbf{u}_p = \nabla\times\left(\frac{\Psi}{r}\,\hat{\mathbf{e}}_\psi\right) \qquad \nabla^2_*\Psi = -r\omega_\psi\ , \tag{2.20}$$

where

$$\nabla^2_* = r\frac{\partial}{\partial r}\left(\frac{1}{r}\frac{\partial}{\partial r}\right) + \frac{\partial^2}{\partial z^2} \tag{2.21}$$

is the Stokes operator. This is a stream function used in axisymmertic cylindrical co-ordinate systems. The contours of constant Ψ follow streamlines of the flow.

[1] In the geophysical context the poloidal term is often referred to as the meridional term.

Extending the ideas of a poloidal-azimuthal decomposition further to the equations of motion, the azimuthal component of equation (2.18) yields the following advection-diffusion-like equation for specific angular momentum $\Gamma = r\,u_\phi$ in the rotating frame

$$\frac{\mathrm{D}\Gamma}{\mathrm{D}t} = -2\Omega r u_r + \nu\nabla_*^2\Gamma \ . \tag{2.22}$$

This is a statement for the conservation of angular momentum in the inertial frame. The $-2\Omega r u_r$ term represents the action of the Coriolis force. As fluid moves radially it experiences a tangential acceleration in the rotating frame necessary in order to conserve angular momentum in the inertial frame. If we were to step back into the inertial reference frame for a moment we could write the total angular momentum as $\Gamma_{Tot.} = \Gamma + \Omega r^2$. It is then a straightforward exercise to arrive at equation (2.22) and see how this term redistributes the intrinsic angular momentum.

In a similar manner, the azimuthal component of equation (2.19) can be manipulated to give the following scalar equation for the evolution of azimuthal vorticity

$$\frac{\mathrm{D}}{\mathrm{D}t}\left(\frac{\omega_\phi}{r}\right) = \frac{\partial}{\partial z}\left(\frac{\Gamma^2}{r^4}\right) + \frac{2\Omega}{r}\frac{\partial u_\phi}{\partial z} - \frac{\beta g}{r}\frac{\partial\theta}{\partial r} + \nu\frac{1}{r^2}\nabla_*^2\left(r\omega_\phi\right) \ . \tag{2.23}$$

On the left is the familiar material derivative, and on the far right is a viscous diffusion term. The other terms may be slightly less familiar, however, and it is worth taking the time to understand their effect. The first term on the right involving axial gradients in angular momentum, $\partial\Gamma^2/\partial z$, represents the process of vortex stretching. Axial gradients in azimuthal flow cause poloidal vortex lines to become distorted such that they obtain a component in the azimuthal direction. This is shown in figure 2.3 which illustrates why this process is often referred to as the 'spiralling up' of vortex lines (Davidson, 2013).

The second term on the left results from the curl of the Coriolis force, and can be understood in a very similar way to the first. Application of the chain rule allows the first two terms on the left to be re-written as

$$\frac{\partial}{\partial z}\left(\frac{\Gamma^2}{r^4}\right) + \frac{2\Omega}{r}\frac{\partial u_\phi}{\partial z} \quad = \quad \frac{2}{r^2}\left(\frac{\Gamma}{r^2} + \Omega\right)\frac{\partial\Gamma}{\partial z} \ ,$$

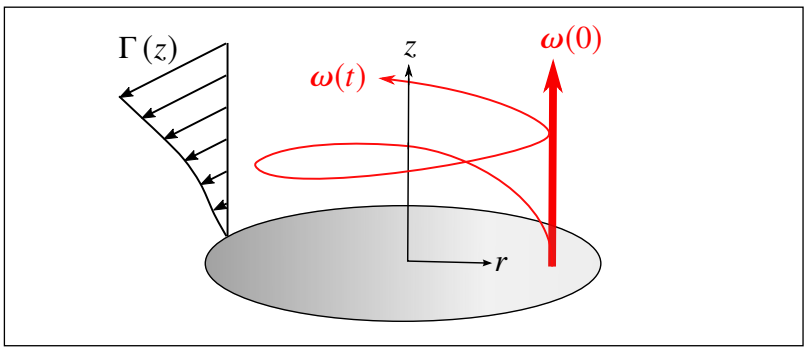

Fig. 2.3 Cartoon illustrating the spiralling up of vortex lines

whereupon the similarity becomes more apparent. Axial gradients in azimuthal flow again act to transfer vorticity from the poloidal to the azimuthal direction, but this time it is vorticity due to the background rotation when viewed in the inertial frame. This appears in the rotating frame as an action of the Coriolis force.

The remaining term results from the curl of the buoyancy force. We see that radial gradients in temperature will act to generate azimuthal vorticity. This can be illustrated through the toy problem in figure 2.4. Consider an initial setup with a tank of water containing in one half warm, positively buoyant fluid, and in the other half cold, negatively buoyant fluid. This gives a negative radial gradient in θ. When released, the warm fluid will rise over the cold to establish a stable stratification as illustrated. The energy released in doing this is converted into poloidal motion, generating azimuthal vorticity.

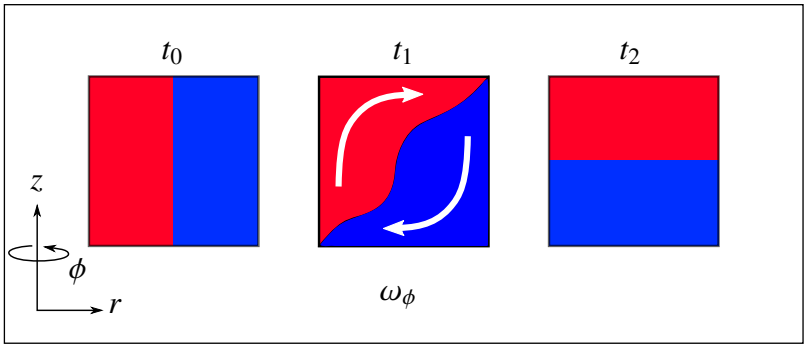

Fig. 2.4 Cartoon illustrating the generation of azimuthal vorticity through horizontal temperature gradients

Chapter 3

Numerical methods

This chapter provides an overview of the numerical methods used in this study. Motivation for a computational approach is given in section 3.1, followed by a discussion of different techniques and justification for the chosen method (Marker and Cell). An overview of the scheme is given in sections 3.2, containing a discussion of the numerical method, and 3.3, which specifically addresses our implementation and any modifications necessary for this study. Details of testing and validation of the code are provided in section 3.4. Finally we give some consideration to numerical accuracy in section 3.5 before summarising the work in section 3.6, along with some suggestions for future development.

3.1 Motivation

In order to study the phenomena in this body of work we decided to adopt a numerical approach for simulating fluid flow. This allows repeated investigations over a wide range of parameters to be performed with easy variation of the key variables affecting behaviour.

A number of different options were considered, including commercial software and in-house codes. It was found, however, that these were not ideally suited to our applications and would have required extensive modification. It was also felt, in some cases, that a lack of knowledge about the implementation of numerical schemes could interfere with the physical processes that we were investigating calling into question any scientific conclusions that might be made based upon the results. Therefore a decision was taken early on to write a custom code that would be capable of handling our specific applications. One aspect we paid particular attention to was the implementation of boundary conditions, since these are extremely important in the flows we shall be investigating. Often there is numerical 'sleight of hand' when implementing boundary conditions in order to simplify or speed up the code. Therefore it was important to seek a numerical method that clearly discretises, and provides control over, the boundary conditions. In addition to this we desire a numerical scheme that is not only reliable and transparent, but also straightforward to implement. Since the focus of this study is on understanding physical processes it was important not to get swept up in the development of complex numerical schemes that add no value to the overall conclusions.

A popular class of numerical methods for two-dimensional incompressible flow are streamfunction-vorticity methods, so-called after the primary variables that they model. These methods are attractive for their relatively simple implementation and the reduced number of variables when compared to a pressure-velocity formulation. This advantage is, however, lost when moving to three dimensions. The main drawback to the streamfunction-vorticity approach lies in the implementation of boundary conditions, which have to be reformulated in terms of vorticity and streamfunction. This process becomes increasingly challenging for more complicated conditions (Ferziger & Peric, 2002). In light of this we instead pursue

a primitive variables approach (pressure and velocity) that will provide greater control over the implementation of boundary conditions.

Investigations of axisymmetric swirling flow were performed by Harlow & Stein (1974) in order to better understand columnar vortices. They used a numerical method known as the Marker and Cell scheme (MAC). Although initially developed for modelling free surfaces and tracking fluid motion (Harlow & Welch, 1965), the internal dynamics of this code can be used to model a wide variety of flows. The method is well documented in the technical reports from the Los Alamos Laboratory where it was developed (Welch *et al.*, 1965; Stein & Harlow, 1974). A discussion of recent developments to the MAC scheme can be found in McKee *et al.* (2004).

3.2 Numerical formulation

The MAC method that is used throughout the course of this work can be formally classified as a finite-difference pressure-correction scheme (Chung, 2002) that operates in primitive variables. Here we give a brief overview of the numerical formulation behind the scheme, details for which can be found in Harlow & Welch (1965), with a more extensive discussion in Fletcher (1997).

The algorithm takes the Navier-Stokes equation (2.1) and makes use of the continuity equation (2.2) to re-write the non-linear convective derivative as follows

$$\frac{\partial \mathbf{u}}{\partial t} + \nabla \cdot (\mathbf{u} \otimes \mathbf{u}) = -\nabla \left(\frac{p}{\rho} \right) + \nu \nabla^2 \mathbf{u} \,, \tag{3.1}$$

where $[\nabla \cdot (\mathbf{u} \otimes \mathbf{u})]_i = \nabla \cdot (u_i \, \mathbf{u})$. Note that, since the fluid is incompressible, the density has also been taken inside the gradient operator. This is known as the conservation form of the Navier-Stokes equation, and is a common approach in the numerical solution of flows using primitive variables. Though mathematically identical to the non-conservation form (equation (2.1)), there are differences between the two when discretised for use in numerical methods. The advantage of using the conservation form from a computational point of view becomes apparent by considering a small volume, whereupon we find that, when discretised, momentum is conserved across the volume. This analysis extends to a larger

grid, with the discretised conservation form of the equations forming a telescoping series and fluxes being conserved across the mesh. In contrast, a non-conservation discretisation gains an additional term for each gridpoint and fluxes may no longer be balanced. Using the conservation form when discretising reduces numerical errors and the effect known as artificial viscosity. A more in-depth discussion about the benefits of the conservation form can be found in Anderson (1995).

The MAC method proceeds as follows. Equation (3.1) is stepped forwards in time based on values at a previous timestep (n) to give an estimation of a new velocity at ($n+1$):

$$\frac{\mathbf{u}^{n+1}-\mathbf{u}^{n}}{\Delta t}+\nabla\cdot(\mathbf{u}^{n}\otimes\mathbf{u}^{n})=-\nabla\left(\frac{p}{\rho}\right)+\nu\nabla^{2}\boldsymbol{u}^{n}\ . \tag{3.2}$$

Taking the divergence of this gives

$$\frac{\nabla\cdot\mathbf{u}^{n+1}-\nabla\cdot\mathbf{u}^{n}}{\Delta t}+\nabla\cdot\nabla\cdot(\mathbf{u}\otimes\mathbf{u})^{n}=-\nabla^{2}\left(\frac{p}{\rho}\right)+\nu\nabla^{2}\left(\nabla\cdot\mathbf{u}^{n}\right)\ . \tag{3.3}$$

We now impose the requirement that the divergence of the updated velocity field be zero in order to satisfy incompressibility. Rearranging then results in the following Poisson equation for pressure

$$\nabla^{2}\left(\frac{p}{\rho}\right)=\nabla\cdot\mathbf{u}^{n}+\Delta t\left(-\nabla\cdot\nabla\cdot(\mathbf{u}\otimes\mathbf{u})^{n}+\nu\nabla^{2}\left(\nabla\cdot\mathbf{u}^{n}\right)\right)\ . \tag{3.4}$$

Solving this yields an intermediate or 'corrected' pressure that can be used in equation (3.2) to obtain the new 'corrected' velocity. This velocity will, within numerical error, satisfy the incompressibility condition.

3.3 Numerical implementation

The MAC method was implemented from scratch using the FORTRAN programming language. The code was developed incrementally, initially without body forces before later adding in the effects of buoyancy and rotation. Since these effects are not included in the original MAC scheme we had to implement them ourselves. This section contains a discussion of how this was done, as well as

highlighting some other important features of the numerical method such as the mesh and boundary conditions. It also contains a discussion of the the structure of the code.

3.3.1 Mesh and discretisation

The MAC method is implemented for an axisymmetric cylindrical polar co-ordinate system on a staggered mesh. This name reflects the fact that different flow variables are stored at different locations on the grid, as illustrated in figure 3.1. The poloidal velocities u_r and u_z are defined at the faces of cells, as illustrated in figure 3.1, whilst the other variables are defined at the cell centres. The main benefit to this approach comes from the fact that pressure and velocity are coupled at adjacent grid points, preventing the effect known as 'checkerboarding' whereby an oscillatory solution manifests as the result of two separate solutions associated with alternate gridpoints (Patankar, 1980; Fletcher, 1997). For simplicity the mesh used in our simulations is always rectangular in the $r - z$ plane, but includes the option for

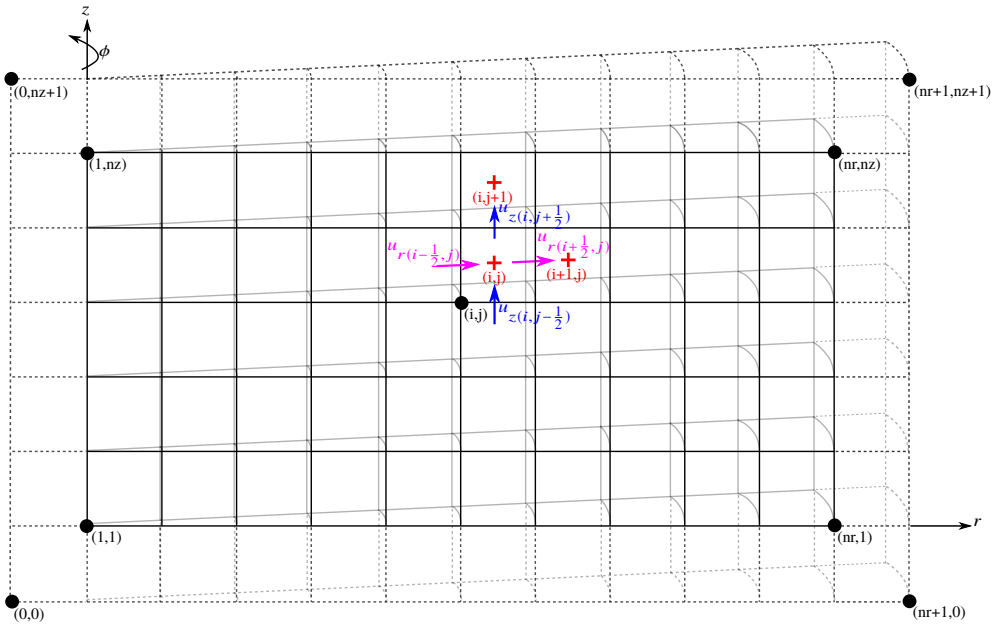

Fig. 3.1 Schematic of the staggered mesh

refinement near the boundaries or in the centre using either quadratic or exponential spacing.

The downside to using a staggered mesh is that it introduces some complexities into the numerical implementation in terms of indexing and discretising, although these can be overcome with due diligence. It also complicates the implementation of boundary conditions since at least one dependent variable will always be undefined on the boundary. To overcome this we use a layer of ghost cells outside our domain indicated by the dashed lines in figure 3.1. By setting the values of the variables for these cells appropriately we can ensure that the required conditions are satisfied on the boundary for our discretised equations.

The equations themselves were discretised using second-order central differences in space, and an explicit first-order difference in time. Details of this discretisation for a two-dimensional Cartesian system can be found for in Welch *et al.* (1965), along with a brief discussion of how it might be modified for two-dimensional cylindrical polar co-ordinates (r, z). This formulation is developed in Stein & Harlow (1974) for an axisymmetric domain with a u_ϕ component. None of these equations contain buoyancy or rotation however, so these terms had to added into the MAC equations and discretised, as discussed below.

A further change from the implementation used in Harlow & Stein (1974) is that, rather than discretising the equation for azimuthal velocity, we instead choose to re-write this component in terms of angular momentum (equation (2.22)). The advantage of doing this is that the equations we have discretised are now more rigorously conservative for angular momentum. A knock-on effect from this, however, is that any u_ϕ terms in the other equations now have to be written in terms of Γ.

Time stepping was performed using the forward Euler method as set out in Welch *et al.* (1965). The advantage of using this scheme is that it is easy to implement in our equations. The downside, however, is that it is only first order accurate. This means that in order to maintain accuracy in our solutions we are required to take smaller timesteps than might be afforded by other, more complex timestepping procedures. However, since we are solving laminar flows and using reasonably modest domains, this restriction should not be overly problematic. The forward Euler method can be shown to be stable with a restriction on maximum

timestep (Ferziger & Peric, 2002). It is worth noting here that there is a trade-off in the MAC scheme with a smaller timestep speeding up each application of the Poisson solver. This is because when stepsize is small, the pressure from the previous timestep provides a good approximation to the new solution.

3.3.2 The Poisson equation

One of the more challenging aspects of writing this code came from solving the Poisson equation for pressure 3.4. The standard approach is to implement an iterative technique, although details in Welch *et al.* (1965) are sparse. Initially we chose to use the tridiagonal matrix (or Thomas) algorithm (Hirsch, 2007), but this was soon replaced by the Gauss-Seidel method utilising successive over-relaxation to speed up convergence (Fletcher, 1997). More recently improvements have been made by solving the Poisson pressure equation by using conjugate gradient methods. This approach was implemented using the biconjugate gradient stabilised method (BiCGStab) (Saad, 2003), but failed to yield any significant improvement over the Gauss-Seidel method in our code. This is likely due to the fact that the pressure from the previous timestep provides a good approximation to the new solution as discussed above.

Although Poisson equations for pressure are often found in primitive variables solvers, there is significant debate about the 'correct' boundary conditions. A discussion of the different approaches can be found in Gresho & Sani (1987) and Gresho (1991). We choose to adopt what we believe to be the most physically grounded approach, with the boundary conditions obtained through the normal projection of the discretised momentum equations onto the boundary.

For a domain with closed boundaries, such as we consider in this work, the resulting boundary conditions for the pressure equation are Neumann (or second-type). An issue arising from this is that the problem becomes singular, that is, any solution to the Poisson equation with these conditions is indistinguishable by the addition of a scalar constant. Although this is not a problem when solving the equations of motion, since only the gradient of pressure is required, it does become an issue when solving the Poisson equation numerically. This is because the results from any iterative solver can float, or even diverge. To overcome this we

enforce a compatibility condition on the domain. For a two-dimensional Cartesian system this is Green's integral theorem as described in Fletcher (1997). For an axisymmetric domain with three velocity components we can extend this approach to show that the compatibility condition is given by Gauss' theorem. Enforcing this as a small correction in our solver then allows it to converge to a solution.

Following development, the Poisson solver was tested on a number of prescribed problems and compared to analytical solutions before being implemented into our numerical scheme.

3.3.3 Boundary conditions

As we have already discussed, the implementation of boundary conditions was a key focus in our numerical work. One of the appealing aspects of the MAC approach is that it is relatively straightforward to write out the appropriate formulation for a range of different conditions. The values of any variables that lie on the boundary can be set exactly, for instance radial velocities at the radial boundary and axial velocities on the upper and lower surfaces. For variables that do not lie on the boundary the process is more challenging. We tackle this by setting their values in the ghost cells that lie outside the domain. This is done in such a way that when these values are inserted into the discretised equations they provide the correct value or condition at the boundary of the domain.

One area we pay particular attention to is the axis. This can cause issues in numerical codes due to singularities that can occur in any terms containing a $1/r$ factor. The staggered mesh is, again, advantageous here, since the only variable located directly on the axis is the radial velocity, u_r, which we know must be zero under axial symmetry. The remaining variables are then set in the ghost cells to satisfy the axial boundary condition. The effect of the axis also becomes important in the internal dynamics of the code whenever derivatives involve a factor of $1/r$ on the axis. To tackle this the code has a separate routine for the `I = 1` column of cells near the axis to deal with these factors. The remainder of the domain is then solved for using the standard discretisation.

In addition to the axis the boundary conditions must be specified at the upper, lower, and radial boundaries. In our code these may be set to be either no-slip

or free-slip. The no-slip boundaries can be specified to rotate at a constant rate, different to that of the domain.

3.3.4 Buoyancy and rotation

Once we had a code that could solve the basic equations of fluid motion, the next major undertaking was to implement the effects of buoyancy. To do this an additional variable for the temperature was added. Rather than the total temperature we use θ, the perturbation to a fixed background temperature T_0 as described in section 2.2. This is added to the discretised equations of motion, and must also be included as a source term in the Poisson pressure equation as

$$\nabla \cdot (\beta\theta\mathbf{g}) = -\mathrm{g}\beta\frac{\partial\theta}{\partial z} \ . \tag{3.5}$$

The addition of a temperature variable also requires the implementation of the heat equation (2.9). This is performed using using a prognostic approach. Following the solution of the equations of motion as described above, the discretised form of equation (2.9) is advanced using the new values for the velocity field to update the temperature field. It should be noted at this point that the temperature and velocity equations are coupled, and therefore a change in one will affect the other. As such, a more accurate approach would be to implement an iterative scheme whereby the updated temperature is fed back into the velocity equation in a loop until convergence is reached. A similar justification for the use of the forward Euler timestepping routine, i.e. that the error will be negligible provided the timestep is small, is used for the current implementation of the temperature equation. However, if changes were made to the timestepping routine or larger timesteps were used then this issue would require attention and an iterative loop should be added.

For our particular application we extend our work on buoyancy a little further to include a linear background stratification of the form $\mathrm{d}T_0/\mathrm{d}z = \text{const.}$, the constant being negative (unstable stratification). In doing this a slight modification

is required to the temperature equation (2.9) such that it becomes

$$\frac{\mathrm{D}\theta}{\mathrm{D}t} = \alpha\nabla^2\theta + \left|\frac{\mathrm{d}T_0}{\mathrm{d}z}\right| u_z \ , \tag{3.6}$$

where θ is now the perturbation to the background linear temperature profile $T_0(z)$.

The final effect of adding a temperature field is that the boundary conditions have to be modified accordingly. For the Poisson equation this involves the projection of the buoyancy terms onto the boundary. It is also necessary to implement boundary conditions for temperature which, due to our representation, require a little thought. The most simple case is when there is zero stratification. A Dirichlet condition $\theta = \text{const.}$ will specify a fixed temperature on the boundary, whilst a Neumann condition, $\nabla\theta \cdot \hat{\mathbf{n}} = \text{const.}$, specifies a fixed heat flux according to

$$\mathbf{q} = -\kappa\nabla\theta \ . \tag{3.7}$$

When $\nabla\theta \cdot \hat{\mathbf{n}} = 0$ the Neumann condition specifies an adiabatic boundary.

Things become more complicated with the addition of stratification. The Dirichlet condition still prescribes a constant temperature on the boundary, but care must be taken to include the effect of the background temperature profile with the temperature on the boundary now being $T_b = T_0(z_b) + \theta$. The Neumann condition still prescribes a heat flux, but this is now augmented by the background stratification as follows

$$\mathbf{q} = -\kappa\left(\nabla\theta + \frac{\mathrm{d}T_0}{\mathrm{d}z}\mathbf{k}\right) \ . \tag{3.8}$$

Care must be taken when setting the value of θ in the ghost cells so that the desired boundary condition is being specified.

Another major addition to the numerical scheme was to implement background rotation. As with buoyancy, this was done by introducing additional terms to the discretised equations of motion as discussed in section 2.3. These changes result in another source term in the Poisson equation for pressure, this time the divergence of the Coriolis force

$$\nabla \cdot (2\boldsymbol{\Omega} \times \mathbf{u}) = -\frac{2\Omega}{r}\frac{\partial\Gamma}{\partial r} \ . \tag{3.9}$$

Since the boundaries are in the rotating frame no modification is necessary to the boundary conditions for $\mathbf{u}$ and θ.

3.3.5 Code structure

Throughout the development process particular attention was given to structure and versatility. This made it easier to make changes at later stages and allowed us to use the code to explore different configurations. Since this is a large scale coding project we adopt a structured programming approach. This paradigm involves breaking the code up into a number of separate tasks. Each of these is then contained within a separate subroutine. By doing this it is possible to test the operation of individual subroutines before their implementation into the rest of the code. This was particularly beneficial when developing the Poisson solver.

Another benefit of this approach is that it makes it easier to modify the code at a later stage. For example, the first implemntation of the MAC method used the Thomas Algorithm to solve the Poisson equation. This was later replaced by an improved solver using the Gauss-Seidel method. Thanks to adopting a modular programming approach the new solver could be built and tested on its own. Once completed it can then be called from the main program in the same way as the previous solver with just a different function call.

The structured programming approach was also beneficial when using our code for different applications, with the subroutines for setting initial conditions and boundary conditions contained in a separate module. This means that when investigating a different application, only this module needs to be changed; there is no need to alter any of the core of the code. Continuing with this idea, all of the program inputs for a particular run are read from a file, with the only parameter passed directly to the program being the location of this file. This means that there is always a clear record held of how the code was initialised for future reference. Where possible the input is given in terms of dimensionless quantities, with only the minimum number of dimensional quantities required to calculate the rest specified.

Figure 3.2 shows a flowchart of the code structure. Each box represents a separate subroutine that is called to carry out a specific function. The name of the subroutine is given in capitals, along with a brief description. The black routines

are common to all simulations and remain unchanged between runs. The routines in blue contain elements that are unique to a particular application of the code and have to be written specifically, for example the initial condition and boundary conditions. These blue subroutines are all contained within a separate file that is selected at compile time.

The code starts by initialising the necessary variables and then calling a subroutine called FILESX, which takes a directory name for the current simulation from the user. After checking that this directory exists, the program creates an output file called conv.dat which is used throughout the run to write information such as the divergence, CFL number, and number of iterations of the Poisson solver at each timestep. The program then reads in data from an input file and calculates any other parameters that are required. This means that we have a record of every simulation and can repeat them if required. Although not indicated on the flowchart, there is the option to re-start the code from a previously saved point. If this option is specified then the code would read in previously saved data and go straight to the TIMESTEP subroutine re-starting from the saved point. In all other cases the MESH subroutine is called that generates the staggered mesh for the simulation and writes this data to file for future use. This is followed by the INITIALISE subroutine that sets the internal values of velocity, pressure, and temperature, applies the boundary conditions, and then writes the zeroth output file.

Once preparation is complete the code proceeds to the timestepping subroutine. This loops repeatedly, performing one full timestep at each iteration. The subroutine takes the properties at the previous timestep and uses them to construct the Poisson equation for pressure. This information is then passed to the subroutine POISSON which prepares the equations in sparse matrix form and applies the pressure boundary conditions. The system is then solved by the Poisson solver in the GAUSSEIDEL subroutine. After a solution is returned, the corrected pressure is used to update the velocities for the current timestep and the boundary conditions are again enforced. Once the new velocity field has been found, the TEMPUPDATE subroutine performs a prognostic update of the temperature field. Before moving on to the next timestep the code checks the CFL and Peclet numbers and the divergence throughout the domain, terminating with an error message if these are outside an appropriate tolerance. Finally information about the current iteration is written to

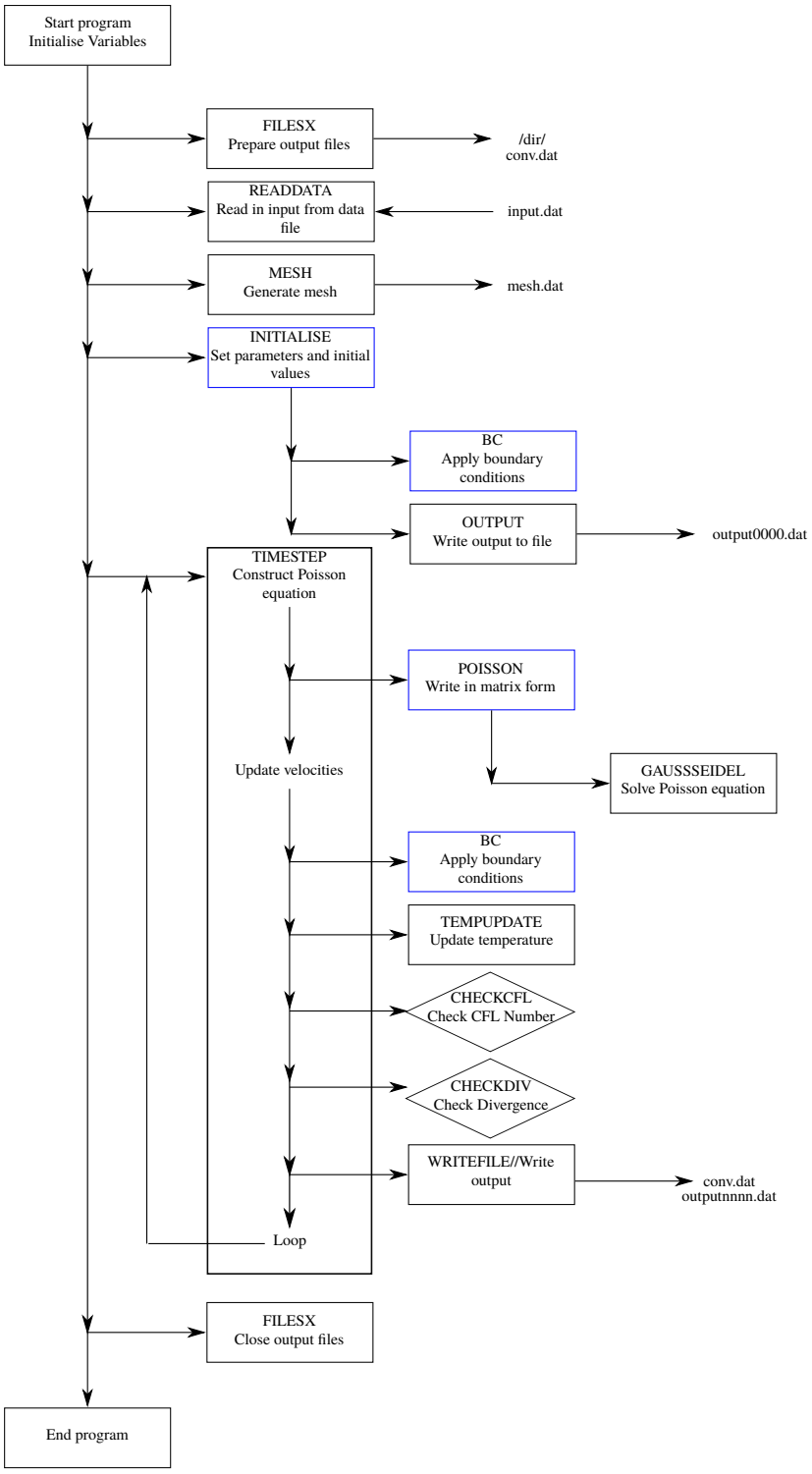

Fig. 3.2 Flowchart showing the structure of the code

the file conv.dat, and an output file is written (if required) with variable values from the staggered mesh calculated at the cell corners.

Once the code has performed the required number of iterations, and the loop over the timestepping subroutine is complete, FILESX is called again, this time to safely close any files that were used for output. Once this is complete the program terminates and a message is sent to notify the user.

All of the results presented in this work were carried out using the code described above running on an OpenSUSE Linux system. The hardware consisted of a Dell Optiplex 750 desktop PC with an intel core i5 processor and 4 gigabytes of random access memory. Post-processing and analysis of the results was performed using Python 2.7, with the Matplotlib package being used for visualisation.

3.4 Test cases and validation

Following the development of the code it is necessary to perform validation to ensure that it works and produces physically realistic results. This section contains a discussion of a number of different test cases that were performed using the code, along with an explanation of what each demonstrates.

3.4.1 The self-destruction of an inviscid spherical vortex

An example from Davidson (2013), this test case takes the initial condition of an isolated patch of azimuthal velocity and allows it to evolve. A poloidal flow is induced that sweeps radially outwards causing the blob to burst under its own centrifugal force and form an exponentially thinning vortex sheet. This process is shown in figure 3.3. The initial condition is given by:

$$\mathbf{u}_p = 0 \,, \qquad u_\phi = \Omega r \, e^{-\left(r^2+z^2\right)/l^2} \,,$$

where Ω is a characteristic angular velocity, and l is the characteristic radius of the Gaussian blob. The contours of angular momentum for this initial condition are shown in figure 3.4a.

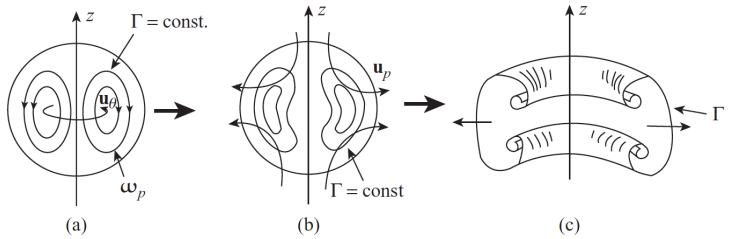

Fig. 3.3 Image taken from Davidson (2013) showing the bursting of the spherical vortex. The initial condition is shown in (a), whilst (b) shows how the induced secondary poloidal flow sweeps the blob radially outwards. Eventually the blob wraps up to form an axisymmetric vortex sheet (c).

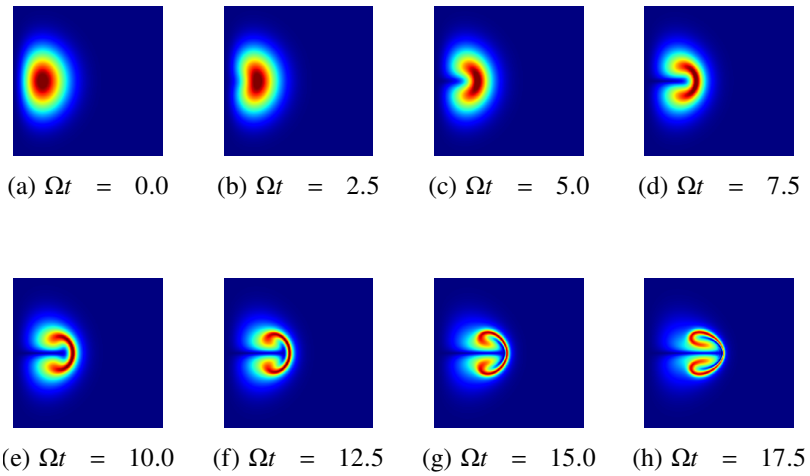

Fig. 3.4 The evolution Γ for the bursting vortex

The purpose of this test case is to examine the internal dynamics of the code without the effects of buoyancy or background rotation. It involves motion in all three directions, has properties that can be monitored and compared to analytical results, and develops in a distinctive way that can be qualitatively observed. This test also provides a measure of code 'quality' in that, at some point, the exponential thinning of the vortex sheet should cause the code to break down. Failure to do so indicates the presence of unwanted and unphysical effects such as excessive artificial viscosity acting to stabilise and force a result.

Figure 3.4 shows the evolution of angular momentum for the case $\Omega = 0.5$ rad s^{-1} and $l = 0.2$ m. We see that the evolution of the vortex in our simulations provides a

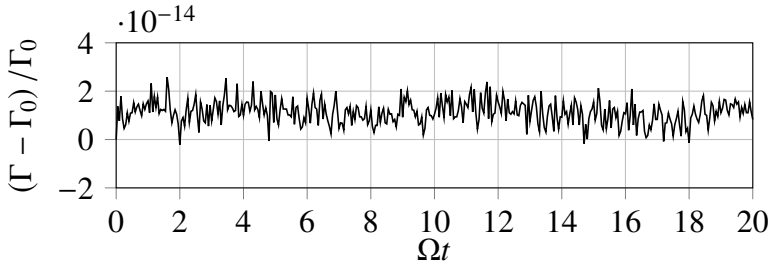

Fig. 3.5 Variation of Γ for the bursting vortex

qualitatively good match to the solution shown in Davidson (2013). As a quantitative measure of performance Davidson *et al.* (2007) show that angular momentum must be conserved for the bursting vortex, even in the presence of viscosity. By tracking the total angular momentum over the course of our simulation, plotted in figure 3.5, we see that there is a maximum deviation of $\pm 10^{-12}$ % from the initial value Γ_0 over the course of the run. This provides quantitative support that the internal dynamics of the code are working correctly and accurately.

3.4.2 The Bödewadt layer

The second test case investigates the flow between two coaxial bounded discs. Rotating flow above a no-slip boundary leads to the development of a boundary layer at the surface. The centrifugal component of pressure from the bulk flow is imposed upon the boundary layer to drive a swirling radial inflow. In order to satisfy continuity there is a weak axial flow upwards, away from the surface. Bödewadt (1940) provides an analytical solution to the Navier-Stokes equations for this case. The calculations may be found in Bödewadt's original paper, and are discussed at length by Greenspan (1968)

As an approximation to the flow described by Bödewadt we examine a cavity with a rotating lid. The lid drives a rotating flow at rate Ω within the cavity, leading to the development of a Bödewadt layer above the base. It is the velocity profile in this layer that will be compared to the similarity solution tabulated in Bödewadt (1940). Provided the cavity is sufficiently large in the radial direction that we can neglect side wall effects away from the radial boundary, the velocity profile should should match the analytical similarity solution. Figure 3.6 show a comparison of

the numerical and analytical solutions for the three velocity components at the lower boundary. We can see that they agree well.

The purpose of this test is to examine the behaviour at the boundaries and the implementation of boundary conditions. At the lower boundary we have a no-slip condition that gives rise to a boundary layer, whilst at the upper boundary we have no-slip with an imposed rotation acting to spin up the flow. Successfully generating the boundary layer matching the similarity solution for all three velocity components confirms our formulation of the no-slip condition is working well and is physically realistic.

3.4.3 The rising thermal

Another example from Davidson (2013), this test case is interesting since it also serves as an illustration of the analogy between stratified and rotating fluids. We consider the development of an isolated patch of heat, the motion of which is governed by the equations of section 2.2. There is an analogy between these equations and those that govern the poloidal motion of the centrifugally bursting vortex discussed above. This can be seen if we replace the buoyancy term $-\beta\theta$ with Γ^2, and $\mathbf{g}$ with $\hat{\mathbf{e}}_r/r^3$. The bursting vortex generated poloidal motion as fluid was driven radially outwards under the action of the centrifugal force. Here poloidal motion is generated as warm fluid rises upwards under the action of the buoyancy force. As a result we expect to observe qualitative similarities between the two test cases. In addition to this a theoretical study by Davidson *et al.* (2007) analyses the evolution of a Gaussian heat distribution and shows that the axial linear impulse of the thermal, defined as $L = \frac{1}{2}\int r\omega_\phi \, \mathrm{d}V$, must increase linearly in time.

We take the initial condition of a Gaussian buoyant blob as described in Davidson *et al.* (2007),

$$\mathbf{u} = 0 \,, \qquad \theta = \Theta \, e^{-\left(r^2+z^2\right)/l^2} \,,$$

where Θ is a characteristic temperature and l is a characteristic lengthscale. This is allowed to evolve freely under the action of the buoyancy force. The results (temperature) are shown in figure 3.7. We see that there are indeed qualitative

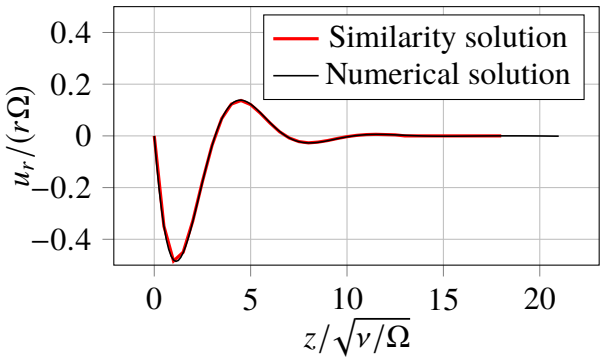

(a) Radial velocity

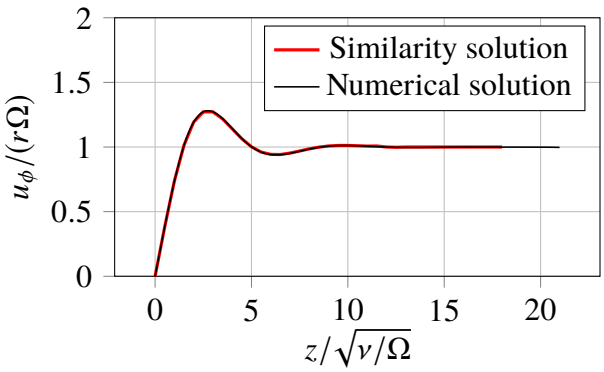

(b) Azimuthal velocity

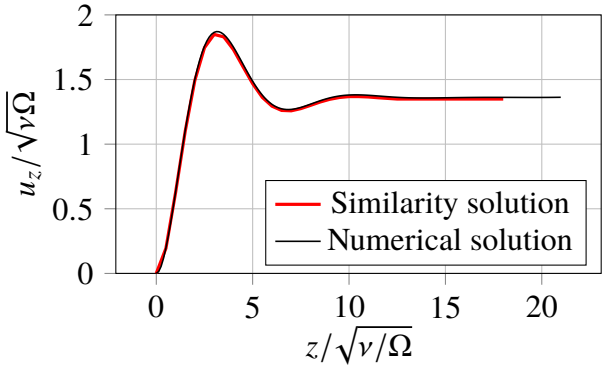

(c) Axial velocity

Fig. 3.6 Comparison of the numerical and analytical solutions for flow in a Bödewadt layer.

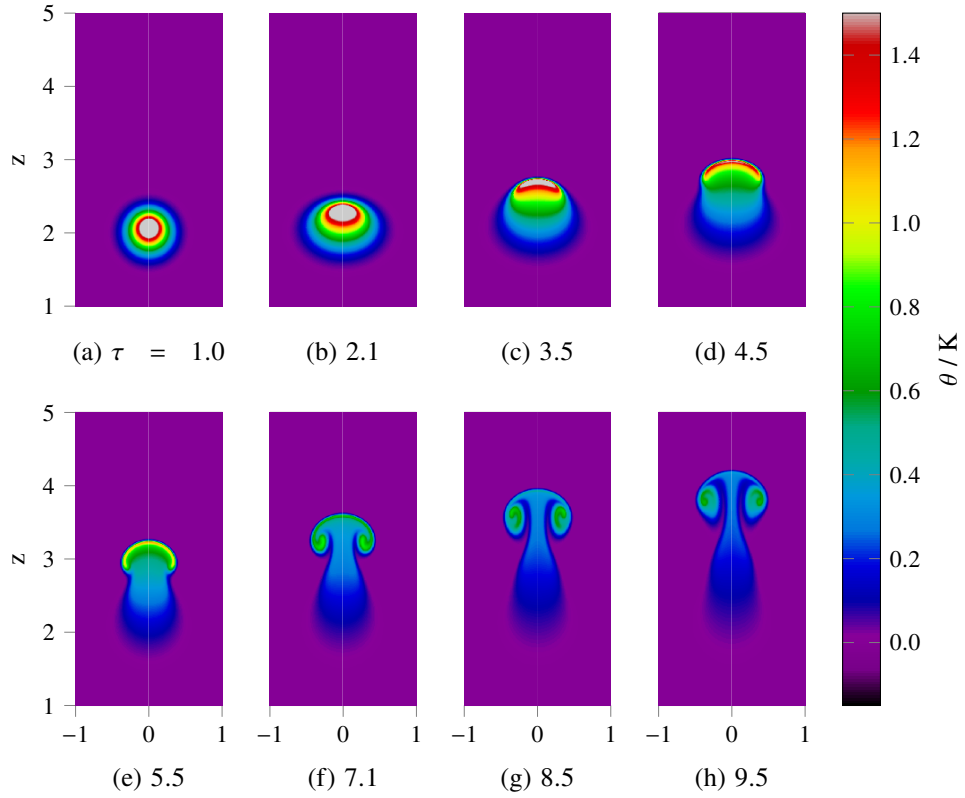

Fig. 3.7 Evolution of the temperature anomaly for the buoyant blob. τ is dimensionless time.

similarities between this and the centrifugally bursting vortex with the centre punching through and the sides wrapping up. The motion this time develops in the axial direction, rather than radially, reflecting the change from $\hat{\mathbf{e}}_r/r^3$ to $\mathbf{g}$. In addition to qualitative features we also track the total axial linear impulse of the fluid from rest to confirm that it does, indeed, scale linearly in time. This is shown in figure 3.8.

This case serves to test the implementation of the buoyancy force and temperature equation in our the numerical scheme.

3.4.4 The flow between co-rotating discs

As an extension to the Bödewadt layer that has already been discussed, this final case serves to test the implementation of background rotation. We again consider

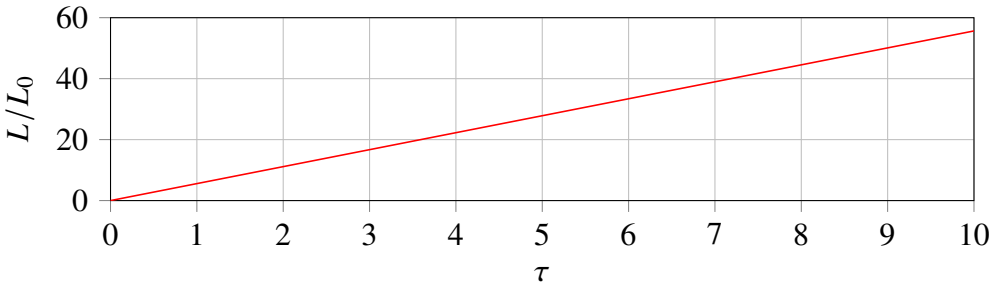

Fig. 3.8 Evolution of dimensionless axial impulse for the buoyant blob. τ is dimensionless time.

the flow between two coaxial plates, this time when both are rotating. If the plates rotate at differential rates, the lower with angular velocity Ω and the top at $\Omega + \epsilon$ ($\epsilon > 0$), then a flow pattern is set up with rotating boundary layers at both the upper and lower surfaces. The lower boundary layer is similar to the Bödewadt layer that has already been discussed, with radial inflow and axial outflow. The upper boundary layer is the opposite, similar to a von Kármán layer, with a radial outflow in the boundary layer, maintained by an axial inflow. Both the Bödewadt and von Kármán layers are particular examples of the more generic phenomenon known as an Ekman layer.

The flow between these layers can be analysed in a reference frame that rotates with the lower boundary at rate Ω, as is done by Acheson (1990). By matching up the equations for the upper and lower boundary layers we find that the motion in the interior is given by

$$u_r = 0 \,, \qquad u_\phi = \frac{1}{2}\Omega\epsilon r \,, \qquad u_z = \frac{1}{2}\left(\nu\Omega\right)^{1/2}\epsilon \,.$$

The boundary layers have a height of approximately $\delta = 4\sqrt{\nu/\Omega}$ (Davidson, 2013), outside of which the flow should follow this solution.

We performed a simulation of the flow between differentially rotating discs, initialised in solid body rotation and running until a steady state was reached. The three velocity components as a function of height at a radius of $0.75R = 32.5\,\delta$, where R is the radius of the container, are plotted as black lines in figure 3.9. The theoretical values for the interior of the flow are shown in red. The height of the

boundary layers, δ, for the upper and lower surfaces is denoted by the dashed lines. We see that outside the boundary layers the numerical and theoretical solutions agree well, indicating that background rotation has been successfully implemented in the code.

3.5 A discussion of numerical accuracy

As with any investigation, experimental or numerical, it is important to have some appreciation of the sources of error and uncertainty. There are a number of measures built into the code to monitor and maintain accuracy.

The use of explicit integration in time results in a Courant–Friedrichs–Lewy (CFL) condition on the maximum timestep in order to maintain stability. This can be written in the form

$$C = \frac{|u|\,\Delta t}{\Delta x} \leq C_{max} \ , \tag{3.10}$$

where C_{max} depends on the numerical scheme. For explicit schemes this is typically 1, although in practice smaller values are often used. The principle behind this is that information travelling at velocity u can propagate at most one grid point at each timestep. The CFL number is checked throughout the domain at each timestep in our code to ensure that it is below the maximum value, with the code terminating if it becomes too large. Simulations that violate the CFL condition can be re-run with a reduced timestep.

A similar stability condition exists for the heat equation. This can be expressed in terms of a diffusion number (Patankar, 1980) as

$$D = \frac{\alpha \Delta t}{\Delta x^2} \leq D_{max} \ , \tag{3.11}$$

where D_{max} is typically $1/2$. When this is exceeded solutions of the temperature field can develop oscillations on the mesh. This condition places a serious limit on the maximum timestep as a function of the mesh size and thermal diffusivity. Like the CFL number, this criterion is checked at each timestep in our code.

Another issue we need to be aware of is artificial viscosity or false diffusion. This is a phenomenon whereby the viscosity in a numerical simulation varies from

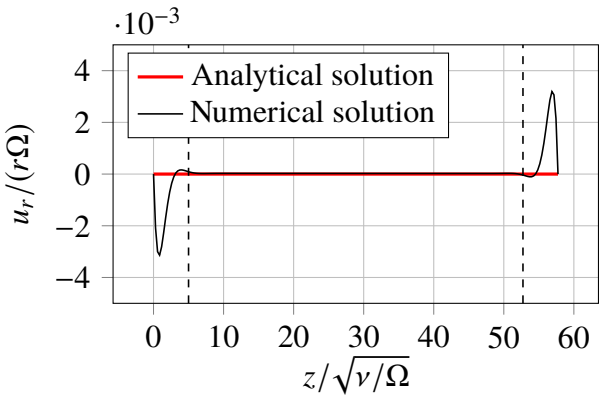

(a) Radial velocity

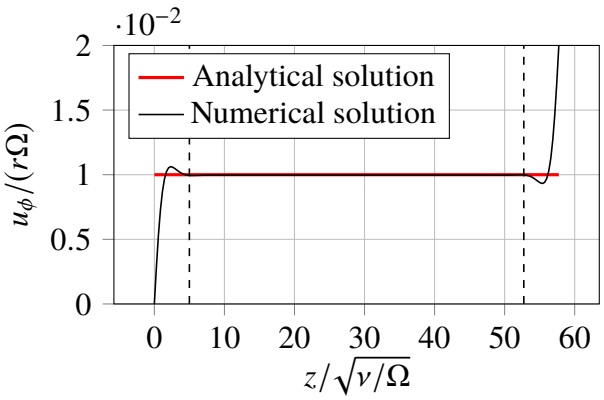

(b) Azimuthal velocity

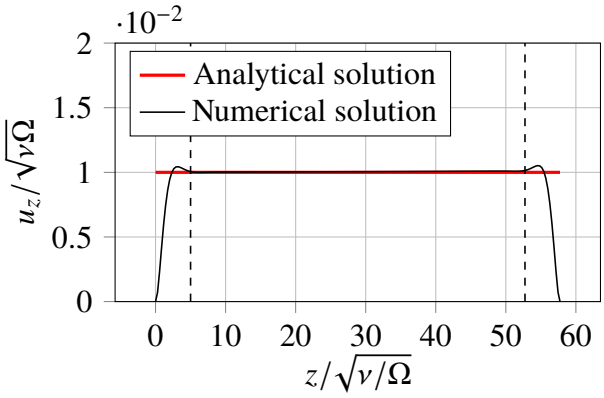

(c) Axial velocity

Fig. 3.9 Velocity profiles between the spinning discs as a function of height at a radius of $0.75R$

that which is prescribed, increasing by an unknown amount at different locations. The effect arises primarily due to the fact that finite difference schemes treat the flow as locally one-dimensional across cell faces, i.e. velocities with both r and z components are broken up and each component treated separately. This is a significant problem when modelling high speed or inviscid flow since many phenomena (e.g. shock waves) are disrupted by the addition of viscosity. For viscous flows it is less of an issue provided any artificial viscosity is small relative to the prescribed viscosity. The effect may reduced by using a more refined mesh, although this introduces restrictions on the time step and computational resources. Ensuring that the divergence throughout the mesh is small at each timestep, as we do in our code, helps to reduce artificial viscosity. It is also beneficial, where possible, to align the grid with the direction of the flow. An extended discussion of artificial viscosity, including an estimation of magnitude, can be found in Patankar (1980).

Another source of error in our numerical scheme is the finite accuracy to which the Poisson equation is solved. This is directly related to the accuracy to which zero divergence is enforced. As with all iterative solvers we do not solve for an exact solution, but rather continuously approach the solution until the change due to further iteration is deemed sufficiently small. To do this the maximum difference at each iteration is recorded and compared to a specified tolerance. Usually this was of the order of 10^{-6} which was found to give reasonable accuracy whilst not taking excessively long to converge. Double-precision format was used for all variables throughout the code to provide maximum accuracy.

In order to monitor performance a number of variables are output to a convergence file at each timestep. These include the maximum CFL and diffusion numbers for the flow, the number of iterations to solve the Poisson equation, and both the average and maximum divergence. By monitoring these residuals we can check that the code is performing to a suitable level of accuracy and locate any potential issues that may have arisen during the course of a simulation. In addition to monitoring these residuals, we also perform spatial and temporal resolution studies for all test cases and applications. This involves increasing the mesh resolution and decreasing the timestep and repeating simulations. If the results are the same, to within a given tolerance, then the the resolution and timestep are deemed sufficiently accurate.

3.6 Summary

We have selected and implemented a numerical scheme (MAC) suitable for simulating axisymmetric laminar flows with swirl. The scheme was selected for its ease of implementation and clearly formulated boundary conditions. The main developments to the MAC scheme that we have made are the addition of the buoyancy and rotational body forces to make it suitable for our applications. We have also implemented a prognostic form of the heat equation to account for thermal conduction. We are concious that this study is not primarily a numerics project, and that the development of this code is necessary step on the way to investigating and understanding our flows of interest. Nonetheless, it is important that this is done well in order for any results to be meaningful and reliable. Therefore we have given thought to the structuring and implementation of the numerical routine, and discuss aspects relating to numerical accuracy. The code has been evaluated at each stage of development using a series of test cases, usually a involving comparison of numerical solutions and analytical results. These tests were performed to confirm that our code produces physically realistic results before we progress to new investigations.

As discussed, the code is written to a level at which we can perform numerical simulations of the phenomena we were investigating and obtain reliable results. However, given further time to develop the code for its own sake there are a number of additional features that might be included to improve performance. These are listed below ordered roughly from least to most complex along with brief discussion.

- Adaptive timestepping. This would allow the code to proceed more rapidly through initial transients or periods of little change. It would also allow for the timestep to be reduced when high gradients form, allowing simulations to proceed instead of causing the code to terminate.

- Improved output. At present the output of the code is stored as a text file which is relatively inefficient and leads to large amounts of storage space being required. Storing this data as binaries would reduce filesizes and be much more efficient. These can still be read into python for post-processing using appropriate function libraries. Alternatively we might use the NetCDF

data format. This is an efficient way of storing data and can easily be read by multiple platforms and programs. The self-describing nature of NetCDF helps prevent errors during post-processing and analysis.

- Improved Poisson solver. We discussed how our solution of the Poisson equation using the Gauss-Seidel method performs well due to the small timesteps used. If we decided to proceed with adaptive timestepping we might find that the BiCGSTAB routine becomes significantly more efficient at larger timesteps.

- Dynamic memory allocation. At present our code has fixed sizes of arrays independent of the mesh size of the simulation. By developing it to have dynamic memory allocation simulations would become more efficient, running faster and using less RAM.

- Iterative temperature solver. As discussed in section 3.3.4, ideally the code should involve an iterative scheme due to the coupled nature of velocity and temperature. It would be good to implement this in a future version of the code to increase confidence in the results. This is especially true if a new timestepping scheme were to be developed that allows for larger timesteps.

- Parallelisation using OpenMPI. Since our code involves repeated looping over large arrays we might seek to implement parallelisation in order to speed it up. The main issue with this is that the slowest part of the code, the Poisson solver, uses an algorithm that cannot easily be parallelised. We found that Gauss-Seidel with successive over-relaxation gave a better performance than a parallelised version of the slower Thomas algorithm. Since its development we have become aware of red-black methods, however, which would allow the our Poisson solver to be re-written for parrallel implementation.

- Improved timestepping scheme - Runge-Kutta. At present we are using the forward Euler timestepping scheme due to its ease of implementation. To maintain an appropriate level of accuracy this requires small timesteps. A beneficial yet significant undertaking would be to implement a more robust timestepping scheme. We suggest a Runge-Kutta scheme, ideally fourth

order which offers a good balance between accuracy and computation. This would be more accurate than the forward Euler scheme and allow a larger timestep to be used.

Chapter 4

Eye dynamics of atmospheric vortices

This chapter investigates the process of eye formation in atmospheric vortices. We begin with a discussion of the internal structures that form at the centre of vortices, reviewing observations and experiments from a number of different fields. This includes examining some existing explanations for how and why these structures form, evaluating their merits and flaws, and also their similarities and differences. Particular attention is paid to the role of azimuthal vorticity in these theories.

To investigate the process of eye formation we consider a simple model of axisymmetric rotating convection in a cylindrical domain. By performing a series of simulations we confirm that it is possible to form an eye using this set-up and investigate its nature. In addition to these results we also include a discussion of the model and how it compares to a real atmospheric vortex.

Our investigations find that, as the thermal forcing is increased, the vortex undergoes a Hopf bifurcation from a state with a steady eye to one in which the eye oscillates. Examining the nature of these oscillations we propose that this behaviour results from an inertial wave trapped in the eye. We posit that this mechanism could perhaps be responsible for high frequency oscillations that have been observed in tropical cyclones.

The work of this chapter appears, in a reduced form, in Atkinson *et al.* (2019).

4.1 The literature on eye formation

4.1.1 Some definitions

The subject of eye formation - the development of a region of reversed (or subsiding) flow, localised to the central axis of a vortex - is a particularly interesting problem. It has attracted the attention of geophysical fluid dynamicists for a long time, with an early discussion by Morton (1966). The phenomenon is perhaps most widely recognised in the weather system known as the tropical cyclone but, as we saw in our review of atmospheric vortices in section 1.2, similar flows have also been observed in columnar vortices such as dust devils (Sinclair, 1973), waterspouts (Golden, 1974), and perhaps also tornadoes (Snow, 1982). Although many observations of the phenomenon have been made, there is still a lack of fundamental understanding as to how or why it forms. A number of different theories have been proposed but the topic remains strongly debated - see the heated exchange between Pearce (2005*b*,*a*) and Smith (2005).

There are a variety of definitions for terms such as 'core', 'eye', and 'eyewall' across different fields which can lead to confusion. Therefore we begin by clearly defining the terms that we shall use in the discussions that follow. We concern ourselves with flows in which the primary motion takes the form of intense swirling flow about some central axis. Such flows often display a secondary poloidal flow consisting of an overturning circulation in the r-z plane, streamlines for which can be seen in figure 4.1. This overturning circulation flows inwards at the base, converging on the axis before rising upwards and then exiting radially outwards

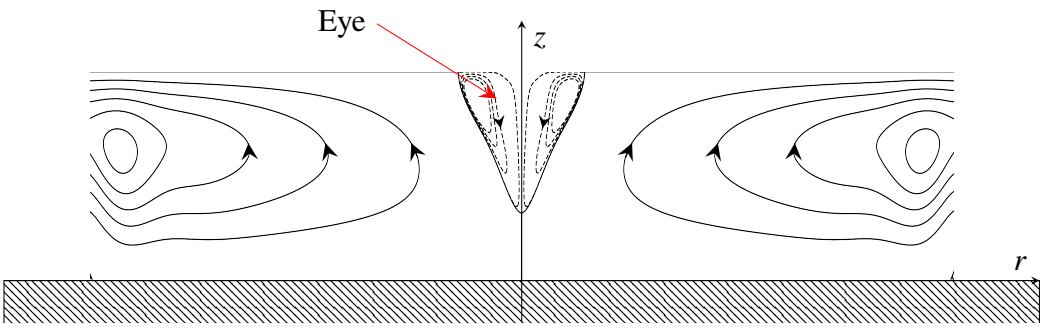

Fig. 4.1 Poloidal streamlines of a generic atmospheric vortex.

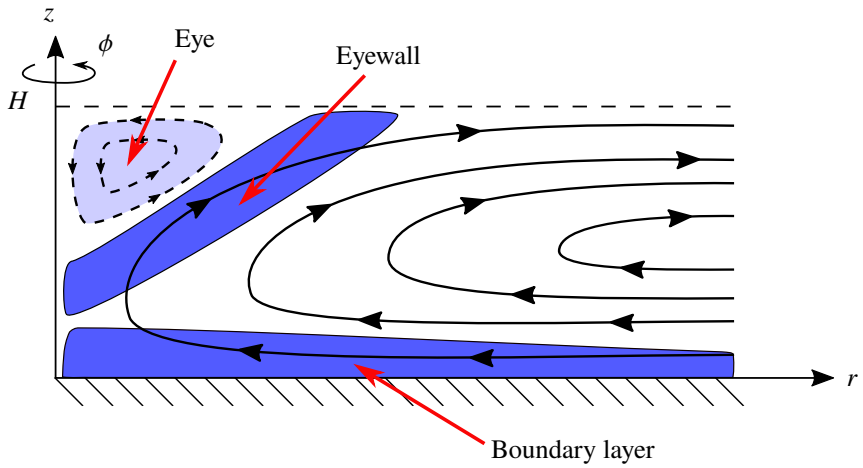

Fig. 4.2 Schematic showing streamlines of the poloidal flow at the centre of a typical atmospheric vortex. Blue regions indicate negative ω_ϕ.

giving positive azimuthal vorticity. Centred on the axis is a weaker region of recirculating flow denoted by the dashed streamlines. Focusing in on this we define the eye as a region of weak, recirculating flow at the centre of the vortex. This is labelled in figure 4.1.

Although the bulk flow has positive azimuthal vorticity, the eye is a region of negative vorticity, surrounded by an eyewall which we define as an intense sloping annulus of negative azimuthal vorticity (the reasons for which will soon become apparent). Another common feature to all of the vortices is the presence of a lower boundary layer which is, as we shall come to see, important in the process of eye formation. This boundary layer can be viewed as a source of negative azimuthal vorticity. These features are shown on the diagram of figure 4.2 where blue indicates regions of negative ω_ϕ. Now that we have a clear image and set of terms we can begin to explore the existing work on this subject.

4.1.2 Eye formation in columnar vortices

A good starting point for this work is the review of geophysical vortices by Morton (1966) which contains not only a qualitative discussion of phenomena, but also

a detailed analysis using the principles of fluid dynamics. A scaling analysis for different vortices suggests that there are several classes of behaviour depending on the relative effects of rotation, buoyancy, and inertia. This indicates that the key dimensionless parameters might be the Rossby number, Reynolds number, and Froude number. An equivalent group that we shall adopt in much of our research, however, is the Ekman, Reynolds, and Prandtl number. Morton notes that geophysical vortices span a wide range of Rossby numbers, remarking that, in some cases, it might be more useful to consider the local rotation in a vortex rather than the background rotation, especially in the intense core. Morton completes his review by posing a number of open questions:

- is axial downflow a common feature in geophysical vortices - indeed, is it a possible feature?
- what is the relative importance of buoyancy in driving vertical flow in the core?
- what is the importance of the lower boundary layer that converges towards the axis where the flow then ascends?

questions that we shall see are still relevant today.

Following on from this we come to some early investigations into columnar vortices by Maxworthy (1972, 1973). The first of these considers the internal structure of columnar vortices using an experimental approach, with flow between spinning discs driven along the axis by a propeller. An unexpected flow structure was observed at the base of the vortex with reversed flow along the axis (figure 4.3). Maxworthy calls this a vortex jump, and believes it occurs in order to match the flow emerging from the boundary layer to the external field. He cites the work on vortex breakdown by Benjamin (1962) proposing that this may be a matching of super- and sub-critical flows. He does, however, acknowledge that there are differences between this flow and the work of Benjamin, in particular the presence of a boundary. Despite these differences the use of the term ‘vortex breakdown’ to describe the structures of figure 4.3b has, perhaps misleadingly, become commonplace amongst subsequent authors.

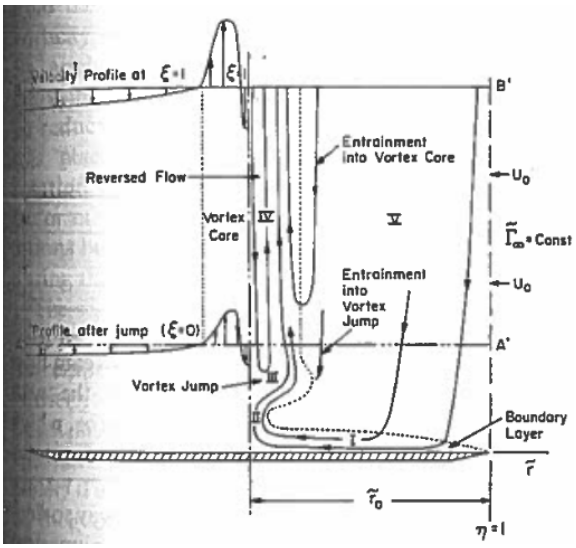

(a) Flow pattern observed

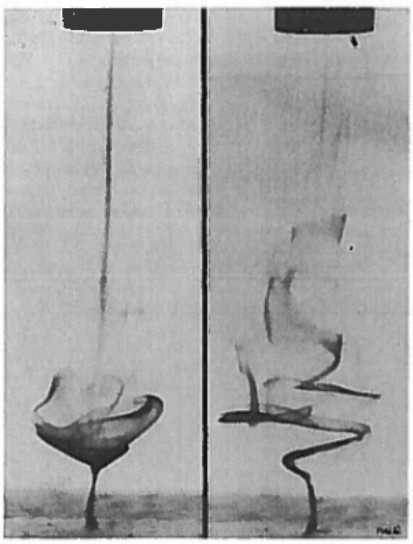

(b) Dye visualisation of the lower flow. The image on the right is a higher intensity flow than on the left.

Fig. 4.3 Results taken from Maxworthy (1972)

Building on this work Maxworthy (1973) looks at sources of vorticity in columnar vortices. He demonstrates how a vortex advected by the wind is capable of sweeping up boundary layer vorticity into the vertical through vortex stretching so as to sustain itself. This theory is supported by some field observations of dust devils. Importantly the study demonstrates an awareness of the boundary layer as a vorticity source, and that boundary layer vorticity can be advected and stretched by a flow to alter itself. The author focuses on vertical vorticity, however, not considering the effect that other components might have.

The work of Maxworthy proved highly influential in the study of columnar vortices in the atmosphere, particularly tornadoes. Snow (1982) provides an in-depth review of the structure and behaviour at the core of tornadoes. He begins by noting that the most appropriate approach to studying these flows is through vortex dynamics, and that vorticity can only be generated by regions of high shear like the boundary layer. He also notes that vortex lines in the boundary layer will form shallow, nearly circular spirals, in contrast to the vertical lines of the

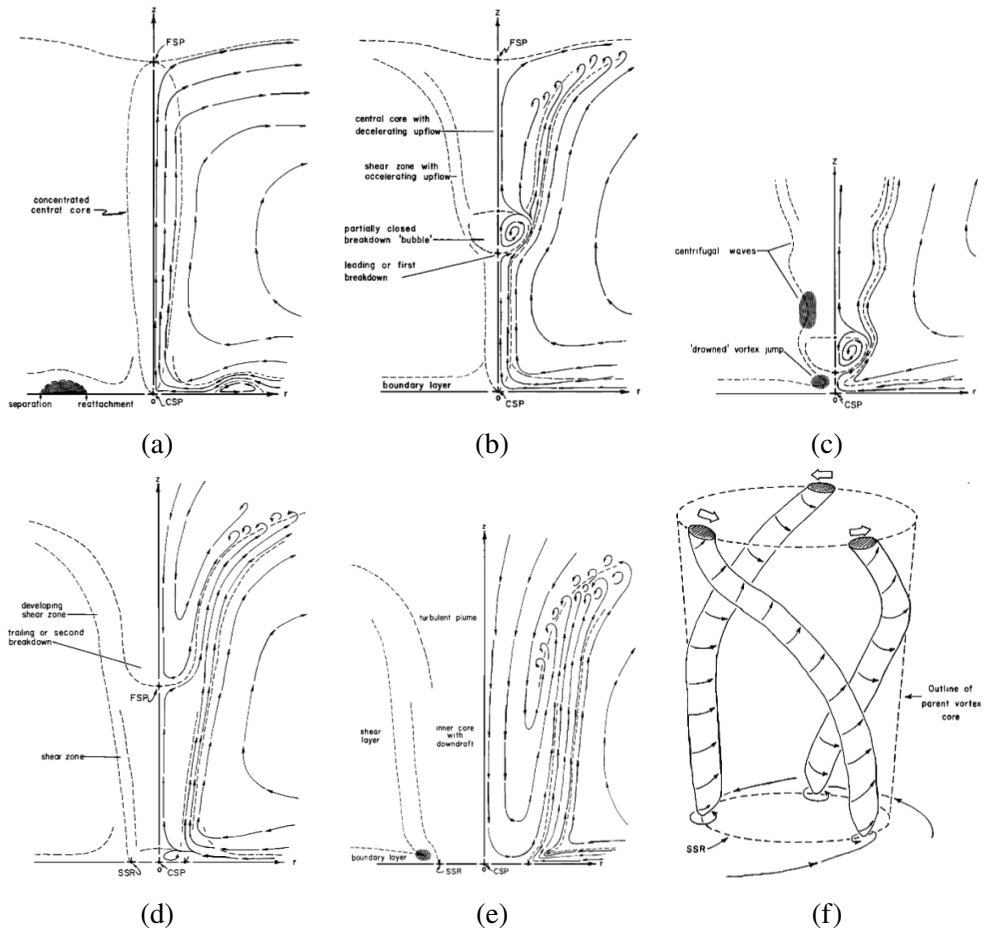

Fig. 4.4 Transition of core flow with increasing swirl from (a) to (f) taken from Snow (1982)

main vortex. The majority of the review is spent discussing the process of core evolution based upon the laboratory experiments of Maxworthy (1972) and Church *et al.* (1979), and numerical work of Rotunno (1979, 1980). Snow notes that these investigations can be a controversial topic, with clear differences to natural phenomena. Nonetheless they have succeeded in providing insight in to a number of aspects of tornado dynamics. The most significant conclusions to be made from these investigations concern the transitioning of the core flow between a number of different configurations as the azimuthal velocity (swirl) at the centre of the vortex increases. These are illustrated in figure 4.4.

For the case of no (or very low) swirl, the flow resembles a converging corner flow that ascends over a broad area. As swirl is increased, the fluid conserves angular momentum and forms a concentrated core as it ascends, approximately in cyclostrophic balance. The maximum axial velocity occurs at the centre (figure 4.4a). As swirl is increased a disturbance develops on the axis, believed to be in response to the axial pressure gradient. Several authors note that this behaviour is reminiscent in appearance of vortex breakdown discussed by Benjamin (1962). Eventually the lower breakdown point descends towards the surface forming what is described as a 'drowned vortex jump' (figure 4.4c). This is clearly visible in experiments, and is also thought to be seen at the base of dust devils and waterspouts. It has been hypothesised that the drowned jump could give rise to a series of standing waves along the core as illustrated in figure 4.4c. Though these waves are described by Snow as 'centrifugal', they are a form of standing inertial wave in a flow as described by Batchelor (1967) and Davidson (2013). Once the disturbance reaches the surface a two-celled vortex forms, with downflow along the axis surrounded by an annulus of rapidly ascending flow (figures 4.4d and 4.4e). Eventually, at the highest levels of swirl, three dimensional instabilities result in the breakup of the flow into a number of smaller vortices (figure 4.4f).

An important point to note here is that the flows in figures 4.4a and 4.4b display radial outflow at upper levels, whilst the experiments and numerical work they are based upon often have axial flow at the upper boundary. This difference could have a significant effect on the flow through changing the axial gradients in angular momentum. Snow reiterates that although vortex breakdown appears in both numerical and laboratory experiments, it has yet to be conclusively observed in nature. The structures seen at intermediate levels of swirl do resemble dust devils and waterspouts, however, and the results at high swirl are not dissimilar to tornadoes. He concludes his review by highlighting areas for future work. These include the evolution of core structure; determining if vortex breakdown occurs in nature, or whether it is an experimental feature; the presence and intensity of the downdraft at the centre; and asymmetries and waves in the core and funnel.

Taking a closer look at the numerical work that heavily influences Snow's review, we come first to two investigations by Rotunno (1977, 1979). Both use an axisymmetric cylindrical domain with axial flow at the top, and a swirling

radial inflow at the base. The first of these (Rotunno, 1977) uses a free-slip lower boundary in an effort to remove the influence of boundary layer vorticity and isolate the behaviour of the upper vortex. Typical results can be seen in figure 4.5. As the

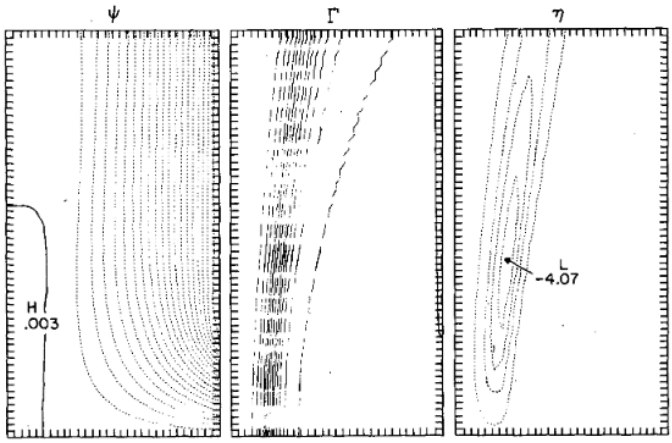

(a) Intermediate flow

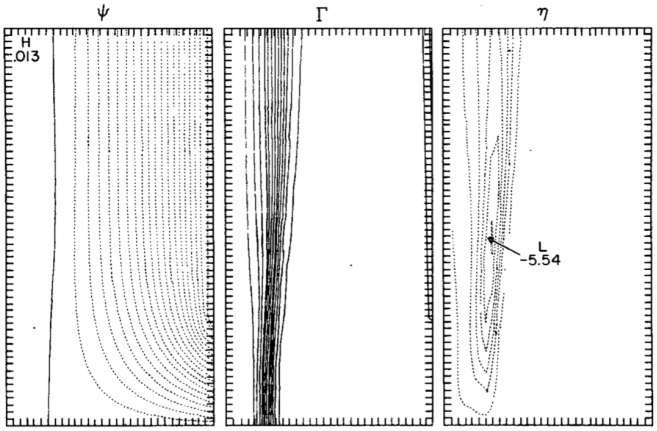

(b) Steady state

Fig. 4.5 Streamfunction Ψ, angular momentum Γ, and azimuthal vorticity (here designated as η) taken from Rotunno (1977)

flow converges towards the centre angular momentum is approximately conserved, with the largest values at the centre of the vortex. The free-slip condition at the base gives $\partial\Gamma/\partial z|_{z=0} = 0$. Above this the contours of angular momentum have a rightward slant meaning that only negative azimuthal vorticity can be generated through $\partial\Gamma^2/\partial z$ in equation (2.23). This leads to the development of a sloping

region of negative azimuthal vorticity, i.e. an eyewall[1], which, in turn, leads to a region at the centre of the vortex that Rotunno describes as a 'downdraft'. The results are compared to laboratory measurements by Ward (1972), and found to agree well in predicting core size and surface pressure dependence on swirl. However, one should be wary of the results of this investigation. Although they match laboratory results well, the effects of an overturning boundary layer flow that generates positive azimuthal vorticity through $\partial\Gamma^2/\partial z > 0$ are absent as a result of using a free-slip boundary. As was remarked by both Morton (1966) and Maxworthy (1973), we expect the influence of the lower boundary layer to be important in determining the properties of the vortex, so removing the no-slip condition is likely to significantly affect the entire flow rather than simply isolating certain features as intended.

Throughout his work Rotunno is critical of a similar study by Harlow & Stein (1974). His main issue is that their inlet boundary condition does not fix the azimuthal vorticity at inlet, making it difficult to analyse any effect this may have on the flow, and limiting how realistic it might be. Indeed, Harlow & Stein make no reference to azimuthal vorticity in their analysis, and any effects are to be inferred by the astute reader. They use an axisymmetric, cylindrical domain with a swirling radial inflow at the base. The main difference between this and the model of Rotunno is that the outflow is located at the top of the radial boundary. Harlow & Stein believe that this is closer to the conditions in a real atmospheric vortex than the models with axial outflow. This configuration forces the streamlines to completely overturn at the top as illustrated in figure 4.6. As a result a region of negative $\partial\Gamma/\partial z$ forms towards the top of the vortex that, in turn, leads to the development of an eyewall and eye. This can be seen in the results in figure 4.6. As azimuthal velocity increases the eye strengthens.

Harlow & Stein do not make use of vortex dynamics in their discussion, instead explaining the formation of the eye by balancing the axial pressure gradient along the axis against shear stresses at the edge of the eye. This provides a correlation between core length and swirl, but is not particularly rigorous in its derivation. They also note that there is a minimum Reynolds number required for eye formation

[1]Rotunno calls it a 'core wall'.

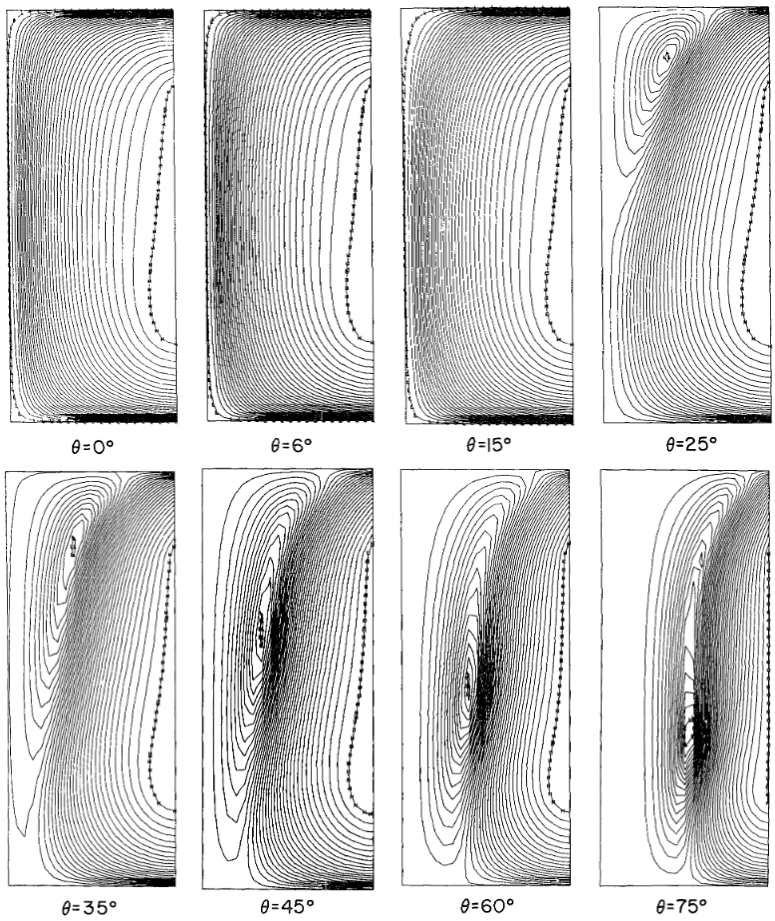

Fig. 4.6 Streamfunction for different values of swirl (increasing left to right and top to bottom) taken from Harlow & Stein (1974)

based upon the radial velocity. They suggest that this critical value lies in the range 25-50.

An interesting observation made during these investigations is that, for large Reynolds numbers, the eye can display oscillatory behaviour. This is illustrated in the streamline plots of figure 4.7 showing the flow at different times. There is little discussion of the phenomenon, other than to observe its occurrence, but one might ask what the origin of these oscillations is and whether they might be related to the standing waves discussed by Snow (1982) and Rotunno (1979) (see below). Oscillations have also been reported in tropical cyclones by Chen *et al.* (2015) who provide a description of high frequency fluctuations observed within the eye.

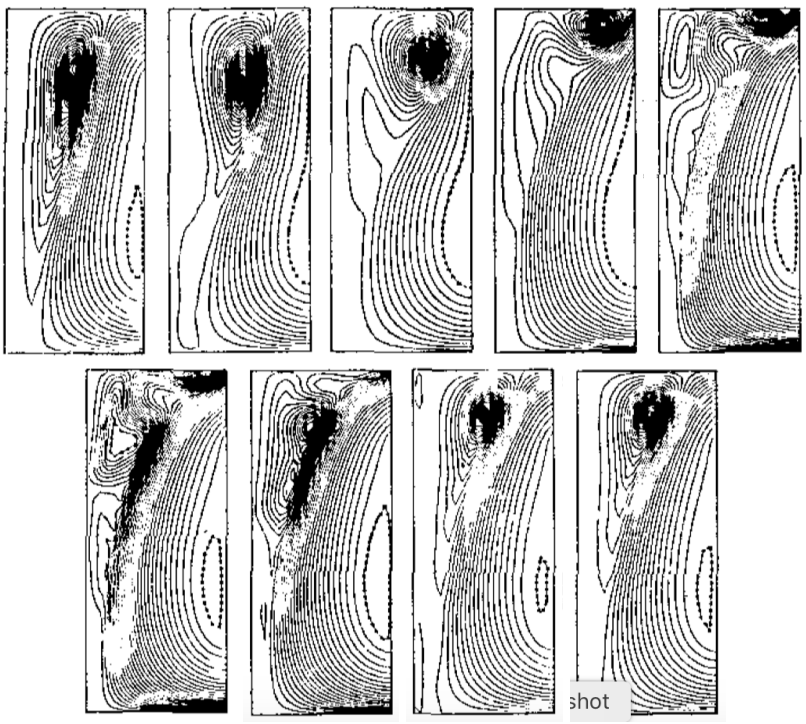

Fig. 4.7 Plots of streamfunction showing the oscillation taken from Harlow & Stein (1974)

These display similarities to oscillations reported by Harlow & Stein (1974) with a fluctuation of vertical velocity within the eye. We might ask if the oscillations observed in each of these cases occur as a result of the same mechanism, and what this mechanism might be.

In addition to their main configuration Harlow & Stein also briefly examine the effect of changing aspect ratio, a no-slip condition at the lower boundary, and an axial outlet at the top of the domain. This is little more than an exploratory exercise with limited discussion, although they do observe that a no-slip lower boundary with axial outlet qualitatively reproduces the 'vortex jump' observed by others. Of note, however, is the observation that an axial outlet causes the eye to disappear. This is not entirely unexpected, as doing this removes the overturning streamlines and the effects of $\partial\Gamma/\partial z$.

The nature of the outlet is one of the key differences between these investigations and the work of Rotunno. For the majority of Harlow & Stein's simulations the

flow is forced to completely overturn, with both the inlet and outlet on the radial boundary. In contrast, all of the simulations performed by Rotunno have an axial exit at the upper surface. By not forcing this overturning the azimuthal vorticity at the centre of Rotunno's vortex could be positive or negative depending on the relative strengths of the swirl and the boundary layer, and an eye may or may not form. This effect can be seen by comparing the streamlines in figures 4.5 and 4.6. Few solid conclusions can be drawn from these results, since they are all one-off cases rather than an exhaustive investigation, but they demonstrate that the internal structure is complex, and sensitive to a number of different parameters.

The no-slip boundary is explored in more detail by Rotunno (1979), building on his previous work. He observes that, for the case with no swirl, the flow converges on the axis, with an adverse pressure gradient causing boundary layer separation. As swirl is increased, the centrifugal pressure of the main flow is imposed upon the boundary layer resulting in a favourable pressure gradient that prevents separation. Azimuthal vorticity is also observed to be large and positive near the axis as flow emerges from the boundary layer into a region with strong positive $\partial\Gamma/\partial z$. A structure develops on the axis matching the vortex breakdown observed in the experiments of Maxworthy (1972) and simulations of Rotunno (1977). Rotunno defines this as *'an abrupt change in the structure with very pronounced retardation along the axis and a corresponding divergence of the stream surfaces near the axis'*. He performs a mathematical analysis, following Benjamin (1962), and concludes that at the breakdown the flow transitions from being supercritical to critical, supporting the theory that this is vortex breakdown in the classical sense. He also observes standing waves and an indication of transition to turbulence in the recirculation. This is expanded upon in a later paper (Fiedler & Rotunno, 1986), where the super- and sub-critical nature is computed in detail and the conditions required for breakdown given.

A related paper (Rotunno, 1980) considers in depth the vorticity dynamics of the swirling boundary layer. The equations of motion are solved in the absence of viscosity for a boundary layer profile prescribed at the inlet. In the absence of swirl Rotunno notes that the boundary layer from the plate is *"... continued into an axial boundary layer ... "* as the negative azimuthal vorticity of the boundary layer is swept upwards. This 'axial boundary layer' of negative azimuthal vorticity is

similar to our definition of an eye wall as an ascending region of negative azimuthal vorticity.

With the introduction of swirl, advection and vortex stretching through the $\partial\Gamma/\partial z$ term results in positive azimuthal vorticity being generated as vortex lines emerge from the boundary layer spiral up. The effect of this is to reduce the amount by which axial velocity is slowed in the centre of the vortex. As swirl is increased further the azimuthal vorticity can become positive, resulting in what Rotunno describes as 'an axial jet'. These results are compared to the earlier numerical simulations and are found to agree well on a number of aspects, but break down when the swirl becomes large and axial downflow is observed.

4.1.3 Eye formation in tropical cyclones

Also making use of the ideas of Morton (1966) are members of the tropical cyclone community. Putting forward a theory on the contentious topic of eye dynamics, Smith (1980) argues that the ideas of Morton can be readily applied to disklike vortices as well as columnar ones. He notes that at the centre of the tropical cyclone the effects of buoyancy are significant, but that the Rossby number will be large. In a similar manner to Harlow & Stein (1974), who explained eye formation by balancing an axial pressure gradient against vertical shear, Smith proposes a mechanism in which the axial pressure gradient approximately balances buoyancy. Vertical motion, or subsidence, is then a second-order effect driven by any slight imbalance in equation (4.1):

$$\frac{\mathrm{D}u_z}{\mathrm{D}t} = -\frac{1}{\rho_0}\frac{\partial p}{\partial z} - \mathrm{g}\frac{\rho'}{\rho_0} \ . \tag{4.1}$$

Taking the flow near the centre to be in cyclostrophic balance, and noting from observations that azimuthal velocity decays with height, an axial pressure gradient (pressure increasing with height) will exist at the centre of the vortex:

$$-\left.\frac{\partial p}{\partial z}\right|_{r=0} = \frac{\partial}{\partial z}\left(\int_0^\infty \frac{\rho u_\phi^2}{r}\,\mathrm{d}r\right) < 0 \ . \tag{4.2}$$

Smith proposes that as the cyclone intensifies this developing pressure gradient forces subsidence at the centre. The subsiding air warms, producing the cloud-free eye, and eventually balances the pressure gradient causing vertical motion to cease. He states that in a balanced state subsidence may still be present due to sinks of buoyancy in the eye leading to a slight imbalance. To finish, Smith notes that in the absence of buoyancy there would be no balance in this system and we would expect a two-celled vortex with axial downflow, though he does not elaborate on this.

Eye dynamics, being as contentious as they are in the tropical cyclone community, resulted in Smith coming into conflict with fellow meterologist Pearce in a series of articles in *Weather* (Pearce, 2005*b*; Smith, 2005; Pearce, 2005*a*), backed up by papers (Pearce, 1998, 2004; Smith, 1980). In these, Pearce puts forward a somewhat flawed model of the tropical cyclone based on a number of incorrect and unphysical arguments. He does, however, raise some notable points that should not be overlooked. The first of these is his consideration of azimuthal vorticity in the flow; how it arises, and its influence. Rather importantly, he appears to be the first author to place a more definite definition on the term eyewall as '*. . . a region of negative azimuthal vorticity in the flow bordering the eye. . .* ' which we have adopted. Pearce believes that the negative vorticity in the eyewall is generated by vertical shear through the process of 'vortex-tilting'. This is vortex stretching by $\partial\Gamma/\partial z$ that converts poloidal vorticity into azimuthal. His model bears a number of similarities to that of Rotunno (1977), perhaps most notably in its discussion of this effect. Both ignore the lower boundary layer, with a conical eyewall developing through axial gradients in Γ. In his rebuttal to Pearce, Smith (2005) states that the negative azimuthal vorticity of the eyewall in fact has its origins in the boundary layer. Smith does not pursue this statement any further however, perhaps not recognising the relevance or importance of the boundary layer and its azimuthal vorticity. This is addressed, however, by Oruba *et al.* (2017) who revise the arguments of Pearce as we now discuss.

Putting forward an alternative argument for eye formation, Oruba *et al.* (2017) present a study in rotating convection inspired by tropical cyclones. They perform numerical simulations of a rotating 'petri dish' driven by heating at the lower surface. They find that, under certain conditions, an eyewall and eye can be generated near the axis (figure 4.8). The eyes in their study are similar to those observed by Harlow

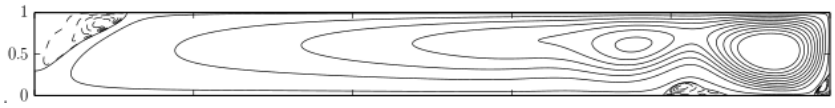

Fig. 4.8 r-z plot of poloidal streamlines showing a vortex with an eye taken from Oruba *et al.* (2017)

& Stein (1974) for columnar vortices, forming as streamlines overturn near the upper boundary. Oruba *et al.* include analysis to show that, when the streamlines completely overturn, there can be no net azimuthal vorticity production by the $\partial\Gamma/\partial z$ term. As a result they conclude that the negative vorticity of the eyewall must have its origins in the lower boundary layer. They also show that in the vicinity of the eye the contributions to azimuthal vorticity from the buoyancy and Coriolis forces are negligible. This might call into question the theory presented by Smith (1980), although it must be remembered that the simulations of Oruba *et al.* are a simplified model, not a full tropical cyclone, and as such they lack certain effects such as latent heat release.

The results of Oruba *et al.* (2017) indicate that there is a critical Reynolds number required for eye formation to occur in their system. Below this, diffusion processes will smear azimuthal vorticity throughout the flow before it can form a strong eyewall. Only flows fast enough to advect vorticity up into the eyewall at strengths that allow diffusion into the eye via a Prandtl-Batchelor process produce eyes. Oruba *et al.* (2017) propose a critical Reynolds number of 37 when using a similar definition to Harlow & Stein who suggested that the critical value lies in the range 25-50. There is no explicit mention of the effect of swirl in the investigations; azimuthal velocity is set up by the Coriolis force and, as a result, cannot be controlled directly. Although they show that there is no net vorticity production in the flow due to axial gradients in Γ, the relative strength of these gradients could still impact eye formation as in the investigations by Rotunno (1980).

4.1.4 Summary of the literature

To summarise, we have considered two fields of research that have diverged following the original review of geophysical vortices by Morton (1966). Both of

these communities (columnar and disklike vortices) have covered some similar ground when looking at the internal structure of vortices, but there are also notable differences in their approaches. One of the largest differences is that the columnar vortex community frequently makes much use of simple models and the principles of fluid mechanics, whilst the tropical cyclone community generally favours large complex models. Despite this we have seen that the arguments based on azimuthal vorticity by Pearce (2004) for tropical cyclones and Rotunno (1977) for tornadoes are, in fact, very similar. The work of Oruba *et al.* (2017) has begun to bridge this gap by providing a simplified model of the tropical cyclone and a theory for eye formation that contains similar elements to the work of both Rotunno (1980) and Pearce (2004). We seek to extend this by asking what additional features this model might show us, and what it might be able to tell us about the similarities between different types of atmospheric vortex.

Based on previous works we define the eye as a recirculating region of negative azimuthal vorticity at the centre of a vortex. This is bounded by a sloping annulus of negative vorticity which we call an eyewall. These features are common to a number of previous experiments and simulations, perhaps most notably the work of Pearce, Rotunno, and Oruba *et al.*. Although these structures have been observed in a variety of atmospheric vortices, there are a number of different theories as to how and why they form. There is, at present, no clear consensus or favoured theory with many overlapping ideas and alternative explanations.

The process of eye formation is most easily examined, we believe, through the paradigm of vortex dynamics. We believe that the the overturning of streamlines and $\partial\Gamma/\partial z$ at the upper levels of the vortex are key. In addition to this, it appears that the lower boundary is important as a source of negative azimuthal vorticity.

Finally we note that the eye-like structures in both columnar vortices and tropical cyclones have been observed to undergo oscillations. Although these observations have been recorded, there is little discussion of the mechanisms by which they are driven.

4.2 A simple model to explore eye formation in disk-like vortices

Like Oruba *et al.* (2017), we consider a shallow, cylindrical (r, ϕ, z), axisymmetric, domain of height H and radius R. The domain has solid boundaries; free-slip at the upper surface and no-slip at the base and side. Both the base and the side wall rotate at a constant rate Ω. The choice of boundary condition at the side might be immediately intuitive and this topic will be discussed later in section 4.6.2. There is a prescribed heat flux in the vertical direction which allows the temperature to be decomposed into the form $T = T_0(z) + \theta(\mathbf{x}, t)$, where $\theta(\mathbf{x}, t)$ is the deviation from the linear background profile $T_0(z) = -|\mathrm{d}T_0/\mathrm{d}z|\, z$. The advantage of this decomposition is that the boundary conditions for a constant vertical heat flux can now be written as $\partial\theta/\partial z = 0$ on the upper and lower surfaces. The radial boundary is adiabatic. These conditions are all summarised in the schematic of the flow domain in figure 4.9.

The reference frame co-rotates with the lower boundary at rate $\mathbf{\Omega}$. Assuming an incompressible Boussinesq fluid with the kinematic viscosity, thermal diffusivity, and expansion coefficient all assumed independent of temperature, the governing equations are given by (2.9), (2.22), and (2.23). It is useful, however, to write the temperature field in terms of a perturbation to the background stratification and replace equation (2.9) by (3.6). Our equations are therefore,

$$\frac{\mathrm{D}\Gamma}{\mathrm{D}t} = -2\Omega r u_r + \nu\nabla_*^2\Gamma\ , \qquad \text{(2.22 repeated)}$$

$$\frac{\mathrm{D}}{\mathrm{D}t}\left(\frac{\omega_\phi}{r}\right) = \frac{\partial}{\partial z}\left(\frac{\Gamma^2}{r^4}\right) + \frac{2\Omega}{r}\frac{\partial u_\phi}{\partial z} - \frac{\beta g}{r}\frac{\partial\theta}{\partial r} + \nu\frac{1}{r^2}\nabla_*^2\left(r\omega_\phi\right)\ , \qquad \text{(2.23 repeated)}$$

and

$$\frac{\mathrm{D}\theta}{\mathrm{D}t} = \alpha\nabla^2\theta + \left|\frac{\mathrm{d}T_0}{\mathrm{d}z}\right| u_z\ . \qquad \text{(3.6 repeated)}$$

We also make use of the Stokes stream function Ψ (equation 2.20)

$$\mathbf{u}_p = \nabla\times\left(\frac{\Psi}{r}\,\hat{\mathbf{e}}_\psi\right) \qquad \nabla_*^2\Psi = -r\omega_\psi\ . \qquad \text{(2.20 repeated)}$$

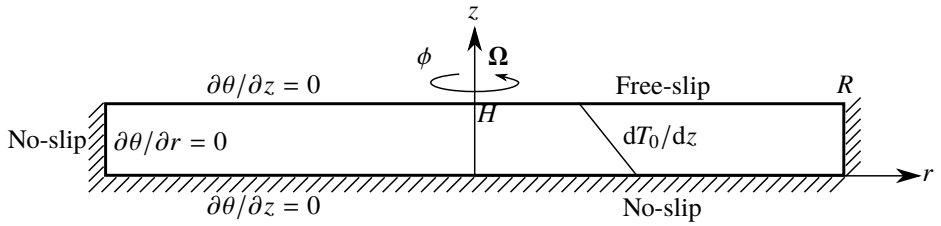

Fig. 4.9 Schematic of the flow domain.

Making use of the characteristic velocity scale $U = \sqrt{g\beta\,|dT_0/dz|}\;H$ we introduce a Reynolds number for the flow as,

$$Re = \frac{UH}{\nu}\ . \tag{4.3}$$

The velocity U is constructed from the thermal and fluid parameters and describes a typical convective velocity. As we shall see, it is typical of the actual velocities observed in the simulations. The three other dimensionless parameters that control the flow are the Prandtl number, $Pr = \nu/\alpha$, the Ekman number, $Ek = \nu/\left(\Omega H^2\right)$, and the aspect ratio $\Lambda = H/R$.

We performed numerical simulations of the flow in the domain shown in figure 4.9 using our axisymmetric code. The simulations use a regular staggered mesh of 1000 radial × 100 axial cells. Spatial and temporal resolution studies were performed by increasing and decreasing both the mesh resolution and timestep by up to two times to ensure that the results were converged. We compare our steady results of eye formation to those of Oruba *et al.* (2017) below and find they agree well. Following their approach we initially chose to keep Pr, Ek, and Λ all fixed at 0.1 and varied Re as our main parameter of interest. Of course, the Reynolds number is a proxy for the thermal forcing of the cyclone, setting the heat flux through the domain.

The first results were obtained by treating the flow as an initial value problem, integrating in time from quiescent consitions until a steady solution was obtained. For subsequent runs we took the common approach of incrementally increasing the forcing (Re) and using the end-state of one simulation as the initial condition for

the next. Provided the increase in Re between cases is not too large compared to the value of Re (i.e. of the order of 10), this allows us to avoid the computational effort associated with calculating the long transients during the initial spin-up.

A number of different parameters were tracked over the course of the simulations as potential ways of characterising the eye. We choose as a diagnostic for the strength of the eye the maximum downwards velocity on the axis. This is the parameter that provided the cleanest time series for measuring variation in the oscillatory cases.

4.3 Results for steady flows

4.3.1 Eye formation

Let us begin by considering relatively weak flows that do not display an eye and gradually increase the forcing. These steady-state results can be seen in figure 4.10 where the poloidal circulation has been plotted using the Stokes stream function, Ψ. In all cases $Ek = Pr = \Lambda = 0.1$. At low Reynolds number (figure 4.10(a)) a single large poloidal convection cell has formed. As Re is increased, the boundary layer at the base intensifies, with strengthening azimuthal vorticity ω_ϕ. This vorticity is swept up into the bulk flow as it converges towards the rotation axis to form the conical region of negative azimuthal vorticity known as the eyewall.

These results are similar to those of Oruba *et al.* (2017) and we see that as Re is increased further, the eyewall strengthens as the upwards advection of vorticity dominates over diffusion. Eventually Prandtl-Batchelor diffusion of negative ω_ϕ out of the eyewall allows for the formation of an eye. The size and strength of the eye grows as we increase Re and the boundary layer vorticity strengthens. The size of the eye does not vary much between $Re = 266$ and $Re = 300$ (figures 4.10d and 4.10e) but it continues to increase in strength. Clearly there must be a critical Reynolds number at which the steady region of reversed flow - the eye - first forms near the top of the axis. Our results suggest that for an aspect ratio, Prandtl, and Ekman number of 0.1 this critical value is $Re \approx 128$; consistent with Oruba *et al.* (2017).

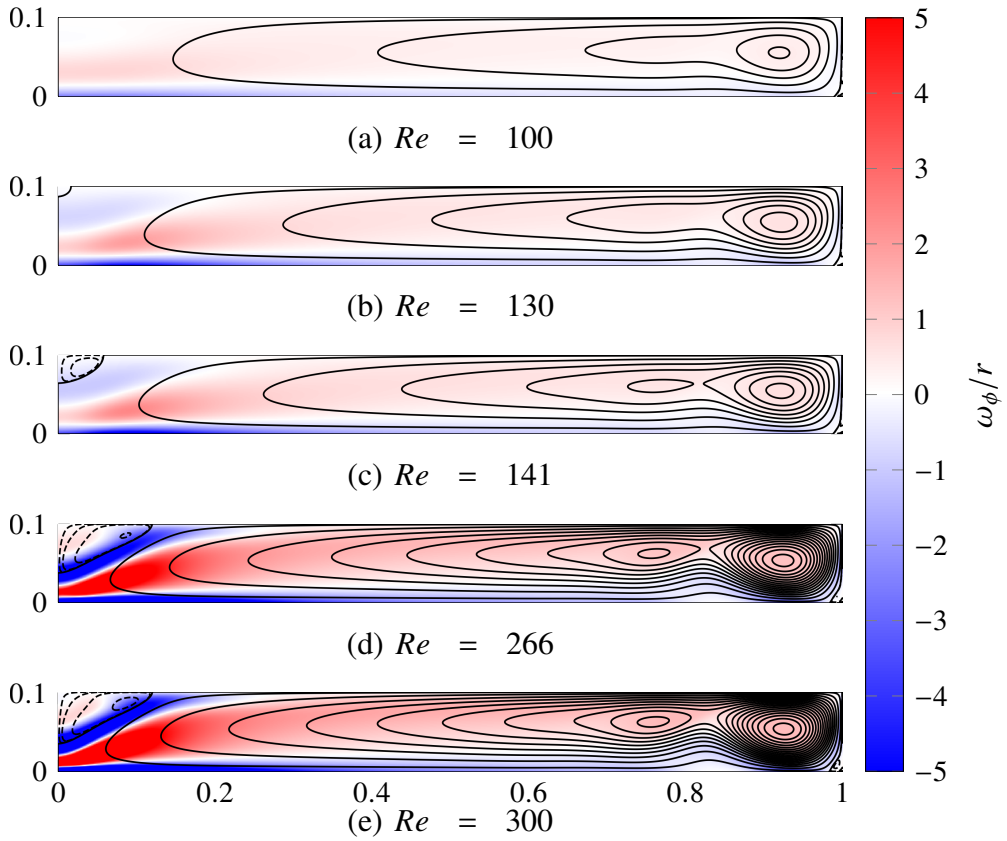

Fig. 4.10 Plots of ω_ϕ/r overlaid with of poloidal streamlines, Ψ, for a variety of Reynolds numbers, showing the formation of a steady eye that grows as forcing is increased. In all cases $Ek = Pr = \Lambda = 0.1$.
Solid streamlines represent the bulk, clockwise circulation, whilst dashed streamlines indicate anticlockwise motion.

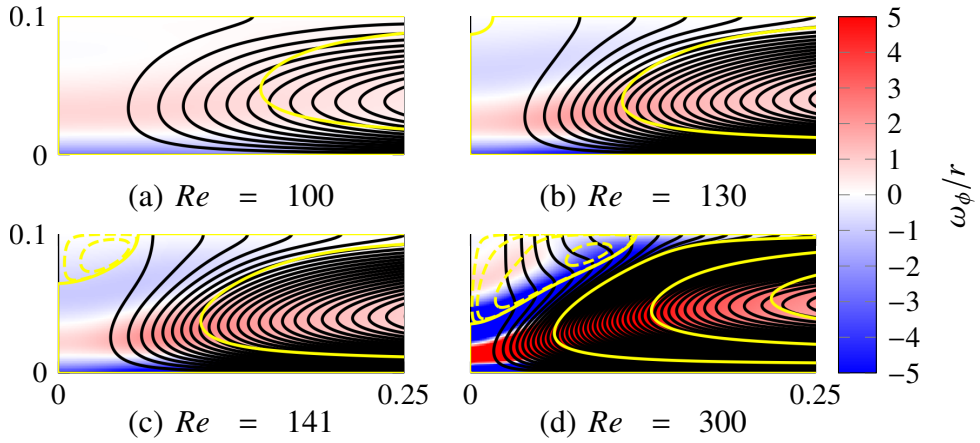

Fig. 4.11 Plots of ω_ϕ/r overlaid with contours of angular momentum, Γ, (black), and streamlines (yellow) for a range of Reynolds numbers with $Ek = Pr = \Lambda = 0.1$.

4.3.2 Angular momentum

In addition to the streamlines it is instructive to also consider the contours of angular momentum. This will later help us understand the mechanism by which oscillations are driven. These contours are shown in figure 4.11 near the eye region where the effects of background rotation are weak (see below). Note that, due to the free-slip boundary condition, the contours of angular momentum must meet the upper surface at right angles. Near the base, however, they lie almost parallel to the lower surface due to the material advection of angular momentum by the inflow and the no-slip boundary condition. Diffusion is strong in the lower boundary layer and eyewall, but outside these areas diffusive effects are weaker and we expect the angular momentum contours to more or less follow the streamlines as per equation (2.22). This is indicated in figure 4.11(a). Close to the axis the poloidal flow is weak, and the contours of Γ peel away from the streamlines as Γ diffuses into the eye in much the same way as ω_ϕ. As a result the contours of angular momentum in the vicinity of the eyewall straighten, becoming more vertical instead of following the poloidal circulation. This can be seen in figures 4.11(b) and 4.11(c).

As Re is increased further and a larger eye develops (figure 4.11(d)) it can be seen that the contours of Γ move further in towards the axis, particularly at the upper levels where the flow in the eye sweeps them inwards. This results in the contours

developing a kink as can be seen in figure 4.11(d). At this point we consider the first term of equation (2.23), $\partial\left(\Gamma^2/r^4\right)/\partial z$. The kinking of the contours of Γ will give positive axial gradients, and therefore act as a source of positive azimuthal vorticity. This can be seen in figures 4.10(d), 4.10(e), and 4.11(d) where the top left region near the axis has developed positive vorticity. This steady state represents an equilibrium between competing effects; there is the diffusion of negative vorticity into the eye from the eyewall, but the resulting flow acts to sweep the contours of Γ inwards to a point at which they become a competing source of positive azimuthal vorticity.

Finally, we consider the angular velocity of the flow in the inertial frame of reference as a combination of the local and background rotation, $\Omega + u_\phi/r$. Plotting this in figure 4.12, normalised by Ω, we see that the absolute rotation in the inertial frame is large (relative to ω) near the axis and in the eye, and weaker towards the outer boundary where it falls to the level of the background rotation. The lower plot shows the z-averaged total angular velocity as a function of radius. It is worth taking a moment to note the distinction between angular velocity and u_ϕ; although rotation near the axis is large, the velocity is low, as for a tropical cyclone, peaking around $r = 0.1\,R$ near the eyewall.

In the next section we show how oscillations develop from this steady flow.

4.4 Oscillatory flows

4.4.1 The transition to oscillating eyes

As the forcing is increased further we observe that, once the Reynolds number exceeds a second critical value, the eye ceases to be steady. The nature of this oscillation is illustrated in figure 4.13. It begins with the familiar recirculating eye near the axis inside the eyewall (figure 4.13(a)). The recirculating region (i.e. the region of negative Ψ) then moves radially outwards towards the eyewall (4.13(b) and (c)). This reaches an extreme around halfway through the oscillation cycle (figure 4.13(d)), where the recirculating region has nearly been pinched off from the axis to exist as an annulus between $r = 0.05\,R$ and $r = 0.10\,R$. At this point the reversed flow near the axis strengthens (figures 4.13e and f) expanding to reconnect

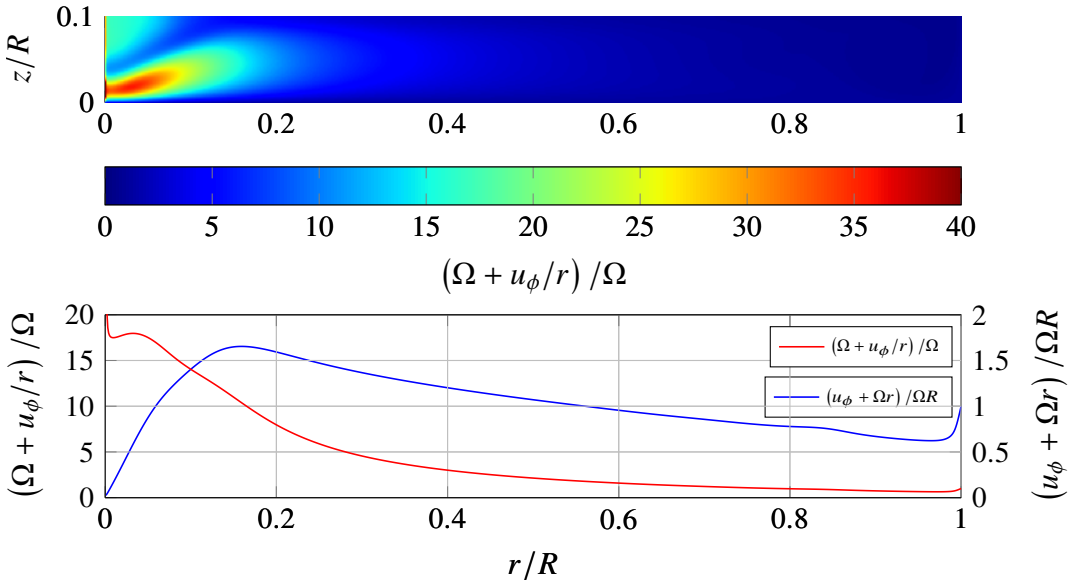

Fig. 4.12 Normalised total angular velocity for the flow (top) and averaged in the z direction (bottom red). Normalised azimuthal velocity averaged in the z direction (bottom blue) $Re = 300$.

with the displaced annulus (figure 4.13(g)) and returning to the starting state of a large eye filling the region between the eyewall and the axis (figure 4.13(h)).

It is useful to examine a time series associated with the oscillations. The maximum downwards velocity on the axis follows the spatial oscillations of the eye with the largest magnitude occurring when the eye is full, and the smallest when it is displaced towards the eyewall. The strength of the oscillations can be obtained from the time series once it reaches a steady amplitude. This is shown in figure 4.14. The Fourier transform of the time series yields the frequency of the oscillations (figure 4.15).

At yet higher values of Re the oscillations cause the eyewall to become significantly distorted. As it snaps back to a fully formed state, a region of negative vorticity is pinched off near the top of the domain and is carried radially outwards along the upper surface. This behaviour is illustrated in figure 4.16, which shows streamlines for the duration of one cycle. We note that the oscillations we observe here display qualitative similarities to those seen by Harlow & Stein (1974) for columnar vortices. Eventually, as forcing continues to increase, the system becomes

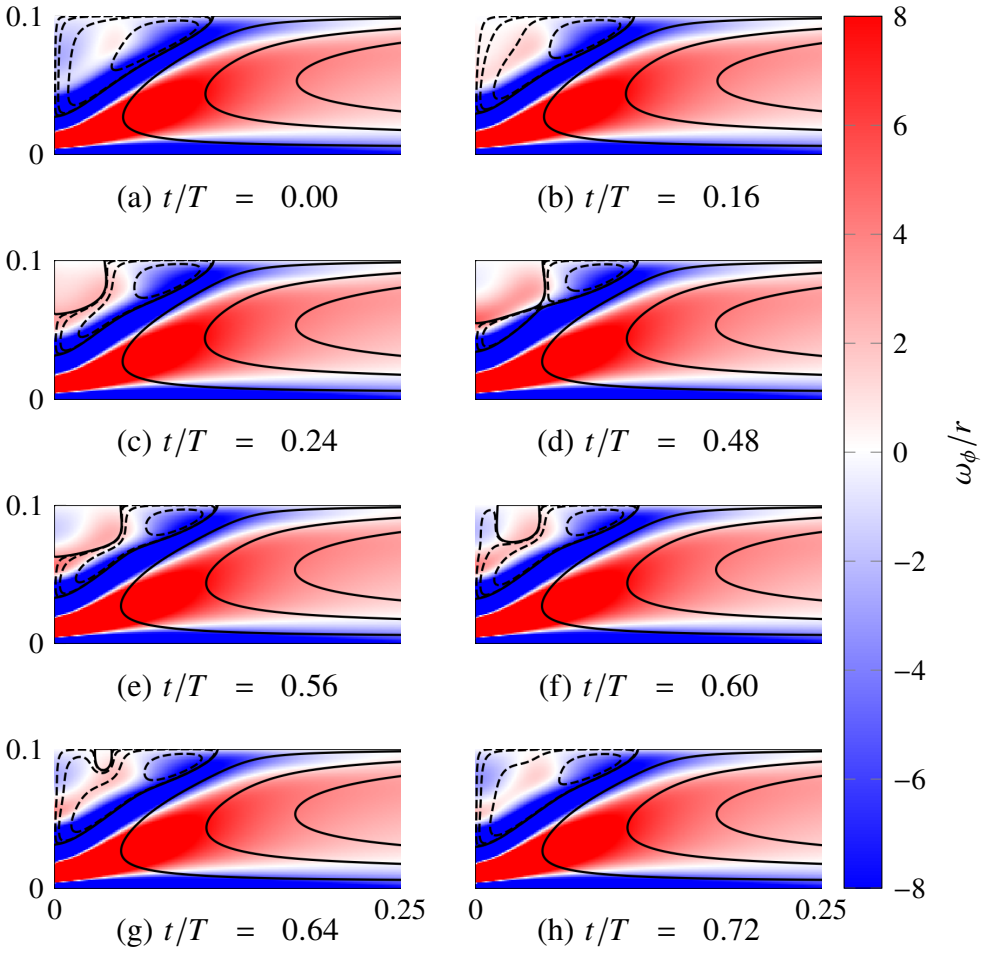

Fig. 4.13 A series of plots showing how streamlines and ω_ϕ/r vary over one complete oscillation cycle (T) for $Ek = Pr = \Lambda = 0.1$, $Re = 400$

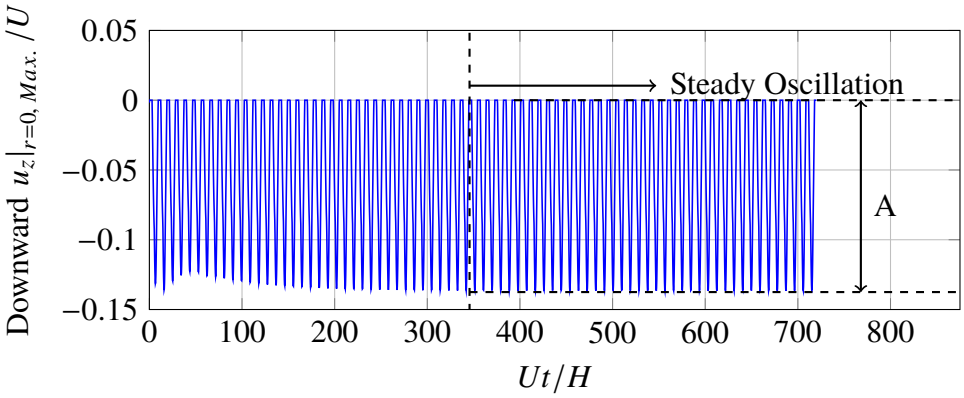

Fig. 4.14 Time series for the case $Re = 480$. Time is scaled by H/U, whilst the maximum downwards velocity on the axis is scaled by U.

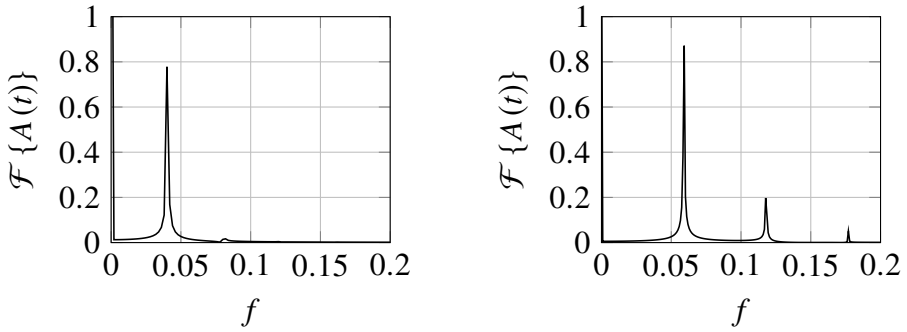

(a) FFT for $Re = 400$

(b) FFT for $Re = 550$

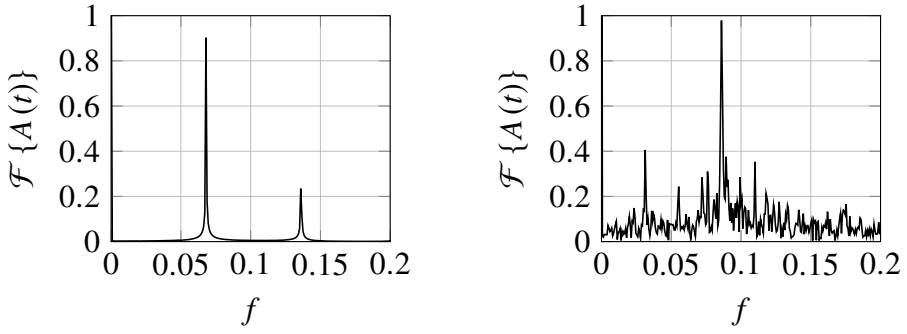

(c) FFT for $Re = 650$

(d) FFT for $Re = 750$

Fig. 4.15 Fourier transforms of the u_z time series for different levels of forcing (Re).

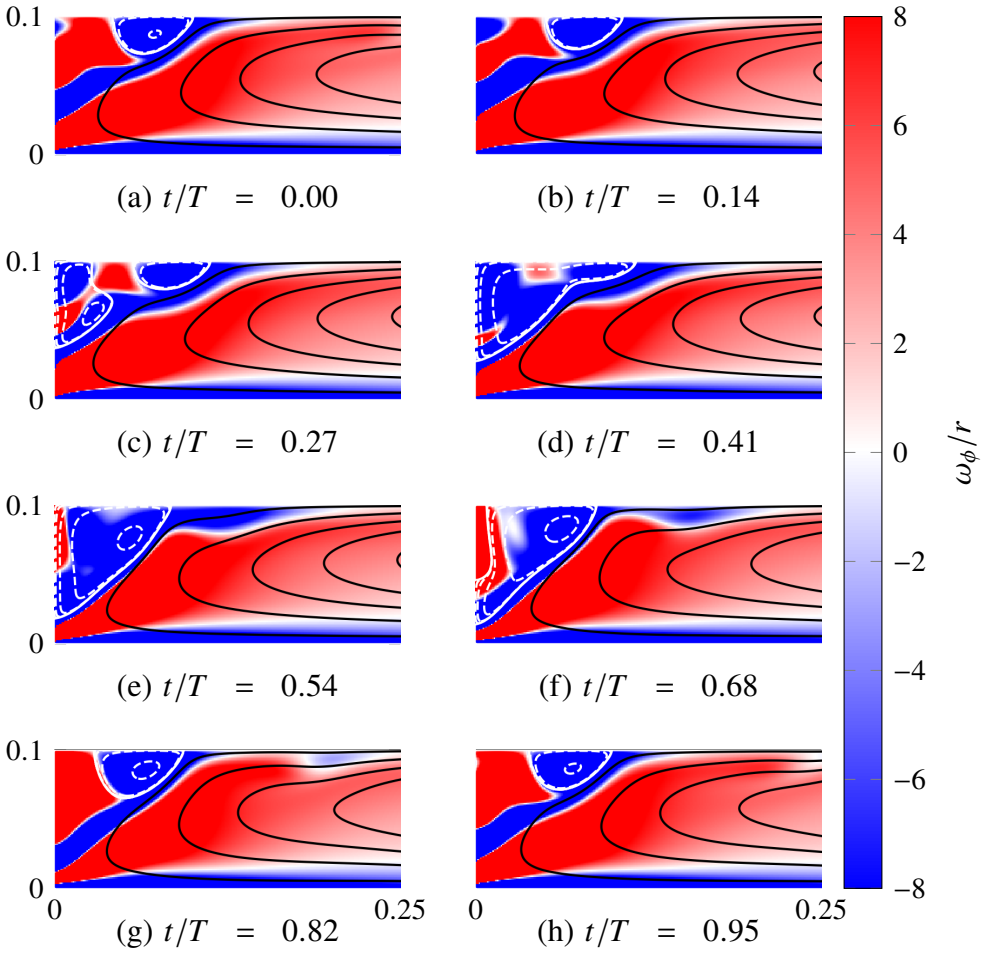

Fig. 4.16 A series of plots showing how streamlines and ω_ϕ/r vary over one complete oscillation cycle (T) for $Ek = Pr = \Lambda = 0.1$, $Re = 650$

increasingly aperiodic with the peaks in the Fourier transforms becoming less clear, and the noise elsewhere in the spectrum increasing. This corresponds to the oscillations becoming increasingly complex with fluctuations in amplitude. This can clearly be seen in the Fourier transform at high Reynolds number in figure 4.15(d).

We find that the critical Reynolds number at which oscillations in the eye begin, for Pr, Ek, and Λ of 0.1, is $Re_c \approx 398$. The nature of this transition can be examined by plotting the amplitude of the oscillations against $(Re - Re_c)$ as in figure 4.17. The amplitude scales with $(Re - Re_c)^{1/2}$ up to a value of $(Re - Re_c)/Re_c = 0.2$.

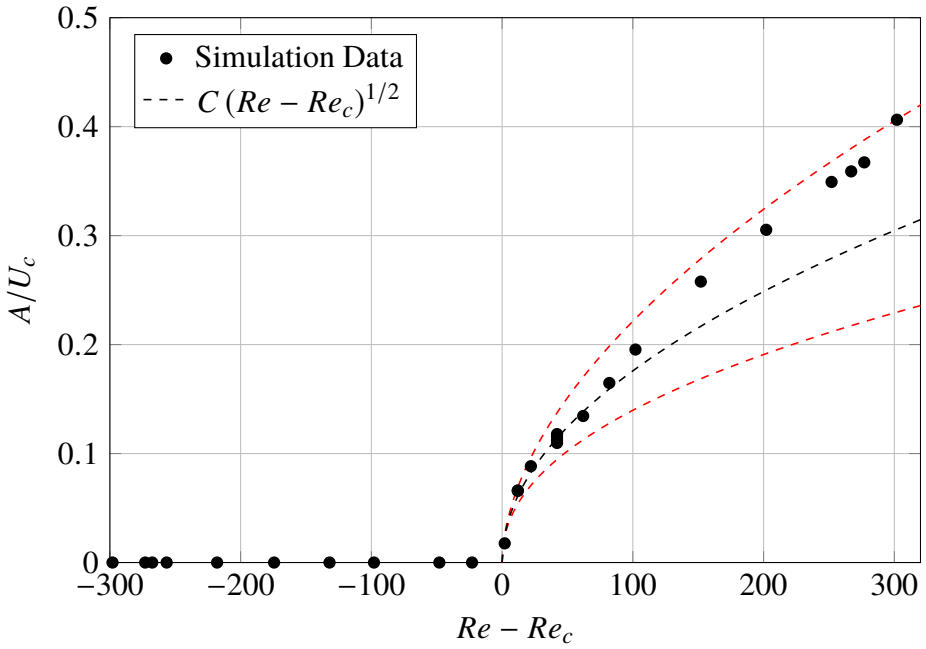

Fig. 4.17 Bifurcation diagram for the oscillating eye. Amplitude of the oscillation has been scaled by U at Re_c. The black dashed line is proportional to $(Re - Re_c)^{1/2}$. The red dashed lines are proportional to $(Re - Re_c)^{0.45}$ and $(Re - Re_c)^{0.55}$.

Beyond this point higher-order effects come in to play. This is typical behaviour of the Landau equation, with the transition to an oscillatory state being a supercritical Hopf bifurcation. Also shown on figure 4.17 are red bounding lines of ±10% in the value of the exponent.

4.4.2 Influence of Ekman number

For rotating flows displaying a bifurcation, such as Taylor-Couette flow, it is common practice to examine the dependence upon the rotation rate of the system. To this end we performed simulations at a variety of Ek around Re_c to see how the critical value for transition changes. The results of this can be seen in figure 4.18. It was observed that the critical Reynolds number at which oscillations begin increases with Ek until around $Ek = 0.125$. Beyond this it appears that only steady eyes can exist. This is because oscillations are viscously damped. Increasing

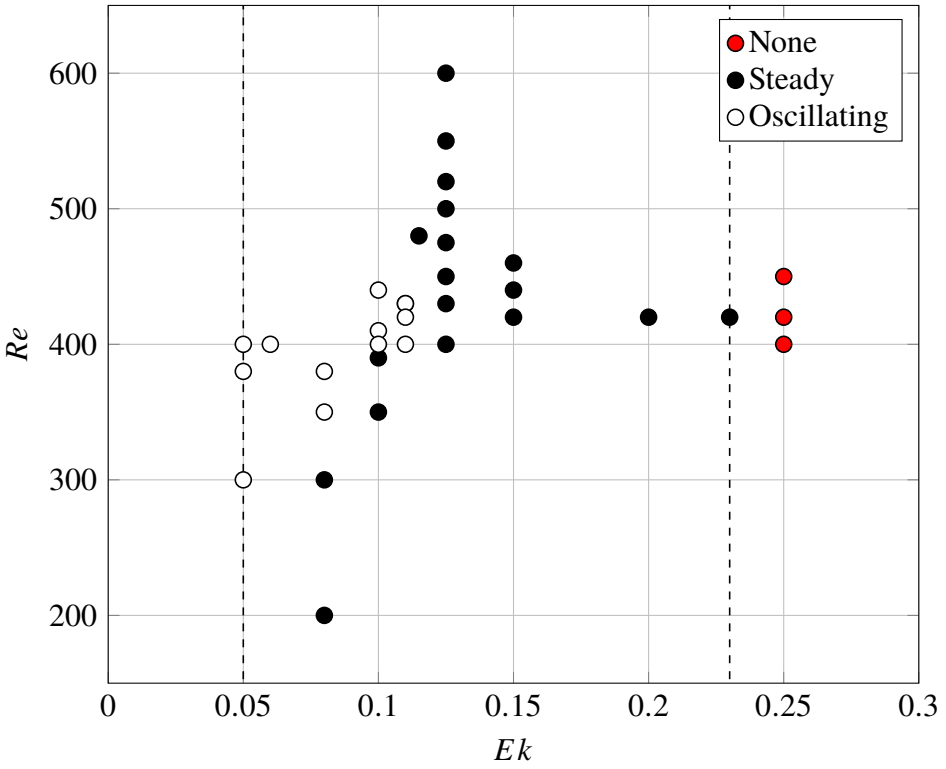

Fig. 4.18 Regime diagram for eyes showing Re plotted against Ek for the case $\Lambda = Pr = 0.1$.

Ek further we found that no eye formed for $Ek > 0.23$, consistent with (Oruba *et al.*, 2018). For Ek less than 0.1, we find that the critical Reynolds number for oscillations falls dramatically as viscous effects reduce.

4.5 The oscillation as a trapped inertial wave

4.5.1 Evidence for a trapped inertial wave

We now seek to describe a physical mechanism by which this oscillation occurs. Perturbations to an incompressible fluid rotating about a central axis are subject to restoring action through the Coriolis force when viewed in the rotating reference frame. This makes such a fluid a wave-bearing system, capable of supporting oscillations known as inertial waves. This phenomenon is described at length in Greenspan (1968) and Davidson (2013). Closed wave-bearing systems often

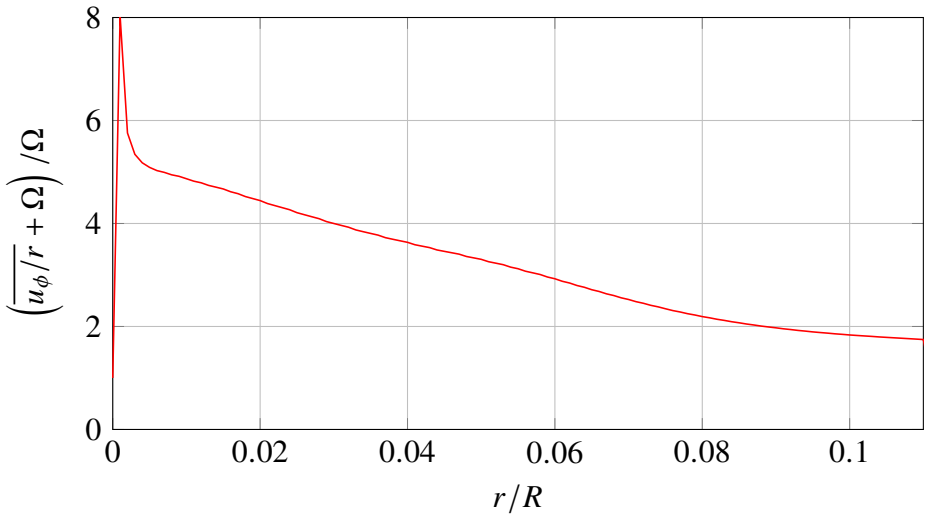

Fig. 4.19 Plot of variation of time and z- average of $\left(u_\phi/r + \Omega\right)/\Omega$ in the eye, Re = 480.

display natural frequencies and associated modeshapes. It is possible, therefore, that the observed behaviour of the eye might be explained by the presence of a 'trapped' or 'standing' inertial wave.

To examine this claim it is necessary to probe the dynamics of the eye a little more closely to see whether it might be capable of sustaining inertial waves. We saw in figure 4.12 that the angular velocity at the centre of the vortex was much higher than the background rotation. We now look more specifically at the rotation in the eye region. Averaging u_ϕ and Ψ in time across one complete cycle we define the time-averaged eye as the region in which $\Psi_{avg.} < 0$. We then average in the z-direction over the eye to examine how u_ϕ, averaged in both time and z, varies with r, as shown in figure 4.19. We see that the mean angular velocity in the eye is significantly larger than the background rotation.

We can introduce a local Rossby number for the flow as,

$$Ro_l = \frac{|\mathbf{u}_p|}{2\,H \cdot \left(u_\phi/r + \Omega\right)},$$

where $\mathbf{u}_p$ is the poloidal velocity. This approach was first suggested by Morton (1966) who notes that, for flows with intense swirl, the effects of rotation from

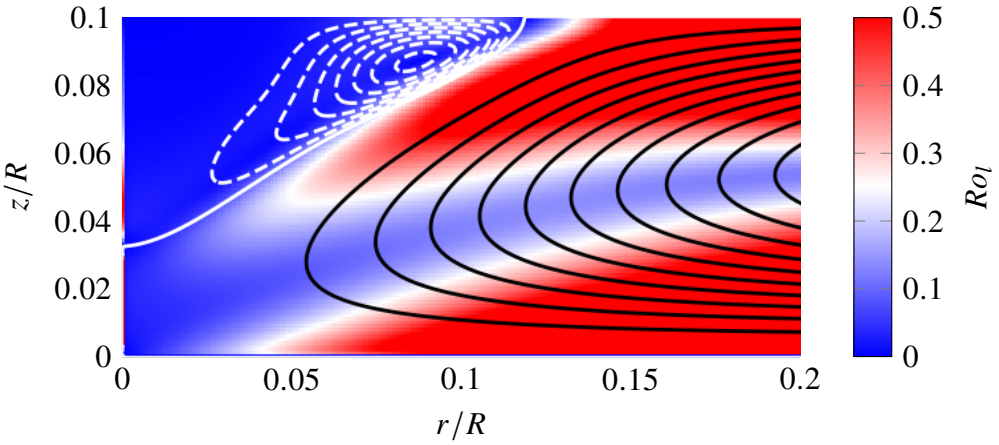

Fig. 4.20 Ro_l in the eye (top) and bulk (bottom) for the case $Re = 350$.

the local flow could well be more significant than those due to any background rotation. Figure 4.20 shows Ro_l for a Reynolds number just below the critical value for oscillations to occur. We can see that Ro_l is small in the vicinity of the eye, and larger in the bulk of the flow, as might be expected. A closer look at the eye region shows a clear change in Ro_l that is bounded by the $\Psi_{avg.} = 0$ streamline at the edge of the eyewall. It is well known (Davidson, 2013) that a requirement for inertial waves to be present is small Rossby number, i.e. rapid rotation. A study by Staplehurst *et al.* (2008) found inertial waves emerging in a rotating fluid for a Rossby number below 0.4. Examining figure 4.20 we see that Ro_l in the eye is well below this, and therefore may be capable of supporting inertial oscillations.

4.5.2 Frequencies of oscillation

Henderson & Aldridge (1992) and Beardsley (1970) study inertial waves in a frustum (a truncated cone), the approximate shape of the eye. They both record a base natural frequency of $\varpi/\Omega = 1.12$ for a given aspect ratio, noting that the modeshapes in the frustum appear to be a perturbed version of those for a cylinder. They also both observe the absence of a modified first mode for a cylinder $(r, \phi, z) = (1, 0, 1)$ in their results, with the lowest mode observed both numerically and experimentally for a frustum being $(1, 0, 2)$. It is possible to calculate an analytical solution for inertial waves in a cylinder (see Appendix A) for which an

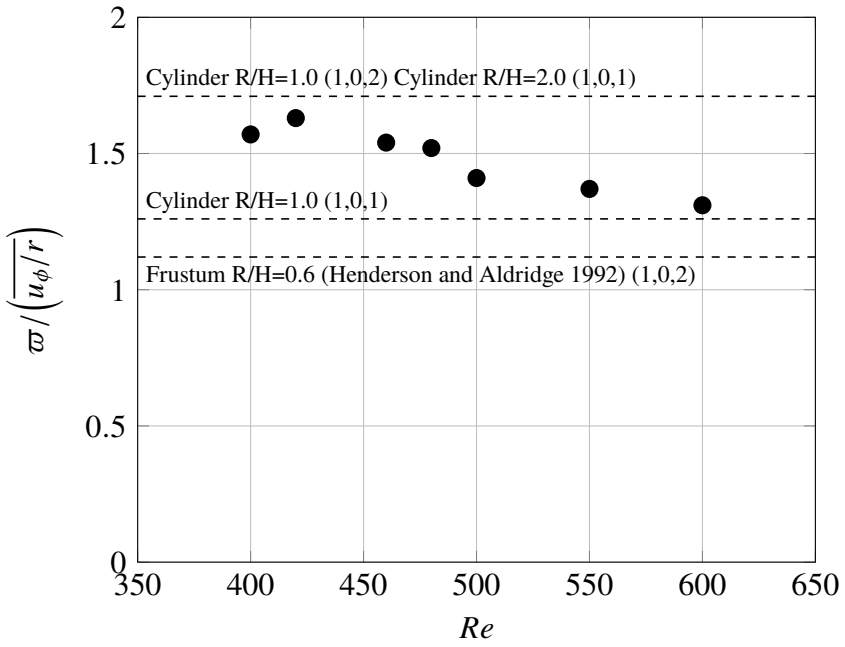

Fig. 4.21 ϖ/Ω for the oscillations vs. Re, along with selected values for a cylinder and frustum for comparison

aspect ratio of $R/H = 1$ gives a frequency of $\varpi/\Omega = 1.26$ for the first mode $(1, 0, 1)$, and 1.71 for the second axial mode $(1, 0, 2)$. Comparing the natural frequency of a cylinder and frustum of the same aspect ratio, we find that $\varpi/\Omega = 1.42$ for mode $(1, 0, 2)$ in a cylinder compared to 1.12 for the frustum discussed above. This provides some indication of how shape changes frequency. These values are all consistent with the general result for inertial waves that the frequency ϖ must lie in the range 0 to $2\,\Omega$, where Ω is the rotation rate. Taking an estimate of the average angular velocity in the eye, we obtain an estimate of $\varpi/\Omega = 1.54$ for our $Re = 400$ simulation. This analysis can be repeated for other values of Re with the results shown in figure 4.21. We see that all of the frequencies for eye oscillations lie within the required bound for inertial waves, with values around those expected for a cylinder or frustum.

We return at this point to discuss further the observations of high frequency oscillations in tropical cyclones by Chen *et al.* (2015). They report fluctuations in a number of parameters in the eye region with a typical period of around 2 h (between 90 and 150 min). One of these parameters is the water vapor convection

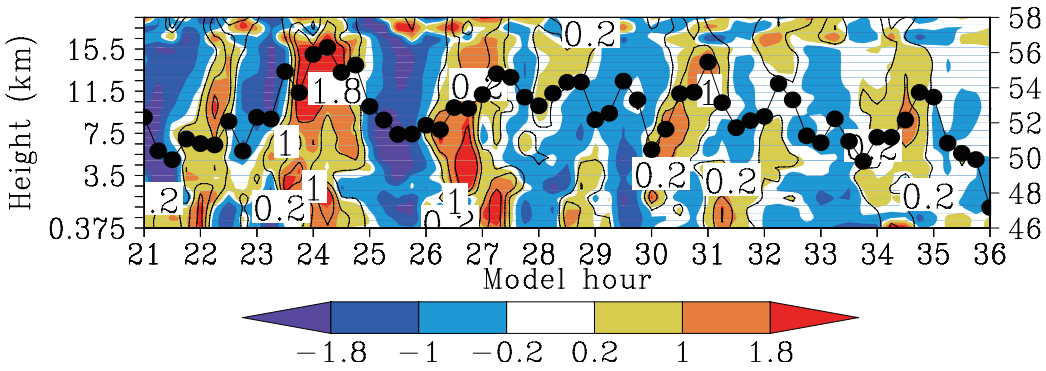

Fig. 4.22 Figure 11(a) from Chen *et al.* (2015) showing oscillations in a simulated Typhoon Hagupit. Colour shows the time-height variation of water vapor convection whilst the black line shows the maximum windspeed in $\mathrm{m\,s^{-1}}$ (scale on right). Reproduced with permission.

which is directly related to the vertical motion. Figure 4.22 shows the variation of this property in the eye region of a simulated Typhoon Hagupit (one of the cyclones in which high frequency oscillations were observed) as a function of height and time. It can be seen that the oscillations occur over the height of the cyclone with a period of approximately 2 h. If we adopt a similar approach to the one taken for our simulations we can estimate the local rotation rate in the core from the reported maximum windspeed. This is around $50\,\mathrm{m\,s^{-1}}$ at a radius of approximately 50 km which gives an angular velocity of $3.6\,\mathrm{rad\,h^{-1}}$. For oscillations with a period of around 2 h this gives an estimation of $\varpi/\Omega = 0.9$ which is of the order observed in our simulations, and below the upper bound of 2 for inertial waves. It is possible, therefore, that these oscillations are caused by trapped inertial waves, although this hypothesis requires further investigation.

4.5.3 The oscillation in terms of angular momentum

Finally we consider the contours of Γ in the eye. These are plotted over the course of one oscillation in figure 4.23. In the bulk flow the contours broadly follow the streamlines, as expected from equation (2.22) when viscosity is small. At the top of the domain they are perpendicular to the upper boundary due to the free-slip boundary condition. In the eye, however, the contours deviate from the streamlines. It can be seen that over the course of one oscillation the contours go from initially

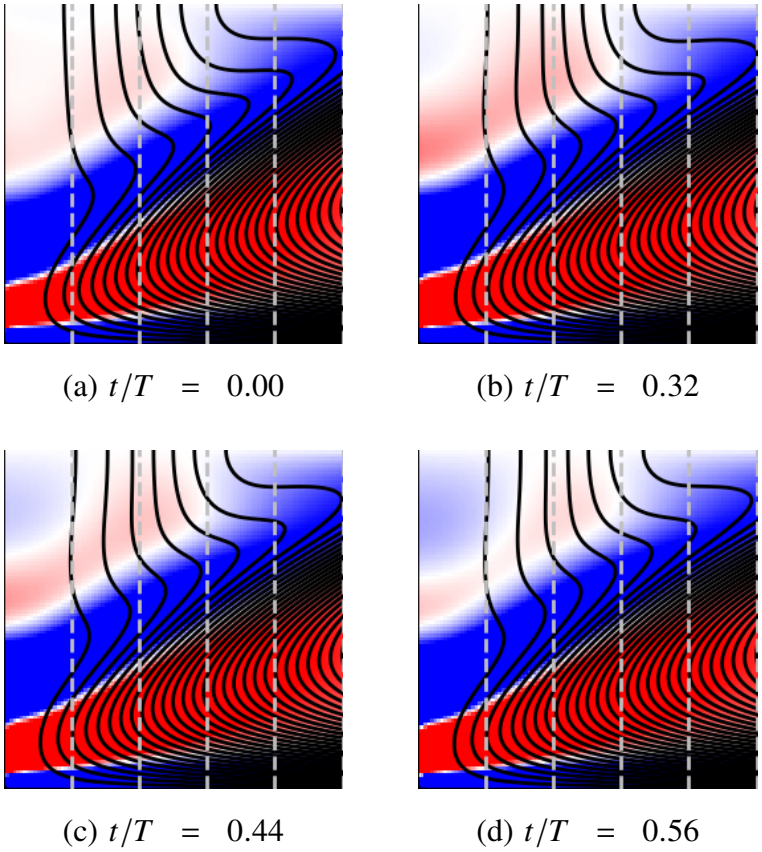

(a) $t/T = 0.00$ (b) $t/T = 0.32$

(c) $t/T = 0.44$ (d) $t/T = 0.56$

Fig. 4.23 A series of plots showing how contours of Γ evolve in the eye over one cycle (T) for $Ek = Pr = \Lambda = 0.1$, $Re = 400$. Colour = ω_ϕ/r.

being close to vertical to lean to the left, then to the right, before returning to their original state in a kind of 'sloshing' motion. Figure 4.24 shows the same phenomenon, but at a higher level of forcing where the motion of the contours is more noticeable. Figure 4.25 shows ω_ϕ/r and the contours of Γ for the first mode of a standing inertial wave in a cylinder computed from the results in Appendix A. Comparing the eye and the cylinder we can see that the two follow qualitatively the same pattern. This is as we might expect given the observations of Henderson & Aldridge (1992) and Beardsley (1970) that standing waves in a frustum are perturbed versions of those in a cylinder.

Equation (2.23) can provide perhaps a more physical understanding of the nature of oscillations. The 'sloshing' of the contours of Γ back and forth leads to a variation of ω_ϕ/r as a result of the $\partial\Gamma/\partial z$ term. Both Rotunno (1980) and

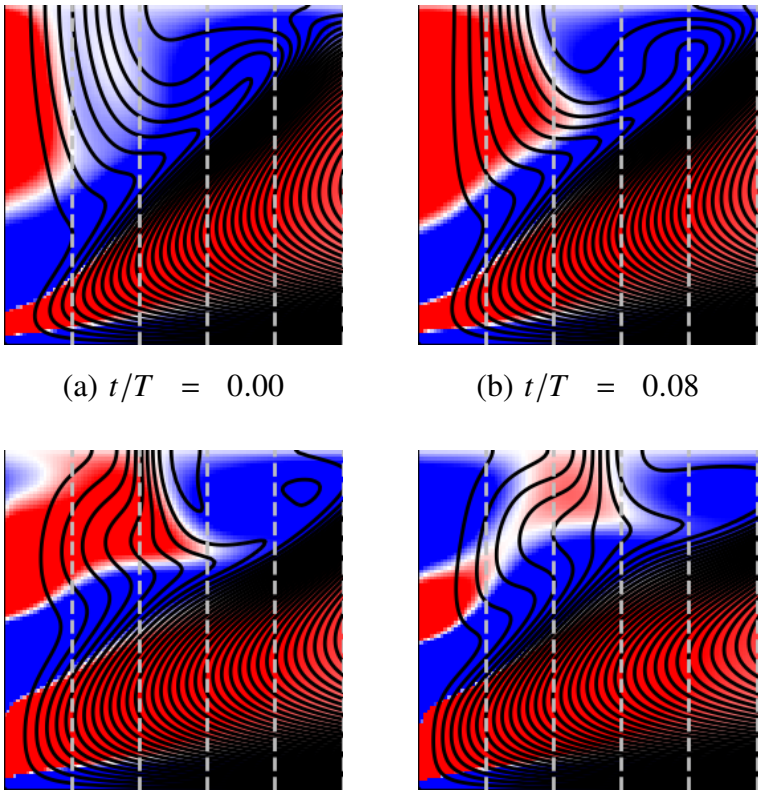

(a) $t/T = 0.00$ (b) $t/T = 0.08$

(c) $t/T = 0.24$ (d) $t/T = 0.40$

Fig. 4.24 A series of plots showing how contours of Γ evolve in the eye over one cycle (T) for $Ek = Pr = \Lambda = 0.1$, $Re = 600$. Colour = ω_ϕ/r.

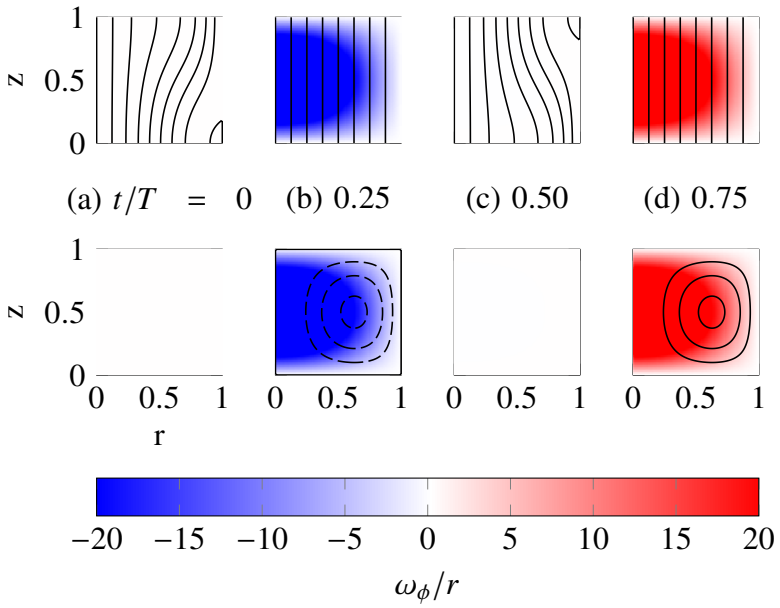

Fig. 4.25 A series of plots showing how contours of Γ (top) and streamlines (bottom) evolve over one cycle (of period T) for a standing inertial wave in a cylinder.

Davidson (1989, 2013) provide good discussions of how this vortex stretching generates azimuthal vorticity. The induced variation in ω_ϕ/r can be seen in figures 4.13, 4.23, and 4.24. The process can be summarised as follows: The flow in the fully formed eye sweeps the contours of Γ radially inwards at the upper levels, causing them to slant to the left. This positive axial variation in Γ generates positive ω_ϕ that counteracts the flow in the eye causing it to be swept outwards towards the eyewall. The flow again carries with it the angular momentum causing a rightward slant to the contours of Γ. This in turn generates negative ω_ϕ and the eye is restored before the process then repeats.

4.6 A discussion of boundary conditions

Although some discussion of the boundary conditions is given in section 4.2 we include a more detailed discussion here. In addition to considering the relevance of the boundary conditions for our numerical model, we also include a discussion of how they compare to the boundary conditions of a real tropical cyclone.

4.6.1 Thermal boundary conditions

First we discuss the thermal boundary conditions on the domain. We have a constant temperature gradient $\mathrm{d}T_0/\mathrm{d}z$ applied between the lower and upper boundaries, with the top being cooler than the base. Rather than impose a fixed temperature however, we choose to prescribe a fixed heat flux at both surfaces by setting $\mathrm{d}\theta/\mathrm{d}z$ to zero. The radial boundary is set to be adiabatic. Since the temperature gradient is the same at both the upper and lower boundaries, there will be no net heat flux into the domain; the heat flux in at the lower boundary is exactly balanced by the flux out at the upper boundary.

Taking the dot product of equation (2.18) with $\mathbf{u}$ gives an equation for the mechanical energy of the fluid

$$\frac{\partial}{\partial t}\left(\frac{\mathbf{u}^2}{2}\right) + \nabla\cdot\left(\frac{\mathbf{u}^2}{2}\mathbf{u}\right) = -\frac{1}{\rho_0}\nabla\cdot(p\mathbf{u}) + \nu\mathbf{u}\cdot\nabla^2\mathbf{u} + \mathrm{g}\beta T u_z \ . \tag{4.4}$$

Multiplying by density gives the rate of work per unit volume and so the term resulting from buoyancy, $\rho\mathrm{g}\beta T u_z$, is the rate at which the buoyancy force does work on the fluid. We can also manipulate the temperature equation as follows:

$$\frac{\partial}{\partial t}\left(\rho c_p T\right) = -\nabla\cdot\left(\rho c_p T\mathbf{u} - \kappa\nabla T\right) \ , \tag{4.5}$$

where κ is the thermal conductivity. This states that, for a steady-state system, the divergence of the total heat flux must be zero. Since the radial wall is adiabatic this tells us that the heat flux through the domain from bottom to top must be fixed.

Based on equation (4.5) we can write the total heat flux $\mathbf{q}_{net}$ as being comprised of an advective heat flux $\mathbf{q}_u = \rho c_p T\mathbf{u}$ and a diffusive heat flux $\mathbf{q}_\kappa = -\kappa\nabla T$. We see that the vertical component of the advective heat flux is proportional to the rate of working of the buoyancy force, with a factor of $(\mathrm{g}\beta)/c_p$. Since the radial wall is adiabatic, $\mathbf{q}_{net}$ is set by the upper and lower boundaries. By choosing the boundary conditions to be fixed heat flux rather than, say, fixed temperature, we provide direct control over the system and ensure that equation (4.5) is satisfied for a steady state. These boundary conditions fix the heat flux through the domain,

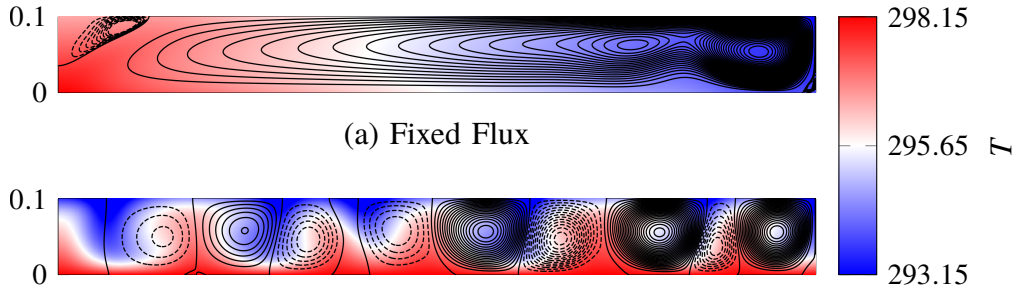

(a) Fixed Flux

(b) Fixed Temperature

Fig. 4.26 A comparison of fixed flux and fixed temperature boundary conditions for $Re = 300$. Poloidal streamlines in black.

thereby limiting the work done by the buoyancy force. This prevents the system from accumulating or losing energy providing a 'thermodynamic brake' of sorts.

In addition to these mathematical observations, we also found the fixed heat flux condition to be crucial for the formation of a single-celled poloidal circulation. When the temperature is fixed, rather than the flux, the solution displays several concentric convection rolls, akin to rotating Rayleigh-Bénard convection. This is illustrated in figure 4.26 which shows two simulations of the same Reynolds number, one with fixed temperature, the other with fixed flux. We see that for the case of fixed flux (figure 4.26(a)) the flow is swept in along the base, gathering thermal energy and increasing in temperature. When sufficiently warm it rises near the axis to reach the top of the domain. The fluid then flows outwards along the upper boundary, losing heat before sinking back down at the outer boundary. In contrast the fixed temperature condition (figure 4.26(b)) leads to the formation of localised hotspots at the base. These buoyant regions then rise to form convection rolls leading to a multicellular structure.

Having addressed the model we now discuss how does these conditions compare to reality. Starting with the lower surface and boundary layer of a cyclone, the mechanisms by which energy is transferred at the air-sea interface are complex, being an area of research in their own right. We restrict ourselves here to discussing ocean-atmosphere boundary conditions presented in the tropical cyclone literature and used in large meteorological simulations. In tropical storm conditions the heat transfer from the sea surface does not occur primarily through simple conduction,

as one might first assume, but is in fact heavily influenced by sea spray. The precise nature of this process is still an active area of research (Gall *et al.*, 2006), but it centres around spray droplets being ejected into the boundary layer. These droplets are at the same temperature and salinity as the ocean, but greatly enhance the effective surface area in contact with the air. The effect of latent heat and evaporation is also important, and meteorologists often work in terms of an equivalent potential temperature to account for this. As a result the thermal boundary condition at the ocean is more complex than fixed temperature, as we found in our simulations.

Perhaps the most relevant work on this topic comes from Emanuel (1986, 1995, 2003) who presents a thermodynamic model for the tropical cyclone, by means of an analogy to the Carnot heat engine. The boundary layer flow along the sea surface is taken as the isothermal compression stage of the cycle. It is proposed (Andreas & Emanuel, 2001) that the heat flux from the surface be modelled as

$$\dot{q} = \rho C_h (h_s - h_a)\, u_* \,, \tag{4.6}$$

where h_a and h_s are the enthalpy of the air and sea at the boundary, C_h is a transfer coefficient, and u_* is the shear velocity of the boundary layer at the surface. A similar formulation was also proposed by Ooyama (1969). The inclusion of the shear velocity encapsulates the fact that sea spray increases at higher windspeeds, enhancing heat transfer. The precise nature of this relationship and formulation of C_h is not well understood at present however (Emanuel, 2003).

As a brief exercise we examine how the enthalpy flux proposed by Andreas & Emanuel (2001) (equation (4.6)) manifests in our numerical model as a function of radius, and how it compares to our assumption of constant flux. For a perfect gas we can write enthalpy as $h = c_p T$. Taking our steady-state numerical solution we set $h_a = c_p \left(T|_{z=0} - T_{ref}\right)$, where T_{ref} is a reference temperature. We can calculate u_* using radial and azimuthal components of velocity. The remaining quantity, h_s, is given a fixed value reflecting the fact that the ocean is an effective thermal reservoir with a heat capacity much larger than air. Since this is only a thought exercise using rough figures we choose C_h to be 1. Based on this we calculate an estimation of $\dot{q}$ which is shown (normalised by our fixed heat flux) as a function of radius in figure 4.27 for different values of h_s.

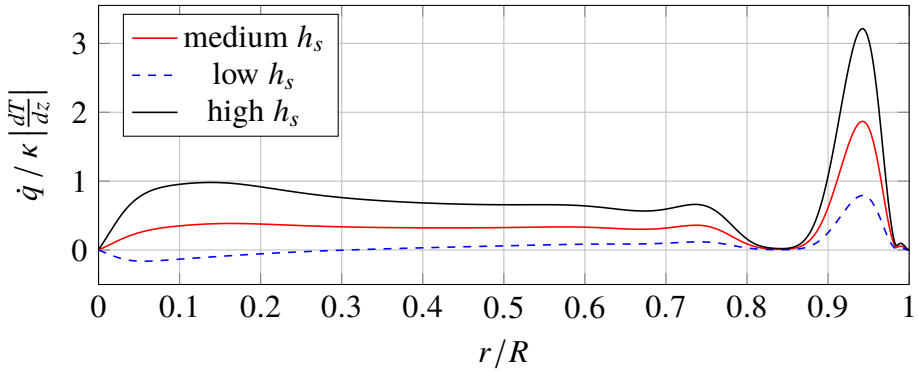

Fig. 4.27 Variation of enthalpy flux along the lower surface for $Re = 300$.

We see that for low ocean enthalpy the expression gives very little heat flux, with the enthalpy of the air in fact rising above that of the ocean as it moves radially inwards and heats up. This is consistent with observations that tropical cyclogenesis requires a minimum ocean surface temperature. As the ocean enthalpy is increased we see that the flux becomes positive across the entire surface remaining relatively constant across much of the radius (from 0.1 to 0.8 r/R), and decreasing in the eye region, consistent with real tropical cyclones (Wang *et al.*, 2001). There is, however, a discrepancy near the radial boundary where the flux displays a large peak. This is due to large radial velocities at the surface beneath a recirculating region that forms in the presence of the rigid radial boundary and covers approximately 10% of the surface.

Although these results came from our simplified model, not a meterological simulation or real data, and contain very rough estimations, they do provide some reassurance about our choice of boundary condition. We find that for suitably large ocean enthalpy, the heat flux is approximately constant across a large region of the base. We also find that, when normalised, this estimation of $\dot{q}$ is of a similar magnitude to the fixed heat flux used in our simulations. Further support can be found in the simulations of Wang *et al.* (2001) whose results suggest that flux is relatively constant across the ocean surface, peaking near the eyewall where windspeeds are largest and the effects of sea spray are most significant.

We now turn our attention to the upper surface of the cyclone. In our model we apply the same boundary condition as at the base; that of constant heat flux.

In real cyclones the majority of the heat loss at the upper levels occurs through radiative transfer, although there are also contributions from turbulent dissipation and precipitation. In the Carnot engine analogy of Emanuel the outflow is taken to be analagous to the isothermal expansion stage. With a focus on radiative transfer one might consider a black body radiation approach, but this becomes complicated due to the fact that clouds are grey bodies, with their emissivity depending on a number of parameters. A study by Rotunno & Emanuel (1987) made the simplification of using Newtonian cooling at the cloud top, but remark that it this is not a very realistic approximation. A later study by Craig (1996) investigated cooling processes in more detail, implementing a complex radiative cooling scheme involving a cloud microphysics parametrisation based on the Meteorological Office global climate model. Meteorological parametrisations are still developing, with cloud physics being an active area of study at present. Craig concluded, however, that a number of other factors have far more significant impacts on cyclone intensity and evolution.

As we have discussed, our model does not seek to replicate all the processes of the tropical cyclone in detail, instead being a simplified model that is still capable of replicating behaviours of interest. As a result we are not able to, nor do we desire to, implement microphysics or parametrisations for various effects such as precipitation. In the analogy of Emanuel (2003) the exact nature of heat loss is not discussed in detail beyond the fact that it occurs at the low temperatures of the upper troposphere. In light of this, the precise nature of heat removal at the upper boundary may not be overly significant. Indeed, the investigations by Rotunno & Emanuel (1987) suggest that variations in the nature of heat loss have a quantitative, but little qualitative effect on their simulations. By setting the heat flux at the upper surface to be constant we are able to match it to the flux at the lower surface. This is numerically convenient, as discussed above, since it ensures a steady heat flux through the domain.

Finally we consider the radial outer boundary. This is relatively small compared to the other two surfaces, so we do not expect it to have a significant contribution to heating effects. As a result it is set to be adiabatic in the model. In a real tropical cyclone the subsiding air at large radii is far less intense than the motions towards the centre, and the descending air typically conserves its heat (Emanuel, 2003). In

light of this, setting the radial boundary to be adiabatic appears to be a reasonable decision. It also fits well with the other boundary conditions in maintaining a steady heat flux through the domain, since the fluxes at the other boundaries are already balanced.

4.6.2 No-slip radial boundary

We now turn our attention to the no-slip radial boundary. This may not immediately appear to be the most intuitive choice, but with further thought it is difficult to define what the best choice would be given that nature does not provide a physical boundary. Our numerical model is bounded, however, and as such we must supply a condition. The rationale behind the no-slip condition comes from considering the overall angular momentum (torque) balance on the domain. Consider the system in the inertial frame so that the Coriolis torque is removed. The conservation of angular momentum for the fluid can then be written as

$$\frac{\mathrm{D}\hat{\Gamma}}{\mathrm{D}t} = \nu\nabla_*^2\hat{\Gamma}\ , \tag{4.7}$$

where $\hat{\Gamma} = \Gamma + \Omega r^2$. There are no external forces or torques acting on the domain. Following Newton's laws this means that the fluid must exert no net torque on the domain. The fluid exerts a force on the boundary through the action of shear stress at no-slip surfaces. In a steady state the net frictional torque on the boundaries due to these forces must be zero.

As we have seen, the flow comprises of regions of cyclonic and anticyclonic rotation. Cyclonic flow is faster than the background rotation, and so will apply a positive torque to any no-slip boundaries. The opposite is true for anticyclonic rotation. The flow along the base is largely cyclonic as a result of angular momentum conservation as we have discussed. As it flows out along the upper boundary it slows, eventually becoming anticyclonic. This can be seen by plotting angular momentum in the rotating frame for a typical cyclone as in figure 4.28. The red region shows the cyclonic flow, and blue the anticyclonic. Providing a no-slip condition at the radial boundary where the flow is anticyclonic allows the torque balance to be achieved with the negative torque on the radial boundary cancelling

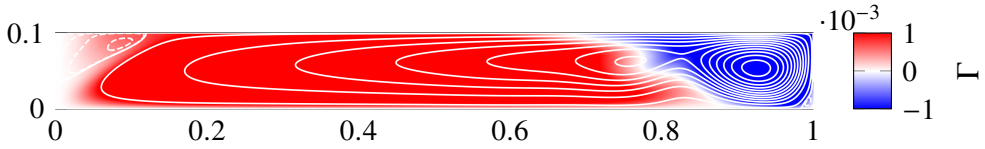

Fig. 4.28 Γ in the rotating frame overlaid with streamlines for $Re = 300$.

the mostly positive torque on the base. This balance is discussed for real tropical cyclones by Frank (1977) who notes a similar structure in contours of Γ as are seen in our results.

To examine this further we performed a simulation with free-slip at the radial boundary. The results can be seen in figure 4.29. We found that a free-slip boundary led to longer transients before achieving a steady state than no-slip, but that the final state for both cases are qualitatively similar. As might be expected, the removal of the no-slip condition at the radial boundary leads to the anticyclonic region growing in size to cover more of the base. This is necessary to balance the total torque on the system in the inertial frame, as discussed above, with the entirety of this balance now occurring on the base of the domain. We also see that as the anticyclonic region at the outer boundary grows, the eye at the axis becomes compressed in the radial direction.

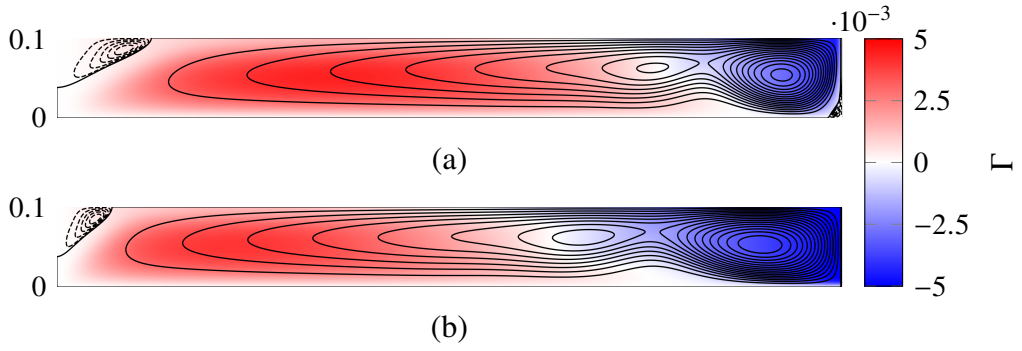

Fig. 4.29 Γ in the rotating frame overlaid with streamlines for $Re = 266$. (a) no-slip (b) free-slip

4.6.3 No-slip lower boundary

The lower boundary in our simulations is treated as no-slip and plays a vital role in generating the boundary layer vorticity that eventually leads to the formation of an eyewall and eye. It is well known that a marine atmospheric boundary layer can form over the ocean surface, but we discuss briefly the nature of this boundary layer. The ocean-air interface is a boundary between two fluids. As a result, it might be more appropriate to adopt a semi-slip condition of the form $\partial \mathbf{u}/\partial z = f(\mathbf{u})$, where surface stresses are a function of the velocity at the surface. This reflects that fact that these surface stresses can induce motion of the water. Indeed, this effect is what causes the surface waves on any large body of water.

A comparison of the no-slip boundary condition to one in which surface stresses act in the direction of wind was performed by Smith (1968) to examine their suitability for modelling tropical cyclones. He concluded that the most realistic results were obtained when the no-slip condition was paired with a suitable eddy viscosity. It was noted, however, that it is not immediately clear what the ideal eddy viscosity should be, and that it will be a function of both r and z. Smith remarks that additional observational data would assist in making estimations of this parameter.

Much like the thermal boundary condition, the momentum boundary condition at the ocean-air interface is also complicated by the effects of sea spray. In addition to a formulation for enthalpy flux, Andreas & Emanuel (2001) also propose that the lower boundary should be subject to a momentum flux of the form $\tau = -C_m \rho \mathbf{u}_*^2$. Here C_m is a parametrised momentum transfer coefficient which takes on different formulations over set ranges of windspeed. A discussion of some of these parametrisations for low windspeeds can be found in Wróbel-Niedzwiecka *et al.* (2019). This flux accounts for the the reduction in momentum caused by drag on sea spray particles that are ejected into the boundary layer. It can also be used to incorporate the effects of wave drag whereby the momentum of the boundary layer is reduced through transfer to water wave motion. Scaling with the square of the windspeed, the effects becomes increasingly significant as storm force winds are approached, with the highest levels of flux in the eyewall region. It has been

found that including these parametrisations in numerical simulations can have a significant effect on the results (Andreas & Emanuel, 2001).

To summarise, there are clearly many different phenomena that contribute to the precise nature of the tropical cyclone boundary layer. Many of these are still being studied and are often represented through various parametrisations. There is currently a lack of data for tropical cyclones that would allow these parametrisations to be improved, mainly due to the difficulties associated with performing these measurements. Perhaps the biggest discrepancy between our work and real boundary layers is that our simulations are laminar whilst real cyclones are highly turbulent (though Smith (1968) proposes an eddy viscosity formulation may be suitable). In terms of our simplified model we are less concerned with the precise nature of the boundary layer than we are simply in its presence as a source of azimuthal vorticity that can lead to the development of an eyewall. As a result the use of no-slip, or indeed any other condition that allows a boundary layer and azimuthal vorticity to develop, is suitable for our purposes.

4.6.4 Free-slip upper boundary

Finally we discuss the upper boundary of our model which is set to be free-slip. The rationale behind this is that there is a significant discontinuity in temperature gradient at the tropopause as the lapse rate changes from positive to negative. This change in stratification acts as a barrier inhibiting vertical motion. as a result rising air flows outwards along the tropopause before cooling and sinking. Although we represent the tropopause as an impermeable boundary this interface is, in reality, an air-air continuum so experiences little shear stress. Therefore we choose it to be free-slip.

The impermeability of the upper boundary becomes particularly relevant when we consider the oscillations of the eye. If these are standing inertial waves, as we propose, then their manifestation is reliant upon reflection from both the upper and lower boundaries. Since the tropopause is not a physical boundary one might ask if waves can be reflected, or if they would instead be transmitted or attenuated. Many tropospheric models make use of a ‘rigid lid’ approximation in a similar manner to our simulations. This has been shown to be a reasonable approximation

in many cases, successfully replicating and explaining such phenomena as resonant interactions (Raupp & Silva Dias, 2009) and atmospheric teleconnections (Kasahara & da Silva Dias, 1986). On the other hand, some simulations make use of more complex boundary conditions that allow waves to be radiated away (Purser & Kar (2002) for example). Some large simulations, such as the Massachusetts Institute of Technology's general circulation model, seek to model the atmosphere as infinite through the use of pressure co-ordinates. A good compromise might perhaps be found somewhere between the rigid lid and a radiative boundary approaches. Recent work by Chumakova *et al.* (2013) proposes a new boundary condition for internal gravity waves at the tropopause that takes on the form of a 'leaky lid'. In brief, this assigns an impedance to the tropopause so that waves are partially reflected and partially transmitted. It is found that this leads to similar behaviour to the rigid lid, with the new modes being sightly distorted versions of those for a rigid boundary. For now we take this as an indication that reflection of waves from the tropopause can occur, and that our rigid lid model is an acceptable approximation. Future research, however, might investigate extending the leaky lid condition to other waves besides internal gravity, and to include effects such as rotation.

4.7 Summary

We have examined the system of rotating convection first proposed by Oruba *et al.* (2017). The resulting flow may form an eye at the centre of a cyclonic vortex. By increasing the forcing we observed that the system can undergo a bifurcation from a state with a steady eye to one in which the eye oscillates. For an aspect ratio, Ekman, and Prandtl numbers of 0.1 we find that the critical Reynolds number at which this transition occurs is 398. Examining how the amplitude of the oscillations varies with increased forcing we conclude that this bifurcation takes the form of a supercritical Hopf bifurcation. We examine the dependence on Ekman number, finding that there is an upper limit beyond which only steady eyes are observed. As the Ekman number is decreased the critical Reynolds number for oscillations falls.

Examining the nature of the oscillations we propose that the behaviour results from a trapped inertial wave at the centre of the vortex. The frequency of the oscillations falls within the expected range for inertial waves, and the motions in

the eye display clear similarities to those of a standing inertial wave in a cylinder. The oscillations of streamfunction that we observe in our simulations appear very similar to the results of Harlow & Stein (1974) for columnar vortices, and we believe that the mechanism discussed above is also responsible for this behaviour. Observations of high-frequency fluctuations in tropical cyclones report frequencies that are within the range expected for inertial waves. Though this is promising, further investigation is required before we can definitively say they are a result of the inertial wave mechanism discussed above.

Calm central regions with axial downflow have been observed in columnar vortices such as dust devils and waterspouts, and perhaps also tornadoes. It is not immediately clear that the same mechanisms are present in columnar vortices however. Despite their similarities as swirling flows in the atmosphere, we note that there also significant differences between the large, disklike tropical cyclone, in which planetary rotation is important, and the smaller columnar vortices. Indeed, one might ask if it is possible for intermediate vortices of aspect ratio ≈ 1 to display these behaviours, and if there is a transition between the two states. One thing we have noted is that the nature of the upper boundary is very significant. When the flow is forced to overturn completely, by the tropopause for a tropical cyclone, or an upper boundary in our simulations and those of Harlow & Stein (1974), negative azimuthal vorticity is recovered and an eyewall can form. If the flow does not overturn, however, as is the case in the work of Rotunno (1979, 1980), then the boundary layer vorticity is not fully recovered and an eyewall structure may or may not form. The nature of the flow at the top of columnar vortices is not well understood at present, therefore further investigation into an appropriate boundary condition is essential in deciding if this is a viable mechanism. Vortex breakdown is a popular phenomenon in the columnar vortex literature to which core structures are often attributed. The presence of inertial waves in our simulations might lead us to ask if this is a contradictory theory, as we first thought, or whether the two are, in fact, linked. It is clear that there are a number of further questions and avenues for research when we consider extending our work to columnar vortices.

Finally we have given some consideration as to how the model used in our investigations compares to a real tropical cyclone, in particular in terms of the boundary conditions that we have used. We found that the behaviour of the model

is particularly sensitive to the thermal boundary conditions, with the vortex and secondary flow failing to develop for the case of constant temperature boundaries.

Chapter 5

Experimental investigation

This chapter reviews experiments carried out at the Geophysical Fluid Dynamics Laboratory in the Atmospheric, Oceanic and Planetary Physics Department of the University of Oxford . The work took place as part of a Short Research Visit funded by the UK Fluids Network. The main aim of this work was to see if it was possible to replicate the numerical results of the previous chapter and establish a cyclonic vortex with a steady eye in a system of rotating convection. We begin with a review of previous experimental work on atmospheric vortices before outlining a plan for a new experiment. This is followed by a discussion of the experiment design and techniques. We present a selection of particle imaging and flow visualisation results from the investigations, along with a discussion of what was learnt. The results include both large scale vortices and also a study of cellular convection. The findings are then summarised, with an outlook and suggestions for future investigations.

5.1 A review of atmospheric vortex experiments

We begin this chapter by reviewing some previous experiments that have been performed to model atmospheric vortices. We pay particular attention to how the flows are generated and any internal structures that might appear.

Let us start by returning to the investigations of Maxworthy (1972), which were discussed in the previous chapter. Here a fully enclosed chamber of water, 30 cm in diameter and 15 cm deep, is driven by a rotating lid and side wall. A swirling flow develops with poloidal motion driven by Ekman layers at the top and bottom surfaces. In addition, a shrouded propeller is used to drive the flow along the axis. This arrangement is shown in figure 5.1. Though unrealistic as an atmospheric vortex, the experiment did result in recirculating flow on the axis that Maxworthy termed vortex breakdown, as discussed in chapter 4. This idea was built upon by Church *et al.* (1979), and the numerical work of Rotunno (1979, 1980) amongst others.

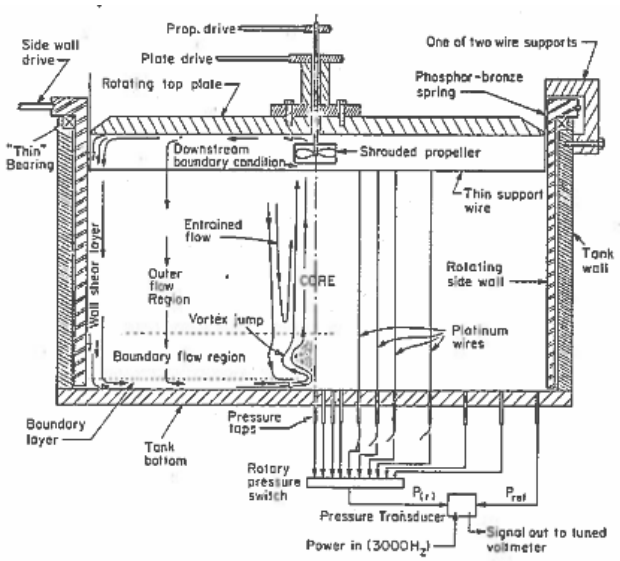

Fig. 5.1 Experimental set-up from Maxworthy (1972)

An alternative experimental set-up that has proved popular in the tornado community is the Ward chamber, illustrated in figure 5.2. Here an axial flow is driven by suction at the top of the experiment. Air enters circumferentially through an opening at lower levels where a rotating mesh imparts swirl. A baffle is used at

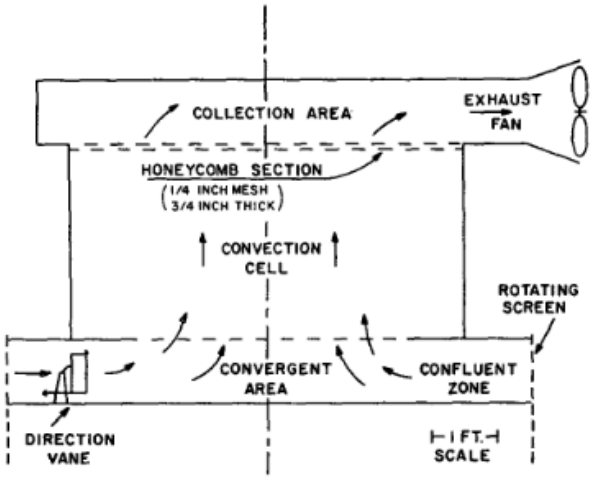

Fig. 5.2 The Ward Chamber of Ward (1972)

the top of the chamber to remove rotation and decouple the fan from the working section. The chamber itself is approximately 2 m in both diameter and height. The Ward chamber was successful in generating a variety of internal structures dependant upon the swirl as documented by Ward (1972). At low levels of swirl a single vortex forms. As swirl is increased, however, the vortex transitions into a two-celled structure with axial downflow. At the highest levels of swirl the vortex breaks up into a number of smaller vortices. These stages are documented in Snow (1982), and were previously illustrated in figure 4.4. The Ward chamber forms the basis for the numerical investigations of Rotunno (1977, 1979) and Harlow & Stein (1974) which were discussed in chapter 4, and replicate some of the behaviours observed in the laboratory experiments. A development of the Ward chamber, the Purdue Vortex Simulator, is discussed by Church *et al.* (1977). It features the addition of 'anti-turbulence panels' at the inlet which stabilise the internal vortex.

The Ward chamber, its designers argue, roughly replicates the conditions at the top of a real atmospheric vortex, though this remains a topic of debate. The issue is highlighted in a recent review paper by Rotunno (2013) who notes that although there have been successes with laboratory investigations of atmospheric vortices, the main problem is tying them in with real-world meteorological observations. It is not clear, at present, what the upper boundary condition to different atmospheric vortices is, or what the most suitable model might be. As we saw in the comparison

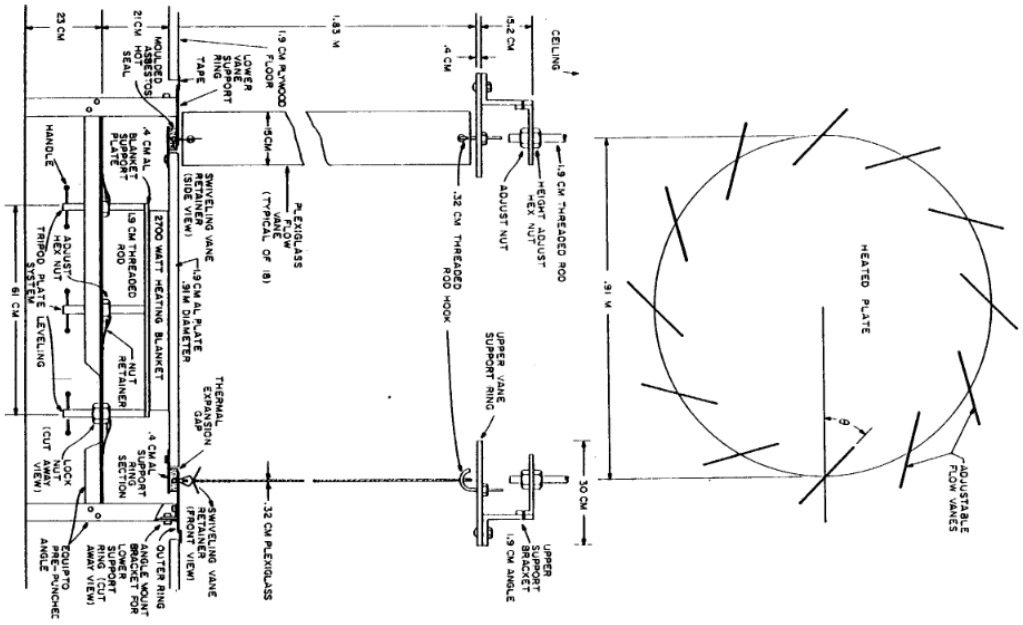

Fig. 5.3 Set-up from Mullen & Maxworthy (1977)

of the numerical investigations of Harlow & Stein (1974) and Rotunno (1977, 1979) in the previous chapter, the nature of this upper boundary can have a significant effect on the flow and any internal structures that might form.

All of the experiments discussed thus far have been driven by suction or fans. In the atmosphere, however, it is less clear as to how flow is driven. Although there is evidence that this approach might be suitable for modelling the tornadoes that form beneath supercells, the same cannot be said for other atmospheric vortices. As we have seen for the dust devil and waterspout, the effects of buoyancy are crucial in establishing the flow. Since many laboratory experiments have focussed in particular on tornadoes this effect is often neglected. This is not the case in the experiments of Mullen & Maxworthy (1977) investigating dust devils. They use a heated base plate to drive axial motion through convection. Tangential velocity is imparted to the flow by a series of vanes around the circumference as illustrated in figure 5.3. Another notable feature of this experiment, in contrast to those discussed previously, is the lack of sidewalls allowing flow to enter (or leave) with swirl throughout its height.

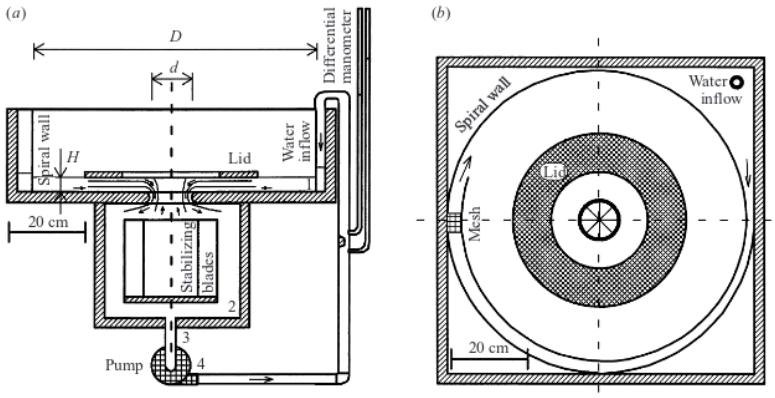

Fig. 5.4 Set-up from Montgomery *et al.* (2002)

All of these experiments have been investigating columnar vortices. Indeed, there is relatively little literature on experiments of disklike vortices. One such case, however, is the work of Montgomery *et al.* (2002) investigating mesovortices in hurricane eyes. Their experimental set-up is shown in figure 5.4. Swirl is imparted by forcing the fluid to follow a spiral pathway around the circumference before it enters the working section. It is then swept under a solid boundary where the authors observe significant boundary layers build up along the surfaces. The main experiment occurs where the flow passes through a central orifice, meant to replicate the eye of the cyclone, and into a lower reservoir. The overall circulation is driven by a pump at the base of the reservoir. Another difference between this and many of the other experiments discussed is the use of water as a working fluid allowing particle image velocimetry and dye as a means of flow visualisation.

Montgomery *et al.* observe that a strong vertical flow resembling an eyewall forms at the edges of the orifice, with a swirling subsidence in the centre. However, they do not believe that the axial subsidence is due to boundary layer effects, instead reasoning that it is driven by a radial pressure imbalance due to the swirling flow. The authors observe that the swirling flow within the eye appears to be 'rotationally stratified' or somewhat two-dimensional following the Taylor-Proudman theorem. Though these investigations are a step forward in terms of investigating disklike vortices, the experiment is designed specifically to model the eye of a mature cyclone with a swirling flow externally enforced. As a result it does not shed any

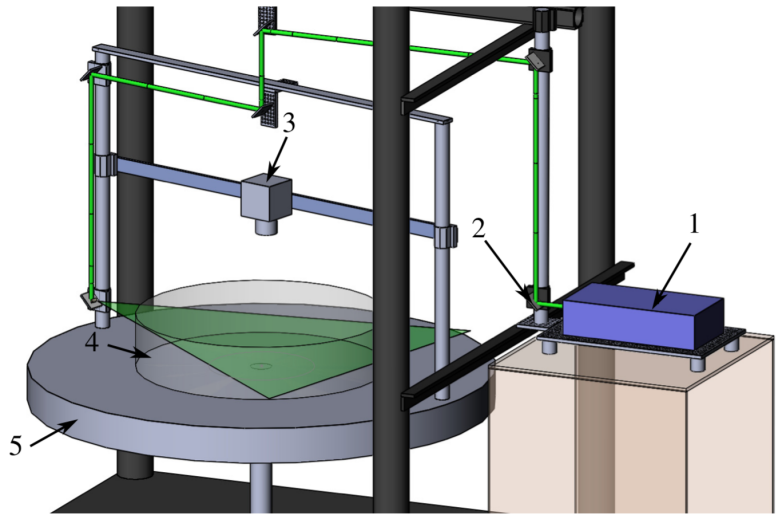

Fig. 5.5 Set-up from Sukhanovskii *et al.* (2016*b*) showing the shallow tank heated at the centre of the base and mounted on a rotating platform.

light on how a large cyclonic vortex might form in rotating convection or how eyes might naturally arise at the centre.

In fact, all of the experiments we have discussed impart swirl to a flow by artificial means such as rotating panels or steering vanes. When investigating columnar vortices, for which the Rossby number is typically large, this may well be a justifiable approach. The issue, however, is that it is difficult to control the conditions at the inflow and establish how internal structures might arise. Indeed, this was one of the main criticisms of the numerical work of Harlow & Stein (1974) who did not provide control over the distribution of azimuthal vorticity at the inlet – a key property in the formation of the eyewall and eye. We finish by considering the most recent work in this area from Sukhanovskii *et al.* (2016*a*,*b*), another investigation into disklike vortices driven by thermal heating at the base. The experiments are performed on a rotating platform allowing swirl to develop more naturally than the experiments above. The apparatus is illustrated in figure 5.5.

A key feature of these experiments is the fact that they establish a single cyclonic vortex with an overturning poloidal flow. Furthermore, there is anticyclonic flow at upper levels as observed in real storms and our numerical investigations. There are, however, no observations of eyes. This is likely due to the way in which thermal

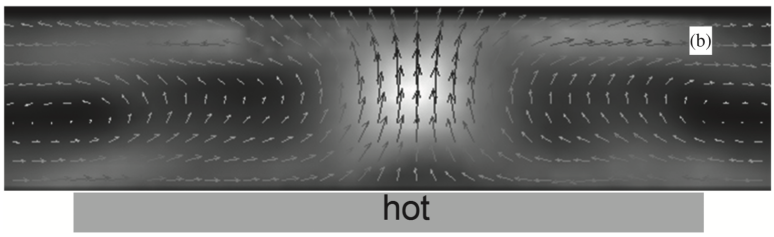

Fig. 5.6 Poloidal flow at the centre of the vortex taken from Sukhanovskii *et al.* (2016*b*).

forcing is applied. In order to create an overturning poloidal circulation, heat is applied only at the centre of the domain generating an axial plume. This allows a cyclonic vortex to be spun up as fluid is drawn in at lower levels to maintain the plume, and ejected at the top, as illustrated in figure 5.6. As a result of strong, localised, thermal forcing forming a plume along the axis, the formation of eyes and any subsiding flow is inhibited. Given that it is possible to produce a single cyclonic vortex in rotating convection with heating at the centre, we might ask whether it is possible to generate a vortex that is capable of maintaining an eye using different thermal boundary conditions.

In summary, we have taken a look at previous experiments of both columnar and disklike atmospheric vortices. There are a number of points to note that might inform our own investigations as follows:

- Far more experiments have been performed for columnar vortices than for disklike vortices.
- The nature of the upper boundary and any outlets (axial vs. radial) can have a significant effect on the flow. There is currently no consensus as to what the most appropriate condition for columnar vortices should be.
- Experiments are often artificially driven. This is usually by a pump, although other cases use a heated centre. The extent to which this affects the flow and any internal structures is not clear.
- Rotation is often artificially enforced. This makes it difficult to control the conditions of the inflow in terms of vorticity, which may affect internal structures.

- Internal structures have been observed in columnar vortices and classified by some authors as vortex breakdown. These bear similarities to the subsiding flow of the eyes we have discussed. As such, we might ask if they arise due to a similar process.

Therefore the primary questions that we shall ask are:

- Is it possible to form a large disklike cyclonic vortex in rotating convection without prescribed forcing (pump or localised heating)?
- If so, can this vortex form an eye at the centre supporting the theory for eye formation discussed in the preceding chapter?
- Finally, if an eye does form, how does it compare to previous experimental observations of internal structures in columnar vortices, and might there be a link between the two?

5.2 Experiment design

At the start of this project we envisaged modelling just the central region of the cyclone in order to study the dynamics of the eye specifically. Early investigations involved flow in a cylinder driven by a pump. The flow was cycled around the outside of the cylinder in a pipe in order to impart swirl in a similar manner to the experiments of Montgomery *et al.* (2002). However, these experiments were unsuccessful in recreating the desired behaviour. We found that the jet that formed upon exit from the spiralling pipe would often persist until it impinged upon the wall of the cylinder, at which point the Coandă effect caused it to stick to the edge rather than spiralling radially inwards. Eventually these efforts were abandoned and we concluded that it would be necessary to model the full cyclone in order to achieve the desired flow structure at the centre. This led us to perform experiments using rotating turntables at the GFD laboratory in Oxford. What follows are the details of these experiments.

Even with a turntable to provide background rotation, there are still a number of challenges in designing a laboratory experiment to emulate the simulations of the previous chapter. The main issues to consider are:

- The upper surface free-slip boundary condition.
- The upper surface temperature boundary condition.
- The lower surface fixed heat flux boundary condition.
- Matching of dimensionless parameters.

To tackle the first of these we decided to perform experiments in a tank with a free surface. Since the top surface of a laboratory experiment should be smooth without waves, the upper boundary should be a reasonable approximation to free-slip. One concern from using this approach in a rotating experiment is that the free surface would become distorted into a concave parabola as a result of the centrifugal force. However, a calculation of this distortion for the rotation rates and tank size used ($0.025\,\mathrm{rad\,s^{-1}}$ and 400 mm) shows that this is negligible in our case. This approach also provides some assistance with the second point concerning the thermal boundary condition. We assume that the laboratory temperature, and hence the air above the free surface, is held at a fixed temperature. This assumption is aided by the fact that the laboratory is climate controlled, and the ambient temperature confirmed to be reasonably steady by thermocouple measurements. Though this allows us to maintain a temperature gradient across the domain, it does not match the fixed-flux boundary condition of our simulations. The heat transfer at the upper surface will change as the water changes in temperature. However, the results of Rotunno & Emanuel (1987) suggest that the structure of the cyclone is not qualitatively sensitive to the precise nature of heat removal at the upper boundary.

The same cannot be said of the lower thermal boundary condition, however. We saw in section 4.6 that changing the lower boundary from constant flux to constant temperature drastically alters the flow. It is relatively easy to impose a constant temperature boundary condition in the laboratory by passing preheated refrigerant under the lower surface. If constructed from copper, or a similar material, the high conductivity rapidly equilibrates the surface to a constant temperature. A constant heat flux condition is somewhat more challenging. One option might be to make use of electric heating, supplying heat by passing current through a resistive heating element. An advantage of this approach would be that the heat flux of a resistive element is directly proportional to the current passing through it. However, if only a

single heating element is used with a high conductivity surface then the temperature across the base will still tend to approach a constant temperature. Therefore it would be necessary to divide the surface into several segments, each utilising an individual, localised heating element to approach a constant flux condition over the surface. This type of arrangement would be challenging to set up and control, and though it has been tried in some cases there are no reports of successful implementation. The apparatus available to us was set up to provide a constant temperature boundary condition as described above, passing heated refrigerant below a copper surface. One of the challenges in the design process was therefore how to modify the boundary to provide something closer to constant flux. The approach we took was to install a thin layer of material with a lower conductivity above the copper base. By constructing a resistor network model for the heat flux through this system we found that this layer allows heat to pass through, but inhibits it from spreading laterally to equilibrate to a constant temperature, thereby providing a closer approximation to constant flux. We prepared a number of circular acrylic base plates of different thickness that could be inserted into the tank. It is clearly challenging to replicate the constant flux boundary condition in a laboratory setting. The results of our investigations, and their relative success, is something that can be evaluated in order to guide future work.

The final important point to discuss is the matching of the dimensionless parameters between simulation and experiment. The simulations of the previous chapter were mostly performed for an Ekman number, Prandtl number, and aspect ratio of 0.1, with Reynolds number varying between 100 and 1000. The first dimensionless number we consider is the Prandtl number. This is a material property set by the viscosity and thermal diffusivity of the fluid we are using. To obtain a Prandtl number of 0.1 would require rather exotic substances, such as liquid metals. Air has a Prandtl number of 0.7. We have opted to use water, which has a Prandtl number of around 7.0 at room temperature. This is because water is convenient, is easier to perform flow measurement and visualisation in, and using liquid rather than gas assists with the upper free-slip boundary condition as discussed. The results of Oruba *et al.* (2018) suggest variation of Pr increases the critical value of Re, but does not prevent eye formation.

Next we consider the aspect ratio. Based upon the investigations of Oruba *et al.* (2018) eyes can form for vortices with aspect ratios between 0.05 and 0.25. The radial dimension is fixed by the geometry of the tank, but the depth can be altered to achieve any aspect ratio. Though we can match this dimensionless parameter, consideration must be given to the practical implications. For a tank of 400 mm diameter we would require a depth of between 10 and 50 mm. In this case the shallow depths become comparable to the thickness of the the LED light sheet (a few mm), which would inhibit visualisation and measurement. It also makes it difficult to control the Reynolds number through maintaining a temperature gradient across the depth as we shall discuss shortly.

For a given fluid (viscosity) and geometry (depth) the only remaining free variable in the Ekman number is the rate of rotation. Based on the investigations of the previous chapter (section 4.4), and also the results of Oruba *et al.* (2018), eyes can form for vortices at Ekman numbers between 0.05 and 0.22. Therefore we choose a rate of rotation to provide an Ekman number within this range. The smaller the tank we use, the slower the rate of rotation that is required. Again, it is important to consider the practical implications in terms of spin-up time and limitations of equipment. For a 400 mm diameter tank of water with an aspect ratio of 0.1, an Ekman number of 0.1 requires a rotation rate of 0.025 rad s^{-1}, i.e. a period of 250 s which is very slow.

Finally we consider the Reynolds number. The only remaining free variable is the temperature gradient. Practically, this is defined by the temperatures of the top and bottom boundaries. For a 400 mm diameter tank of water filled to give an aspect ratio of 0.1, a Reynolds number of 400 requires a temperature difference of only 0.6 °C between the upper and lower surfaces. The results of Oruba *et al.* (2018) suggest that increasing aspect ratio and Prandtl number will require higher Reynolds numbers to form an eye, but this illustrates how the differences in temperature required are practically very small.

With all of this considered we can see that the experiment will be very sensitive to control parameters which could present a challenge to performing precise quantitative measurements. Nonetheless, it is possible to access the correct parameter regime (with the exception of Prandtl number) from the simulations so

we decided to proceed. In the following section we discuss the precise details of the experimental set-up used to perform the investigations.

5.2.1 Experimental set-up

The experimental set-up in the GFD laboratory at Oxford is shown in figure 5.7 with a CAD model (5.7a) alongside a photo of the apparatus (5.7b). It consists of an upright cylindrical vessel mounted on a turntable allowing rotation about the axis of symmetry. The vessel was constructed of perspex, with a diameter of 400 mm, height of 200 mm and wall thickness of 25 mm. The turntable sits on a levelled base and supports a variety of experimental apparatus in addition to the tank as discussed below. It is driven directly by a servo-controlled permanent magnet DC motor, the control panel for which is shown in figure 5.8. The motor is capable of providing rotation rates of $0.01\,\mathrm{rad\,s^{-1}}$ and above, with higher speeds being more stable. An aluminium extrusion structure above the experimental area supports an overhead camera and carries connections to overhead wiring that interfaces between the laboratory and rotating frame. This structure also allows a shroud to be attached around the experiment up to the height of the camera. This was done to eliminate external lighting, reduce reflections on the surface of the experiment, and limit disruption due to air currents in the laboratory.

The entire base of the tank is made from copper painted matt black and is temperature controlled from below by passing a refrigerant (R507) through a series of pipes around the circumference and the centre. The temperature of the refrigerant was regulated using a *Huber* Unichiller device (figure 5.9) capable of delivering up to $29\,\mathrm{l\,min^{-1}}$ at temperatures in the range -20 to $100\,^{\circ}\mathrm{C}$. It could be set to the nearest $0.1\,^{\circ}\mathrm{C}$ with a stability of $\pm 0.2\,^{\circ}\mathrm{C}$. The temperature of the laboratory was controlled to within $\pm 1.5\,^{\circ}\mathrm{C}$ by an air conditioning unit set at $20\,^{\circ}\mathrm{C}$.

The turntable had a Firewire camera mounted above the tank, fixed in the rotating frame. This was an *Imaging Source* DFK 31BF03.H model, chosen for its high picture quality and lossless compression, and capable of taking up to 30 images per second with a resolution of 1024×768 pixels. The camera accepts a number of different lenses to provide the best image size and focussing for the experiment. The investigations presented here used a 12 mm diameter lens. In

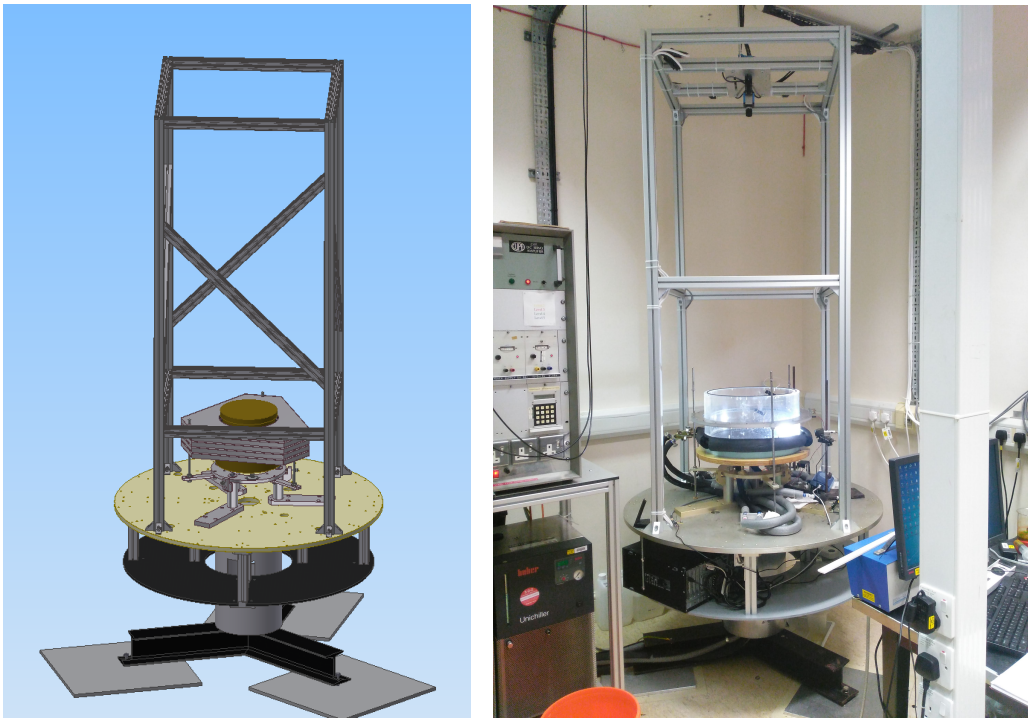

(a) CAD model provided by AOPP (b) Photograph of the rig

Fig. 5.7 The rotating rig at AOPP

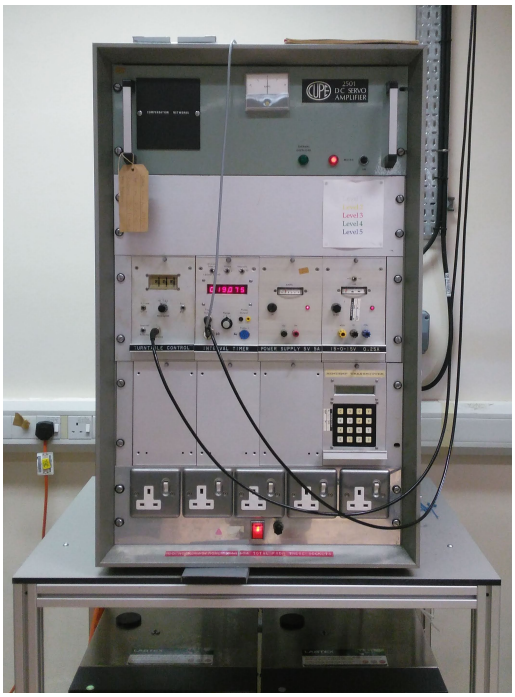

Fig. 5.8 Control panel for the DC Servo motor

Fig. 5.9 Unichiller device for controlling base temperature

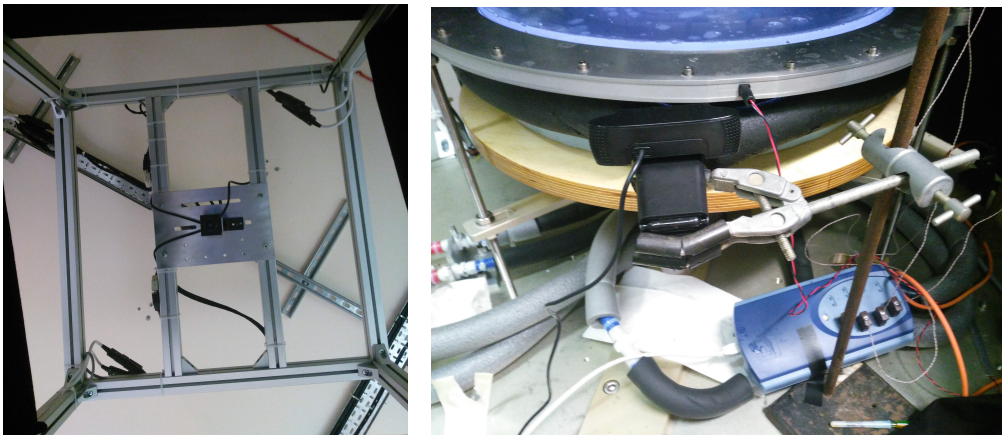

(a) Overhead camera (b) Side mounted camera

Fig. 5.10 Cameras mounted on the rotating platform to take images of the experiments

addition to this a *Logitech* C920 HD camera capable of recording at 30 frames per second with a resolution of 1920×1080 was mounted at the side of the tank to record images in the vertical plane. These cameras are shown in figure 5.10.

The temperature of the experiment was monitored at various locations using type T thermocouples, chosen for their accuracy and stability. They are accurate to $\pm 1.0\,^{\circ}\mathrm{C}$, and were connected to a *Picolab* TC-08 data logger (visible in figure 5.10b) which has an accuracy of $\pm 0.5\,^{\circ}\mathrm{C}$. Thermocouple locations included the base of the tank, the surface of the fluid, above the surface, and in the ambient air of the laboratory. There were also several internal thermocouples built into the base plate of the experiment to monitor the temperature across the lower surface. The data logger was connected via USB, along with the cameras, to a computer housed on the rotating platform. This was then accessed remotely from the laboratory frame over a wireless connection.

In order to visualise the experiment the tank was lit using various methods. To illuminate the entire flow a strip of white LEDs was placed at the edge of the tank. It was also possible to restrict visualisation to a horizontal plane by using an annulus that surrounded the experiment. The annulus contains white light LEDs behind a transparent slit to form a collimated light sheet. It could be raised and lowered on threaded rods to different heights in order to illuminate different planes of the

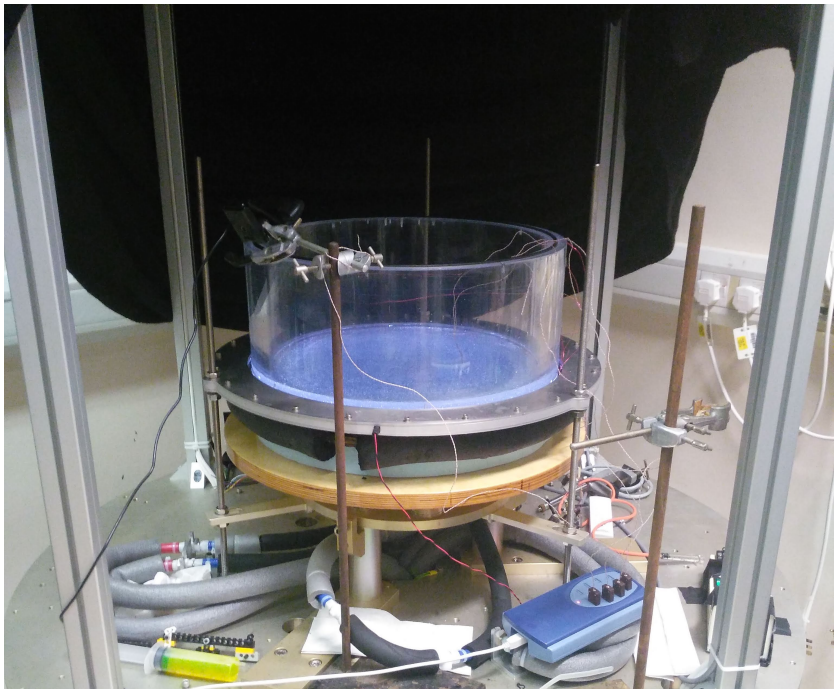

Fig. 5.11 The perspex tank surrounded by the lighting annulus

experiment. Due to a ring of thermal insulation surrounding the edge of the base it was not possible to lower the light sheet all the way down to illuminate the flow at the lower boundary. Instead we were restricted to performing PIV measurements in the mid- to upper levels of the flow.

The working fluid for the experiments was water with a kinematic viscosity of $1.00 \times 10^{-6}\,\mathrm{m^2\,s^{-1}}$ and a thermal diffusivity of $0.14 \times 10^{-6}\,\mathrm{m^2\,s^{-1}}$. Flow visualisation was provided by injecting a concentrated solution of fluorescein. This was done using a hypodermic needle suspended in the flow, controlled remotely using a syringe driver mounted on the rotating platform. In other cases pliolite particles were suspended in the fluid to allow particle imaging measurements to be made. These were usually 355-500 µm in size, although smaller particles (down to 50 µm) were used in some cases. In some of the particle-laden experiments glycerol was added to the water to increase its density and to make the particles neutrally buoyant. The density and viscosity of the water-glycerol mixture were calculated from the volume fractions using the model of Volk & Kähler (2018).

5.2.2 Data acquisition and processing

As discussed previously, images of the flow were captured using a camera mounted above the tank in the rotating frame. The frame rate and gain were controlled remotely using the *ICCapture* camera software. It is advisable to keep the gain low so as to minimise noise in the images. This results in a trade-off since lower values of gain require longer exposure times (lower frame rates). The frame rate was set to be appropriate for the experiment so that particle movement between successive images was not too large, after which a low but acceptable value of gain was chosen.

Post processing was performed using the UVmat software package from LEGI (2018). This is a free MATLAB toolbox covered under the GNU public licence that can be used to visualise and analyse a wide variety of data. It is specifically designed for laboratory use, however, and contains particle imaging velocimetry (PIV) software. More specifically, the software employs correlation imaging velocimetry (CIV). This is a particular type of PIV algorithm (cross-correlation based pattern matching) that tracks translation, rotation, and shear in a flow. It does this by comparing two successive images with a given time separation. The first image is divided up in to a grid of boxes of $m \times n$ pixels, each of which is called a correlation box (a typical box size would be 10×10 pixels). Another domain, known as the search box, is defined as a larger area around a correlation box with size $i \times j$ pixels. The algorithm then calculates the correlation between a correlation box from the original image and the locations it could take within the search box in the new image. The peak in the correlation function is taken as the new location, with the distance from the original image providing a displacement field.

The algorithm requires some fine-tuning to select appropriate sizes for the correlation and the search boxes for each application, and also the time between images. Correlation box size depends upon the particle seeding density so as to get an identifiable image, whilst the search box and time interval depend upon flow velocity. The correlation box needs to experience enough motion to generate a displacement field, but not so much that it moves beyond the search box boundaries or becomes distorted to the extent that it no longer bears resemblance to the original box. The time interval and search box are typically chosen such that

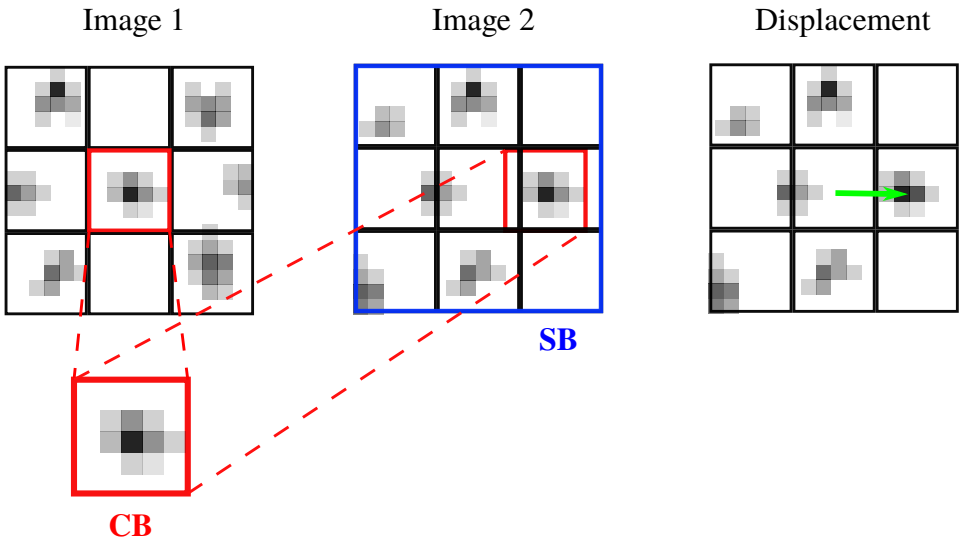

Fig. 5.12 Illustration of the CIV process.

the displacement between images is around 5-20 pixels. Unlike more traditional particle imaging techniques approaches, CIV does not need to resolve the motion of individual tracer particles making it well suited for analysing flows with a variety of spatial scales. The algorithm is also capable of sub-pixel accuracy through interpolation of the correlation function.

The CIV process is illustrated in figure 5.12. Two images are shown, divided into correlation boxes (CB). CIV is then performed using the central box of image 1. This correlation box is compared to locations throughout the search box (SB) in image 2 to generate a correlation function. The location corresponding to the maximum correlation is shown in red. Based on the position in image 2 relative to the original position of the correlation box in image 1, a displacement can be calculated, shown by the green arrow. Given a time interval between the images, this displacement can be converted into a velocity. By repeating this process across the images, the CIV algorithm generates a velocity vector field for the flow between the two images.

A more in-depth discussion of PIV can be found in Raffel *et al.* (2007), whilst the CIV algorithm is discussed specifically in Fincham & Spedding (1997) and Fincham & Delerce (2000).

Temperature was recorded over time using the *Picolog* software. This interfaces with the data logger to provide a temperature time series for each thermocouple. It is possible to record up to 16 different channels at once and generate both a graphical and csv file output.

5.2.3 Methodology

Experiments were performed by filling the the tank to the required depth with water and setting the light sheet to the desired height. If PIV investigations were to be performed then pliolite particles were added to the fluid. It is important to select an appropriate particle size for the PIV software to work well. This can be guided by considering the pixel size of the camera used to capture images, but ultimately requires some fine-tuning depending upon the nature of the experiment. We found that 355-500 µm particles worked best for our application. It is also important to consider the particle density and mixing. To control this, a solution of particles was prepared by mixing in a small quantity of water with a wetting agent using a magnetic stirrer. This was then added to the experiment gradually until the desired seeding density was achieved. When particles were used it was necessary to ensure that they were neutrally buoyant since the experiments took place over long timescales. This was done by adding glycerol to the fluid and measuring its density until it matched that of the particles. If there were any bubbles from the wetting agent or poorly wetted particles on the surface of the water, these were removed with a suction pump before performing any experiments. For investigations using fluorescein a hypodermic needle was positioned at the desired location in the tank using a support frame constructed from LEGO.

After the necessary preparation the tank was set rotating and left until the fluid approached a state of solid-body rotation. Following this the cameras and thermocouples began recording data. The heating, which was pre-set to a specific temperature, was then switched on. An example time series of temperatures during an experiment is shown in figure 5.13. We see that the temperature of

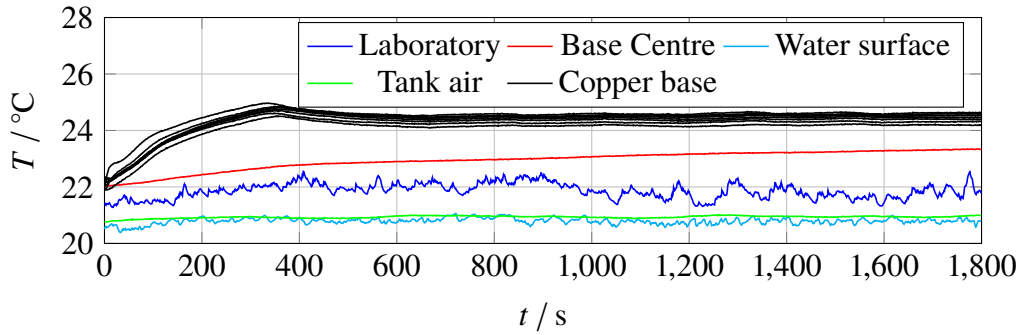

Fig. 5.13 Temperature variation over the course of one of the experiments.

both the surface and the air above remains relatively constant over the course of the investigation. The temperature of the copper base rapidly heats up after it is switched on before being held steady at the set temperature. The temperature recorded on the base of the tank lags behind this as a result of the acrylic base plate, rising slowly over the course of the experiment. This suggests that the Reynolds number is gradually increasing, but we cannot say how the heat flux varies without further measurement. It was possible to adjust the temperature during the course of the experiment, and sometimes we adopted an approach similar to the simulations where the system would be recorded at one temperature, then stepped to another. The experiments could not run for an indefinite period of time, however, as the water gradually increased in temperature. Whenever this became noticeable from the thermocouple measurements the experiment was left to cool or the working fluid replenished.

5.3 Results

In this section we discuss the results from the investigations. We begin with the PIV results which provide insight in to the overall structure of the flow, discussing the different patterns that were observed in the investigations. We finish this section with some observations of cellular convection from investigations outside our main parameter range of interest.

5.3.1 PIV results

PIV measurements were made to determine the structure and patterns of the flow. The measurements are made at the upper levels illuminated by the horizontal light sheet. Since the flow evolves slowly it was difficult to observe structures using the naked eye. We use the PIV measurements to assist us in seeing the flow patterns. The first objective, as discussed above, is to examine whether it is possible to form a single large cyclonic vortex. A number of investigations were performed to gather data and explore the parameter space. Here we present a selection of the results that illustrate our main observations.

In a number of cases we observe a cyclonically swirling flow that fills the entire tank. This can be seen in figure 5.14a which shows the velocity field near the upper surface. These investigations were performed at an Ekman number of 0.133 and aspect ratio of 0.165. The Reynolds number was of the order of 1200. This cyclonic flow appears to be a relatively robust feature of our experiments, observed in numerous runs around this parameter range. We also note that anticyclonic structures were rarely observed, likely as a result of the imposed background rotation.

The formation of a singular cyclonic vortex is promising, and indicates that the experiment can support a somewhat axisymmetric flow without too many adverse three-dimensional effects. However, there are a number of discrepancies between the flows observed in the laboratory and those presented in the preceding chapter. The first of these is the fact that the vortex was not necessarily centred on the axis in all cases. Indeed, in figure 5.14a it can be seen that the centre of rotation is displaced to one side, an observation that we shall discuss shortly. The location of this off-centre axis of rotation was observed to drift slowly over the course of the experiment. It should be noted that such asymmetries are not entirely unexpected, as we have moved from enforced axial symmetry to three-dimensional flow.

We also note a lack of an anticyclonic flow towards the outer boundary as observed in the numerical simulations and required for a torque balance on the system. This may well be linked to another discrepancy we observed; the flows did not appear to spiral, but rather seemed to follow roughly circular streamlines about the centre of rotation. In our simulations the development of an anticyclonic region

arose due to the conservation of angular momentum as the flow spiralled radially outwards. If the flow follows closed streamlines in a single horizontal plane, this effect will be not be present.

In addition to the cyclonic vortex we also frequently observed the development of a double vortex. This flow pattern can be seen in figure 5.14b. It consists a pair of large scale vortices, one cyclonic and one anticyclonic, roughly dividing the tank in two. This division can be seen more clearly in figure 5.15 which shows the curl of the vector field. It can clearly be seen that one half (yellow) contains positive vorticity, i.e. cyclonic rotation, whilst the other (blue) is largely negative, i.e. anticyclonic.

Another interesting observation is that flows seem to be able to transition between these two structures. In figure 5.14 the single cyclonic vortex was observed to split in two over the course of the experiment. This clearly breaks the assumptions of axial symmetry we have previously made in our analysis. It is likely that the splitting and merging is related to the centre of rotation being off-axis in the single vortex case as noted above. A possible explanation for the double vortex structure is that it is a wave number 1 instability of the flow. This can be seen best from the vorticity plot of figure 5.15, which clearly shows its dipolar nature. The decomposition of a tropical cyclone into azimuthal modes is discussed by Reasor *et al.* (2000). They note that, although axisymmetric to zeroth order, the structure of a cyclone contains significant amounts of wave number 1 and 2 modes, particularly whilst undergoing changes in intensity and structure. They believe that these modes may occur as a result of vortex stretching transferring vorticity from the horizontal to the vertical direction. They suggest that the wave number 1 mode, as we perhaps see in our laboratory experiments, could be due to enhanced convection on one side of the cyclone. We have already discussed how our lower boundary does not precisely replicate the constant flux condition of our simulations and might lead to the formation of localised hotspots. As such it could be that the dipolar structure that we observe occurs due to enhanced convection in a particular region, though we cannot know for certain without more detailed measurements.

By considering the axisymmetric and dipolar structures as two separate modes we might also be able to explain the off-axis vortex of figures 5.14a and 5.16a as being a superposition of the two modes. The combination of a strong axisymmetric

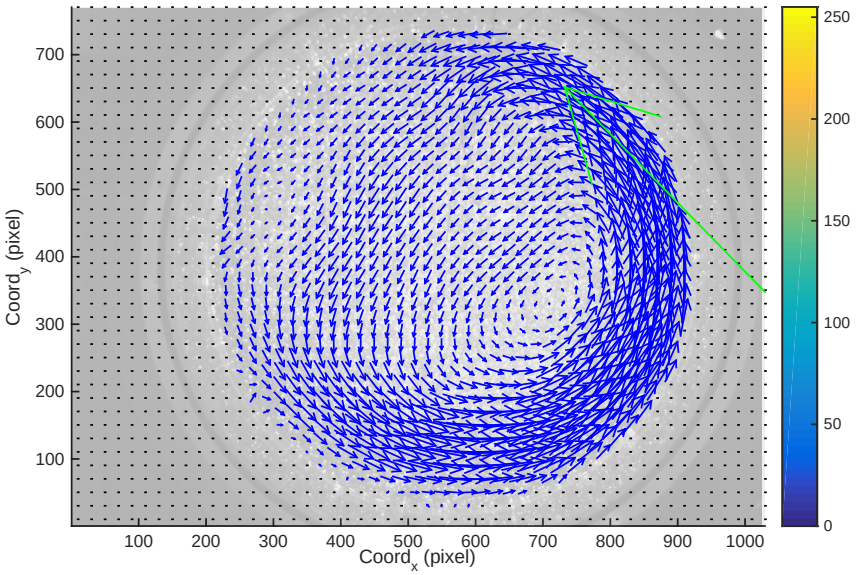

(a) Velocity for $Re = 1225$

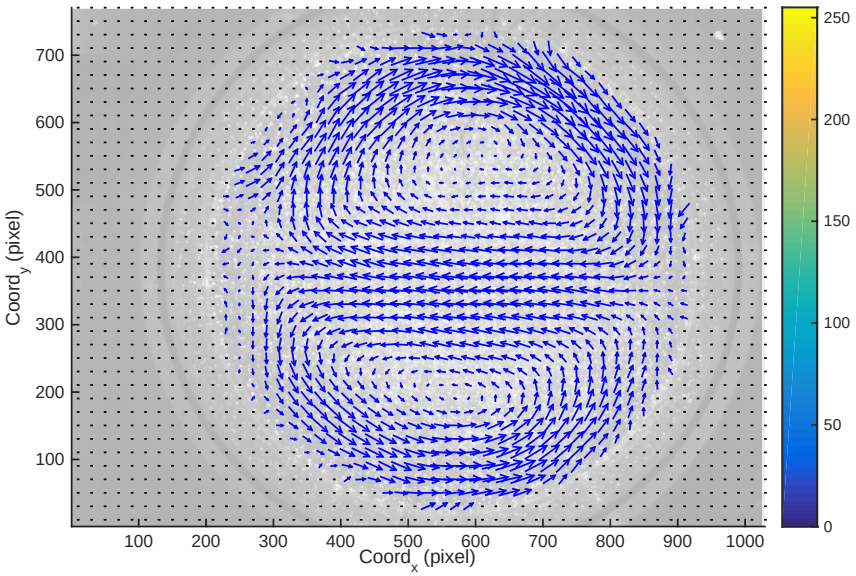

(b) Velocity for $Re = 1525$ at a later time.

Fig. 5.14 Velocity vector fields from an experiment with $Ek = 0.133$, $\Lambda = 0.165$ overlaid on an image of the tank.

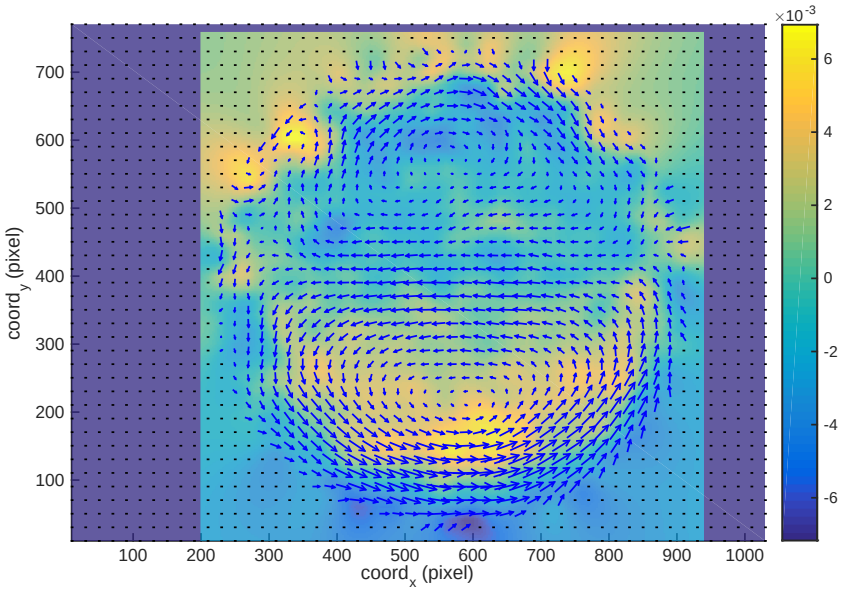

Fig. 5.15 Velocity field of figure 5.14b showing a double vortex, overlaid on the vertical vorticity field.

structure and a weaker dipole would result in an off-axis vortex. Further investigations are required to explore this idea in more depth, however. In particular, performing a modal decomposition and looking at the transitions between the single and dipolar states as a function of different modes might be illuminating.

In one case we observed that as the temperature increased a dipolar state transitioned into a flow that was anticyclonic at the upper levels, spiralling outwards from the centre of rotation. This is shown in figure 5.16a and is the experiment that most closely resembles the cyclone structure discussed in the previous chapter. This is encouraging, although we note that there is no evidence of an eye at the centre of this structure. One explanation for this might be that the Reynolds number is too low for the process of eye formation and a higher temperature gradient is required in order to form an eye. This might be due to the fact that we are using a Prandtl number that is significantly different to the simulations, but could also be caused by uncertainties in our Reynolds number. As we saw in figure 5.13, the temperature gradient across the acrylic base when calculated from thermocouple measurements is lower than that based upon the temperature of the copper base. As a result the Reynolds numbers reported here could be overestimates, and may

need to be larger than those in the simulations to form a vortex as a result of the increased Prandtl number.

Following the development of an anticyclonic vortex we increased the temperature gradient further to see if it might develop an eye. This, however, led to the flow becoming highly three-dimensional, as shown in figure 5.16b. This is not unexpected since significant heating at the base will eventually lead to buoyancy dominating over rotational effects. Localised warm regions form at the base giving rise to thermal plumes which carry fluid upwards to the surface where it cools before sinking back down. The development of these structures indicates that efforts to mimic a constant flux boundary condition have become ineffective. The behaviour we see is that expected for a constant temperature boundary condition as discussed in the previous chapter.

Before finishing our discussion of the PIV results, it is worth mentioning the behaviour observed in figure 5.17. We can see from the velocity field see that the flow is dominated by a large scale radial influx at the outer boundary. This was found to be caused by a rapidly rising annulus of buoyant fluid at the outer boundary. This is due to the fact that, though the base plates were designed to be close fitting, they were approximately 2 mm less in radius than the tank in order to be inserted and removed. As a result the thin region around the edge of the base could heat the fluid far more effectively than elsewhere in the tank. This causes enhanced convection at the edges, with fluid rising up and then moving radially inwards. Though this was not an issue at short timescales with low heating, the effect dominated when experiments ran for longer and larger temperature gradients were used.

5.3.2 Rotating cellular convection

This section details some observations that were made outside of our main parameter range but are interesting and worthy of discussion. It is relatively well known that fluids heated from beneath can organise in to a cellular structure following the onset of convection. The first observations of this phenomenon were documented by Bénard (1900), who lends his name to generic convection in a fluid heated from below. Once a critical value of Rayleigh number is exceeded convection

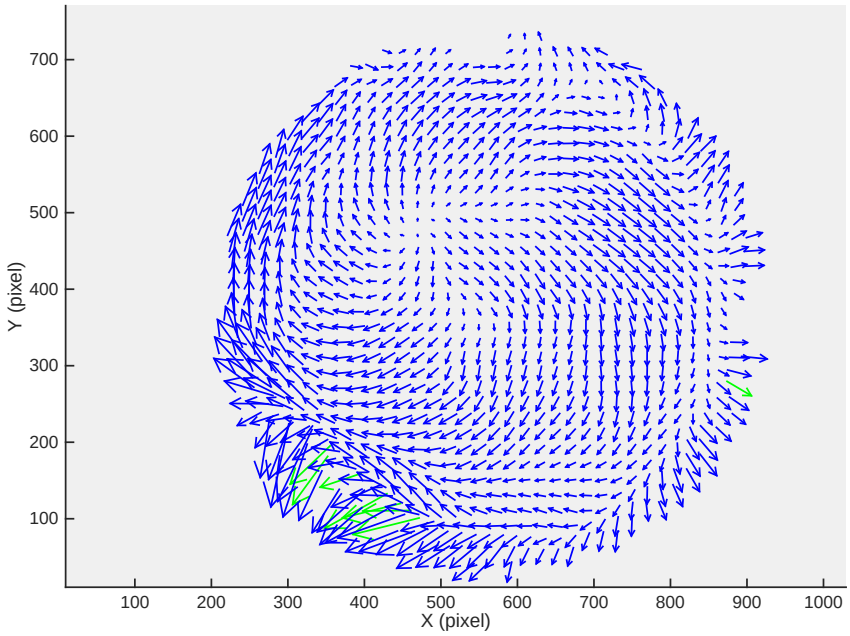

(a) Velocity for $Re = 1600$ displaying an anticyclonically spiralling flow.

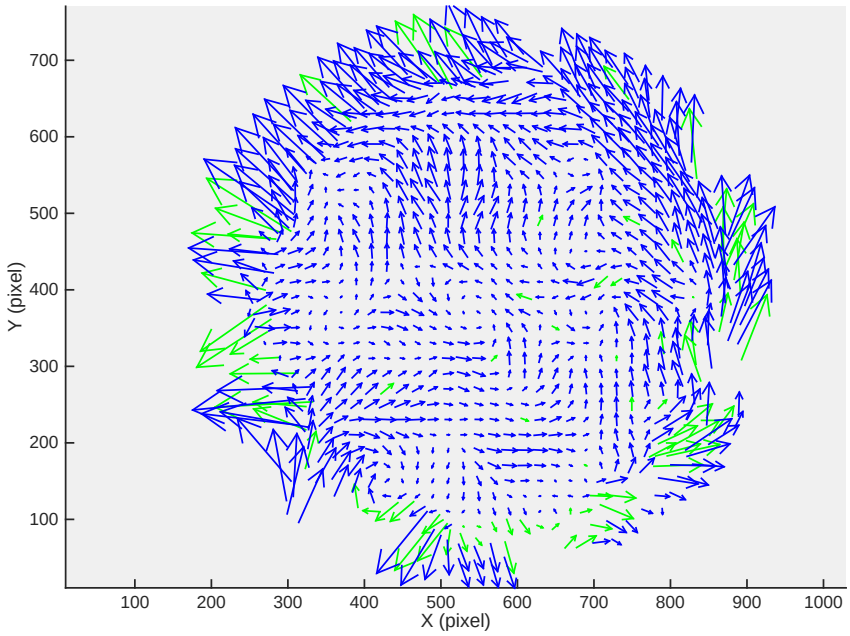

(b) Velocity for $Re = 1900$ showing significant three-dimensional effects.

Fig. 5.16 Velocity fields from an experiment with $Ek = 0.133$, $\Lambda = 0.165$.

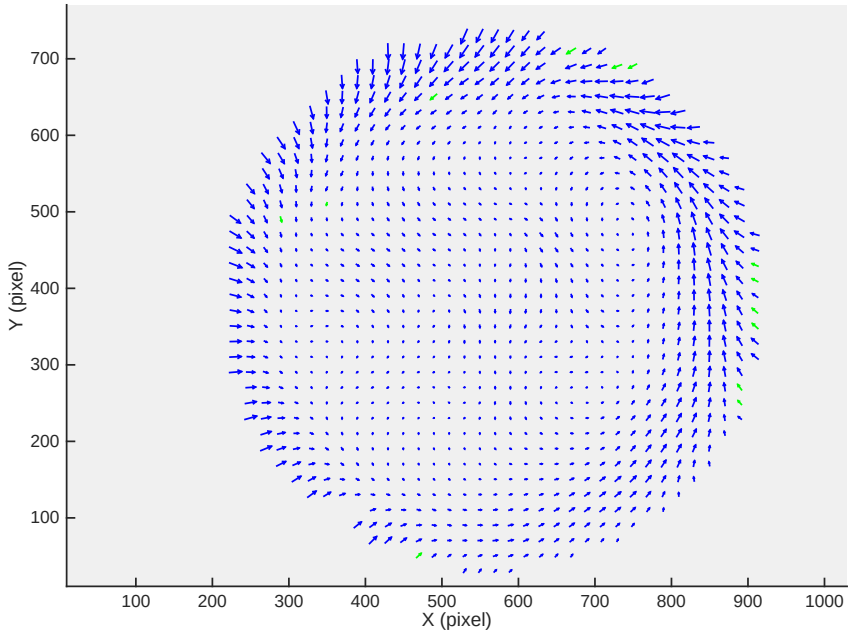

Fig. 5.17 Velocity field showing enhanced flow at the outer boundary

begins, with a cellular structure maintained until around 10 times the critical value (Chandrasekhar, 1981). Beyond this the motion becomes unsteady and irregular, transitioning to turbulence. A number of different arrangements are possible for this cellular lattice, but when one of the boundaries is a free surface it tends to take the form of a honeycomb comprised of regular hexagons. Convection is enhanced at the free surface by the effects of surface tension and sometimes referred to as Bénard-Marangoni convection (Maroto *et al.*, 2007). Figure 5.18a shows the remarkable regularity of the lattice[1] in a thin layer of silicone oil containing aluminium flakes. The close up image in figure 5.18b shows how fluid rises at the centre of the hexagon before moving outwards to the edges where it descends.

An interesting question is what happens when the system we have just described undergoes rotation. A theoretical discussion of the effects is given by Chandrasekhar (1953), with a physical interpretation provided by Veronis (1959). The combination of these studies is summarised in Chandrasekhar (1981). It is found that once a critical Rayleigh number (which is now a function of rotation) is exceeded, the fluid still forms a regular lattice of convection cells. A hexagonal honeycomb is, again,

[1]Note, the defect in the lattice is located above a small dent in the lower boundary.

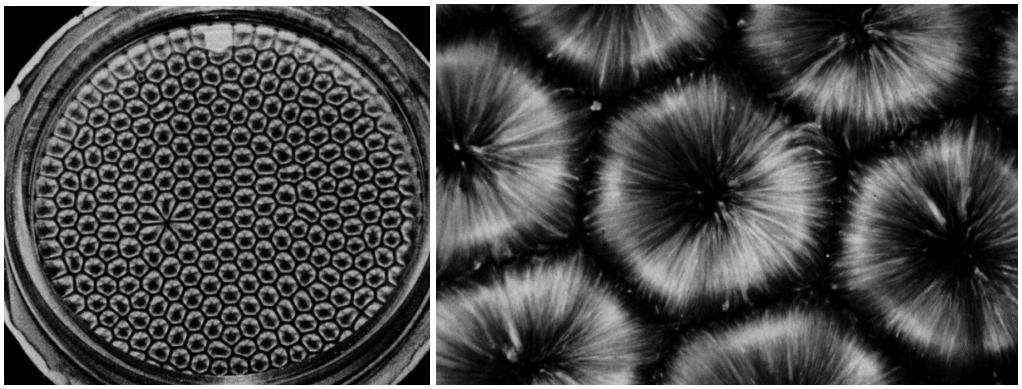

(a) Lattice structure of convection. (b) Close up image of a hexagonal convection cell.

Fig. 5.18 Hexagonal cell structure from experiments on surface-tension-driven Bénard convection. Images taken from Koschmieder (1974) and a photograph by Velarde, Yuste and Salan via Van Dyke (1982).

the preferred pattern when there is one free surface. There is a notable difference between the rotating and non-rotating cases, however, due to the influence of the Coriolis force. As fluid rises at the centres of cells and moves radially outwards towards the edges it experiences this transverse force causing it to take a helical path, spiralling anticyclonically. The opposite is true as it converges on the corners of the hexagon and begins to descend. Figure 5.19 from Veronis (1959) shows how the hexagonal cells are distorted under the action of rotation. The critical Rayleigh number required for the onset of convection also increases. This is due to the 'stiffening' effect of rotation on a fluid that acts to inhibit vertical motion, as described by the Taylor-Proudman theorem. Despite the extensive mathematical analysis, experimental observations of these helical cells are relatively rare. Some observations were made by Rossby (1969) which showed the cellular divisions from above, but not the internal structure.

In relation to the overarching theme of these investigations we note that it was, at one time, hypothesised that these structures might be responsible for polygonal eyes observed in some tropical cyclones such as those illustrated in figure 5.20. This theory has been superseded, however, and it is now believed that these shapes are the result of internal gravity waves within the eye (Lewis & Hawkins, 1982). These structures still hold relevance to geophysical fluid dynamics, however, and

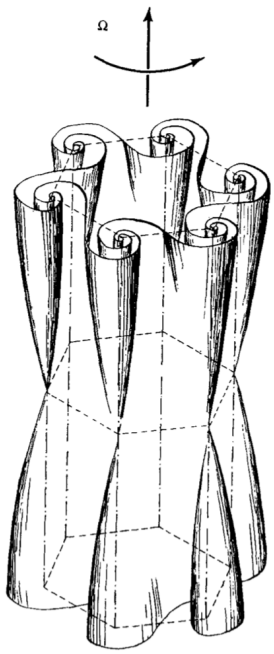

Fig. 5.19 Sketch of the vortices in the convection cells that form a hexagonal structure taken from Veronis (1959).

are believed to be involved in the formation of convective Taylor columns in the Earth's outer core (King & Aurnou, 2012; Aurnou *et al.*, 2015).

We performed a short series of experiments at an increased rate of rotation during which we observed the formation of the cellular structures described above. The non-dimensional parameters for these investigations are summarised in table 5.1, along with an estimation of the forcing and a description of the observed structure. The level of forcing is based on estimates of the critical Rayleigh number Ra_c from Veronis (1959). The experiments were performed in a similar manner to those discussed previously. First the tank was set rotating until the fluid was in a state of solid body rotation. Following this the heating was switched on and allowed to stabilise. We then inject a quantity of fluorescein near the base to show the motion of the fluid. Images were captured simultaneously from above and the side.

Figure 5.21 shows the development of the flow structures taken during experiment 3. The fluorescein is injected at time 0 in figure 5.21a. This is followed by some turbulent motion resulting from the impingement of the jet on the base in

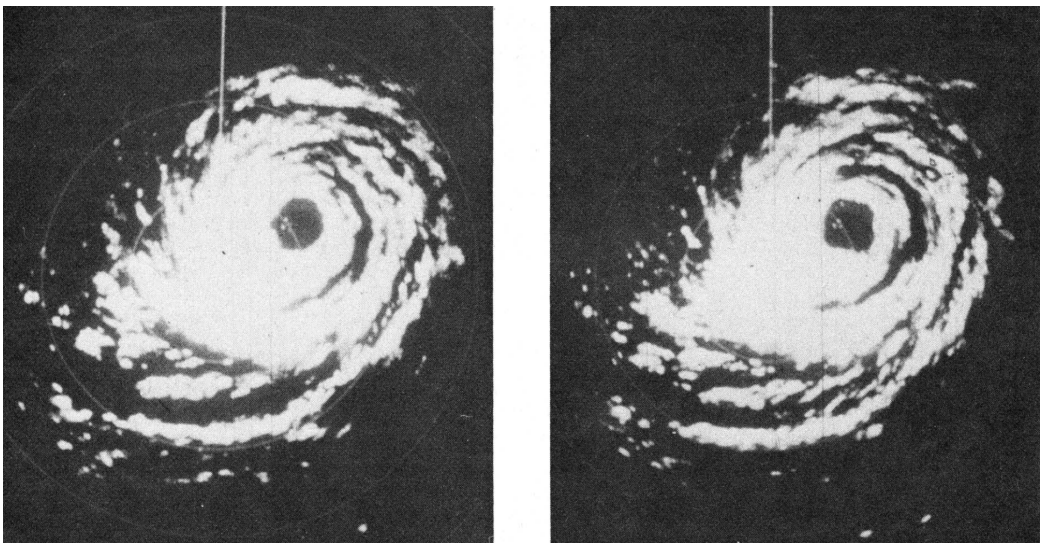

Fig. 5.20 Polygonal structures observed at different times during the life cycle of Hurricane Betsy (1965). Images taken approximately 1 h apart. Image taken from Lewis & Hawkins (1982).

Experiment	$Ra \times 10^{-5}$	$Ek \times 10^{3}$	Ro	Ra/Ra_c	cell structure
1	1.3	5.7	3.6	5.0	irregular
2	6.3	2.5	2.2	5.3	irregular
3	25.2	1.3	0.6	0.6	regular
4	36.8	1.0	0.9	2.6	regular
5	11.4	1.9	1.7	6.1	irregular

Table 5.1 Details of experiments on cellular rotating convection.

(figure 5.21b) before the fluorescein eventually settles near the base of the tank (figure 5.21c). The convective motions can begin to be seen in figure 5.21d as fluorescein is swept up at the centre of the cells forming a series of spikes. These continue to develop into columns over the course of figures 5.21e and 5.21f, growing towards the surface. The columns can be seen in the overhead images as bright spots. Looking at the rightmost column in figure 5.21f (side view) we see that the fluid is beginning to spiral anticyclonically outwards as it moves towards the edges of the cell.

This spiralling becomes much clearer in figure 5.21g as the fluorescein reaches the top of the fluid and begins to spread at the surface. As a result the lattice of hexagonal cells begins to become visible. After an extended period the fluorescein has had time to cycle round the cells, making the edges of the lattice much clearer (figures 5.21j and 5.21k). Descending fluorescein at the edges of the cells makes it hard to see any in the side images, though it is possible to see new towers forming on the periphery as they take on fluid that has descended in neighbouring cells.

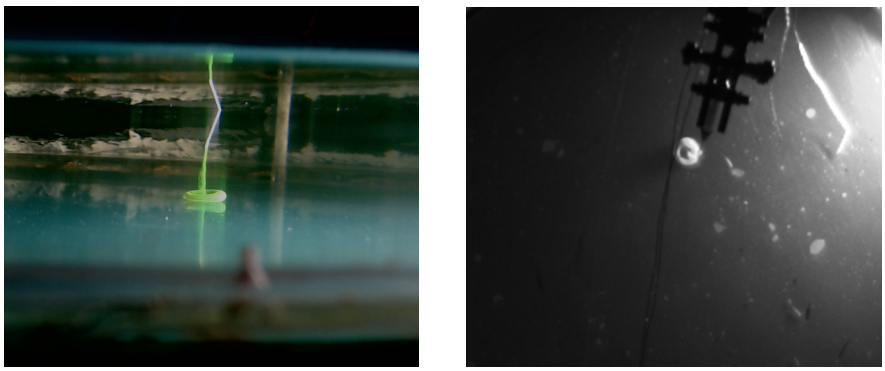

(a) 0 s

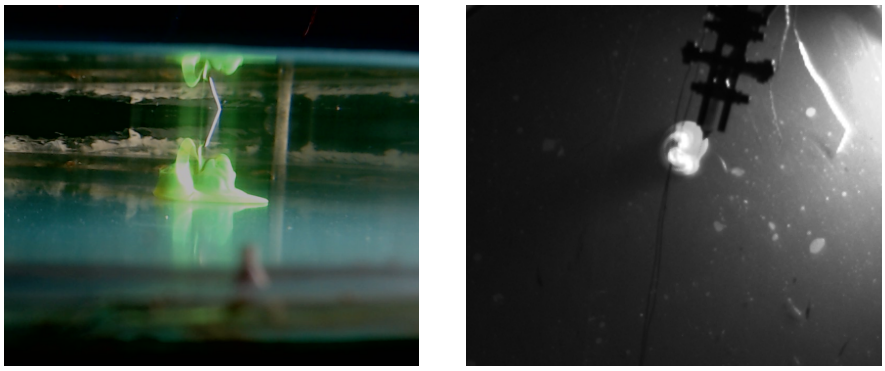

(b) 15 s

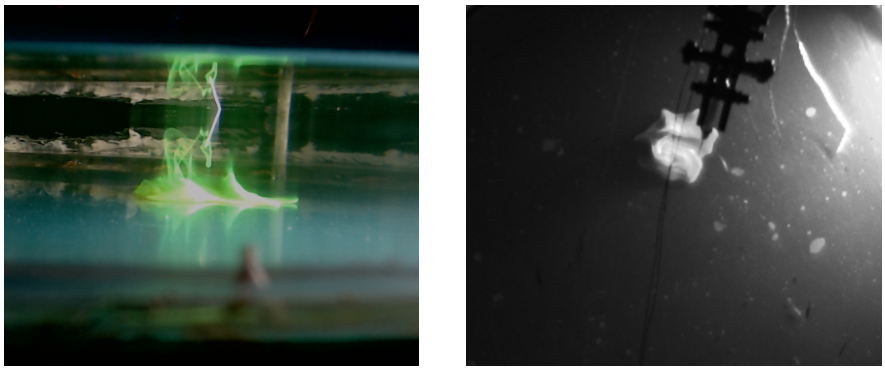

(c) 65 s

Fig. 5.21 Fluorescein visualisations of the formation of convection cells taken from the side (left) and top (right) for a range of times after injection.

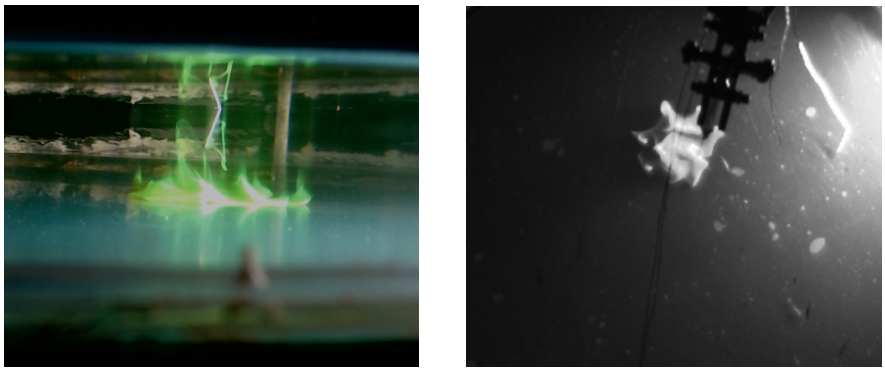

(d) 90 s

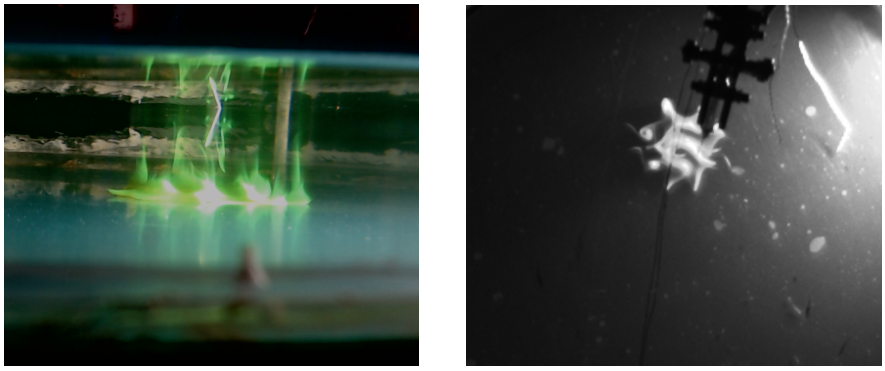

(e) 110 s

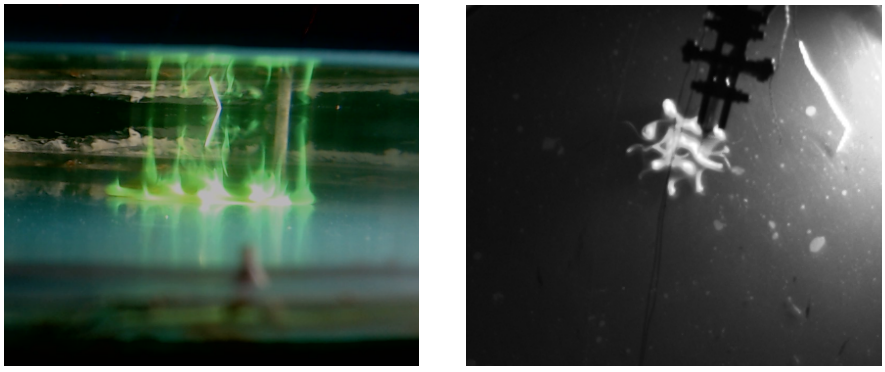

(f) 125 s

Fig. 5.21 continued.

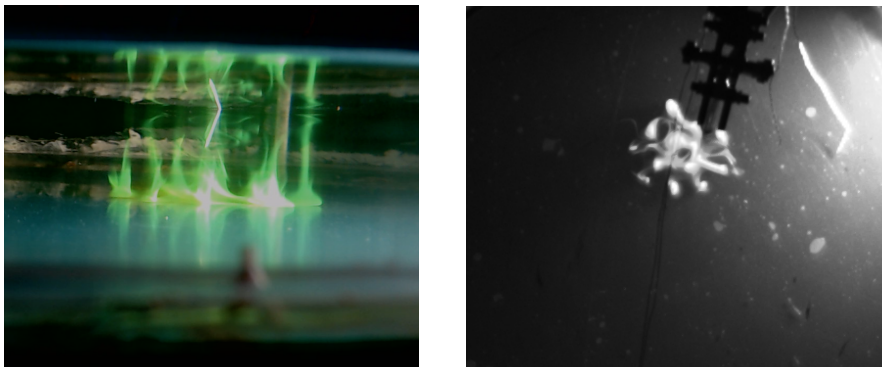

(g) 145 s

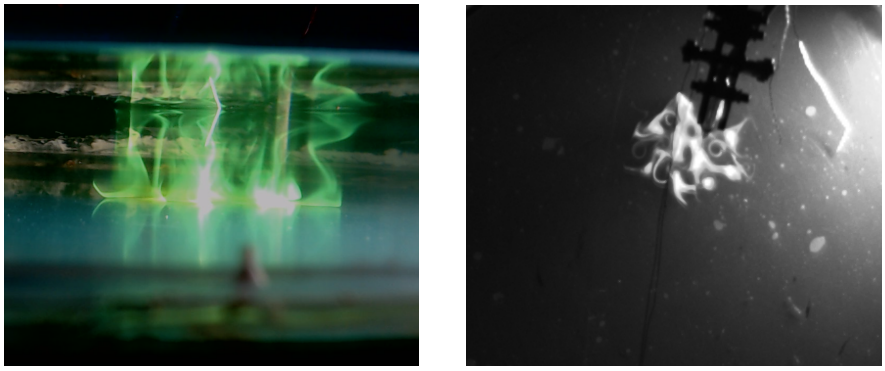

(h) 215 s

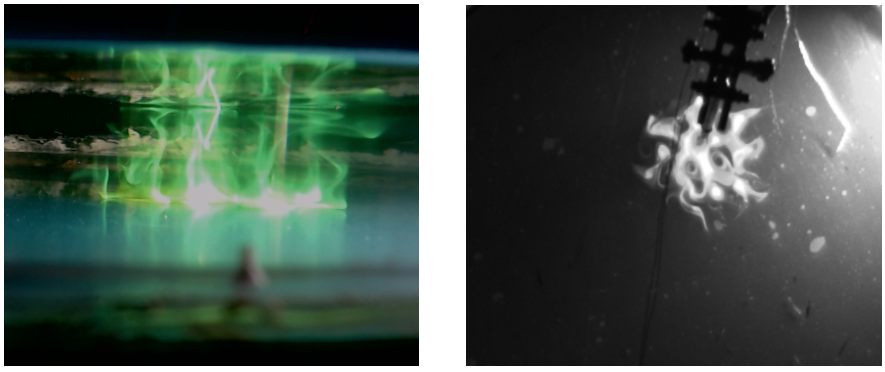

(i) 285 s

Fig. 5.21 continued.

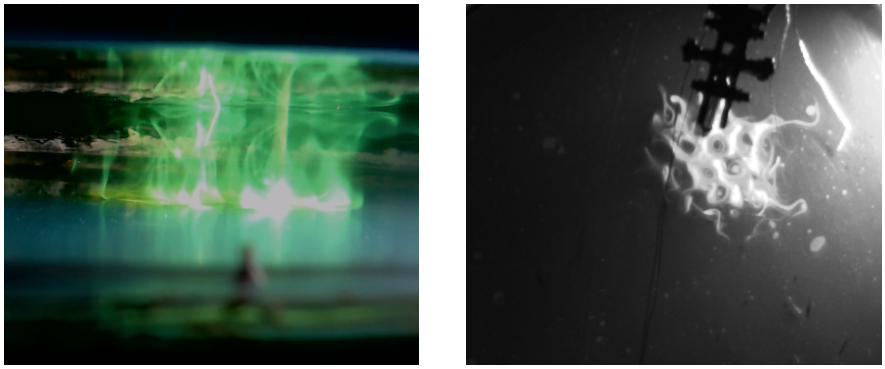

(j) 385 s

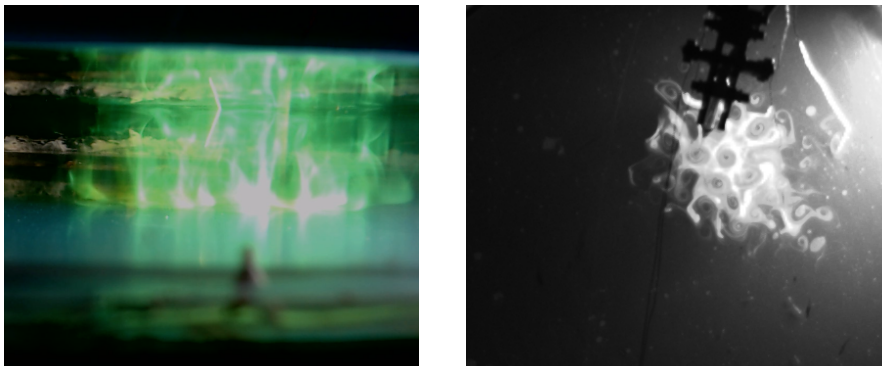

(k) 505 s

Fig. 5.21 continued.

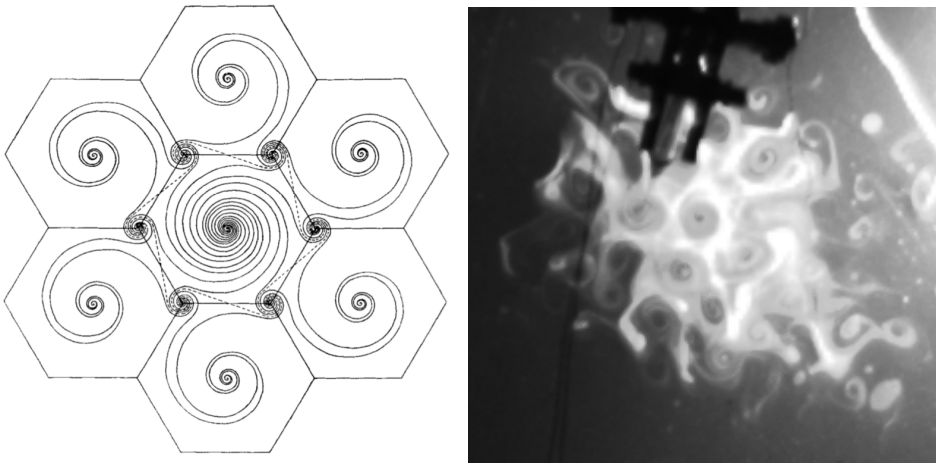

(a) Sketch taken from Veronis (1959). (b) Fluorescein image from experiments.

Fig. 5.22 Top view of the hexagonal cells.

Our experiments are compared to the theoretical sketches of Veronis (1959) in figures 5.22 and 5.23. The first of these shows the hexagonal lattice structure viewed from above. It is possible to see how the cells tessellate together in a regular fashion, with the edges clearly defined by brighter regions of fluorescein. We can also see how the fluid spirals anticyclonically outwards from the centre of the cells under the action of the Coriolis force, much in the same way the outflow of a tropical cyclone does. Figure 5.23 shows the side view of convection cells, again alongside a sketch by Veronis. From this angle we can see the three-dimensional structure of the cells and how the column forms an anticyclonic helix that spirals upwards and outwards at the top.

We estimate the critical Rayleigh number for the onset of convection, and hence how many times supercritical each of the experiments was (table 5.1). We also record the appearance of the cellular structure for each of the experiments as either 'regular' or 'irregular'. These two descriptions are illustrated in figure 5.24. The regular structure matches the sketches of Veronis in figure 5.22a with a repeating lattice of tessellating hexagons. The irregular pattern still shows a cellular structure, but the individual vortices no longer take regular shapes and hence do not tessellate to form a regular lattice. Instead we see each cell appearing as an anticyclonic

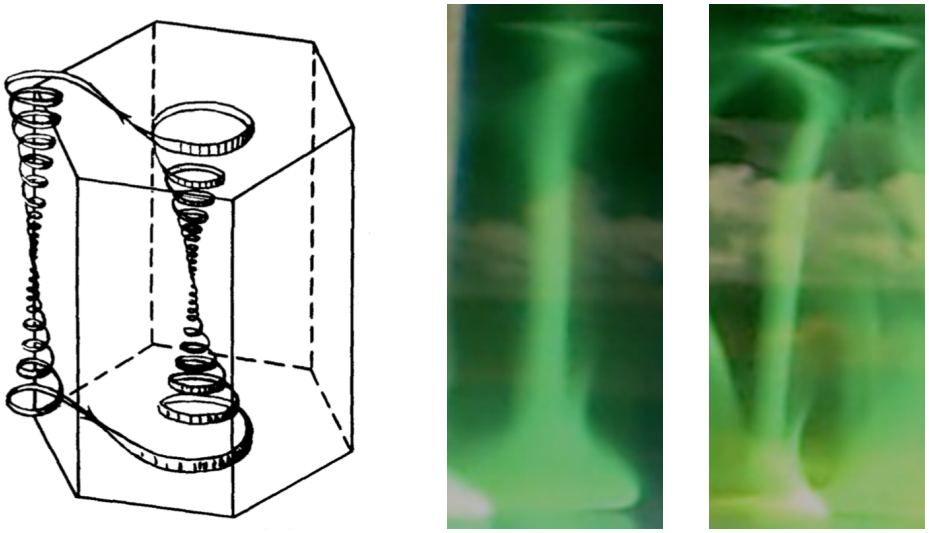

(a) Sketch taken from Veronis (1959). (b) Fluorescein images from experiments.

Fig. 5.23 Side view of the hexagonal cells

spiral at seemingly random positions, sometimes interfering with neighbouring cells.

Based on our estimations of critical Rayleigh number in table 5.1 we see that the irregular structure is associated with higher levels of supercriticality. This is to be expected since the convective structure transitions to a turbulent state as the forcing continues to increase. What is interesting, however, is that we observe a regular cellular pattern for a subcritical Rayleigh number (experiment 3). We

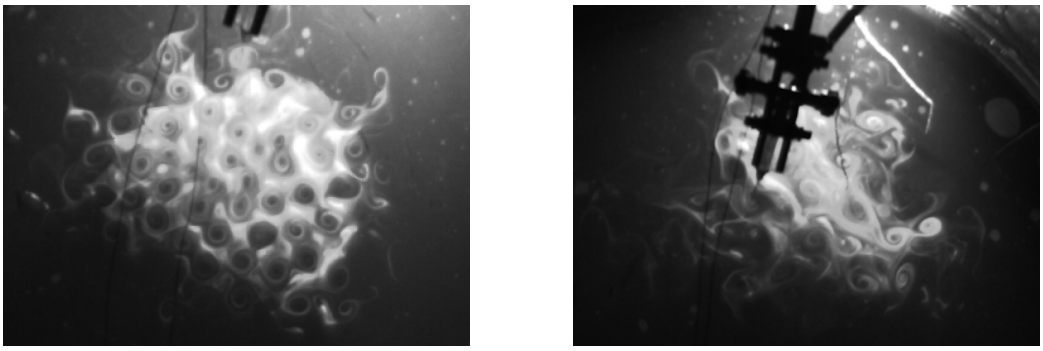

(a) Regular cell structure. (b) Irregular cell structure.

Fig. 5.24 Illustration of different cell structures.

believe this is due to errors in estimating the Rayleigh number for our experiments based on the temperatures of the base and surface as discussed previously. Future investigations might make more accurate estimations of these values, and further explore the transitions between different states and how the wavelength of the cells varies.

5.4 Discussion

The work described in this chapter was intended to be a series of preliminary experiments to explore whether it is possible to replicate the behaviour seen in the simulations of the preceding chapter in a laboratory setting. As such, many of the results are qualitative in nature and serve mainly to guide future experimental work.

We have seen that it is possible to form large scale vortices using this experimental set-up, but that the flow could transition between a single cyclonic vortex and a dipolar state. We hypothesise that these may be modal solutions that occur in the absence of enforced axial symmetry. In order to explore this idea further it is necessary to gather more results and perform a modal decomposition to examine the contents of the overall structure. It would be interesting to capture the transition between the dipolar and single vortex states and examine this in terms of different modes. One possible explanation is that the growth in asymmetric modes is driven by asymmetries in convection that locally enhance vortex stretching, as suggested by Reasor *et al.* (2000).

We did observe one vortex that resembled our simulations, with fluid spiralling anticyclonically outwards at the upper surface. This flow did not, as far as we could tell, display an eye at the centre, and when we increased the forcing it became unsteady and highly three-dimensional. We note that that a number of the flows we observed displayed asymmetries that could not have existed in our simulations due to the assumption of axial symmetry. This is one of the benefits of performing laboratory experiments.

The main difficulty in performing these experiments accurately is due to the fact that they are highly sensitive to a number of parameters. Perhaps the most significant of these is the temperature gradient that has to be maintained over the depth of the fluid. Since this is a relatively small distance in our experiments (30 mm)

the temperature difference was also quite small ($\approx 1\,^{\circ}\mathrm{C}$). This is comparable to the error in the thermocouples and the accuracy of the heating system, making it difficult to control and giving errors in the estimation of the Reynolds number. If the heating is too low then we fail to generate motion, instead obtaining warm fluid through conduction. If the heating is too high then it results in a highly convective three-dimensional system. The parameter range between these two states was small and difficult to control in our experiment.

To tackle this issue we might consider using a larger tank. This would allow a greater depth of working fluid and hence a larger temperature gradient. An additional advantage to this would be that a larger tank requires faster rotation which would reduce the spin-up time. The characteristic spin-up time, $1/\left(\Omega\sqrt{Ek}\right) = H/\sqrt{\nu\Omega}$ (Davidson, 2013), is currently around 5 minutes. This means that the experiment must be left between 30 and 60 minutes to reach a state of solid body rotation before heating can begin. A larger tank would, however, be more prone to asymmetries which we have already seen affect the experiments.

Though we took care to match the Reynolds number, Ekman number, and aspect ratio of our experiments to the simulations as best we could, the one parameter we had little control over was the Prandtl number. Since this is a material property there is little that can be done to influence it besides changing the working fluid, and the value for water is an order of magnitude different from that used in the simulations. Though the work of Oruba *et al.* (2018) suggests that the influence of Pr on eye formation is relatively weak, they do not explore this far. Future work might make use of simulations to explore the influence of much larger Pr and understand how the system will behave with water as a working fluid. It is worth noting that simply using a different liquid for the working fluid would be a challenge because any that match the desired parameters tend to be rather exotic and tightly controlled, for example liquid metals or Benzene. As an alternative one might explore using a gas as the working fluid since they typically have Prandtl numbers closer to 0.1. However, due to the reasons already discussed in section 5.2 we believe a liquid is still the most practical approach.

A final implication from our investigations was highlighting the importance of the lower boundary condition. Though we tried using a base plate to limit conduction, we were not able to evaluate how successful this was. It is clear

that there were limitations, however, since strongly heated experiments displayed three-dimensional convection reminiscent of a constant temperature boundary. In order to better evaluate the nature of the thermal boundary condition, future experiments might make use of heat flux sensors installed on the lower boundary. It might also be worth considering a different method of heating. It would be better to re-design the system to provide heat across the entire base. Alternatively we might explore electric heating. This would simplify the experiment by no longer requiring refrigerant to be exchanged between the inertial and rotating frames. It could also provide better control over the Reynolds number by using a feedback loop connected to the thermocouples. It might also be worth exploring the possibility of approximating a constant heat flux condition through the use of multiple separate electric heating elements, though this approach entails numerous practical difficulties as discussed.

In terms of improving the measurements taken during the experiment, the main issue we experienced was the inability to perform measurements at the bottom of the tank due to the thermal insulation interfering with the light sheet. It would have been extremely useful to examine the lower layers using PIV measurements and any future experiment design should ensure that this is possible. Another development to the PIV measurements might be to make use of a laser lighting sheet as was done by Sukhanovskii *et al.* (2016*b*). The LED annulus provides a sheet whose thickness is large relative to the depth of the fluid. A future study might also wish to use multiple light sheets, rather than just the one available during our experiments. This would allow the entire depth of each run to be imaged, rather than being restricted to a single plane each time. Such an arrangement is described in Marshall & Read (2018).

Another improvement to the PIV system would be the ability to image the poloidal plane. This would be the best way to understand the internal structure of the flow, and be useful in a system with secondary flow. We attempted this in our experiments by shining collimated light from the side, but found the curved surface of the tank caused significant dispersion of the beam. It would be better to illuminate the flow from above in a similar manner to Sukhanovskii *et al.* (2016*b*). A similar effect is observed when imaging from the side of the tank. The curved surface significantly distorts the image away from the centre due to refraction. A

common approach to overcome this is to insert the cylindrical tank into a square one, and fill the space between the two with water. Since water has a similar refractive index to perspex there is negligible distortion to the image.

The practical implications from our experiments are just as important as any of the scientific results. Since the investigations were performed over a short period of time using pre-existing apparatus they were not expected to produce highly accurate results. Instead they were intended to be a preliminary study examining if it might be possible to explore the model presented in chapter 4 in the laboratory. We have shown that it is possible to generate large scale vortices, some of which resemble the flow in our simulations. As a result of these investigations we have highlighted a number of improvements that could be made in the design of any future experiment. The overall conclusion is that the early results are promising, and that it is worth studying this phenomenon in the laboratory in the future. To do so, however, one would need to invest in an improved set-up and pay particular attention to the implementation of the lower thermal boundary condition.

5.5 Summary and outlook

In this chapter we described a series of laboratory experiments intended to examine the possibility of replicating our simulations. We have shown that it is possible to build a laboratory experiment that is similar to the model used in our simulations. Furthermore, we found that it is possible to generate large scale vortices using this set-up, some of which bear a closer resemblance to our simulations than others. With further work to explore the parameter space more thoroughly, taking more time to repeat experiments and perfect techniques, it should be possible to narrow down and reproduce the more promising experiments reported here. In addition there are a number of suggestions we can make to improve future experiments. These have been summarised below.

Unfortunately none of our experiments displayed an eye at the centre of the vortex so we made little progress in answering the questions raised at the start of this chapter. We do not believe that it is impossible to perform this experiment, but it certainly requires further work. We believe that the main issue at present relates to the difficulty of enforcing a fixed flux boundary condition which is critical to the

development of the vortex. With more work we hope that the experiment would be able to reliably generate a vortex in which the possibility of generating an eye can be explored and the internal structures studied in more depth.

In addition to investigating the model of chapter 4, we also performed some experiments outside of this parameter regime that displayed rotating cellular convection. This is an interesting topic with much theoretical work performed by Chandrasekhar and Veronis, but relatively few examples of the phenomenon being observed in the laboratory. Our imaging with fluorescein shows not only the hexagonal lattice of cells, but also the path taken by the fluid within cells. We see how the fluid rises upwards at the centre of the cells following an anticyclonic helical path radially outwards at the top. It is nice to have clear visualisations that can be compared to the theoretical descriptions. We made calculations of criticality for the experiments, but believe there to be significant errors in these estimations at present.

These experiments were intended to be a short series of investigations to investigate laboratory experiments as an avenue of research into eye formation. A large amount of time was spent developing and learning to use the apparatus. It is hoped that the work described here might inspire future investigations that build upon our work and spend time fine-tuning the parameter regime to yield results.

5.5.1 Suggestions for future experimental work

A number of recommendations were made for future experiments as a result of our preliminary study. These are detailed above in our discussion but can be summarised as follows:

- Development of the lower boundary heating to provide a better approximation to constant flux.
- Development of the flow visualisation and PIV set-up to capture more of the flow, in particular the poloidal plane.
- Numerical investigation into the influence of large Prandtl number on eye formation.

In light of the results from our investigations, we suggest that future experiments might focus on:

- Repeatable generation a large-scale cyclonic vortex.
- Performing modal decomposition to examine the flow structure and characterise azimuthal asymmetries.
- Imaging the poloidal plane of the experiment as well as horizontal planes down to the boundary layer.
- Exploring eye formation in a large-scale cyclonic vortex.

Chapter 6

The evolution of laminar thermals

In this chapter we investigate the development of laminar thermals. We begin (section 6.1) with an overview of thermals in the atmosphere and the motivation for this study. We discuss work by previous authors looking at the development of thermals, both laminar and turbulent, noting that there are gaps in our understanding that we might seek to fill. In particular, we note the opportunity to provide a mathematical framework for the entire life cycle, rather than examining each stage separately. Such a framework is developed in section 6.2.

We present a series of numerical simulations of axisymmetric, isolated, laminar thermals that develop from buoyant blobs. We find that, as time progresses, the thermals transition through a number of distinct stages, undergoing several morphological changes before ending up as a vortex ring. We discuss this life cycle in sections 6.4 - 6.8, starting with an overview before taking a closer look at the key stages; buoyant blob, mushroom cap, and buoyant vortex ring. We also discuss how successive vortex rings may form from the wake of the first.

In section 6.9 we examine the effect of Reynolds and Prandtl number, finding that viscous effects are relatively unimportant at early times, but that thermal diffusion can have a significant impact on development. We show that the early stages of development are key in determining the final properties of the ring, with rings consistently containing the same proportion of the initial heat and having a consistent vorticity flux. The key findings of the study are then summarised in section 6.10.

The work of this chapter appears, in a reduced form, in Atkinson & Davidson (2019).

6.1 Introduction

The evolution of isolated patches of buoyant fluid is, on the surface, a relatively simple problem in fluid mechanics, yet it turns out to be more complex than might at first be thought. Parcels of fluid that move and evolve relative to their environment under the action of the buoyancy force are often known as thermals, a name taken from the atmospheric phenomenon exploited by birds and glider pilots (Scorer, 1978) but also used to describe a wider range of buoyant phenomena.

Atmospheric thermals of the kind used for gliding develop as a result of concentrated low-level heating. This can be from natural sources, the most common example being solar heating, or man-made, for example cities or factories. The general approach adopted by both birds and pilots upon identifying a thermal is to fly into the rising air. Once they enter the thermal they fly around in circles, staying within the rising air and being lifted to a greater height. Rise velocities can vary depending on conditions, but are typically several metres per second. Once they reach the top of the thermal birds and pilots exit, beginning a slow descent and looking for the next thermal by which they may continue their journey. This method of flying is illustrated in figure 6.1 and is incredibly energy efficient.

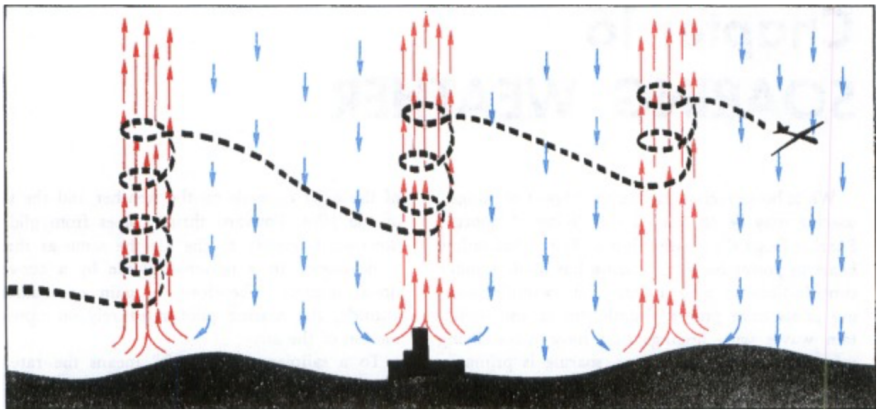

Fig. 6.1 The gliding process, from FAA & NOAA (1975)

Pilots are trained to look for subtle signs of thermal activity on the ground such as colour changes due to temperature, topographic features that may actively promote thermal formation, and the motion of dust or vegetation indicating the convergence of air. To the untrained eye, however, the effect of atmospheric thermals can most easily be seen in the form of cumulus clouds, such as those in figures 6.2a and 6.2b. As warm air near the ground rises its temperature drops following the lapse rate. As it continues to rise, the temperature of the air eventually falls below the dew point causing water vapour to condense, becoming visible as a cumulus cloud. As it condenses, latent heat is released from the water vapour. This, in turn, drives further convection causing the thermal to continue ascending, in some cases to form a towering cumulus (cumulus congestus) formation such as those in figures 6.2c and 6.2d. The tower of cloud traces the path of the thermal as it ascends above the dew point.

In some cases, when there is much moist convection and sufficient atmospheric instability, cumulus clouds may develop further into cumulonimbus and rise even higher. These may be cumulonimbus calvus (figure 6.2e) or, in regions of deep moist convection, cumulonimbus incus that rise to the tropopause to form distinctive anvil tops (figure 6.2f). Cumulonimbus formations are often accompanied by storms and may give rise to other atmospheric phenomena such as waterspouts. Of course, by the time we reach this stage we have left behind the notion of an isolated patch of buoyant fluid for processes that occur on a much larger scale in regions of deep convection.

Returning to the activities of gliders, they separate thermals into two forms, as illustrated in figure 6.3 which is taken from the Aviation Weather Handbook (FAA & NOAA, 1975). 6.3a shows what is known as a thermal column or 'chimney', but would be more familiar to fluid dynamicists as a plume. Here air is continuously heated at the ground and rises upwards in a steady stream. Sometimes, when heating is slow or intermittent, the rising warm air may be pinched off to form what pilots refer to as a 'bubble' thermal. This isolated patch of buoyant fluid is what fluid dynamicists would refer to as a thermal. Figure 6.3c shows the theorised structure of a bubble thermal. As it ascends the parcel of air wraps up into a turbulent vortex ring with air rising fastest at the centre surrounded by a downdraft.

(a) Fair weather cumulus.
Ralph Kresge, NOAA

(b) Cumulus on the Colorado Plateau.
Sean Linehan, NOAA

(c) Towering cumulus.
James Lee, NOAA

(d) Towering cumulus, West Virginia.
Janet Ward, NOAA

(e) Cumulonimbus calvus over Connecticut.
Versageek

(f) Cumulonimbus incus with distinctive anvil top.
Hussein Kefel

Fig. 6.2 A variety of cloud types associated with thermals and moist convection.

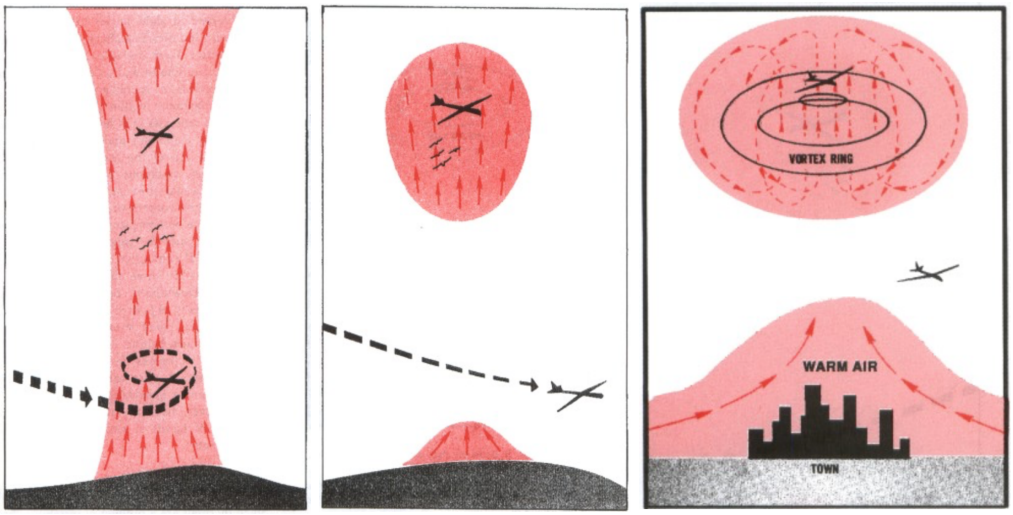

(a) Chimney thermal (b) Bubble thermal (c) Vortex ring structure of a developed bubble thermal

Fig. 6.3 Illustrations of thermals for gliding from FAA & NOAA (1975)

The importance of understanding these flows was recognised by Scorer (1957) who performed a series of experiments to characterise turbulent thermals. By tipping dense sodium sulphate solution into fresh water he was able to observe how thermals grew in size for different values of buoyancy. Under the Boussinesq approximation the motion of negatively buoyant fluid is the mirror image of that of positively buoyant fluid with the same absolute value of buoyancy. As a result it is possible to conduct experiments 'upside-down' and reach the same conclusions using dense, sinking fluid instead of light, rising fluid. This is a popular choice amongst experimentalists since it is far easier to constrain and release dense material at the top of a tank than light fluid at the base. Scorer's experiments provide support for an axisymmetric model that predicts a turbulent mass of buoyant fluid will have cap-height h and radius R scaling in time as $h \sim R \sim t^{1/2}$. Some comparisons are made to towering cumulus formations in the atmosphere, but it is noted that the model does not include the effects of latent heat release that generate additional buoyancy as the thermal rises. The work does, however, qualitatively replicate the behaviour seen in the atmosphere to provide an understanding of the physical effects that influence thermal motion.

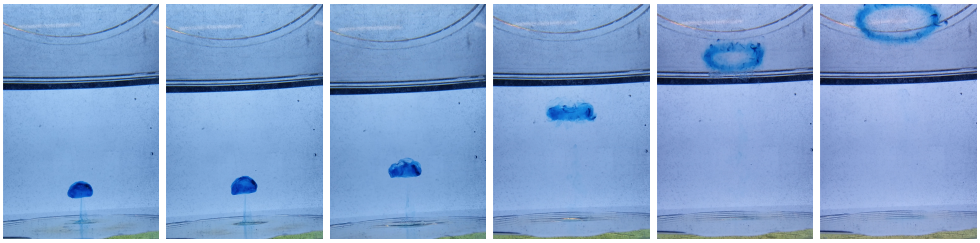

Fig. 6.4 Laboratory observations of a laminar thermal.

It is worth noting that at the end of his study Scorer mentions the work of Turner (1957) on buoyant vortex rings. It had long been theorised that turbulent thermals in the atmosphere develop a vortex ring-like structure, and the late stages of Scorer's experiments lend support to this. He observes that thermals become 'hollowed out' by exterior fluid, with velocities around the cap being reminiscent of a vortex ring-like structure. A brief but important comment by Scorer that we shall return to at length during our study of laminar thermals is that the circulation, or vorticity flux, of a thermal can only increase when there is buoyant material on the symmetry axis.

This early work by Scorer has been extensively built upon with further investigations, simulations, and models being developed for turbulent thermals and cloud formations. The laminar analogue is somewhat less well studied however. An early description of the phenomenon can be found in *On Growth and Form* by D'Arcy Thompson (1961) with a buoyant blob of fluid being the start of a 'long story' that is 'deserving to be considered'. He describes an array of 'beautiful vorticoid configurations' as the phenomenon develops, noting its resemblance to the medusa or jellyfish. This behaviour is illustrated in figure 6.4 which shows an experiment conducted as part of this study. The experiment is similar to that of Sànchez *et al.* (1989), where a dyed buoyant thermal is released into fresh water. Following release, the thermal has developed into a mushroom cap with a wake which subsequently detaches. The cap then wraps up into a buoyant vortex ring.

Further inspiration might be drawn from another geophysical phenomenon; volcanic vortex rings. These have been observed for many years at locations all over the Earth. The most extensive records are for the volcanoes Etna and Vesuvius in Italy, where the emission of rings has been recorded in literature since at least

1724, as summarised by Fuentes (2014). An early description of the phenomenon can be found in della Torre (1755) from which the image in figure 6.5a is taken. This shows Vesuvius from the town of Boscotrecase (now part of Naples), 6 km to the southeast of the crater. The Neapolitan professor of physics describes the rings, noting that *'To the sight they seemed to rise twice as high as the mountain is from Atrio. They were of a very white colour, and they were made of a matter so dense and persistent that there was one that stayed in the air for more than one quarter of an hour, and another one that stayed more than three. They disappeared very slowly as the matter forming them rarefied and diluted.'* Figure 6.5b shows a photo of such a ring taken at Mount Etna. The ascending ring of buoyant material is made visible against the sky by smoke and steam in its core.

Early efforts to explain this phenomenon (Capocci, 1846) centred around the ejection of buoyant material from an orifice in a similar manner to the rings of Turner (1957). As a result it was hypothesised that the rings resulted from the rapid pulsation of gas from narrow vents. There is a great deal of sensitivity to orifice shape and ejection velocity for stable ring formation to occur in this way however. Due to a lack of observations at the point of formation for volcanic rings there is still no clear consensus on how they form (Whitehouse, 2000). It is clear that they must be composed of buoyant material, since they expand radially as they ascend, and we note that the ring of figure 6.5b bears a close resemblance to late stages of the experiment in figure 6.4. Could it be that these rings form from parcels of buoyant air ejected from the volcano without the need for a suitably shaped orifice or starting impulse? A description that might give us reason to at least consider this theory can be found in the autobiography of Charles Babbage (1864) who observed volcanic rings whilst visiting Vesuvius in 1828. He recounts *'The situation of my apartments during my residence at Naples enabled me constantly to see the cone of Vesuvius, and the continual projections of matter from its crater. Amongst these were occasionally certain globes of air, or of some gas, which, being shot upwards to a great height above the cone, spread out into huge coronets of smoke, having a singular motion amongst their particles.'* Could these 'globes' be similar to the starting buoyant blob of figure 6.4 that wraps up into a ring?

Motivated by what lies beneath volcanoes, Griffiths (1986) investigated the development of thermals in high viscosity fluids in an effort to understand motions

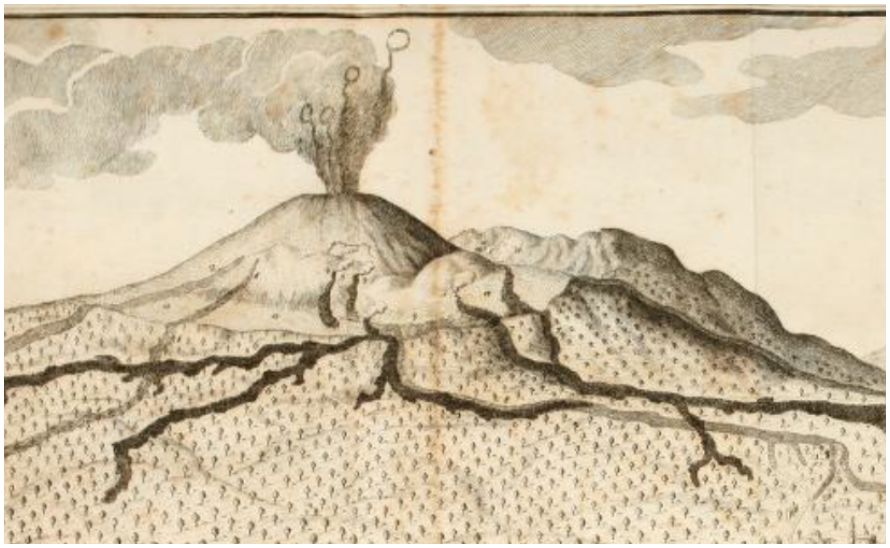

(a) Sketch of rings over Vesuvius
From della Torre (1755) digitized by The Getty Research Institute and made available through www.archive.org.

(b) Ring above Mount Etna
Angelo Salemi

Fig. 6.5 Volcanic vortex rings

in the mantle. He observed that the thermals formed a cap, sometimes developing further into what he called a 'toroidal chemical ring'. The existence of distinct stages of development is apparent from these observations, but a detailed examination of the different structures and clear explanations for their formation is not readily available. Shlien & Thompson (1975) and Shlien (1976) performed experiments with heat injection at a point, and observed the development of a thermal from a point source that starts to accelerate, develops into a cap-like structure, and then into a buoyant vortex ring. They note these key stages of development, but their experiments are limited in that they only observe the temperature field through shadowgraph data. Their discussion of the cap is brief, simply noting that the thermal transitions through this stage en route to forming a buoyant vortex ring. Their observations of the ring match well the theory of Turner (1957). Aside from these studies, the different stages in the life cycle of a laminar thermal are more frequently studied as separate phenomena in their own right. To the best of our knowledge, no-one has yet treated the blob, cap, and ring as different stages of the same process and tried to link their development.

A model for the mushroom-like cap that develops from a buoyant disturbance is presented by Davidson *et al.* (2007). They make predictions about how the structure and velocities of the cap will develop, but without any comparison to experiments or simulations. As a result they do not make any observations about how the cap develops into a ring, and note an apparent paradox in their model in that the cap velocity tends towards a constant value whilst the total axial impulse of the fluid continues to grow linearly in time.

Gharib *et al.* (1998) performed experiments on non-buoyant vortex rings generated using an impulsive piston. They propose the existence of a universal timescale for the pinch off of the vortex ring from the trailing wake. At long times the vorticity flux of the ring is constant, and equal to that of the entire domain at an earlier time t. When t is made into a dimensionless property t^* it is found to be independent of the strength of the impulse generated by the piston. This is rationalised by arguing that a stable vortex ring represents a maximum in energy subject to a given impulse and vorticity flux. As a result, a critical non-dimensional energy can be calculated for the vortex ring. Gharib *et al.* suggest that once the developing flow from the piston drops below this critical value the ring pinches off from the developing wake

to move away as a stable vortex ring. This theory is debated by Linden & Turner (2001), however, who present an alternative explanation for the observations. Assuming that the properties impulse, vorticity flux, and energy are conserved during the transformation from ejected fluid into a ring, they perform a matching to the Norbury (1973) family of vortex rings. Their results show that the formation time t^* resulting from maximising the vorticity flux of the ring for a given energy could in fact be much higher than the values observed by Gharib *et al.*. Linden & Turner show instead that a volume constraint (that all ejected fluid is contained within the core of the ring) imposes a value of t^* close to that observed in the experiments. The analysis is independent of the formation process and they note that, for the Reynolds numbers considered, viscous effects have little time to act during this stage.

We have performed numerical simulations of laminar thermals and observed an interesting life cycle in which a buoyant perturbation develops, via an initial transient, into a mushroom-like cap structure, and then into a buoyant vortex ring. This behaviour was illustrated in figure 6.4. The primary purpose of this study is to characterise the entire life cycle of a laminar thermal, from its initiation and development into a mushroom-like cap, through to the separation of a buoyant vortex ring at the front and the development of the resulting wake. One surprising finding is that the wake can itself roll up to form a secondary vortex ring.

6.2 Development of a mathematical framework

Consider an axisymmetric, incompressible, Boussinesq fluid where the kinematic viscosity, ν, and thermal diffusivity, α, are both assumed independent of temperature. The governing equations for this system are given in section 2.2. The absence of rotation in equation (2.23) gives the following equation for the evolution of azimuthal vorticity,

$$\frac{\mathrm{D}}{\mathrm{D}t}\left(\frac{\omega_\phi}{r}\right) = -\frac{\mathrm{g}\beta}{r}\frac{\partial\theta}{\partial r} + \nu\frac{1}{r^2}\nabla_*^2\left(r\omega_\phi\right) \ , \tag{6.1}$$

which we note can be re-written as,

$$\frac{\mathrm{D}}{\mathrm{D}t}\left(\frac{1}{2}r\omega_\phi\right) = \mathrm{g}\beta\theta + \nabla\cdot\mathbf{F} + \frac{1}{2}\nu\nabla_*^2\left(r\omega_\phi\right) \ , \tag{6.2}$$

where the flux $\mathbf{F}$ is given by

$$\mathbf{F} = \frac{1}{2}\left(u_r^2 - u_z^2\right)\hat{\mathbf{e}}_\mathbf{z} - u_r u_z\hat{\mathbf{e}}_\mathbf{r} - \frac{1}{2}\mathrm{g}\beta\theta r\hat{\mathbf{e}}_\mathbf{r} \ . \tag{6.3}$$

It follows from equations (6.1) and (6.2) that, for a localised disturbance (see Davidson *et al.* (2007)),

$$\frac{\mathrm{d}}{\mathrm{d}t}\int_{V_\infty}\left(\frac{\omega_\phi}{r}\right)\mathrm{d}V = 2\pi\mathrm{g}\beta\int_{-\infty}^{\infty}\theta_{r=0}\,\mathrm{d}z + 4\pi\nu\int_{-\infty}^{\infty}\left(\frac{\omega_\phi}{r}\right)_{r=0}\mathrm{d}z \ , \tag{6.4}$$

and

$$\frac{\mathrm{d}}{\mathrm{d}t}\int_{V_\infty}\frac{1}{2}r\omega_\phi\,\mathrm{d}V = \int_{V_\infty}g\beta\theta\,\mathrm{d}V \ , \tag{6.5}$$

for an infinite domain, V_∞, with the fluid at rest and $\theta = 0$ in the far field. Note that the buoyant growth of the integral of ω_ϕ/r in equation (6.4) depends only upon the centreline temperature. Equations (6.4) and (6.5) can be related to more familiar properties of the flow through the following expressions:

$$\Phi = \frac{1}{2\pi}\int_{V_\infty}\frac{\omega_\phi}{r}\,\mathrm{d}V \ , \tag{6.6}$$

where Φ is the flux of azimuthal vorticity (or circulation) in the axisymmetric system, and

$$\mathbf{L} = \int_{V_\infty} \frac{1}{2} r\omega_\phi \, \mathrm{d}V \, \hat{\mathbf{e}}_\mathbf{z} = \frac{1}{2} \int_{V_\infty} (\mathbf{x} \times \boldsymbol{\omega}) \, \mathrm{d}V \, , \tag{6.7}$$

where the integral on the right is the net linear impulse of the fluid in an infinite domain ($\mathbf{x}$ being a position vector). The property $\mathbf{L}$ can be related to the net linear momentum according to $\mathbf{L} = \int \mathbf{u} \, \mathrm{d}V$ (Saffman, 1992). Note that, since the temperature equation (2.9) requires $\int T \mathrm{d}V$ = constant across the domain, (6.5) implies a linear growth in $\mathbf{L}$,

$$|\mathbf{L}| = t \int_{V_\infty} \mathrm{g}\beta\theta \, \mathrm{d}V \, . \tag{6.8}$$

Note also that, when the viscous term is weak in (6.4), it is well approximated by

$$\frac{\mathrm{d}\Phi}{\mathrm{d}t} = \mathrm{g}\beta \int_{-\infty}^{\infty} \theta_{r=0} \, \mathrm{d}z \, . \tag{6.9}$$

Dimensional analysis can be performed using some characteristic length scale and temperature for the thermal, say l and $\hat{\theta}$ respectively, based upon the initial condition as discussed below (equation 6.14). There are two dimensionless groups that define the problem, a Reynolds number Re, and a Prandtl number Pr,

$$Re = \frac{Ul}{\nu} \quad , \quad Pr = \frac{\nu}{\alpha} \, , \tag{6.10}$$

where U is the velocity scale

$$U = \sqrt{\mathrm{g}\beta\hat{\theta}l} \, . \tag{6.11}$$

In addition to these dimensionless groups, a characteristic timescale, impulse, and vorticity flux for the problem can be defined as,

$$t_0 = \frac{l}{U} \quad , \quad L_0 = Ul^3 \quad , \quad \Phi_0 = Ul \, . \tag{6.12}$$

We shall use these to non-dimensionalise quantities, with $\tau = t/t_0$ being dimensionless time.

We also introduce the non-dimensional variable,

$$\gamma = \frac{l^2 \Phi}{|\mathbf{L}|}\,, \tag{6.13}$$

as a diagnostic for the flow. Mathematically this is a dimensionless ratio of the zeroth and second moments of the vorticity field. It tells us about the relative compactness of the vorticity distribution around the axis; the more spread out the vorticity is, the smaller the value of γ. This is because both L and Φ are integrals of vorticity, but are weighted differently by factors of r. The more compact the vorticity distribution the larger the value of Φ and the smaller the value of L.

6.3 Numerical investigations

We performed a series of numerical investigations using our axisymmetric finite-difference code. The domain is large relative to the size of the thermal, with a radius of $R = 14\,l$, and a height of $H = 80\,l$, where l is a characteristic lengthscale of the thermal).

The boundary conditions on the domain are no-slip and adiabatic. Simulations were performed using a mesh of at least 4000 axial $\times$ 350 radial cells, with a finer resolution near the axis than at the edges. Spatial and temporal resolution studies were performed by increasing and decreasing both the mesh resolution and timestep and ensuring that the results were converged.

We use the same initial condition as Davidson *et al.* (2007) with $\mathbf{u} = 0$ and a Gaussian temperature perturbation of the form

$$\theta = \hat{\theta} \exp\left(-\frac{r^2 + z^2}{l^2}\right) \tag{6.14}$$

in an ambient background $\theta = 0$. The location of the Gaussian blob is $r = 0$ and $z = H/10$ above the bottom of the domain.

A range of cases for different Re and Pr were examined, details of which are given in table 6.1. They cover a range of Reynolds numbers with the Prandtl number fixed at 1.0, but also include some variation in Prandtl number for a Reynolds number of 225.8.

Simulation	Re	Pr
1	71.0	1.0
2	124.8	1.0
3	175.2	1.0
4	200.4	1.0
5	225.8	1.0
6	331.9	1.0
7	504.9	1.0
8	712.6	1.0
9	225.8	2.0
10	225.8	0.1
11	225.8	0.5
12	225.8	0.75

Table 6.1 Details of thermal simulations

6.4 An overview of the life cycle

The laminar thermal passes through a number of phases during its life cycle. These can be summarised as the buoyant blob, the mushroom-like cap, and the buoyant vortex ring, each of which will be discussed in detail shortly. To illustrate these stages we take a typical simulation at $Re = 225.8$ and $Pr = 1$. As we shall see, for this simulation a blob is maintained in the time range $\tau = 0$ - 4, the cap for approximately $\tau = 7$ - 17, and the ring from $\tau = 23$ onwards.

There are a number of key events in the life cycle that characterise each of the stages, and the transitions between them. These are illustrated below, and can be described as follows. First, vorticity is generated by radial temperature gradients. This results in a Gaussian distribution of ω_ϕ/r developing immediately following initiation. Both the vorticity and temperature fields are shown in figure 6.6a. This Gaussian distribution is relatively short lived, however, as the blob begins to lift under the action of buoyancy forces. The effect of this is greatest at the centre of the buoyant blob, as can be seen in figure 6.6b. The temperature field is advected with the fluid, as is ω_ϕ/r, although ω_ϕ/r continues to be generated by radial temperature gradients.

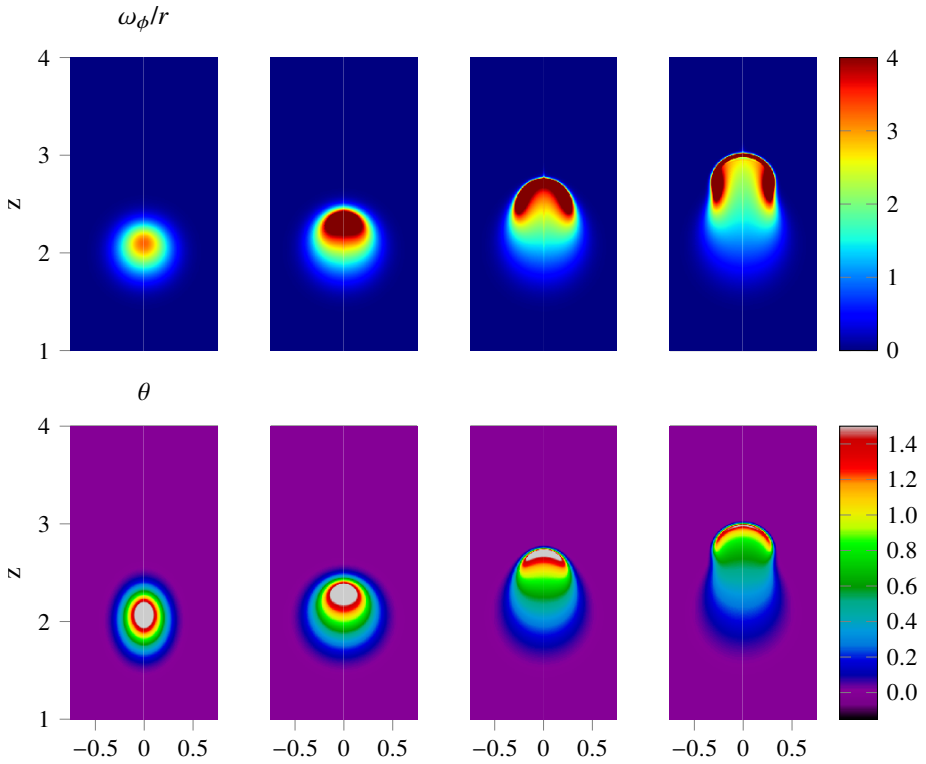

(a) $\tau = 1.0$ (b) 2.1 (c) 3.5 (d) 4.5

Fig. 6.6 Early stages in the development of a thermal. Contours of ω_ϕ/r (top) and temperature (bottom) at different dimensionless times τ.

As the blob continues to lift, it enters a stage of significant distortion, with cooler fluid being swept in from the rear. The faster moving fluid near the axis advects the temperature and ω_ϕ/r upward into a rapidly thinning front at the leading edge of the blob. This can be seen in figures 6.6c and 6.6d from τ = 3.5 - 4.5. In addition to this thinning front, the higher temperature fluid is also displaced radially outwards into a cylindrical annulus, carrying with it vorticity. This is illustrated in figure 6.6d, and marks the end of the buoyant blob and transition towards the mushroom cap.

This transition from blob to mushroom-like cap is characterised by the roll-up at the sides of the thermal taking place from τ = 5.0 - 7.0. The vorticity that has been displaced radially outwards in a concentrated annulus below the front induces a rotational motion and begins to wrap up on itself, as shown in figure 6.7a, to form the lobes that will eventually become the buoyant vortex ring. The induced motion of this vorticity field sweeps fluid upwards at the centre of the thermal and radially outwards at the front, causing the front to thin at an ever increasing rate as predicted by Davidson *et al.* (2007).

The mushroom cap is established by figure 6.7b, τ = 7.0. The thermal continues to entrain fluid at the rear, increasing its volume and stretching the front further to a point at which it pinches apart at the axis. As can be seen by comparing the upper images of figures 6.7b and 6.7c, this occurs between τ = 7.0 and τ = 8.5, with further investigation showing it to be around τ = 8.0. This is the first of several morphological changes. It can be seen in figure 6.7c that once punctured this thin front is rapidly swept up into the lobes of vorticity. Below the mushroom cap a warm wake forms where the thermal has passed through. Although cooler than the cap, high radial gradients in temperature define a sharp edge to this region generating new vorticity that forms trailing tendrils below the cap. These can be seen developing in figures 6.8c and 6.8d.

Up until the formation of the cap, the thermal has been accelerating from its starting position as we will show shortly. Once the mushroom cap has been achieved, however, the acceleration falls and the cap tends towards a constant velocity, u, as predicted by Davidson *et al.* (2007). Fluid continues to be entrained at the base of the cap as the vorticity in the lobes induces a flow radially inwards and up along the axis. As a result of this motion the trailing tendrils of vorticity

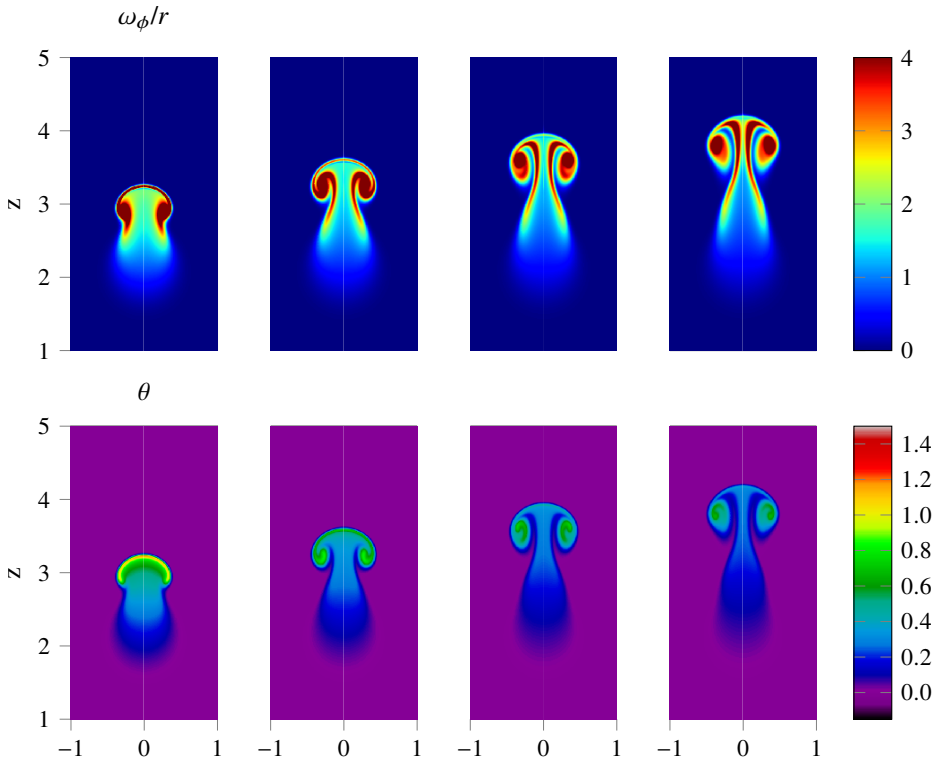

(a) τ = 5.5 (b) 7.1 (c) 8.5 (d) 9.5

Fig. 6.7 Intermediate stages in the development of a thermal. Contours of ω_ϕ/r (top) and temperature (bottom) at different dimensionless times τ.

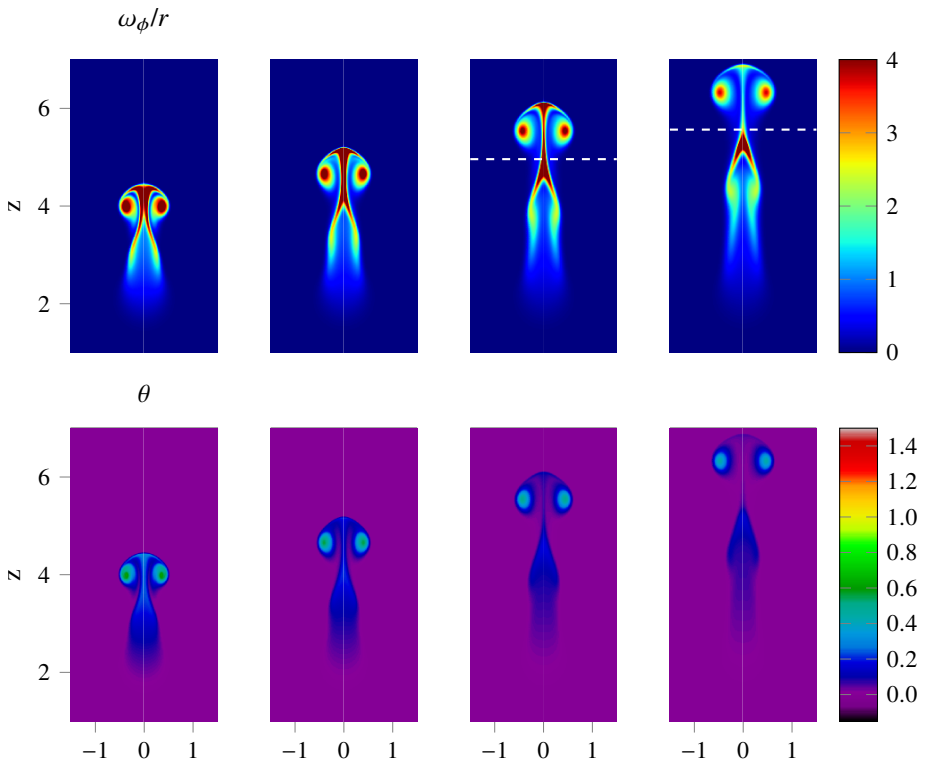

(a) τ = 10.5 (b) 13.5 (c) 17.4 (d) 21.0

Fig. 6.8 Later stages in the development of a thermal. Contours of ω_ϕ/r (top) and temperature (bottom) at different dimensionless times τ.

are swept inwards towards the axis and stretched vertically resulting in necking that can be seen developing in figure 6.8b. Eventually this reaches a point where the stem of vorticity connecting the cap to the wake becomes sufficiently weak, as illustrated in figure 6.8d, that we can consider two distinct regions of flow; the buoyant vortex ring and the wake. This transition process is illustrated in figures 6.8b to 6.8d and marks the second morphological change. The upper part of the stem, which is connected to the cap, is swept upwards and out along the front of the cap to eventually become wrapped up in the buoyant vortex ring. As a result, the cap shape is preserved until around $\tau = 17.0$. Beyond this point the vast majority of the vorticity has been swept up in the ring and it can now be regarded as a separate region of flow moving off ahead of the wake. The lower portion of the trailing vorticity stem is subsumed by the wake, and begins to display qualitative similarities to the developing thermal of figure 6.6d. Indeed, we find that after a period of time the wake can evolve in a similar way to the initial thermal and produce a second mushroom-like cap that separates in the same way to form a secondary vortex ring. The early stages of this behaviour can be seen in figure 6.9 and will be discussed in section 6.8.

There are a number of quantities of interest that can be observed over the course of this cycle. Plotted in figures 6.10 and 6.11 are the impulse L and flux Φ for the entire flow, and also individually for the ring and wake. This was achieved by splitting the domain into two regions with the mushroom cap or ring contained within the upper one and the wake below. This is indicated in figures 6.8 and 6.9 by the white dashed lines. (The white lines indicate the minimum in $\int \omega_\theta \, \mathrm{d}r$ as a function of z as a way of distinguishing the two parts.) It can be seen from figure 6.10 that the impulse for the overall flow increases linearly in time, consistent with (6.8), as does the impulse of both the cap-come-ring and the wake. Figure 6.11 shows that the vorticity flux of the overall flow increases monotonically, but the rate of increase slows as hotter fluid is swept away from the axis. This is consistent with equation (6.9). The flux of the cap attains a constant value as the buoyant ring is formed. The dimensionless parameter γ can be calculated and is plotted in figure 6.12. It can be seen that γ for the entire flow initially begins to fall at an increasing rate as the blob accelerates before starting to level off as the cap and ring form. Once formed, γ of the cap/ring decreases as τ^{-1}, reflecting the linear

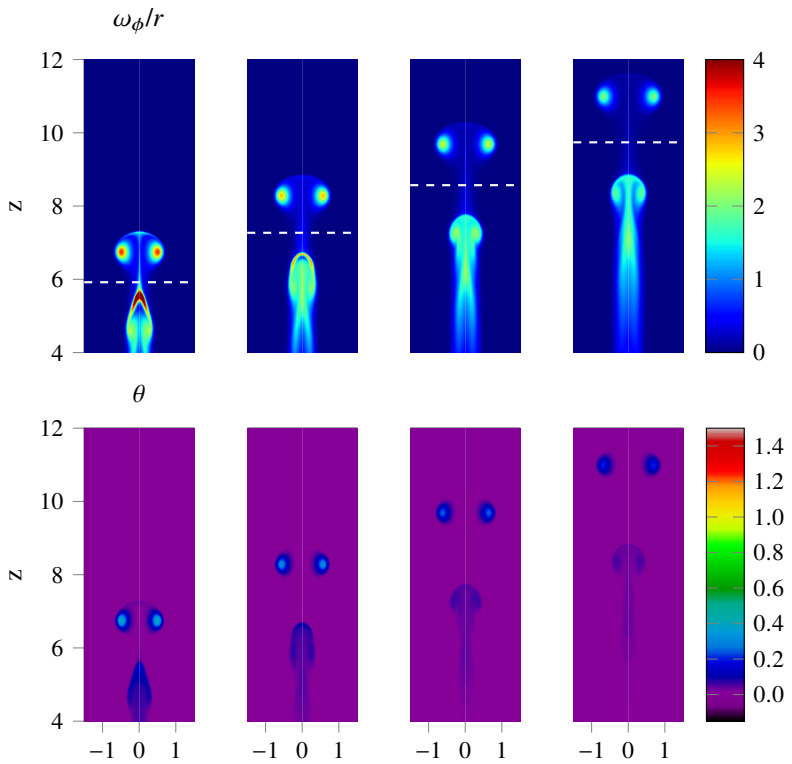

(a) $\tau = 23.1$ (b) 30.8 (c) 38.5 (d) 46.2

Fig. 6.9 Late stages in the development of a thermal. Contours of ω_ϕ/r (top) and temperature (bottom) at different dimensionless times τ.

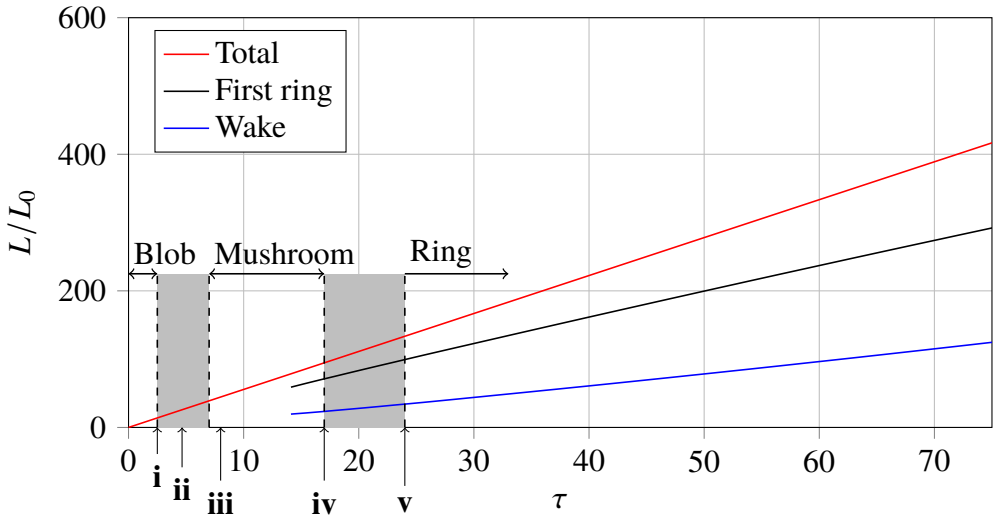

Fig. 6.10 Evolution of impulse for the thermal, the first ring, and the wake. The grey regions denote transition between stages whilst i-iv denote key points in the life cycle as discussed in the text. These are: i the end of constant acceleration and the blob phase, discussed in 6.5 ; ii the inflexion point in γ and beginning of roll-up, discussed in 6.5; iii the pinching apart of the cap front, discussed in 6.6; iv the point at which the ring core becomes stronger than the stem, discussed in 6.6; v the separation of the buoyant ring and wake by necking, discussed in 6.7.2. Note that iii occurs shortly after the beginning of the mushroom cap phase discussed in 6.6. The dashed black line is the total impulse predicted by equation (6.8).

growth in L and constant Φ. γ of the wake initially rises, reaching a maximum as the wake begins to roll up into a second cap around $\tau = 18$, beyond which point it too falls monotonically like the first ring.

Figure 6.13 shows the maximum dimensionless vertical velocity on the axis. It can be seen that the blob initially undergoes a period of constant acceleration until around $\tau = 2.5$. After this the acceleration decreases, with the velocity attaining an approximately constant value from $\tau = 7.0$ - 15.0. This coincides with the mushroom cap phase of the thermal, as predicted by Davidson *et al.* (2007). Beyond this the velocity begins to fall as the thermal transitions into a buoyant vortex ring.

We will now discuss in more detail the different stages of the flow explaining the observations above and examining the transitions between each stage.

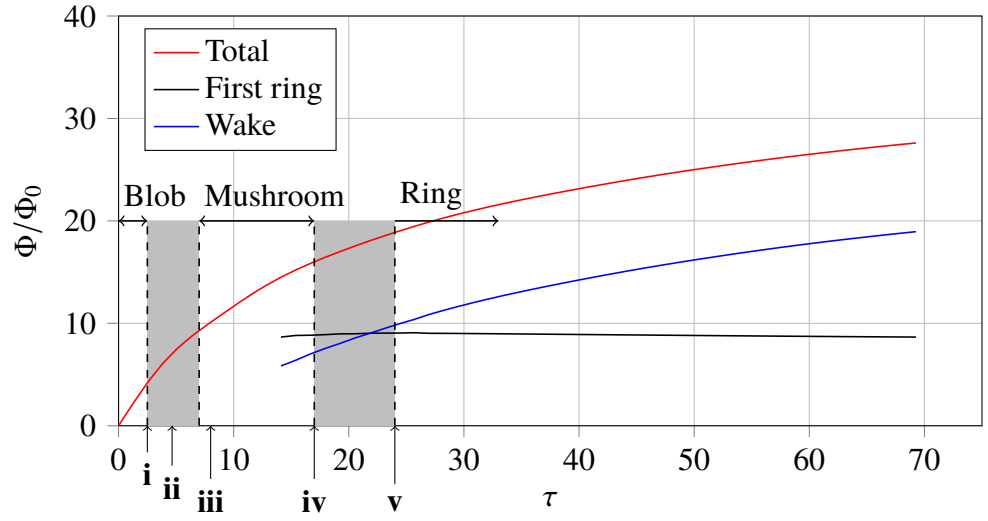

Fig. 6.11 Evolution of flux for the thermal, the first ring, and the wake. Points i-v as for figure 6.10.

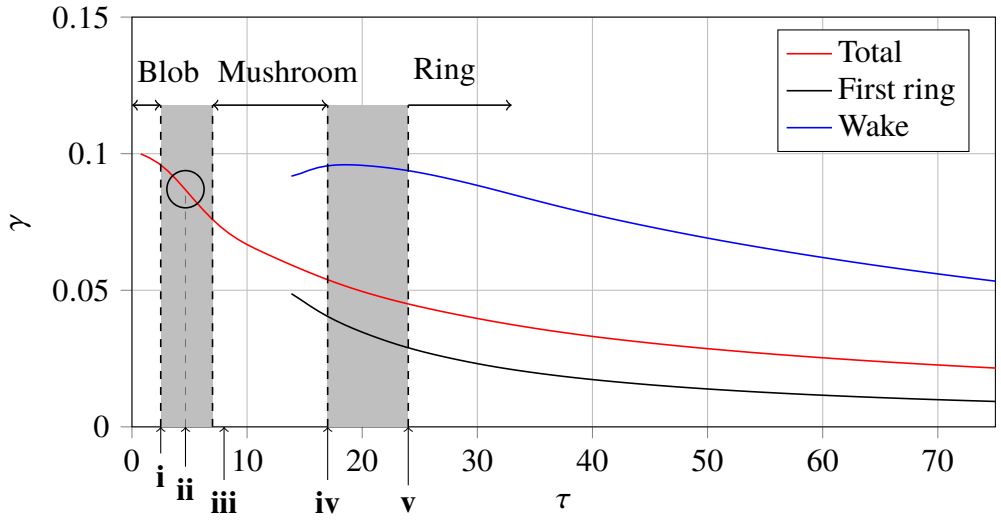

Fig. 6.12 Evolution of γ for the thermal, the first ring, and the wake. Points i-v as for figure 6.10 with the inflexion point (ii) circled.

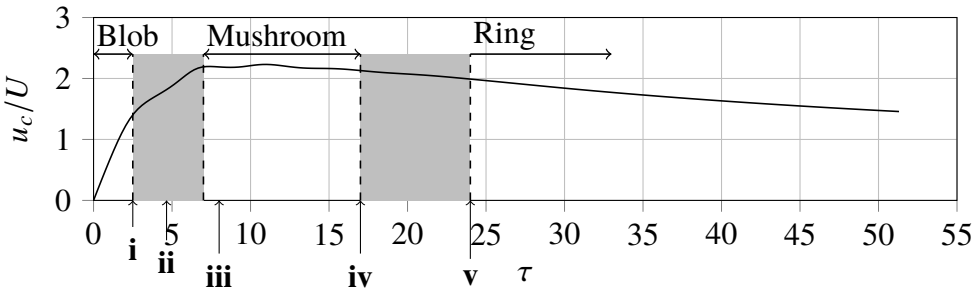

Fig. 6.13 Maximum dimensionless vertical velocity on the z-axis against τ. Points i-v as for figure 6.10.

6.5 Stage 1: The buoyant blob

The first stage in the development of the thermal is take-off of the initial temperature perturbation and compression into a front. Starting with undisturbed fluid, we initially have zero vorticity, ω_ϕ, and no motion. The very first stage, therefore, is vorticity generation by radial temperature gradients (figure 6.6a). Following this, the hottest fluid in the centre of the thermal begins to rise fastest under the action of buoyancy, and the ω_ϕ/r and θ fields are compressed into rapidly thinning fronts (figures 6.6b and 6.6c).

It can be seen from figure 6.13 that the thermal initially undergoes a period of approximately constant acceleration. This was observed experimentally by Shlien (1976) who state that they could offer no simple interpretation for the behaviour. It can be understood, however, by considering the terms in equation (2.18). At $\tau = 0$ there is no fluid motion, and $\mathbf{u}$ remains small for some time. Initially, therefore, there must be a balance between $\partial\mathbf{u}/\partial t$ and $-\mathbf{g}\beta\theta$. Since, in the absence of significant motion, θ evolves only slowly through diffusion, the vertical velocity must increase approximately linearly in time, i.e.constant acceleration. The neglect of $\mathbf{u}\cdot\nabla\mathbf{u}$ by comparison with $\partial\mathbf{u}/\partial t$ is valid for times such that $t \ll l/U$, and the requirement that the diffusion of θ is small during this period is satisfied provided that $Ul/\alpha \gg 1$ (see the appendix at the end of this chapter). As the velocity increases however, the balance of terms in equation (2.18) changes with the buoyancy now increasingly being balanced by $\mathbf{u}\cdot\nabla\mathbf{u}$. As a result the acceleration begins to fall, and the front of the thermal approaches a steady velocity, as discussed by Davidson *et al.* (2007).

The end of the period of roughly constant acceleration marks the end of the buoyant blob phase, with the change in force balance and approach to constant maximum velocity marking the transition from blob to mushroom cap.

Looking at the plot of γ for the entire flow (figure 6.12), there is an inflexion point around $\tau = 4.5$ accompanied by a morphological change as the lobes of the thermal begin to roll up. To understand this, note that Φ increases monotonically according to equation (6.9) as the temperature front thins along the axis. At short times this growth in Φ is linear, but as hot fluid is radially displaced the source term decreases, so the value of Φ increases at an ever slowing rate. Since impulse increases linearly in time, as discussed above, an inflexion point becomes inevitable, with γ transitioning from $\gamma \sim \tau^0$ to $\gamma \sim \tau^{-1}$. This coincides with the transition into the mushroom cap phase.

6.6 Stage 2: The mushroom cap

As a front forms at the leading edge of the thermal, fluid is displaced to the sides (figure 6.6d) and vorticity collects in a torus, covered by a thin cap or front (figure 6.7b). There are trailing tendrils of vorticity to the rear that form due to the sharp radial temperature gradients at the edge of the wake. This vorticity distribution drives rotational motion in the r-z plane acting to sweep the upper part of the tendrils in towards the axis. As a result of this induced motion the front now thins at an exponential rate matching the behaviour predicted by the inviscid model of Davidson *et al.* (2007). Defining the front as the region along the axis where temperature is above $0.25\ \hat{\theta}$ we can plot its thickness and confirm that it thins exponentially from $\tau \approx 5.5$, where roll up into the cap begins, until $\tau \approx 8$ when the cap starts to fade through viscous diffusion. This is shown in figure 6.14.

Another result of our study in support of the model of Davidson *et al.* (2007) is that, after the initial transient and roll-up, the velocity of the cap attains an approximately constant value. This is shown in figure 6.13 for the duration of the cap phase from $\tau = 8$ to $\tau = 17$. We choose the point at which the cap attains this velocity to mark the end of the transition from buoyant blob to mushroom cap. Although this behaviour was predicted by their model, Davidson *et al.* (2007) noted this as an apparent paradox in their analysis since equation (6.5) requires impulse

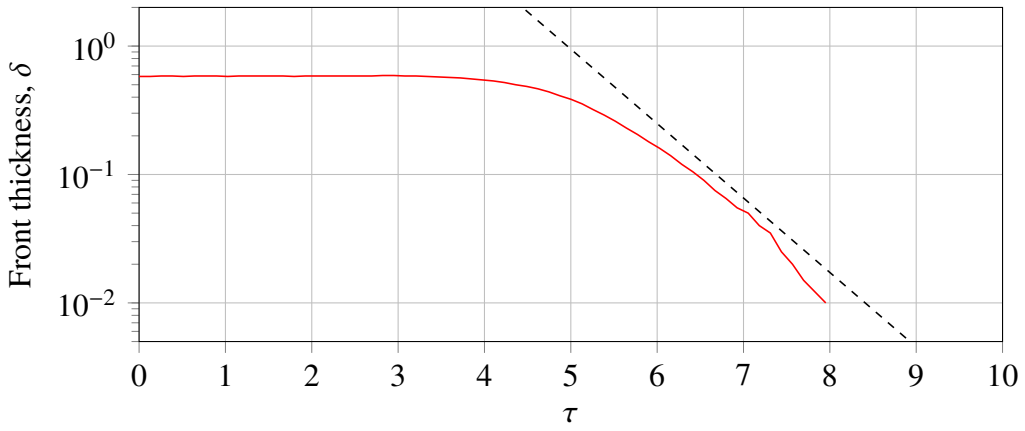

Fig. 6.14 Thickness of the temperature front vs. time. The dashed line indicates an exponential rate of decay.

to increase linearly in time. For an object of constant volume, this requires the mean velocity to increase linearly in time. They hypothesised that the result might be explained by the generation of ω_ϕ being large lower down in the stem of the mushroom. This is in fact incorrect, as our results show, with a large amount of impulse still being generated in the cap (figure 6.10). The paradox can instead be explained by the fact that the thermal cap expands radially. Relating linear impulse to momentum in the form $\mathbf{L} = \int \mathbf{u}\, dV$, a scaling analysis gives $L \sim u_c R_c^3$, where u_c is a characteristic cap velocity and R_c is the outer radius of the cap. Since u_c tends towards a constant value, we would expect R_c to scale with $t^{1/3}$ in order to be consistent with linearly increasing impulse. This is indeed what we observe in figure 6.15 plotting R_c^3 against τ.

As the temperature front rapidly thins the source term in equation (6.9) decreases and so the rate of generation of vorticity also decreases. As a result, the flux Φ of the cap tends towards a constant value as the front is pulled apart and swept into the lobes. The impulse L continues to increase linearly in time, and as such γ for the cap decreases at a rate proportional to τ^{-1}. The wake that is left behind by the cap consists of the trailing tendrils of vorticity bounding a smear of higher temperature fluid. As the mushroom cap moves off ahead of the wake, the height of the wake increases, and so the rate of generation of Φ in the wake also increases in accordance with equation (6.9). This is why γ for the wake increases over the course of the mushroom stage.

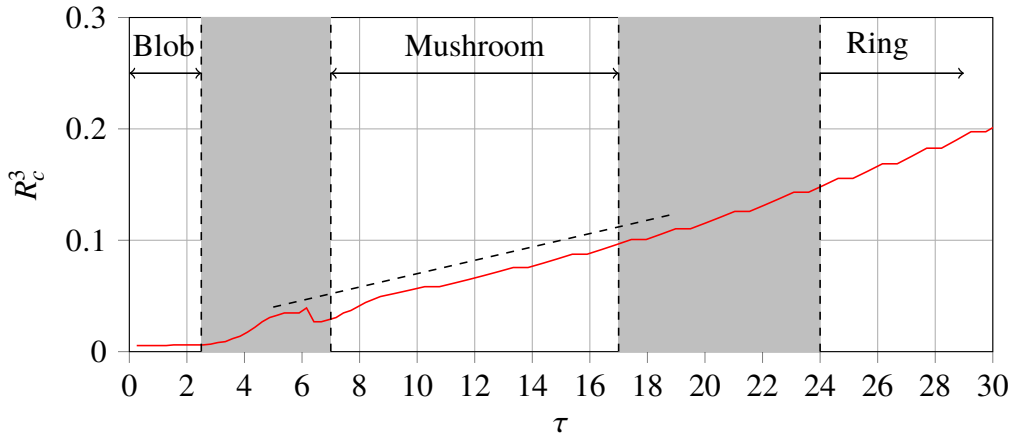

Fig. 6.15 R_c^3 vs. τ for the thermal.

As the mushroom cap progresses it wraps up a significant portion of ω_ϕ/r from the front and the stem into the lobes that will eventually form the core of the buoyant vortex ring. As a diagnostic we consider the relative strengths of ω_ϕ/r in the stem and the lobes of the developing ring. The value of ω_ϕ/r on the axis falls below that at the centre of the forming ring at around $\tau = 17$, marking an end to the mushroom cap and the start of the transition into two separate structures; buoyant vortex ring and wake. We see from figure 6.12 that the end of this stage is marked by the wake approaching a maximum in γ. As the stem becomes thinner, the wake ceases to lengthen along the axis and so the rate of generation of Φ in the wake remains roughly constant. Since L increases at a constant rate γ experiences an extremum.

6.7 Stage 3: The buoyant vortex ring

The mushroom cap is subsequently observed to evolve into a buoyant vortex ring that moves off ahead of the trailing wake. We consider initially the motion of this ring after separation using the same methodology as above, before then tying these flow regimes together and examining the separation process.

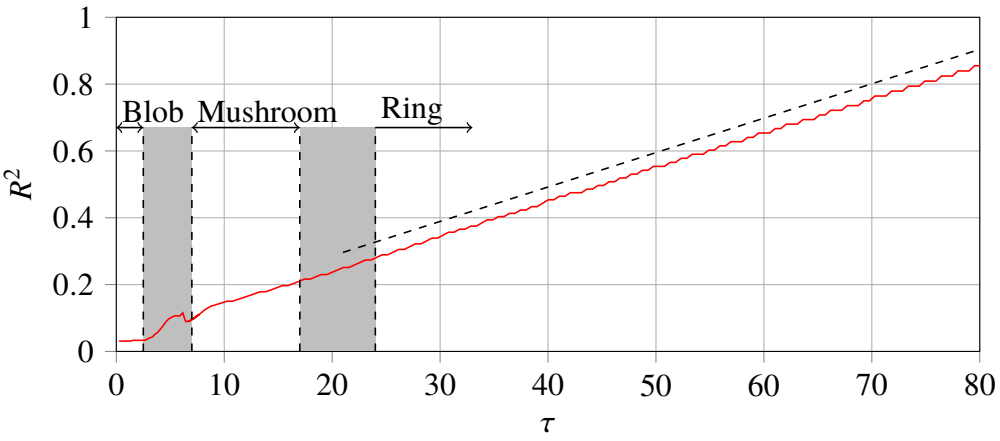

Fig. 6.16 R^2 vs. τ for the thermal.

6.7.1 The evolution of the ring

For a vortex ring containing all of its buoyant material in its core, equation (6.9) tells us that the flux (or circulation) of the ring must remain constant. In addition to this, equation (6.8) tells us that the impulse of the vortex ring must be increasing linearly in time at a rate proportional the thermal energy contained within the core of the ring. Both of these results are in agreement with the analysis of Turner (1957). For a thin-cored vortex ring of mean radius R and flux Φ, the impulse can be approximated (from equations (6.6) and (6.7)) as $L \approx \pi R^2 \Phi$. For this to be consistent with the linearly increasing impulse and constant flux, the ring radius R must increase at a rate proportional to $t^{\frac{1}{2}}$. This is again in agreement with the analysis of Turner (1957) and consistent with the results of our simulations. Figures 6.10 and 6.11 show that the flux of the ring remains constant whilst its impulse increases at a constant rate. Plotting R^2 against τ in figure 6.16 confirms that the radius of the ring scales as $R \sim t^{1/2}$. As was seen in the cap phase, the seemingly paradoxical result that the ring is decelerating (figure 6.13) whilst impulse is increasing can be explained by the fact that the radius is increasing, as we now discuss.

For a vortex ring of the kind sketched in figure 6.17 with global radius R, core radius a ($a << R$[1]), and a uniform distribution of vorticity ω_θ in the core, the

[1]Of course, during the formation process from a thermal the developing vortex ring is not initially thin-cored.

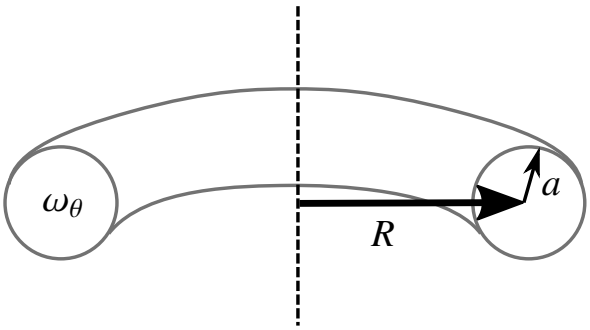

Fig. 6.17 Schematic cross section of a thin-cored vortex ring.

velocity of the ring, V, can be calculated (Saffman (1992); Batchelor (1967); Lamb (1932)) as:

$$V = \frac{\Phi}{4\pi R}\left[\ln\left(\frac{8R}{a}\right) - \frac{1}{4}\right] \quad . \tag{6.15}$$

Given the results above, this tells us that buoyant vortex rings must decelerate as they rise, with a rise velocity scaling as $t^{-1/2}\ln t$. In addition to this we note the slightly counter-intuitive result (as did Turner (1957)) that the more buoyant a ring is, the faster it will expand radially and decelerate. This follows from the result $L \approx \pi R^2\Phi$ and the fact that Φ is constant whilst the rate of increase of L, and hence rate of radial increase, is proportional to buoyancy of the ring.

6.7.2 The separation process

We now return to consider the separation of the ring from the wake following the end of the mushroom cap phase (around $\tau = 17$). Let us start by considering more closely the flow between the two separating structures, ring and wake, by looking at the streamlines in figure 6.18a. We see that the stem connecting the ring and wake experiences a stretching flow in the axial direction due to the poloidal velocity induced by the ring. Figures 6.18b and 6.18c show strain rates of the fluid. ϵ_{zz} is the axial strain rate in the axial direction; how much u_z changes in the z direction i.e.

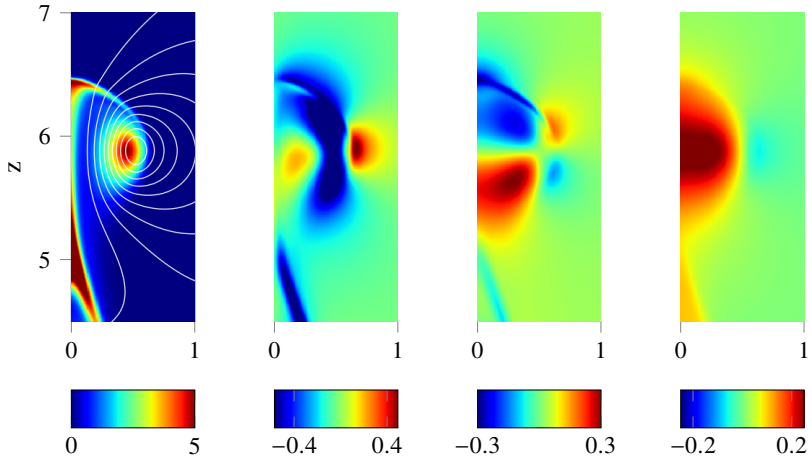

(a) ω_θ/r (b) ϵ_{rz} (c) ϵ_{zz} (d) u_z

Fig. 6.18 Vorticity, strain-rate components, and axial velocity of the thermal at $\tau = 19.0$.

how much the fluid is being stretched axially. ϵ_{rz} is a shear strain rate describing how u_r changes in the z-direction and u_z changes in the r-direction. It can be seen that the dominant strain rate in the stem is ϵ_{zz}, with positive values from the base of the stem to midway up, consistent with axial stretching. Past the core of the ring the axial strain rate becomes negative due to the proximity of the cap. The main contributions of ϵ_{rz} occur where fluid is being stripped away in the cap and wrapped up into the core of the ring, away from the axis and stem.

It is important to note here that as the ring and wake separate, the wake rises slower than the ring. This means that the stem connecting the two structures is being stretched from the base of the stem upwards. The vertical velocity (figure 6.18d) is largest on the axis at the height of the core of the ring, but small at the base of the stem. So the lower part of the stem is being stretched in the axial direction while squeezed in by the entrained ambient fluid. The effect of this is a rapid reduction in the value of ω_ϕ/r on the axis of the stem, as we now discuss.

Consider a cylindrical material volume that encloses part of the stem, as shown in figure 6.19. If we track its progress in the range $\tau = 15$ - 21, we find that the volume undergoes large axial stretching whilst contracting radially to conserve volume. The start and end points are shown in figure 6.19. The volume integral of

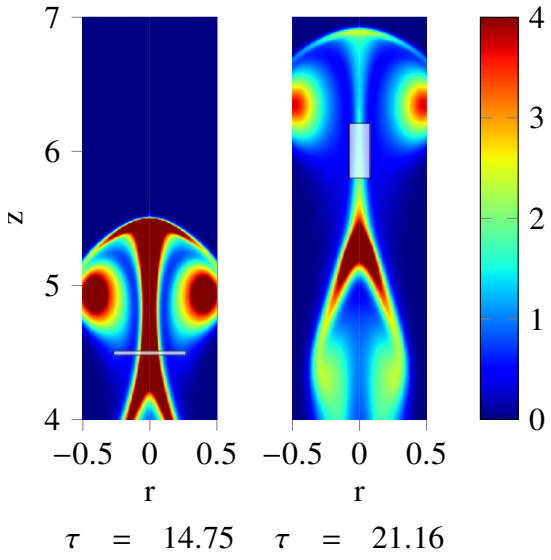

Fig. 6.19 Images of ω_ϕ/r showing the start and end position of a material volume (white square).

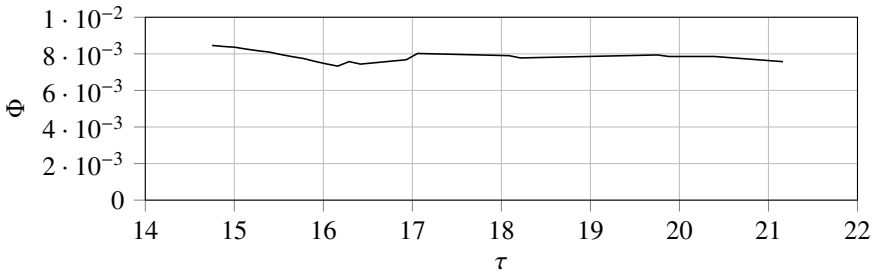

Fig. 6.20 Vorticity flux for a material volume enclosing the stem

ω_ϕ/r (Φ) is plotted in figure 6.20 and we see that Φ is approximately conserved, reflecting the relative weakness of the thermal source term in (6.9). Nonetheless, it is clear from our results that the vorticity on the axis of the stem weakens to a point at which the ring can be considered as a separate entity from the wake to which it was once attached. Since the temperature gradients in the stem are small we can approximate equation (6.1) by

$$\frac{\mathrm{D}}{\mathrm{D}t}\left(\frac{\omega_\phi}{r}\right) \approx \nu \frac{1}{r^2}\nabla_*^2\left(r\omega_\phi\right) \quad . \tag{6.16}$$

We now see that as the stem is stretched and thinned by advection, we expect diffusion of ω_ϕ/r radially outwards. The process of axial stretching therefore helps maintain high gradients in ω_ϕ/r, enhancing the radial diffusion. Eventually this radial diffusion weakens the centreline value of ω_ϕ/r sufficiently such that we no longer consider it a connection between ring and wake.

Thus the end of the transition to a buoyant vortex ring occurs when ω_ϕ/r in the stem connecting the ring to the wake becomes sufficiently weak by diffusion that we can consider them to be two individual structures. Based on this we define the end of the transition period as the time at which ω_ϕ/r in the stem falls below 20% of that in the core of the ring. This occurs at $\tau = 24$. By this point the ring has attained a limiting value of Φ which persists for the remainder of its ascension.

6.8 The wake and multiple vortex rings

We have discussed the formation of a buoyant vortex ring and its detachment from the wake. Of further interest, however, is the fact that subsequent mushroom caps may form from the thermal wake. These, in turn, may become buoyant rings that detach and follow the first. This behaviour can be seen in both figures 6.9 and 6.21. The impulse and flux of the thermal wake is always increasing in time through the same processes as for the initial buoyant blob (equations (6.8) and (6.9)). As a result we can have further caps and rings forming that follow the same process of development.

Looking at the wake in figure 6.8 we see that the radial temperature gradients generate trailing tendrils of vorticity. As these strengthen they become unstable and begin to roll up on themselves, moving in towards the axis. Following these developments further into figure 6.9 we see the development of the new mushroom cap. The base of the stem that was left by the primary vortex ring is radially stretched to form a new front. The trailing tendrils that wrapped up become the lobes. The cap then proceeds to develop in much the same way as the primary. Looking at γ for the wake in figure 6.12, we note that the roll up of the tendrils coincides with an increase in γ as the vorticity distribution becomes more compact. This reaches a maximum at around $\tau = 18$ after which the vorticity distribution expands as it wraps up to form a second mushroom cap.

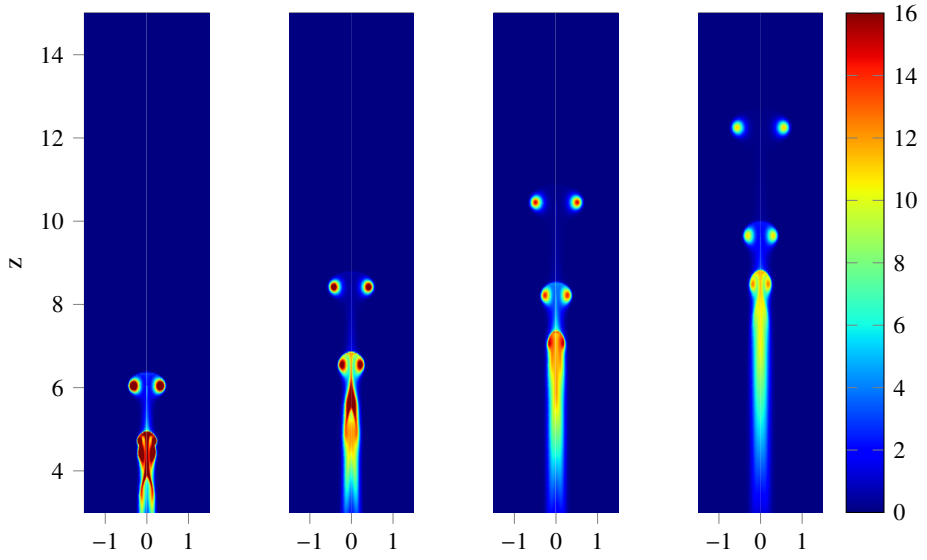

(a) $\tau = 19.2$ (b) 32.1 (c) 44.9 (d) 57.7

Fig. 6.21 Development of a second vortex ring from the wake left by the separation of the primary vortex ring. ω_ϕ/r plotted for $Re = 332$

The non-dimensional impulse and flux of the primary and secondary rings are shown in figures 6.22 and 6.23 as a function of Re. Impulse is significantly reduced in the second ring, whilst the flux is approximately half that of the primary ring. These reductions are, in part, because we are normalising with respect to the initial temperature field, which is not appropriate for the wake. However, it is also clear that the rate of increase of L has been reduced in the second ring. To understand this we must consider again equations (6.8) and (6.9). The rate of generation of impulse scales with the total heat, whilst the rate of flux generation depends upon the heat on the axis. The primary ring wraps up much of the initial heat into its core resulting in it having a much higher rate of impulse generation. An effect of wrapping up into a ring is that hot fluid is removed from the axis, preventing any further increase in flux. In contrast to this the wake, though containing less heat than the first ring, remains stretched out along the axis for a much longer period prior to wrapping up to form the second ring. As a result the flux continues to increase. By the time it separates, the second ring contains around half the flux of the first. Since impulse is much lower than flux for the second ring compared to

the first, γ is larger. Following wrap up into a second ring and separation from the wake the value of γ decreases monotonically as τ^{-1}, just like the primary ring. The larger value of γ for the second ring demands that it is more radially compact than the first.

For some simulations it was observed that further vortex rings could form from the wake of the second provided it did not experience significant diffusive effects in temperature and vorticity. This behaviour can be seen for $Re = 332$ and $Pr = 1.0$ in figure 6.21. The primary ring has moved off ahead by $\tau = 32$ and a second cap has begun to form, connected to the lower wake by a stem of vorticity. By $\tau = 44$ we see that the stem has weakened as the second ring moves off ahead. Finally, at $\tau = 58$, we see that the two rings are now clearly separate structures ahead of a wake which is capped by a third developing mushroom cap.

6.9 Influence of Re and Pr

We now turn our attention to the effects of viscosity and thermal diffusion on the development of the thermal. To do this we look at a number of simulations across a range of both Reynolds and Prandtl number. We again use the non-dimensional impulse and flux, in addition to other properties, to draw parallels and make comparisons between the different cases.

6.9.1 Influence of Re

Figure 6.22 shows the impulse of the entire flow and the first and second rings for different Reynolds numbers. It is immediately apparent that there is some independence across Reynolds number in this range with the dimensionless impulse of both the first and second rings being almost the same in all cases. Likewise, figure 6.23 displays good collapse in the final flux for both rings for different Reynolds numbers. The total flux of the domain follows the same qualitative pattern for all Re, although we see the curves diverge at later times with more flux generated at higher Reynolds numbers.

Note that the collapse of impulse requires that each ring contains the same proportion of the initial heat (equation (6.8)). This is confirmed by calculating the

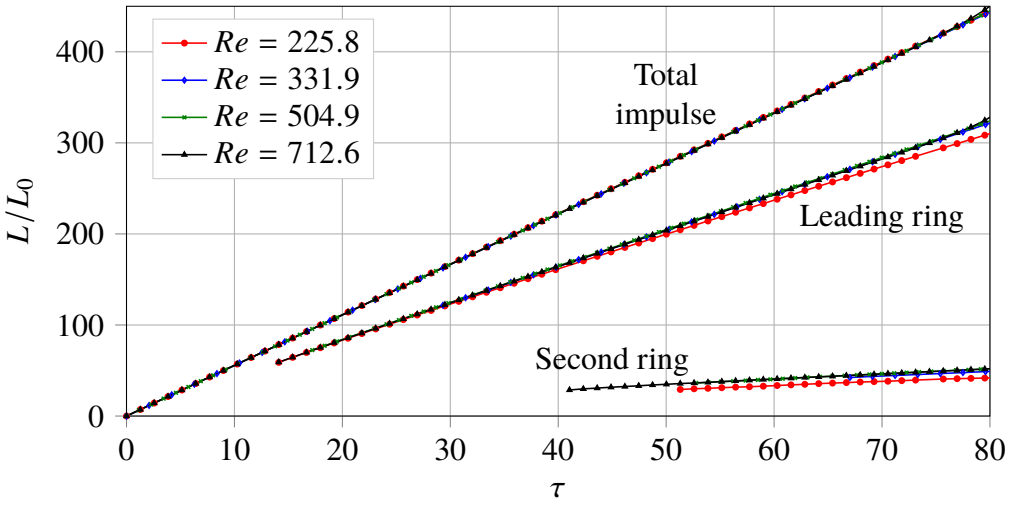

Fig. 6.22 Non-dimensional analysis of impulse for several simulations at $Pr = 1.0$ and different Re.

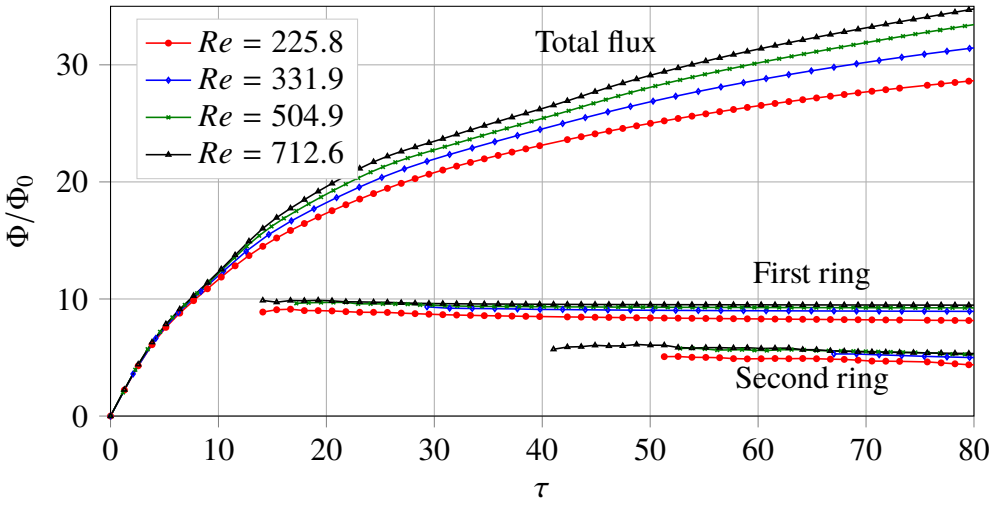

Fig. 6.23 Non-dimensional analysis of flux for several simulations at $Pr = 1.0$ and different Re.

Re	Pr	Φ_1/Φ_0	Φ_2/Φ_0	% heat$_1$	% heat$_2$	τ_{ring}
71.0	1.00	7.8	-	56	-	-
124.8	1.00	8.3	4.6	60	12	41.0
175.2	1.00	8.6	4.7	64	11	29.5
200.4	1.00	8.7	4.8	65	11	28.0
225.8	1.00	8.8	4.9	67	11	24.4
331.9	1.00	9.1	5.2	69	11	22.0
504.9	1.00	9.4	5.4	70	11	21.3
712.6	1.00	9.3	5.6	71	11	21.3

Table 6.2 Key properties for varying Re at $\tau = 80$

thermal energy contained in the vortex rings. Table 6.2 lists the ring properties at $\tau = 80$ when the first two vortex rings are separate from the wake. The value % heat gives the percentage of the initial heat contained within a ring. We see that for a Reynolds number of 332 and above that the first ring consistently contains approximately 70% of the initial heat, with 11% in the second ring. The $Re = 226$ case is slightly lower (67% and 11%) but still collapses relatively well with the higher Reynolds number results. This behaviour is not maintained at lower Re however. For $Re = 71$ we find that the first ring contains a lower proportion of the total heat and that a second ring does not form at all from the wake as seen in figure 6.24. This observation would suggest that there is a critical point below which a second vortex ring will not be produced.

The independence from Re at early times can be explained by noting that the characteristic timescale t_0 has no dependence on viscosity. Indeed, following initialisation as a patch of heat in quiescent fluid, the main balance in equation (2.1) occurs between $\partial\mathbf{u}/\partial t$ and $-\mathbf{g}\beta T$ giving the initial acceleration. As the blob begins to lift and roll up in to the mushroom cap, the balance transitions to be between $\mathbf{u}\cdot\nabla\mathbf{u}$ and $-\mathbf{g}\beta T$ giving a constant cap velocity as discussed. These processes occur between $\tau = 0$ - 15, i.e. of the order of t_0. Consider a timescale based on ν as $t_\nu = l^2/\nu$, which is the relevant timescale for viscous effects to act given smooth initial conditions of lengthscale l. The ratio of this to our characteristic timescale based on buoyancy gives $t_\nu/t_0 = Re$. Based on this we can surmise that,

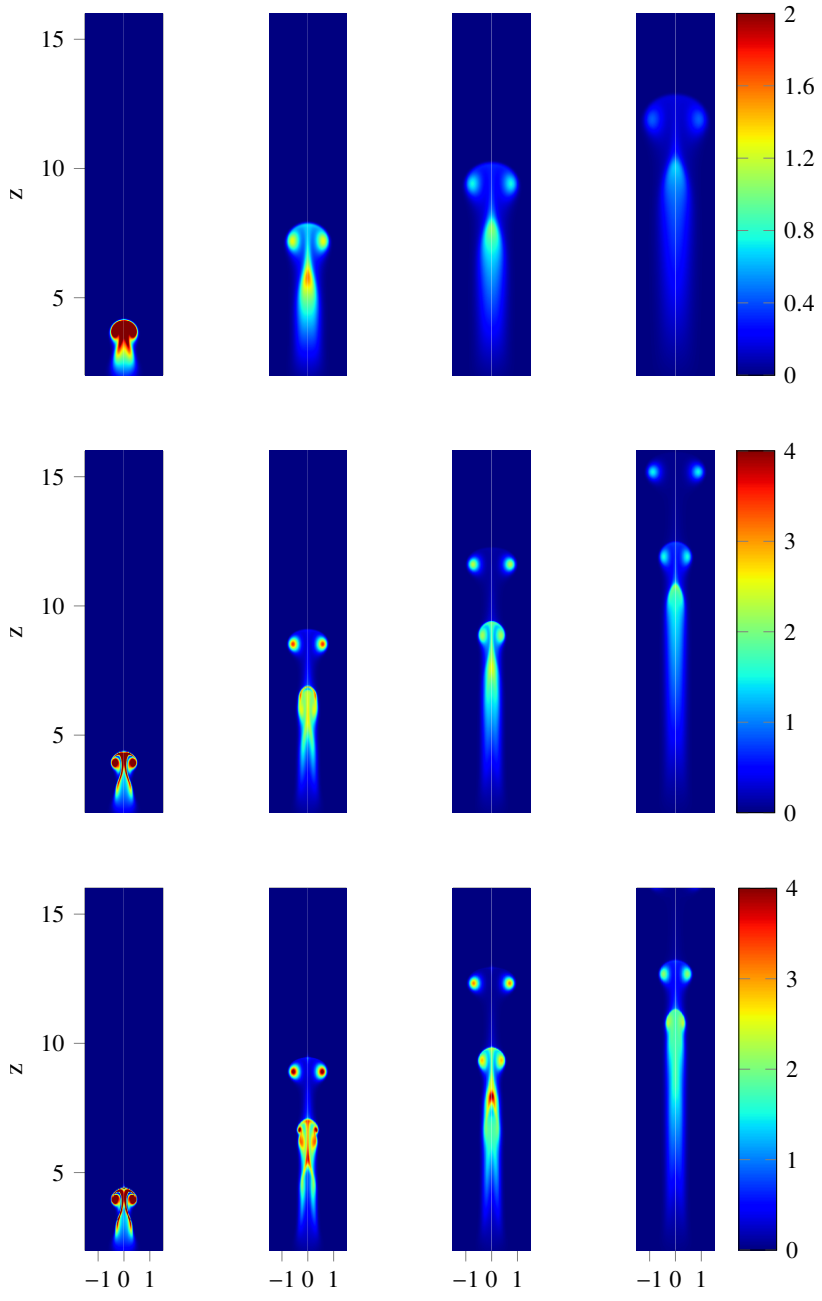

(a) τ = 10.3 (b) 32.1 (c) 50.0 (d) 75.0

Fig. 6.24 Development of ω_ϕ/r a thermal for $Re = 71$ (top), $Re = 226$ (middle), and $Re = 332$ (bottom). In all cases $Pr = 1$. Note different scale for $Re = 71$.

for sufficiently high Reynolds number, viscous effects must only come into play at timescales somewhat longer than it takes for the thermal to wrap up into the mushroom cap. Since this process involves the formation of the core of the vortex ring, the ring is not significantly influenced by viscosity with its properties largely independent of Re. These properties are then retained at longer timescales as the ring ascends.

This is not to say that there is no effect however. It is clear from figure 6.23 that the total flux begins to diverge from around $\tau = 15$. Since the primary ring displays a good collapse in Φ/Φ_0 the source of this discrepancy must lie in the wake. Furthermore we know that, once formed, the ring cannot contribute to the generation of Φ since all the heat is contained in the core (equation (6.9)). It can be seen from figure 6.24 that as Reynolds number decreases, ω_ϕ/r in the wake becomes weaker and more diffuse. To understand why this is we must consider equations (6.1) and (6.9), and also note that these results are all for a Prandtl number of 1. Therefore as Reynolds number falls, so does the Péclet number, and so the effects of thermal diffusivity increase. Since the initial condition is quiescent fluid, we can disregard the effects of viscosity at early times when there is little motion. The same cannot be said for thermal diffusion however. Immediately following initialisation thermal diffusion will act to spread out the heat, reducing the radial temperature gradients that generate vorticity (equation (6.1)). For low Reynolds number ($Re = 71$) this has an impact early on, with significantly lower ω_ϕ/r across the entire thermal. The ring also contains a noticeably lower proportion of the initial heat. We noted above that, once formed, the ring maintains its flux so the main effects of thermal diffusion at later times must occur in the wake. When thermal diffusion is larger, the warm wake will expand and temperature gradients reduce. As a result, the generation of ω_ϕ/r is reduced. This leads to the diverging lines of Φ/Φ_0 in figure 6.23 and weaker ω_ϕ/r in the wake.

6.9.2 Influence of Pr

In order to isolate the effects of thermal diffusivity we examined the effect of varying Prandtl number between 0.1 and 2.0 for a fixed Reynolds number of 225.8. This introduces a second diffusive timescale based upon the thermal diffusivity, t_α,

Re	Pr	Φ_1/Φ_0	Φ_2/Φ_0	% heat$_1$	% heat$_2$
225.8	2.00	8.8	4.9	67	11
225.8	1.00	8.8	4.9	67	11
225.8	0.75	9.0	5.2	59	12
225.8	0.50	9.0	5.7	44	14
225.8	0.10	5.6	-	2	-

Table 6.3 Key properties for varying Pr at $\tau = 80$

defined in a similar way to t_ν. For $Pr = 1.0$, $t_\alpha = t_\nu$, so when the viscous timescale is long in comparison to the formation time, so is t_α. Therefore we deduce that for $Pr > 1$ there should be no significant difference in the results. However, for Prandtl numbers below 1, t_α may become comparable to the formation time even when t_ν remains large. In these cases we find that diffusive effects interrupt the formation process by smearing out heat as discussed above. Table 6.3 lists the key values for a range of Prandtl numbers at a fixed τ. As expected, for $Pr > 1$ the properties of the first and second ring are identical, with formation occurring before diffusive effects have time to act. For lower Prandtl numbers the first vortex ring contains less of the initial heat and both the rings and wake are weaker in ω_ϕ/r. This is illustrated in figure 6.25. For the case $Pr = 0.1$ it becomes particularly apparent how diffusion destroys the sharp radial gradients in temperature that lead to the generation of vorticity tendrils and secondary rings. The proportion of heat contained in the second ring actually increases as Pr falls, although this likely results from the fact that the wake is left with increased heat. For $Pr = 0.1$ although a second cap is developing at our chosen value of τ it has not progressed enough for its values to be well defined.

Since viscous effects have little impact at the early stages of the development process we see that, provided the effects of heat transfer are also negligible, the end of the blob phase (constant acceleration), start of the cap phase (constant velocity, $R^3 \sim t$), and end of the cap phase (stem weaker than lobes) all develop according to a universal timescale. There is some discrepancy at the end of the transition to the ring however which is recorded in table 6.2 as τ_{ring}. We find that as Re falls, the time for ω_ϕ/r in the stem to fall below 20% of that in the core increases. Saffman

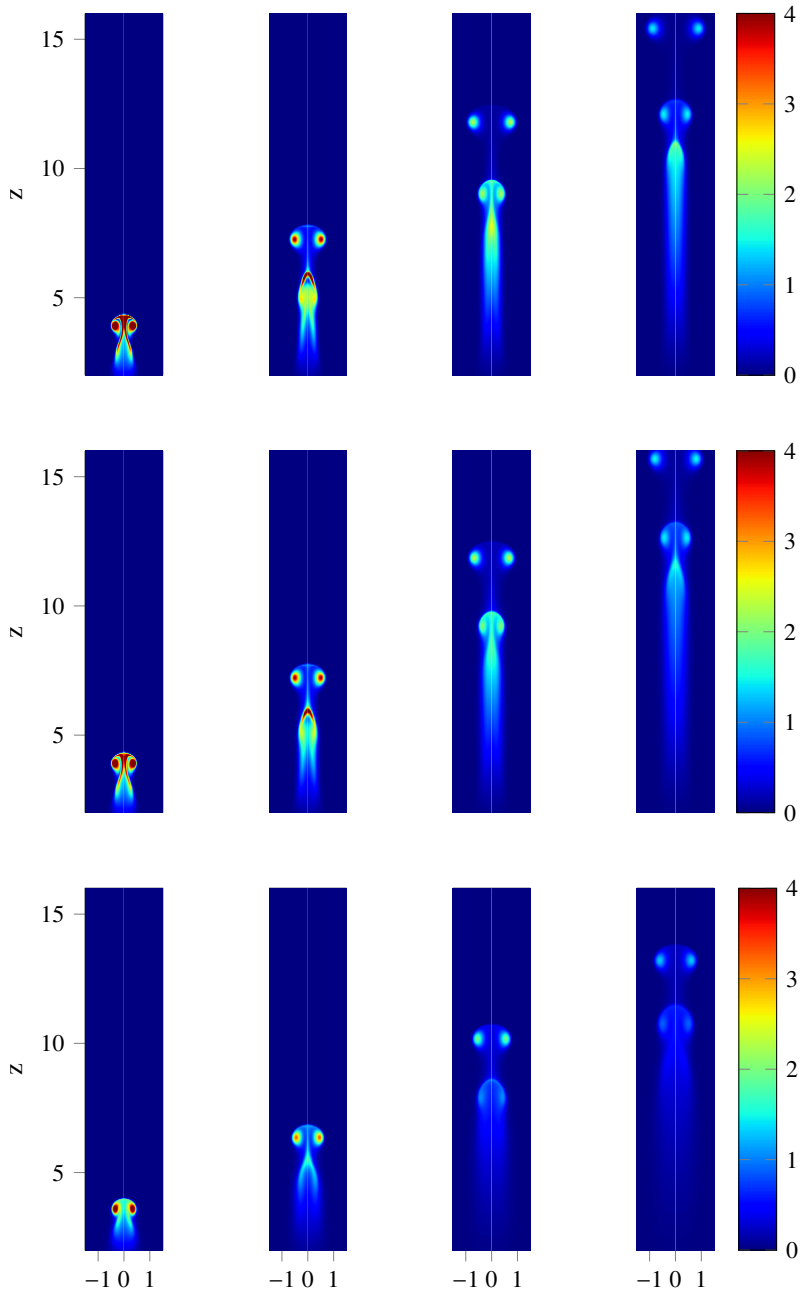

(a) τ = 10.26 (b) 25.65 (c) 51.31 (d) 76.96

Fig. 6.25 Development of ω_ϕ/r a thermal $Re = 225$ for $Pr = 1.0$ (top), $Pr = 0.5$ (middle), and $Pr = 0.1$ (bottom).

(1970) examined the effect of viscosity on thin cored vortex rings. He showed that diffusion of vorticity will cause the core radius a to increase at rate $(4\nu t)^{1/2}$. This is accompanied by a decrease in peak vorticity. The rise velocity of equation (6.15) becomes

$$V_{visc.} = \frac{\Phi}{4\pi R}\left[\ln\left(\frac{8R}{\sqrt{4\nu t}}\right) - 0.558\right] , \tag{6.17}$$

indicating that the more viscous a fluid, the slower a vortex ring (of a given buoyancy) will ascend. As a result rings of a lower Reynolds number will rise more slowly, and thus the stem connecting the ring to the wake will be stretched more slowly. Since the stretching process encourages the diffusion of ω_ϕ/r away from the axis we might expect that faster rising rings separate more quickly.

6.10 Summary

We have characterised the behaviour of the flow resulting from a buoyant perturbation in an otherwise quiescent fluid. To do this we broke the flow down into three key stages; the buoyant blob, the mushroom cap, and the buoyant vortex ring. We also looked at the evolution of the wake left behind by the ring. Although these phenomena have previously been discussed individually, we believe that this is the first time the development from buoyant blob to mushroom cap and on into a buoyant vortex ring has been treated with a consistent mathematical framework across all stages as a single phenomenon.

The equations we have used can link the results of Shlein for buoyant blobs to those of Turner for buoyant vortex rings. By examining the evolution of the impulse, flux, and γ, we identified key points in the development of the thermal such as the roll-up of the cap and separation of the ring from the wake. We have taken a closer look at the mushroom cap stage, examining and explaining the scaling of cap radius with time ($R^3 \sim t$), and providing validation for the model presented by Davidson *et al.* (2007). We have also shown that this approach gives equivalent results for buoyant vortex rings when compared to the analysis performed by Turner (1957). We find that radial expansion of the slowing ring ($R^2 \sim t$) is required for compatibility with linearly increasing impulse. As a result of this new approach we have also been able to shed light on a number of unsolved problems from previous

works. We show that the constant acceleration of the buoyant blob observed by Shlien (1976) can be explained by considering the dynamic balance at early times. We also resolved the apparent paradox raised by Davidson *et al.* (2007) by noting that the radial expansion that occurs during the mushroom cap phase allows the impulse to continue increasing whilst the cap tends towards a constant velocity.

Exploring the effect of Reynolds and Prandtl number, we have shown that the early stages of development are key in determining the final properties of the buoyant vortex ring. We found that there is an independence in properties above a critical Reynolds number due to cap formation occurring on a timescale where viscosity has no significant effect. The independence of impulse arises from the fact that, when forming, the ring always wraps up the same proportion of the initial heat into its core. In contrast we find that the effects of thermal diffusion can have a significant effect on the early stages of development when there is little motion. Thermal diffusion acts to smooth out the temperature field, inhibiting the generation of vorticity.

Finally, by considering the behaviour of the wake left behind by the ring, we show that the formation of secondary vortex rings is entirely to be expected. Buoyant fluid left behind by the first ring can undergo a similar process, forming a cap and eventually a secondary buoyant vortex ring that separates to follow the first. Again, the effects of thermal diffusion can become noticeable in the wake where the smoothing of temperature gradients interferes with vorticity generation and inhibits the production of successive rings.

Appendix

Appendix 6.A Scaling analysis at early times

Given that $\mathbf{u}$ is small for small t we can approximate equation (2.18) as,

$$\frac{\partial \mathbf{u}}{\partial t} \sim \mathbf{g}\beta\theta \implies \mathbf{u} \sim \mathbf{g}\beta\theta t \ . \tag{6.18}$$

Based on this we can quantify the relative sizes of the advective terms in both equation (2.18) and (2.9) as,

$$\begin{aligned} \frac{\frac{\partial \mathbf{u}}{\partial t}}{\mathbf{u}\cdot\nabla\mathbf{u}} \quad &\sim \quad \frac{\frac{\partial \theta}{\partial t}}{\mathbf{u}\cdot\nabla\theta} \quad \sim \quad \frac{l}{ut} \\ &\sim \quad \frac{l}{t\,(g\beta\theta t)} \\ &\sim \quad \frac{l^2}{U^2\,t^2} \ . \end{aligned} \tag{6.19}$$

Hence we can define a timescale over which we may regard the advective terms to be small as follows:

$$\left.\begin{aligned} \tfrac{\partial \mathbf{u}}{\partial t} &\gg \mathbf{u}\cdot\nabla\mathbf{u} \\ \tfrac{\partial \theta}{\partial t} &\gg \mathbf{u}\cdot\nabla\theta \end{aligned}\right\} \quad \text{for} \quad t \ll \frac{l}{U} \ . \tag{6.20}$$

Now we turn our attention to the thermal diffusion. Based on the above analysis we can approximate equation (2.9) for small t as,

$$\frac{\partial \theta}{\partial t} \sim \alpha\nabla^2\theta \sim \alpha\frac{\theta}{l^2} \ . \tag{6.21}$$

A scaling analysis then gives

$$\frac{\Delta\theta}{\hat{\theta}} \sim \frac{\frac{\partial\theta}{\partial t}t}{\hat{\theta}} \sim \frac{\alpha\frac{\hat{\theta}}{l^2}t}{\hat{\theta}} \sim \frac{\alpha t}{l^2} \sim \left(\frac{l_\alpha}{l}\right)^2 , \tag{6.22}$$

where $\Delta\theta$ is a typical change in temperature and l_α is the diffusion length. In order to regard thermal diffusion as negligible ($\Delta\theta/\hat{\theta} \ll 1$) we therefore require,

$$\frac{\alpha\,(l/U)}{l^2} \ll 1 , \tag{6.23}$$

or alternatively

$$Pe = \frac{Ul}{\alpha} \gg 1 , \tag{6.24}$$

where Pe is the Péclet number.

Chapter 7

Concluding remarks

In this chapter we review the main findings of this thesis around the theme of modelling and understanding atmospheric vortices. As well as the results directly from this work we also ponder the wider implications relating to the study of environmental flows. We complete our appraisal by outlining some potential avenues for future research that might build upon this work.

7.1 Eye dynamics

In chapter 4 and Atkinson *et al.* (2019) we reviewed a number of pieces of work relating to the study of atmospheric vortices, in particular focussing on those concerning internal structures in the flow. Notably we brought together two areas of research (columnar and disklike vortices) that for a time have been on separate paths, despite both being concerned with similar phenomena. In our review we demonstrated how similar conclusions have been reached by both communities, albeit sometimes being presented in different ways. In particular we highlight the importance of azimuthal vorticity to the structure and evolution of atmospheric vortices, noting that it features in many works, even if not explicitly named.

Our work builds upon a theory for eye formation proposed by Oruba *et al.* (2017), where boundary layer vorticity is swept up into the flow to form an eyewall and, subsequently, an eye. We first confirm these results, and the importance of azimuthal vorticity in forming internal structures, through a series of numerical

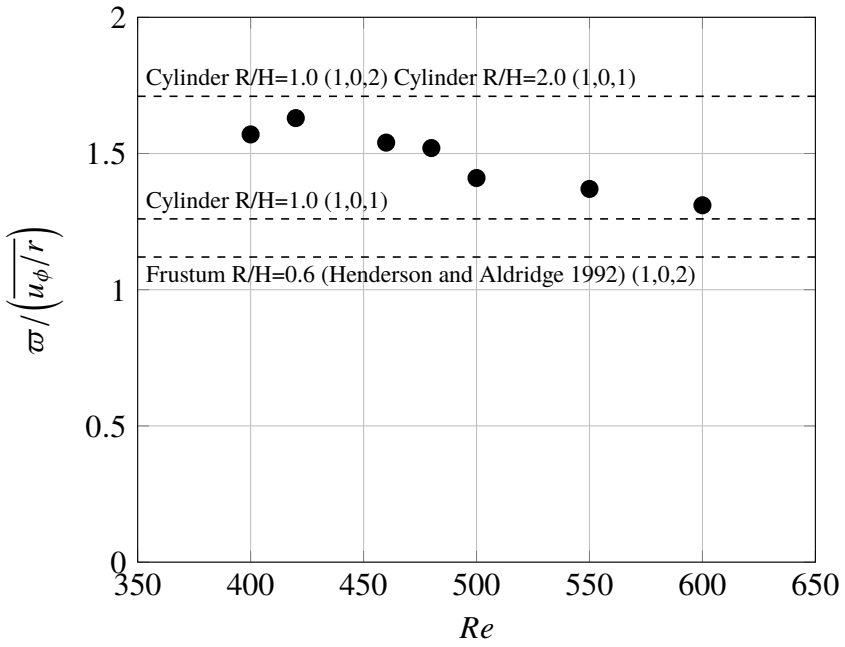

Fig. 7.1 Reproduction of figure 4.21 showing the frequencies of eye oscillations.

simulations. Following this we increase the thermal forcing to a point at which we observe a Hopf bifurcation to an oscillatory state. We propose that this oscillation occurs as a result of a trapped inertial wave at the centre of the vortex. A range of evidence to support this theory is presented, including a comparison of streamlines and angular momentum to a standing inertial wave in a cylinder, and a comparison of the frequencies for inertial waves in a cylinder, frustum, and our simulations. Figure 7.1 is a summary of these results. There is evidence that similar oscillations have been observed in numerical models of columnar vortices (Harlow & Stein, 1974), and we further theorise that such oscillations may be present in real tropical cyclones based on the observations of Chen *et al.* (2015), though more work would be required to confirm this. We finish chapter 4 by comparing our model to a real tropical cyclone and discussing its limitations.

There are a number of questions that follow on from this work that might provide avenues for future investigation. Perhaps the most obvious extension would be to explore the presence of inertial waves in real cyclones by probing further the observations of Chen *et al.* (2015) and others. It might also be worth exploring

large meteorological simulations to look for evidence of these waves and explore how they might vary in a more complex system.

In a similar vein it would be interesting to begin building the model used in chapter 4 back up to include more realistic atmospheric effects and see how they affect the behaviour. One of the most obvious changes to make would be to include the effects of turbulence. Perhaps the easiest way to do this would be with a large eddy simulation (LES). Another important change, particularly to support any experimental work like that of chapter 5 would be to relax the axisymmetry constraint of our simulations and explore three-dimensional effects. Other examples of effects to investigate include latent heat release and more complicated thermal boundary conditions.

Another area that we would like to explore is how our results extend to columnar vortices. Since eye-like structures have been observed in both disklike and columnar vortices could it be that there is a similar process at work in both? Results of other authors (Rotunno, 1977, 1979, 1980; Harlow & Stein, 1974) show similarities to ours, most notably the presence of an annulus of negative azimuthal vorticity that we term the eyewall. It would be interesting to explore how these results might be interpreted, and ideas developed, using the theory for eye formation discussed in this work. In terms of oscillations in this system we note that vortex breakdown is often cited as a cause of internal structure in columnar vortices. It is known that classical vortex breakdown can be interpreted as the manifestation of trapped inertial waves, so could it be that the oscillations we observe eventually lead to vortex breakdown in a columnar structure? Finally the presence of an upper boundary, forcing the flow to overturn, is key in the generation of an eyewall and eye. The nature of this upper boundary is one of the largest differences between disklike and columnar vortices, and is still poorly understood for columnar atmospheric vortices. Future work might extend our simulations to look at the effect of this upper boundary and examine the transition between disklike and columnar vortices as aspect ratio varies.

The numerical investigations were followed by some laboratory experiments that were described in chapter 5. The main objective of these was to examine the theory for eye formation presented previously, specifically the possibility of replicating our simulations in the laboratory. We showed that it is possible to build

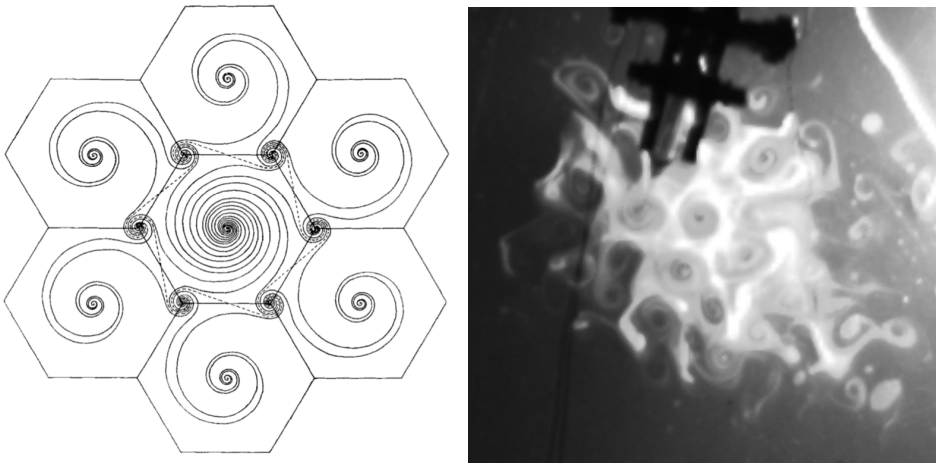

(a) Sketch taken from Veronis (1959). (b) Fluorescein image from experiments.

Fig. 7.2 Reproduction of figure 5.22 showing the top view of the hexagonal cells.

a laboratory experiment similar to the model used in our simulations, and that this was capable of supporting large scale flows. However, we were not able to successfully produce an eye at the centre of a stable cyclonic vortex. We believe that further improvements to the experiment are needed before the desired results can be obtained. A number of suggestions for future work and development, in particular focussing on the enforcement of a fixed-flux thermal boundary condition, were provided. We hope that future experiments might build upon our preliminary investigation to make this a success.

In addition to investigating the model of eye formation we also performed some experiments outside of this parameter regime into rotating cellular convection. An example of this is shown again in figure 7.2. Though there has been much theoretical work on this topic, there are relatively few examples of the phenomenon being observed in the laboratory. Our imaging with fluorescein illustrates not only the hexagonal lattice of cells, but also the path taken by the fluid within cells, rising upwards at the centre before following an anticyclonic helical path outwards at the upper surface. These observations were compared to the theoretical descriptions as shown in figure 7.2.

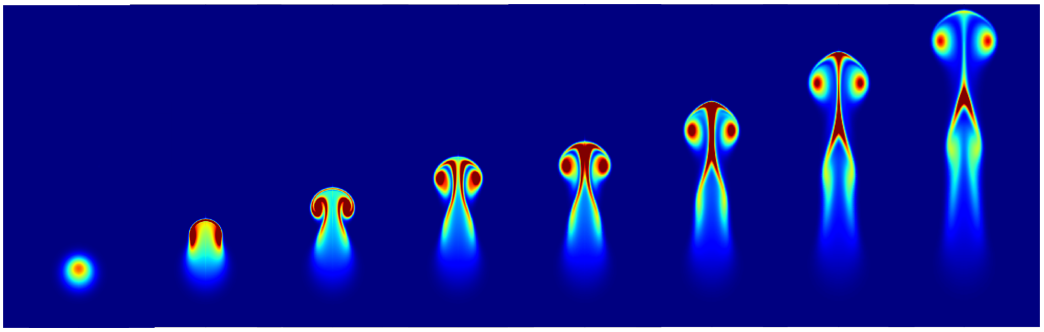

Fig. 7.3 The early stages of evolution of a laminar thermal (plots of ω_θ/r as in chapter 6).

7.2 Thermals

In chapter 6 and Atkinson & Davidson (2019) we present a mathematical framework by which the entire life cycle of a laminar thermal might be analysed. We observed that thermals transition through three main stages; the buoyant blob, the mushroom cap, and the buoyant vortex ring. The early stages of this development are illustrated again in figure 7.3. Though each of these stages has been discussed before, we believe this to be the first time that development has been treated as a single phenomenon across all three using a consistent mathematical framework. By examining the evolution of the impulse, flux, and their ratio γ, we identify and examine key points in the life-cycle of the thermal such as the roll-up of the cap and separation of the ring from the wake.

We observe that the vortex rings produced display an independence above a critical Reynolds number due to cap formation taking place on a timescale where viscosity has no significant effect. The same cannot be said for the effects of thermal diffusion, however, which act to smooth out the temperature field, thereby inhibiting the generation of vorticity. This can have a significant effect at early times when there is little motion. Overall we find that the early stages in the development are key in determining the final properties of the buoyant vortex ring that is produced. As a final result we show, by considering the behaviour of the wake left behind by the ring, that the formation of secondary vortex rings is entirely to be expected. Buoyant fluid left behind by the first ring undergoes a similar process, forming a cap and eventually a secondary buoyant vortex ring that separates to follow the first.

The turbulent thermal, to which the subject of chapter 6 is an analogue, is a prevalent phenomenon in the atmosphere. Though there are various examples, perhaps the most extensive studies come from the field of atmospheric moist convection where thermals are important in the development of clouds. Observations of turbulent thermals display similar behaviour to our laminar analogue, rising up to form caps and then rings that eventually break apart. We hope that the framework that we have presented for the study of laminar thermals might be extended to the turbulent case to provide new approaches to examining these structures.

As a final application we also discussed the captivating phenomenon of volcanic vortex rings. Though some theorise these rings are produced by air exiting an orifice, there is no conclusive evidence for this. Since these rings display qualitative similarities to our simulations and experiments we suggest that they could instead form as a result of buoyant anomalies, with the rings being the final stage of a laminar thermal. Of course, proving this is challenging due to a lack of observations, but it is a theory that might perhaps be explored in the future.

7.3 Closing thoughts

As we draw this thesis to a close we reflect briefly upon the wider role of the work that has been presented. In this study we developed two laminar analogues for atmospheric phenomena. The first of these displayed a behaviour that was mathematically classifiable, and could be explained in the context of the laminar system. Having done this we are now able to look for examples of inertial waves in nature. Without observing them in the model, one might never have considered inertial waves as being relevant in the study of atmospheric vortices or as a candidate to explain oscillations.

Our impromptu but rewarding excursion into laminar thermals illustrates the role of mathematical theory. By constructing a novel framework to study overall development, we were able to tackle some previously unresolved questions about laminar thermals. Looking at the broader picture also allowed us to make links between the later stages in the development and the early timescales. It is hoped that some of these ideas might be carried across to analyse atmospheric convection.

Recalling the quote by the statistician Box, time will tell if our models are useful but we hope that they are. Regardless, it is clear from our investigations that the use of simplified models and analogies can be instructive and will remain important in providing insight into observations and behaviours that cannot be easily explained or understood. This is true not only in the field of geophysical fluid dynamics, to which our analogies and results are linked, but across science as a whole. It is clear that these approaches, alongside improvements in computational modelling and data acquisition, will continue to be essential in the quest to understand our planet.

References

Acheson, D. J. 1990 *Elementary fluid dynamics*. Oxford University Press.

Anderson, J. D. 1995 *Computational fluid dynamics, the basics with applications*. McGraw-Hill.

Andreas, E. L. & Emanuel, K. A. 2001 Effects of sea spray on tropical cyclone intensity. *Journal of the atmospheric sciences* **58** (24), 3741–3751.

Atkinson, J. W. & Davidson, P. A. 2019 The evolution of laminar thermals. *Journal of Fluid Mechanics* **878**, 907–931.

Atkinson, J. W., Davidson, P. A. & Perry, J. E. G. 2019 Dynamics of a trapped vortex in rotating convection. *Phys. Rev. Fluids* **4**, 074701.

Aurnou, J. M., Calkins, M. A., Cheng, J. S., Julien, K., King, E. M., Nieves, D., Soderlund, K. M. & Stellmach, S. 2015 Rotating convective turbulence in earth and planetary cores. *Physics of the Earth and Planetary Interiors* **246**, 52–71.

Babbage, C. 1864 *Passages from the Life of a Philosopher*. Longman and Co.

Batchelor, G. K. 1967 *An introduction to fluid dynamics*. Cambridge University Press.

Beardsley, R. C. 1970 An experimental study of inertial waves in a closed cone. *Studies in Applied Mathematics* **49** (2), 187–196.

Bénard, H. 1900 Étude expérimentale des courants de convection dans une nappe liquide.—régime permanent: tourbillons cellulaires. *Journal de Physique Théorique et Appliquée* **9** (1), 513–524.

Benjamin, T. B. 1962 Theory of the vortex breakdown phenomenon. *Journal of Fluid Mechanics* **14** (04), 593–629.

Bödewadt, U. T. 1940 Die drehströmung über festem grunde. *Zeitschrift für Angewandte Mathematik und Mechanik* **20** (5), 241–253.

Box, G. E. P. 1979 Robustness in the strategy of scientific model building. *Tech. Rep.* 1954. Mathematics Research Centre University of Wisconsin-Madison.

Brooks, H.E. 2004 On the relationship of tornado path length and width to intensity. *Weather and forecasting* **19** (2), 310–319.

Capocci, E. 1846 Su di un poco noto fenomeno vulcanico. *Rendiconto dell'Accademia delle Scienze di Napoli* **5**, 14–18.

Chandrasekhar, S. 1953 The instability of a layer of fluid heated below and subject to coriolis forces. *Proceedings of the Royal Society of London. Series A. Mathematical and Physical Sciences* **217** (1130), 306–327.

Chandrasekhar, S. 1981 *Hydrodynamic and hydromagnetic stability*. Dover.

Chen, S., Lu, Y., Li, W. & Wen, Z. 2015 Identification and analysis of high-frequency oscillations in the eyewalls of tropical cyclones. *Advances in Atmospheric Sciences* **32** (5), 624–634.

Chumakova, L. G., Rosales, R. R. & Tabak, E. G. 2013 Leaky rigid lid: New dissipative modes in the troposphere. *Journal of the Atmospheric Sciences* **70** (10), 3119–3127.

Chung, T. J. 2002 *Computational Fluid Dynamics*. Cambridge University Press.

Church, C. R., Snow, J. T. & Agee, E. M. 1977 Tornado vortex simulation at purdue university. *Bulletin of the American Meteorological Society* **58** (9), 900–908.

Church, C. R., Snow, J. T., Baker, G. L. & Agee, E. M. 1979 Characteristics of tornado-like vortices as a function of swirl ratio: A laboratory investigation. *Journal of the Atmospheric Sciences* **36** (9), 1755–1776.

Craig, G. C. 1996 Numerical experiments on radiation and tropical cyclones. *Quarterly Journal of the Royal Meteorological Society* **122**, 415 – 422.

Davidson, P. A. 1989 The interaction between swirling and recirculating velocity components in unsteady, inviscid flow. *Journal of Fluid Mechanics* **209**, 35–55.

Davidson, P. A. 2013 *Turbulence in rotating, stratified and electrically conducting fluids*. Cambridge University Press.

Davidson, P. A., Sreenivasan, B. & Aspden, A. J. 2007 Evolution of localized blobs of swirling or buoyant fluid with and without an ambient magnetic field. *Physical Review E* **75** (2), 026304.

Emanuel, K.A. 1995 Sensitivity of tropical cyclones to surface exchange coefficients and a revised steady-state model incorporating eye dynamics. *Journal of the Atmospheric Sciences* **52** (22), 3969–3976.

Emanuel, K.A. 2000 A statistical analysis of tropical cyclone intensity. *Monthly Weather Review* **128** (4), 1139–1152.

Emanuel, K.A. 2003 Tropical cyclones. *Annual review of earth and planetary sciences* **31** (1), 75–104.

Emanuel, K. A. 1986 An air-sea interaction theory for tropical cyclones. part i: Steady-state maintenance. *Journal of the Atmospheric Sciences* **43** (6), 585–605.

FAA & NOAA 1975 *Aviation Weather For Pilots and Flight Operations Personnel*. Federal Aviation Administration.

Farman, J. C., Gardiner, B. G. & Shanklin, J. D. 1985 Large losses of total ozone in antarctica reveal seasonal clox/nox interaction. *Nature* **315** (6016), 207.

Ferziger, J. H. & Peric, M. 2002 *Computational methods for fluid dynamics*. Springer.

Fiedler, B. H. & Rotunno, R. 1986 A theory for the maximum windspeeds in tornado-like vortices. *Journal of the atmospheric sciences* **43** (21), 2328–2340.

Fincham, A. M. & Delerce, G. 2000 Advanced optimization of correlation imaging velocimetry algorithms. *Experiments in Fluids* **29** (1), S013–S022.

Fincham, A. M. & Spedding, G. R. 1997 Low cost, high resolution dpiv for measurement of turbulent fluid flow. *Experiments in Fluids* **23** (6), 449–462.

Fletcher, C. A. J. 1997 *Computational techniques for fluid dynamics 2: Specific techniques for different flow categories*. Springer.

Frank, W. M. 1977 The structure and energetics of the tropical cyclone i. storm structure. *Monthly Weather Review* **105** (9), 1119–1135.

Fuentes, O. V. 2014 Early observations and experiments on ring vortices. *European Journal of Mechanics-B/Fluids* **43**, 166–171.

Gall, J. S., Kwon, Y. & Frank, W. 2006 The effect of sea spray on tropical cyclone intensity. *27th Conference on Hurricanes and Tropical Meteorology* .

Gharib, M., Rambod, E. & Shariff, K. 1998 A universal time scale for vortex ring formation. *Journal of Fluid Mechanics* **360**, 121–140.

Golden, J. H. 1968 Waterspouts at Lower Matecumbe Key, Florida, 2 September 1967. *Weather* **23** (3), 103–115.

Golden, J. H. 1971 Waterspouts and tornadoes over south Florida. *Mon. Wea. Rev* **99**, 146–154.

Golden, J. H. 1974 The life cycle of Florida Keys' waterspouts. i. *Journal of Applied Meteorology* **13** (6), 676–692.

Gray, W. M. 1967 Global view of the origin of tropical disturbances and storms. *Technical paper no. 114* .

Greenspan, H. P. 1968 *The theory of rotating fluids*. Cambridge University Press.

Gresho, P. M. 1991 Incompressible fluid dynamics: some fundamental formulation issues. *Annual review of fluid mechanics* **23** (1), 413–453.

Gresho, P. M. & Sani, R. L. 1987 On pressure boundary conditions for the incompressible navier-stokes equations. *International Journal for Numerical Methods in Fluids* **7** (10), 1111–1145.

Griffiths, R. W. 1986 Thermals in extremely viscous fluids, including the effects of temperature-dependent viscosity. *Journal of Fluid Mechanics* **166**, 115–138.

Harlow, F. H. & Stein, L. R. 1974 Structural analysis of tornado-like vortices. *Journal of the Atmospheric Sciences* **31** (8), 2081–2098.

Harlow, F. H. & Welch, J. E. 1965 Numerical calculation of time-dependent viscous incompressible flow of fluid with free surface. *Physics of Fluids* **8** (12), 2182.

Helmholtz, H. 1858 Über integrale der hydrodynamischen gleichungen, welche den wirbelbewegungen entsprechen. *Journal für die reine und angewandte Mathematik* **55**, 25–55.

Henderson, G. A. & Aldridge, K. D. 1992 A finite-element method for inertial waves in a frustum. *Journal of Fluid Mechanics* **234**, 317–327.

Hirsch, C. 2007 *Numerical Computation of Internal and External Flows: The Fundamentals of Computational Fluid Dynamics*. Elsevier Science.

Holton, J. R. & Hakim, G. J. 2012 *An introduction to dynamic meteorology*, , vol. 88. Academic Press.

Kasahara, A. & da Silva Dias, P. L. 1986 Response of planetary waves to stationary tropical heating in a global atmosphere with meridional and vertical shear. *Journal of the atmospheric Sciences* **43** (18), 1893–1912.

King, E. M. & Aurnou, J. M. 2012 Thermal evidence for taylor columns in turbulent rotating rayleigh-bénard convection. *Physical Review E* **85** (1), 016313.

Knaff, J.A., Longmore, S.P. & Molenar, D.A. 2014 An objective satellite-based tropical cyclone size climatology. *Journal of Climate* **27** (1), 455–476.

Koschmieder, E. L. 1974 Bénard convection. *Adv. Chem. Phys* **26**, 177–212.

Lamb, H. 1932 *Hydrodynamics*. Cambridge University Press.

LEGI 2018 Matlab toolbox uvmat. http://servforge.legi.grenoble-inp.fr/projects/soft-uvmat/wiki, accessed: 2018-06-01.

Lewis, B. M. & Hawkins, H. F. 1982 Polygonal eye walls and rainbands in hurricanes. *Bulletin of the American Meteorological Society* **63** (11), 1294–1300.

Linden, P. F. & Turner, J. S. 2001 The formation of 'optimal'vortex rings, and the efficiency of propulsion devices. *Journal of Fluid Mechanics* **427**, 61–72.

Lovelock, J. E. & Margulis, L. 1974 Atmospheric homeostasis by and for the biosphere: the gaia hypothesis. *Tellus* **26** (1-2), 2–10.

Lugt, H. J. 1983 *Vortex flow in nature and technology*. Wiley-Interscience.

Markowski, P. M. & Richardson, Y. P. 2009 Tornadogenesis: Our current understanding, forecasting considerations, and questions to guide future research. *Atmospheric Research* **93** (1), 3–10.

Maroto, J. A., Pérez-Munuzuri, V. & Romero-Cano, M. S. 2007 Introductory analysis of bénard–marangoni convection. *European journal of physics* **28** (2), 311.

Marshall, S. D. & Read, P. L. 2018 An experimental investigation of blocking by partial barriers in a rotating baroclinic annulus. *Geophysical & Astrophysical Fluid Dynamics* **112** (2), 97–129.

Maxworthy, T. 1972 On the structure of concentrated, columnar vortices. *Astronautica Acta* **17** (4-5), 363–374.

Maxworthy, T. 1973 A vorticity source for large-scale dust devils and other comments on naturally occurring columnar vortices. *Journal of the Atmospheric Sciences* **30** (8), 1717–1722.

McDonald, J.R. & Mehta, K.C. 2009 Development, implementation and implications of the enhanced Fujita scale. *SMiRT 20 - Espoo (Helsinki), Finland* **04** (2a).

McKee, S., Tomé, M. F., Cuminato, J. A., Castelo, A. & Ferreira, V. G. 2004 Recent advances in the marker and cell method. *Archives of Computational Methods in Engineering* **11** (2), 107.

Montgomery, M. T., Vladimirov, V. A. & Denissenko, P. V. 2002 An experimental study on hurricane mesovortices. *Journal of Fluid Mechanics* **471**, 1–32.

Morton, B. R. 1966 Geophysical vortices. *Progress in Aerospace Sciences* **7**, 145–194.

Morton, B. R., Taylor, G. I. & Turner, J. S. 1956 Turbulent gravitational convection from maintained and instantaneous sources. *Proceedings of the Royal Society of London. Series A. Mathematical and Physical Sciences* **234** (1196), 1–23.

Mullen, J. B. & Maxworthy, T. 1977 A laboratory model of dust devil vortices. *Dynamics of Atmospheres and Oceans* **1** (3), 181–214.

Munroe, R. 2016 Earth temperature timeline. https://xkcd.com/1732/.

Neumann, C.J. 1993 *Tropical Cyclones of the North Atlantic Ocean, 1871-1992*, , vol. 6. National Oceanic and Atmospheric Administration, National Weather Service.

Norbury, J. 1973 A family of steady vortex rings. *Journal of Fluid Mechanics* **57** (3), 417–431.

Ooyama, K. 1969 Numerical simulation of the life cycle of tropical cyclones. *Journal of the Atmospheric Sciences* **26**, 3–40.

Oruba, L., Davidson, P. A. & Dormy, E. 2017 Eye formation in rotating convection. *Journal of Fluid Mechanics* **812**, 890–904.

Oruba, L., Davidson, P. A. & Dormy, E. 2018 Formation of eyes in large-scale cyclonic vortices. *Phys. Rev. Fluids* **3**, 013502.

Patankar, S. 1980 *Numerical heat transfer and fluid flow*. Hemisphere Publishing Coorporation.

Pearce, R. P. 1998 A study of hurricane dynamics using a two-fluid axisymmetric model. *Meteorology and Atmospheric Physics* **67** (1-4), 71–81.

Pearce, R. P. 2004 An axisymmetric model of a mature tropical cyclone incorporating azimuthal vorticity. *Quarterly Journal of the Royal Meteorological Society* **130** (596), 259–293.

Pearce, R. P. 2005*a* Comments on "Why must hurricanes have eyes? –revisited". *Weather* **60** (11), 329–330.

Pearce, R. P. 2005*b* Why must hurricanes have eyes? *Weather* **60** (1), 19–24.

Purser, R. J. & Kar, S. K. 2002 Radiative upper-boundary conditions for a non-hydrostatic atmosphere. *Quarterly Journal of the Royal Meteorological Society: A journal of the atmospheric sciences, applied meteorology and physical oceanography* **128** (582), 1343–1366.

Raffel, M., Willert, C. E., Wereley, D. T. & Kompenhans, J. 2007 *Particle image velocimetry: a practical guide*. Springer.

Rafkin, S., Jemmett-Smith, B., Fenton, L., Lorenz, R., Takemi, T., Ito, J. & Tyler, D. 2016 Dust devil formation. *Space Science Reviews* **203** (1), 183–207.

Rasmussen, E.A., Turner, J. & Thorpe, A.J. 2004 Polar lows: Mesoscale weather systems in the polar regions. *Quarterly Journal of the Royal Meteorological Society* **130** (596), 371–372.

Raupp, C. F. M. & Silva Dias, P. L. 2009 Resonant wave interactions in the presence of a diurnally varying heat source. *Journal of the Atmospheric Sciences* **66** (10), 3165–3183.

Reasor, P. D., Montgomery, M. T., Marks Jr, F. D. & Gamache, J. F. 2000 Low-wavenumber structure and evolution of the hurricane inner core observed by airborne dual-doppler radar. *Monthly Weather Review* **128** (6), 1653–1680.

Richardson, L. F. 1922 *Weather prediction by numerical process*. Cambridge University Press.

Rossby, H. T. 1969 A study of bénard convection with and without rotation. *Journal of Fluid Mechanics* **36** (2), 309–335.

Rotunno, R. 1977 Numerical simulation of a laboratory vortex. *Journal of the Atmospheric Sciences* **34** (12), 1942–1956.

Rotunno, R. 1979 A study in tornado-like vortex dynamics. *Journal of the Atmospheric Sciences* **36** (1), 140–155.

Rotunno, R. 1980 Vorticity dynamics of a convective swirling boundary layer. *Journal of Fluid Mechanics* **97** (03), 623–640.

Rotunno, R. 2013 The Fluid Dynamics of Tornadoes. *Annual Review of Fluid Mechanics* **45** (1), 59–84.

Rotunno, R. & Emanuel, K. A. 1987 An air-sea interaction theory for tropical cyclones. part ii: Evolutionary study using a nonhydrostatic axisymmetric numerical model. *Journal of the Atmospheric Sciences* **44** (3), 542–561.

Ryan, J. A. & Carroll, J. J. 1970 Dust devil wind velocities: Mature state. *Journal of Geophysical Research* **75** (3), 531–541.

Saad, Y. 2003 *Iterative methods for sparse linear systems*. SIAM.

Saffman, P. G. 1970 The velocity of viscous vortex rings. *Studies in Applied Mathematics* **49** (4), 371–380.

Saffman, P. G. 1992 *Vortex dynamics*. Cambridge University Press.

Sànchez, O., Raymond, D. J., Libersky, L. & Petschek, A. G. 1989 The development of thermals from rest. *Journal of the Atmospheric Sciences* **46** (14), 2280–2292.

Scorer, R. S. 1957 Experiments on convection of isolated masses of buoyant fluid. *Journal of Fluid Mechanics* **2** (06), 583–594.

Scorer, R. S. 1978 *Environmental aerodynamics*. Halsted Press.

Shlien, D. J. 1976 Some laminar thermal and plume experiments. *Physics of Fluids* **19** (8), 1089–1098.

Shlien, D. J. & Thompson, D. W. 1975 Some experiments on the motion of an isolated laminar thermal. *Journal of Fluid Mechanics* **72** (01), 35–47.

Sinclair, P. C. 1966 A quantitative analysis of the dust devil. PhD thesis, The University of Arizona.

Sinclair, P. C. 1973 The lower structure of dust devils. *Journal of the Atmospheric Sciences* **30** (8), 1599–1619.

Smith, R. K. 1968 The surface boundary layer of a hurricane. *Tellus* **20** (3), 473–484.

Smith, R. K. 1980 Tropical Cyclone Eye Dynamics. *Journal of the Atmospheric Sciences* **37** (6), 1227–1232.

Smith, R. K. 2005 "Why must hurricanes have eyes?"–revisited. *Weather* **60** (11), 326–328.

Snow, J. T. 1982 A review of recent advances in tornado vortex dynamics. *Reviews of Geophysics* **20** (4), 953–964.

Staplehurst, P. J., Davidson, P. A. & Dalziel, S. B. 2008 Structure formation in homogeneous freely decaying rotating turbulence. *Journal of Fluid Mechanics* **598**, 81–105.

Stein, L. R. & Harlow, F. H. 1974 Numerical solution of the flow structure in tornado-like vortices. *Tech. Rep.* LA-5713-MS. Los Alamos Scientific Laboratory.

Strahan, S. E. & Douglass, A. R. 2018 Decline in antarctic ozone depletion and lower stratospheric chlorine determined from aura microwave limb sounder observations. *Geophysical research letters* **45** (1), 382–390.

Sukhanovskii, A., Evgrafova, A. & Popova, E. 2016*a* Horizontal rolls over localized heat source in a cylindrical layer. *Physica D: Nonlinear Phenomena* **316**, 23–33.

Sukhanovskii, A., Evgrafova, A. & Popova, E. 2016*b* Laboratory study of a steady-state convective cyclonic vortex. *Quarterly Journal of the Royal Meteorological Society* **142** (698), 2214–2223.

Thompson, D. W. 1961 *On Growth and Form*. Cambridge University Press.

della Torre, G. M. 1755 *Storia e fenomeni del Vesuvio esposti dal pd Gio. Maria Della Torre....* Presso Giuseppe Raimondi.

Turner, J. S. 1957 Buoyant vortex rings. *Proceedings of the Royal Society A: Mathematical, Physical and Engineering Sciences* **239** (1216), 61–75.

Vallis, G. K. 2016 Geophysical fluid dynamics: whence, whither and why? *Proceedings of the Royal Society A: Mathematical, Physical and Engineering Sciences* **472** (2192), 20160140.

Vallis, G. K. 2017 *Atmospheric and oceanic fluid dynamics*. Cambridge University Press.

Van Dyke, M. 1982 *An album of fluid motion*. Parabolic Press Stanford.

Veronis, G. 1959 Cellular convection with finite amplitude in a rotating fluid. *Journal of Fluid Mechanics* **5** (3), 401–435.

Veronis, G. 1970 The analogy between rotating and stratified fluids. *Annual Review of Fluid Mechanics* **2** (1), 37–66.

Vince, G. 2009 One last chance to save mankind. *NewScientist* .

Volk, A. & Kähler, C. J. 2018 Density model for aqueous glycerol solutions. *Experiments in Fluids* **59** (5), 75.

Wang, Y. 2012 Recent research progress on tropical cyclone structure and intensity. *Tropical Cyclone Research and Review* **1** (2), 254–275.

Wang, Y., Kepert, J. D. & Holland, G. J. 2001 The effect of sea spray evaporation on tropical cyclone boundary layer structure and intensity. *Monthly Weather Review* **129** (10), 2481–2500.

Ward, N. B. 1972 The exploration of certain features of tornado dynamics using a laboratory model. *Journal of the Atmospheric Sciences* **29** (6), 1194–1204.

Welch, J. E., Harlow, F. H., Shannon, P. J. & Daly, J. B. 1965 The MAC Method. *Tech. Rep.* LA-3425. Los Alamos Scientific Laboratory.

Whitehouse, D. 2000 Etna hoops it up. *BBC News* .

Woodhouse, M. J., Hogg, A. J., Phillips, J. C. & Sparks, R. S. J. 2013 Interaction between volcanic plumes and wind during the 2010 eyjafjallajökull eruption, iceland. *Journal of Geophysical Research: Solid Earth* **118** (1), 92–109.

Wróbel-Niedzwiecka, I., Drozdowska, V. & Piskozub, J. 2019 Effect of drag coefficient formula choice on wind stress climatology in the north atlantic and the european arctic. *Oceanologia* .

Wurman, J., Straka, J. M. & Rasmussen, E. N. 1996 Fine-scale doppler radar observations of tornadoes. *Science* **272** (5269), 1774.

Appendix A

Inertial waves in a cylinder

Here we provide the derivation for standing inertial waves in a cylindrical geometry. The solution is for a cylinder of radius R and height H, axially aligned with the rotation axis. The cylinder and the fluid inside rotates at rate Ω. We seek wave solutions as perturbations to the solid body rotation. The boundary conditions on the domain are zero velocity normal to the surfaces, i.e. $u_r = 0$ on $r = R$ and $u_z = 0$ on $z = 0$ and $z = H$.

We start with the equations for angular momentum and vorticity in a rotating fluid, neglecting viscous effects:

$$\frac{\mathrm{D}\Gamma}{\mathrm{D}t} = -2\Omega r u_r \ , \tag{A.1}$$

and

$$\frac{\mathrm{D}}{\mathrm{D}t}\left(\frac{\omega_\phi}{r}\right) = \frac{\partial}{\partial z}\left(\frac{\Gamma^2}{r^4}\right) + \frac{2\Omega}{r}\frac{\partial u_\phi}{\partial z} \ . \tag{A.2}$$

The vorticity can be written in terms of the Stokes stream function as

$$r\omega_\phi = -\nabla_*^2 \Psi \ , \tag{A.3}$$

whilst the velocity can be written as

$$\mathbf{u}_p = \nabla \times \left(\frac{\Psi}{r}\hat{\mathbf{e}}_\phi\right) = \left(-\frac{1}{r}\frac{\partial \Psi}{\partial z}, \, 0, \, \frac{1}{r}\frac{\partial \Psi}{\partial r}\right) \ , \tag{A.4}$$

such that our boundary conditions become

$$\left.\frac{\partial \Psi}{\partial z}\right|_{r=R} = 0 \quad , \quad \left.\frac{\partial \Psi}{\partial r}\right|_{z=0,H} = 0 \ . \tag{A.5}$$

We seek solutions of small amplitude which allows us to linearise the equations as follows:

$$\frac{\partial \Gamma}{\partial t} = -2\Omega r u_r \ , \tag{A.6}$$

and

$$\frac{\partial}{\partial t}\left(\frac{\omega_\phi}{r}\right) = \frac{2\Omega}{r}\frac{\partial u_\phi}{\partial z} \ . \tag{A.7}$$

Taking the time derivative of equation A.7 allows it to be combined with equation A.6 to eliminate Γ and write the equation in terms of streamfunction:

$$\frac{\partial^2}{\partial t^2}\left(\nabla_*^2 \Psi\right) = -\left(2\Omega\right)^2 \frac{\partial^2 \Psi}{\partial z^2} \ , \tag{A.8}$$

which we can see will support waves of the form $\Psi = \hat{\Psi}\left(r, z\right) \exp\left[i\varpi t\right]$. Substituting this expression results in

$$\nabla_*^2 \hat{\Psi} = \left(\frac{2\Omega}{\varpi}\right)^2 \frac{\partial^2 \hat{\Psi}}{\partial z^2} \ . \tag{A.9}$$

Using separation of variables we assume that the solution can be written in the form

$$\hat{\Psi}(r, z) = r\Psi_r(r) \sin\left(kz\right) \ , \tag{A.10}$$

where k is a wavenumber $(n\pi)/H$. Substituting this results, after some algebra, in

$$r^2 \frac{\partial^2 \Psi_r}{\partial r^2} + r\frac{\partial \Psi_r}{\partial r} + \left(\eta^2 r^2 - 1\right)\Psi_r = 0 \ , \tag{A.11}$$

where

$$\eta = k\sqrt{\left(\frac{2\Omega}{\varpi}\right)^2 - 1} \ , \tag{A.12}$$

which we recognise as a Bessel equation with the solution

$$\Psi_r = C_1 J_1\left(\eta r\right) + C_2 Y_1\left(\eta r\right) \ . \tag{A.13}$$

We require solutions to remain finite at the axis which tells us that $C_2 = 0$. Applying the radial boundary condition results in

$$\eta R = \zeta_m \ , \tag{A.14}$$

where ζ_m is the mth zero of the Bessel function J_1. Rearranging this tells us that the frequency of the oscillations for the mode $(r, z) = (m, n)$ is

$$\varpi_{m,n} = \frac{2\Omega}{\sqrt{1 + \left(\frac{H\zeta_m}{n\pi R}\right)^2}} \ , \tag{A.15}$$

which is consistent with the requirement that inertial waves have a frequency between 0 and $2\,\Omega$. Finally this allows us to write down an expression for the streamfunction of the mode (m, n) as being

$$\Psi_{m,n} = A\, r\, J_1\left(\frac{\zeta_m}{R} r\right) \sin\left(\frac{n\pi}{H} z\right) e^{\left(i\varpi_{m,n} t\right)} \ , \tag{A.16}$$

from which we can obtain expressions for Γ, ω_ϕ, and $\mathbf{u}_p$.